Analyses of multi-species greenhouse gases and related tracers using novel measurements at Weybourne Atmospheric Observatory, Norfolk, UK

By

Leigh S. Fleming

A thesis submitted to the School of Environmental Sciences of the University of East Anglia in partial fulfilment of the requirements for the degree of Doctor of Philosophy

School of Environmental Sciences

University of East Anglia, UK

March 2023

Abstract

Carbon dioxide (CO_2) is the most important greenhouse gas that influences anthropogenic climate change, yet a full understanding of the carbon cycle is still lacking. Measurement of CO_2 alone provides a limited understanding of carbon cycle processes. Measurement of other gas species as 'tracers' provides additional information regarding carbon cycle processes. This thesis explores novel measurements of tracers, and novel methods for tracer applications for use in carbon cycle studies, using the Weybourne Atmospheric Observatory (WAO), UK, as a case study.

A 'Picarro G2207-*i*' O_2 analyser was tested in the laboratory and at WAO. The potential benefits of this analyser are reduction in calibration gas consumption and fewer drying requirements. The built-in water-correction procedure did not sufficiently correct for the influence of water vapour on the O_2 mole fraction. A reference gas cylinder was required to reduce the influence of baseline drift. When measuring dry, ambient air, the G2207-*i*'s results showed an average difference from the established O_2 analyser of 13.6±7.5 per meg. The overall performance was not quite as good as established analysers.

Radon-222 was used to derive monthly maritime 'background' concentrations for multiple atmospheric gases. These backgrounds were compared to those calculated from other methods. The radon-derived backgrounds displayed good agreement with other methods, with some variability depending on the processes involved in a species' sources and sinks. The radon method appropriately filtered air masses which had recent interaction with terrestrial land masses.

Measurement of $\delta^{13}C$, $\delta^{18}O$ and $\delta^{17}O$ in CO_2 using an Aerodyne TILDAS analyser were conducted at WAO, and used to calculate $\Delta^{17}O$. Two calibration methodologies were explored, with small differences between the results. The repeatability of the $\delta^{13}C$, $\delta^{17}O$ and $\delta^{18}O$ were all within the WMO goals; the $\Delta^{17}O$ results were outside the goals, but in the context of ambient variability, still allow useful interpretation.

List of contents

List of tables

List of figures

Acknowledgements

Firstly, the biggest thank you to my supervisory team: Andrew Manning, Grant Forster, and Penelope Pickers, for their support and guidance throughout this PhD, always making time for my questions, and for their many comments on my drafts. Thank you, Andrew, for taking the time to explain the nuances of O_2 and CO_2 measurements (and many other things) to me over many long meetings. Thank you, Grant, for always helping me at Weybourne and reminding me that everything will be OK. Thank you, Penelope, for helping me understand isotopologues, and for running the Aerodyne.

Thank you to Marica Hewitt, for help with orders and running the flagging script for the Ren O_2/CO_2 system every week and to Alex Etchells for building the software for the Picarro O_2 system and Ren, and for helping me at Weybourne.

In relation to Chapter 2, I am very grateful to Gregor Lucic and Magdalena Hofmann at Picarro Inc. for the loaning of the G2207-*i* analyser and their feedback on a draft manuscript.

I also extend my gratitude to Matthew Ashfold at the University of Nottingham Malaysia for providing me with NAME footprints and to Alistair Manning at the University of Bristol for providing the NAME modelled backgrounds used in Chapter 3.

Thank you to the many lifelong friends I have made in Norwich during this PhD, and our numerous trips to sample Norwich's 'fine' pubs, that have kept me somewhat sane over the past 4 years.

Finally, thank you to my parents for their endless support (emotional and financial…) through my 10 years of being a student at UEA, which has felt like a lifetime.

Chapter 1 Introduction

1.1 Climate change and the global carbon cycle

Anthropogenic influence on the global climate is now a well-established fact, and is unequivocally the primary cause of increasing global warming (e.g., IPCC, 2021a) (Figure 1.1). The Earth's global average surface temperature has increased by around 1.1°C relative to the 1850-1900 average (Gillett et al., 2021). The impacts of this warming are already being observed: for example, the average ocean surface temperature has increased by 0.88°C between the periods 1850-1900 and 2011-2020, global mean sea level has risen 0.20 m over the period 1901-2018, and the frequency and intensity of hot climate extremes have increased on a global scale since 1950 (IPCC, 2021a).

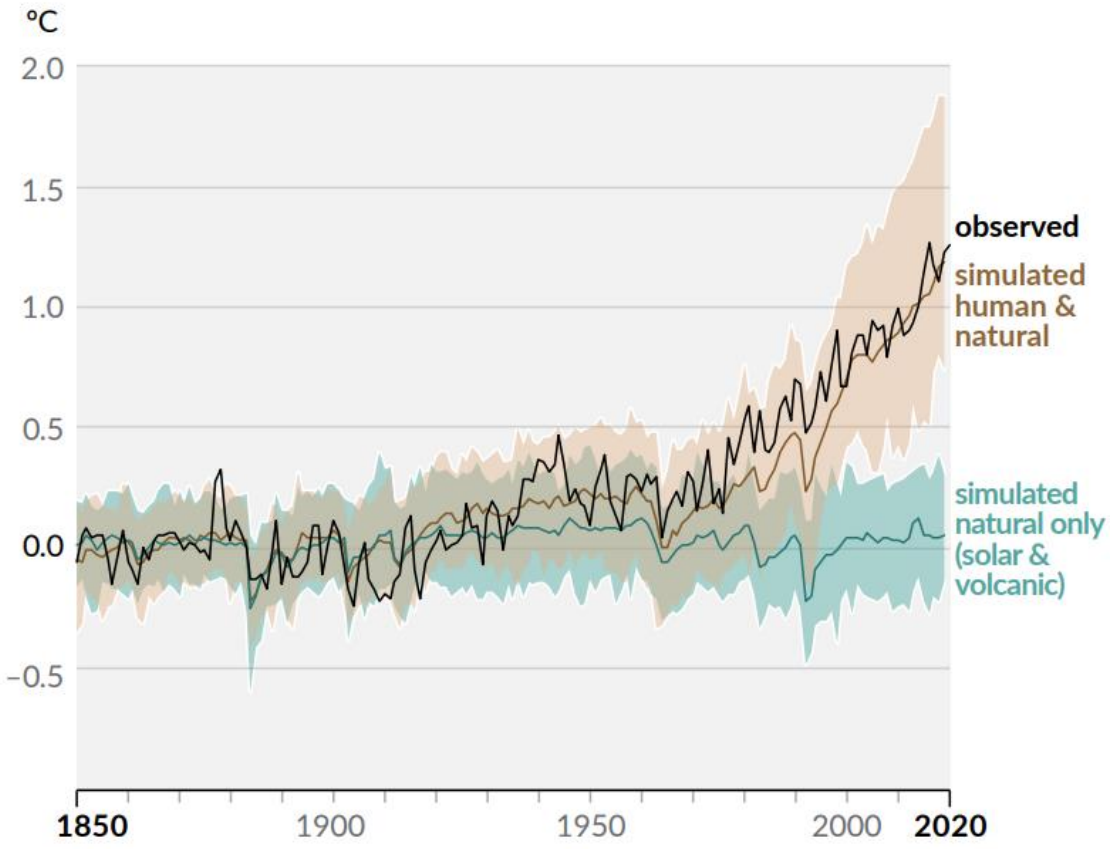

Figure 1.1. Change in the global surface temperature (annual averages) as observed (black line) and simulated using 'human and natural' (brown line) and 'natural only' (green line) factors (Source: IPCC, 2021b). In recent decades, the natural only forcing cannot explain the observations.

Greenhouse gases (GHGs) are a major contributing factor in controlling the global surface temperature, due to the 'greenhouse effect'. These gases absorb infrared radiation emitted by the Earth within the atmosphere that would otherwise

be reflected back into space. Without any GHGs the Earth would be more than 30°C cooler and uninhabitable for life. However, increases in the abundance of GHGs in the atmosphere are disturbing this natural greenhouse effect through additional radiative forcing, and causing global temperatures to rise. Since 1950, the increase in GHG emissions to the atmosphere has been the dominant cause of human-induced climate change, with carbon dioxide (CO_2) being the most important, having contributed approximately 80% of the effective change in radiative forcing from 1750 to 2019 (Forster et al., 2021). The mole fraction of CO_2 in the atmosphere has increased from approximately 277 ppm in 1750, at the start of the industrial era, to 412.4 ± 0.1 ppm in 2020 (Friedlingstein et al., 2020).

The climate science community has developed a number of Shared Socioeconomic Pathways (SSPs) which describe potential future pathways for greenhouse gas emissions and socio-economic factors (O'Neill et al., 2014; Riahi et al., 2017). Figure 1.2 shows model projections for global temperature change, global land precipitation change, September Arctic sea ice area, and global mean sea level change under a range of these different SSPs. The figure shows both the range of potential future outcomes depending on the pathway as well as the large degree of uncertainty of the future impacts of anthropogenic forcings on the climate system. The modelling of future impacts of a changing climate is further complicated by numerous feedback processes which can act to either amplify or suppress changes in the climate.

Due to the impacts of a changing climate already experienced, and the modelled future impacts and feedback uncertainties, limiting future warming through reductions in anthropogenic GHG emissions has become a topic of major political and scientific discussion. A key outcome of this recognition is that 194 nations and the European Union (EU) have signed and ratified the Paris Agreement with the intent of "holding the increase in the global average temperature to well below 2°C above preindustrial levels and pursuing efforts to limit the temperature increase to 1.5°C above preindustrial levels, recognising that this would significantly reduce the risks and impacts of climate change" (UNFCCC, 2015, p. 2). However, the discussion of the relationship between GHG emissions and climate targets is set within the context of, and hindered by, the uncertainties which characterise the climate's response to GHG emissions.

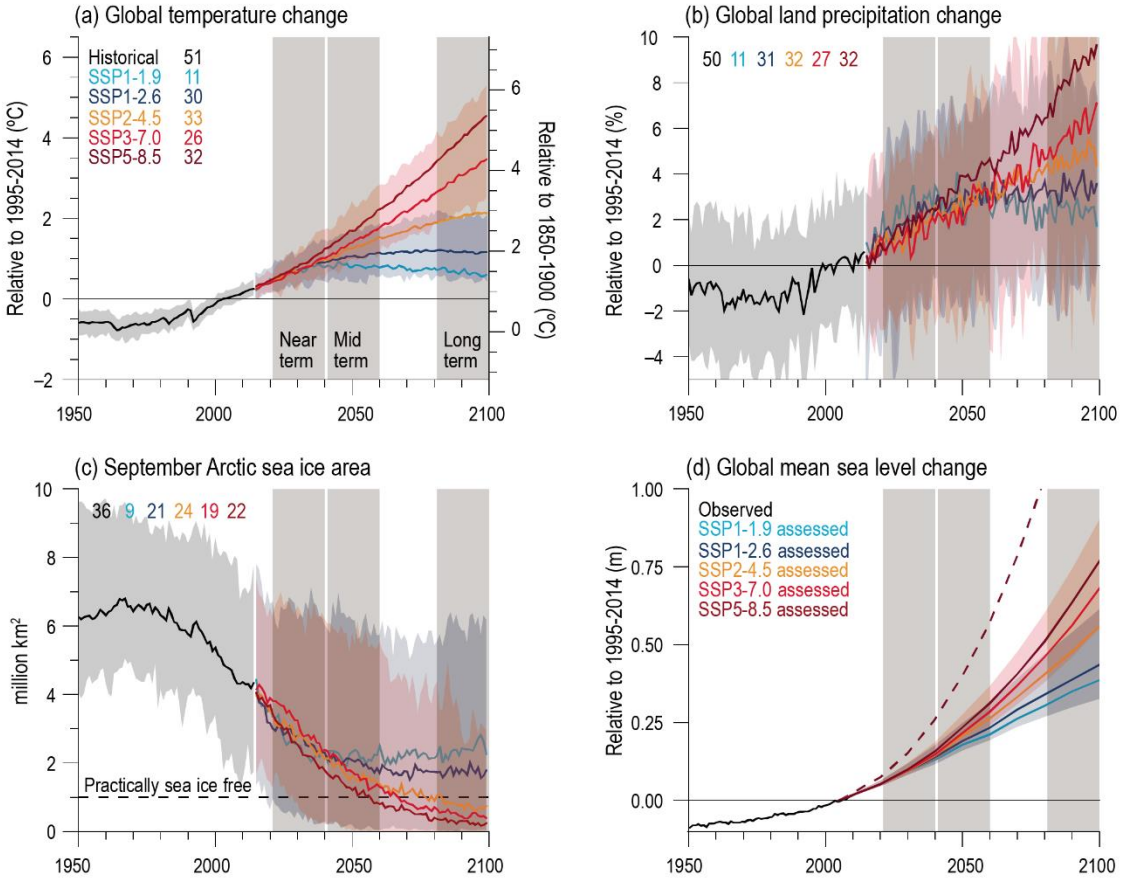

Figure 1.2. IPCC AR6 modelled historical and projected indicators of global climate change from the Coupled Model Intercomparison Project Phase 6 (CMIP6) (O'Neill et al., 2016). (a) Global surface air temperature, (b) global land precipitation change, (c) September Arctic sea ice area, and (d) global mean sea level. The black lines show CMIP6 historical evolution, with uncertainty shaded in grey. The coloured lines show the CMIP6 model projection in each indicator for Shared Socioeconomic Pathways (SSP) 1-1.9, 1-2.6, 2-4.5, 3-7.0, and 5-8.5 (Lee et al., 2021).

One of the largest uncertainties in the climate's response to CO_2 emissions can be attributed to a lack of full understanding of the processes involved in the carbon cycle, since climate projections are currently hindered by the inability to characterise feedbacks between a changing climate and the sources and sinks of CO_2 (Friedlingstein et al., 2014). Anthropogenic CO_2 emissions occur on top of the natural carbon cycle (Figure 1.3) that circulates carbon between four major reservoirs: the atmosphere, oceans, the terrestrial biosphere, and the geosphere. The residence time of carbon within these reservoirs ranges from a few years for the atmosphere to decades or centuries for the terrestrial biosphere, soils, and the ocean. In general, the geosphere is not relevant in the context of anthropogenic climate change due to residence times in this reservoir being on the scale of millennia.

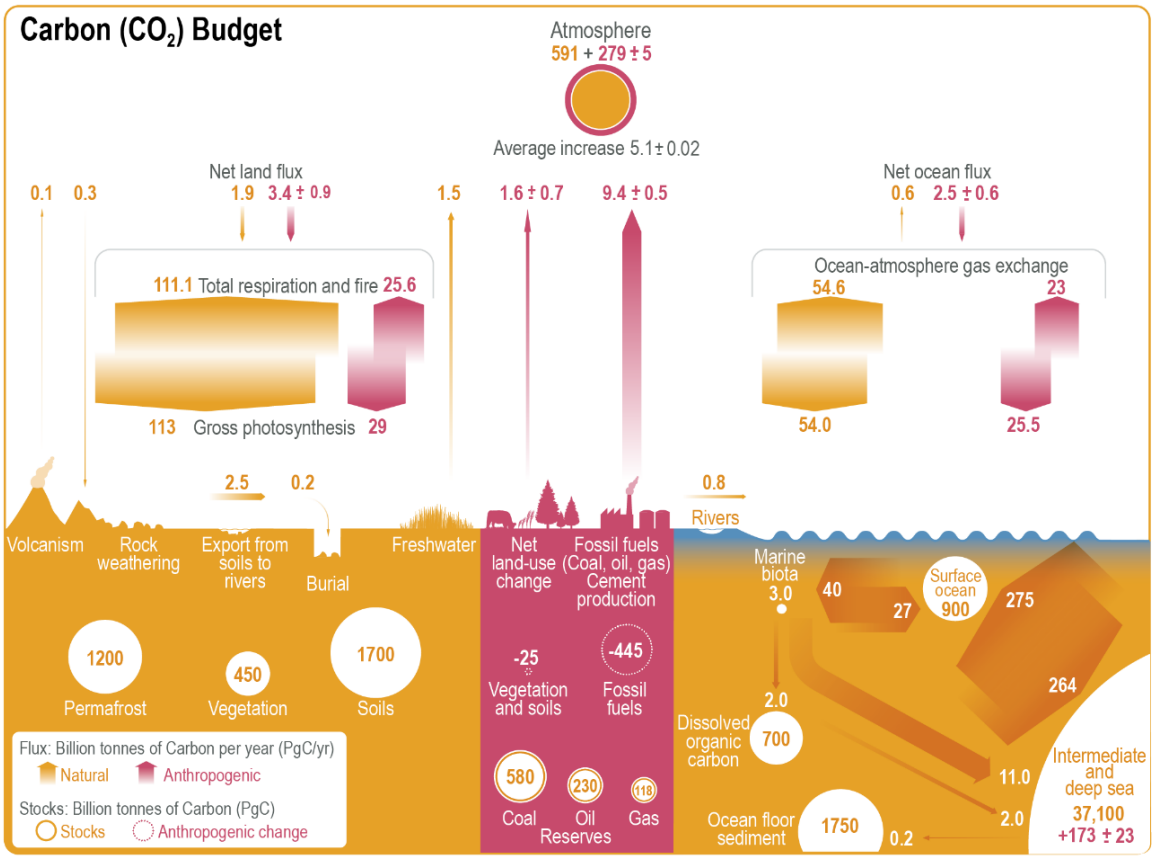

Figure 1.3. Simplified schematic of the global carbon cycle from Canadell et al. (2021). Numbers represent reservoir mass in PgC and fluxes in PgC yr^{-1}. Yellow numbers and arrows represent pre-industrial (pre-1750) natural carbon reservoirs and fluxes. Pink numbers and arrows represent anthropogenic changes to the carbon reservoirs and anthropogenic fluxes averaged over the decade 2010-2019.

Over the decade 2010-2019, 10.9 ± 0.9 PgC yr^{-1} were emitted from anthropogenic activity as CO_2 into the atmosphere, including land use change. Of this amount, 46 % remained in the atmosphere, 23 % was taken up by the ocean, and 31 % was stored in the terrestrial biosphere (Canadell et al., 2021). These ocean and land carbon sinks play a very important role in mitigating the effects of anthropogenic climate change; however, the future roles and sizes of these sinks are uncertain due to climate-carbon cycle feedback processes. Recent observations show that ocean carbon processes are beginning to change in response to the growing ocean carbon sink; in the future these changes are expected to significantly contribute to a weakening of the ocean sink (Canadell et al., 2021). Due to continuing ocean acidification there is evidence of a reduced CO_2 storage capacity, and in addition, ocean warming and changes in circulation and biology will likely cause enhanced outgassing of CO_2 (Gruber et al., 2023).

The land carbon sink is largely controlled by the rates of photosynthesis and respiration, resulting in relatively large fluxes to and from the atmosphere,

respectively. Current evidence suggests that land carbon storage is presently increasing at a global scale (Sitch et al., 2015), with a key role being played by increased levels of atmospheric CO_2 enhancing photosynthesis, meaning greater CO_2 uptake (referred to as the CO_2 fertilisation effect) (Ainsworth and Long, 2005). However, there are also signs that the trend of the increasing land sink may be slowing down (Peñuelas et al., 2017), where the positive effects of increased atmospheric CO_2 on carbon storage may be offset by increasing temperatures (Fernández-Martínez et al., 2019) and changes in precipitation patterns and water availability (Humphrey et al., 2018; Humphrey et al., 2021). It is clear that there are a large number of uncertainties associated with climate-carbon cycle feedbacks and that a better understanding of the carbon cycle and the processes that govern it is needed in order to better assess the future impacts of climate change.

1.2 Atmospheric carbon dioxide

CO_2 in the atmosphere has been measured accurately since 1958 at the Mauna Loa Observatory, Hawaii (Figure 1.4; black) by the Scripps Institution of Oceanography (SIO), and, since the 1970s, concurrently by the National Oceanic and Atmospheric Administration (NOAA; not shown in the figure) . This atmospheric CO_2 record, known as the 'Keeling curve', shows the long-term increasing trend due to fossil fuel combustion and land-use change, and the seasonal cycle caused by increased terrestrial photosynthesis over respiration during spring and summer, and the opposite during autumn and winter, in the northern hemisphere (black line). Figure 1.4 also shows the atmospheric CO_2 mole fraction time series from the South Pole, Antarctica (red line); as with Mauna Loa there is a long-term increase due to fossil fuel combustion and land use change. However, the seasonal cycle at the South Pole is of a much smaller magnitude than at Mauna Loa, owing to a much smaller terrestrial biosphere in the southern hemisphere.

Since the first continuous CO_2 record was established at Mauna Loa, a number of networks of monitoring sites that measure atmospheric CO_2 mole fractions to a high degree of precision and accuracy have been established, either from in-situ continuous measurements or from regularly collected flask samples analysed in a central laboratory (e.g. Manning et al., 2011; Keeling and Graven, 2021; Heiskanen et al., 2022).

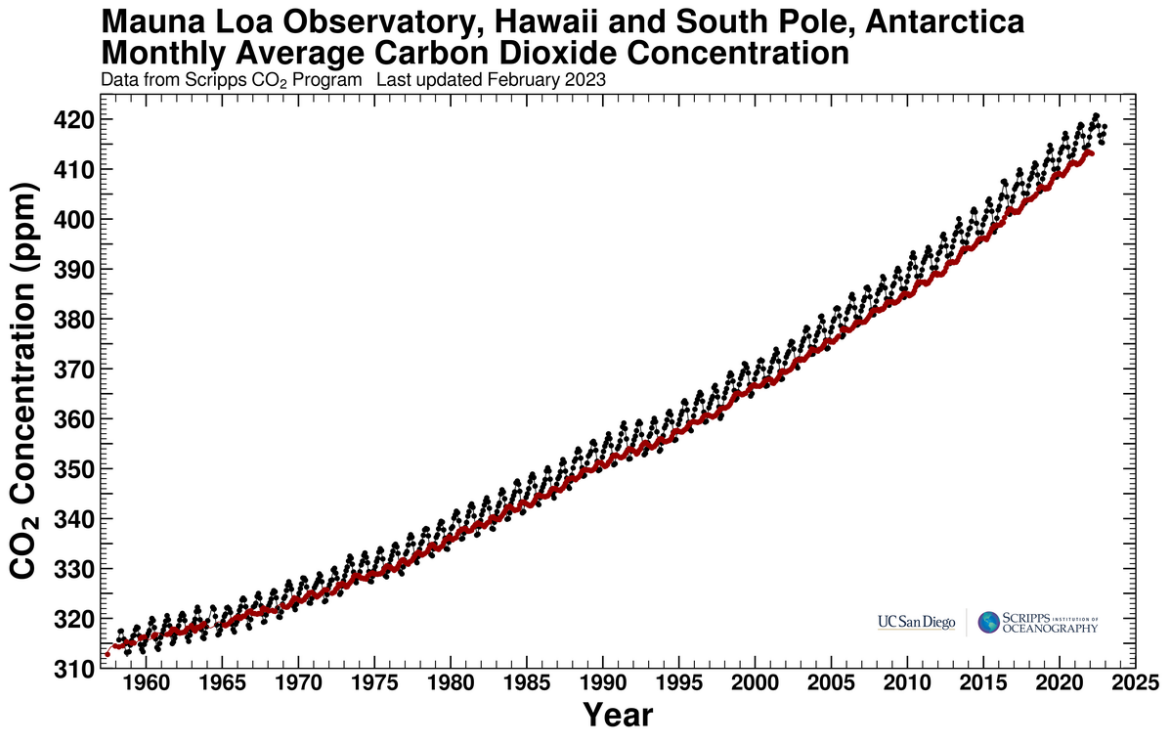

Figure 1.4. Atmospheric CO_2 mole fraction measured at the Mauna Loa Observatory, Hawaii (black) and the South Pole, Antarctica (red) by the Scripps Institution of Oceanography. Monthly averaged data are shown as dots. (https://scrippsco2.ucsd.edu/graphics_gallery/mauna_loa_and_south_pole/mauna_loa_and_south_pole.html).

These measurement networks provide reliable measures of CO_2 mole fraction in the atmosphere. However, for atmospheric gas species such as CO_2 that have numerous flux mechanisms, measurement of the atmospheric mole fraction alone is inadequate to attribute and quantify the contribution of the different sources and sinks to the atmospheric abundance (Weiss and Prinn, 2011; Vardag et al., 2015; Pickers et al., 2022). In order to gain a profound understanding of the processes governing the carbon cycle and climate feedbacks, to accurately represent these processes in models, and to understand how sources and sinks may change under future climate scenarios, there is a need to distinguish the contributions to the atmospheric CO_2 mole fraction from different sources and sinks. There are three types of methods used for distinguishing the influence of CO_2 from different processes: 'bottom-up' inventory techniques, 'top-down' measurement and modelling studies, and those based on 'tracer' measurements.

'Bottom-up' techniques based on inventory, economic or statistical data have been used in a number of applications. For example, bottom-up techniques are used to estimate CO_2 emissions from fossil fuels based on emission factors being applied to statistical data, such as fuel consumption, which are scaled-up to a regional or

national scale (e.g., Gurney et al., 2019; Han et al., 2020); however, there are significant uncertainties associated with these inventories (Peylin et al., 2011). Inventory techniques have also been used to quantify the land carbon sink (e.g. Baker et al., 2004; Pan et al., 2011; Williams et al., 2014); however, these methods have coarse temporal resolution and can have large biases for local applications due to the methods used for inventory sampling (Williams et al., 2014). More recently, inventory methods have been used to quantify fossil fuel CO_2 emissions reductions resulting from COVID-19 lockdowns (Le Quéré et al., 2020).

Another commonly used method for estimating fluxes from measurements of CO_2 mole fractions is to combine the measurements with atmospheric transport models, in so-called top-down inversion modelling methods (e.g. Bousquet et al., 1999; Rödenbeck et al., 2003). Examples of uses of inversion models include estimation of changes in the land (e.g. Stephens et al., 2007b; Bastos et al., 2020) and ocean carbon sinks (Le Quéré et al., 2007). However, there are still large uncertainties in these methods such as estimating boundary layer height, modelled atmospheric transport and errors related to the resolution of the model (Tolk et al., 2008; Munassar et al., 2023).

The third method for understanding the factors contributing to the measured atmospheric CO_2 mole fraction, which will be explored in this thesis, is through the measurement of other atmospheric gas species, known as tracers.

1.3 Measurement of tracers for understanding atmospheric CO_2 variations

Since the growth of the CO_2 atmospheric measurement networks, observations of other gas species have also seen a major expansion. Measurement of other species, alongside the measurements of CO_2, can be used as markers for distinct processes such as atmospheric mixing or exchange with other reservoirs. Such species, when used in this manner, are referred to as 'tracers'. Tracers are therefore a critical tool for the analyses of time series of CO_2 in atmospheric research.

One type of tracer method is the measurement of species which share flux mechanisms with CO_2 during different carbon cycle processes. For example, carbon monoxide (CO) can be produced together with CO_2 in specific ratios as a result of incomplete combustion depending on fuel type and combustion efficiency (Djuricin et al., 2010). Variations in CO, alone and in combination with other tracer species, have

therefore been used to identify and quantify fossil fuel CO_2 ($ffCO_2$) fluxes (e.g., Gamnitzer et al., 2006; Turnbull et al., 2006; Lopez et al., 2013; Young et al., 2023). Carbonyl sulfide (COS) is another example of a species which shares flux mechanisms with CO_2, with the primary sink of COS being uptake by vegetation and soils; COS is therefore being utilised as a tracer for terrestrial CO_2 uptake (e.g. Berry et al., 2013; Spielmann et al., 2019; Parazoo et al., 2021).

Another tracer method is the measurement of isotopic ratios of CO_2. For example, the radiocarbon ratio ($^{14}C/^{12}C$) of atmospheric CO_2 has been used as a tracer for $ffCO_2$ emissions on various scales (e.g. Turnbull et al., 2009; Djuricin et al., 2010; Miller et al., 2012). Due to its relatively short half-life of 5730 ± 40 years (Godwin, 1962), radiocarbon is absent in fossil fuels due to radioactive decay, whereas all other sources of CO_2 contain radiocarbon mole fractions close to that of ambient air (Turnbull et al., 2006; Graven and Gruber, 2011); thus, the combustion of fossil fuels depletes the atmospheric ratio of $^{14}C/^{12}C$ (Keeling, 1979). However, measurements of the radiocarbon content of air are very expensive, and cannot be performed continuously (Gamnitzer *et al.,* 2006), with additional issues in certain regions, such as the UK, owing to interference from nuclear power plant ^{14}C emissions (Graven and Gruber, 2011; Vogel et al., 2013).

As well as providing information regarding CO_2 fluxes, tracers also have other applications in atmospheric research. One key difficulty in understanding the processes influencing the atmospheric CO_2 mole fraction (and that of other gas species) is defining the 'background' or 'baseline' mole fraction. Background air is typically defined as air that is free of local influences, and therefore characteristic of a large portion of the atmosphere. Atmospheric gas species with long residence times in the atmosphere lead to a background mole fraction that is controlled by sources and sinks; any pollution events then occur on top of this background; the quantification of the different components of the measured mole fraction therefore first requires a separation of 'background' and 'non-background' signals. Some tracers can be used to define background air, based on their presence or absence in an air mass. For example, CO, NO_x and black carbon have all been used as tracers to isolate background air masses (Tsutsumi et al., 2006; Zellweger et al., 2003; Pu et al., 2014; Fang et al., 2015), due to being co-emitted with CO_2 during combustion processes.

The following sections will introduce the tracers investigated in this thesis, and their applications.

1.3.1 Atmospheric oxygen

Oxygen (O_2) is the second most abundant species in the atmosphere, after nitrogen, with a mole fraction of about 20.94%. The mole fraction of oxygen in the atmosphere varies as a result of photosynthesis, respiration, and combustion. The application of O_2 as a tracer for carbon cycle processes is based on the fact that fluxes of CO_2 and O_2 are strongly anti-correlated in some processes and not in others. The main processes influencing atmospheric O_2 and CO_2 are shown schematically in Figure 1.5.

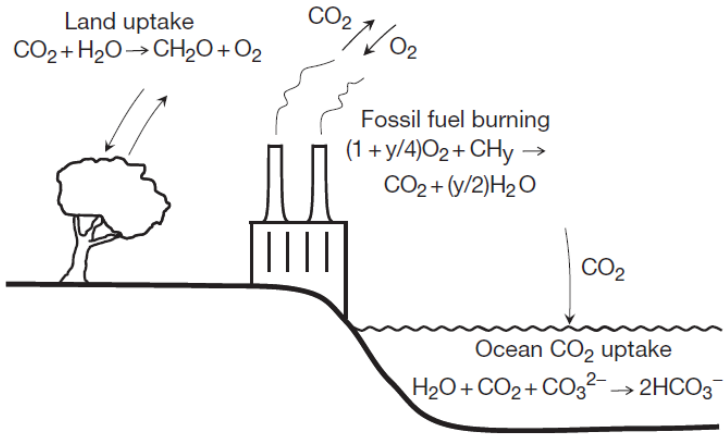

Figure 1.5. Schematic of the main processes influencing the long-term trends in atmospheric O_2 and CO_2 (Keeling and Manning, 2014).

Fluxes of O_2 and CO_2 to and from the atmosphere due to terrestrial photosynthesis and respiration are strongly anti-correlated. This relationship can be represented conceptually using Eq. (1.1),

$$6CO_2 + 6H_2O \leftrightarrow C_6H_{12}O_6 + 6O_2 \quad (1.1)$$

During this process, on average, 1.1 moles of O_2 are consumed for each mole of CO_2 produced, and vice versa, hence the mean global O_2:CO_2 oxidative ratio (OR) is approximately 1.1:1.0 mol mol^{-1} (Severinghaus, 1995). Eq. (1.1) suggests an OR of exactly 1, but this is a simplified version of terrestrial exchange, neglecting the incorporation of nutrients such as nitrates and phosphates. This OR is variable at different spatial and temporal scales from between 0.9 to 1.2 mol mol^{-1}, with uncertainties regarding this variability (e.g. Masiello et al., 2008; Worrall et al., 2013; Battle et al., 2019; Faassen et al., 2023; Yan et al., 2023).

Fluxes of CO_2 and O_2 arising from fossil fuel combustion are also strongly anti-correlated (Eq. (1.2)) (Keeling and Manning, 2014).

$$C_xH_y + (x + \frac{y}{4})O_2 \rightarrow xCO_2 + \frac{y}{2}H_2O \quad (1.2)$$

where C_xH_y represents the composition of the fuel, which could be coal, natural gas, or hydrocarbons. This process has a globally weighted average OR of 1.4:1.0 mol mol^{-1}. This OR varies depending on fuel type: liquid fuels have an OR of 1.44 mol mol^{-1}, solid fuels have a typical OR of 1.17 mol mol^{-1}, and gases typically have an OR of 1.95 mol mol^{-1} (Keeling, 1988b; Steinbach et al., 2011).

Fluxes of CO_2 and O_2 between the ocean and atmosphere are, in contrast, uncoupled. This results from differences in the solubility and seawater chemistry between CO_2 and O_2. When CO_2 dissolves in seawater, it dissociates to form carbonate and bicarbonate ions; whereas, in contrast, O_2 is chemically inert in seawater and not involved in the ocean carbonate reactions that buffer changes in atmospheric CO_2.

Atmospheric O_2 has been measured from fortnightly flask samples collected at the Mauna Loa Observatory, Hawaii since the early 1990s by SIO (Scripps Institution of Oceanography). Figure 1.6 shows the O_2 and CO_2 time-series from Mauna Loa, which are anti-correlated. O_2 shows a long-term decreasing trend due to fossil fuel combustion. The seasonal cycle in O_2 is driven by exchange with the terrestrial biosphere and oceans, with a release of O_2 into the atmosphere during the spring and summer, and uptake during autumn and winter.

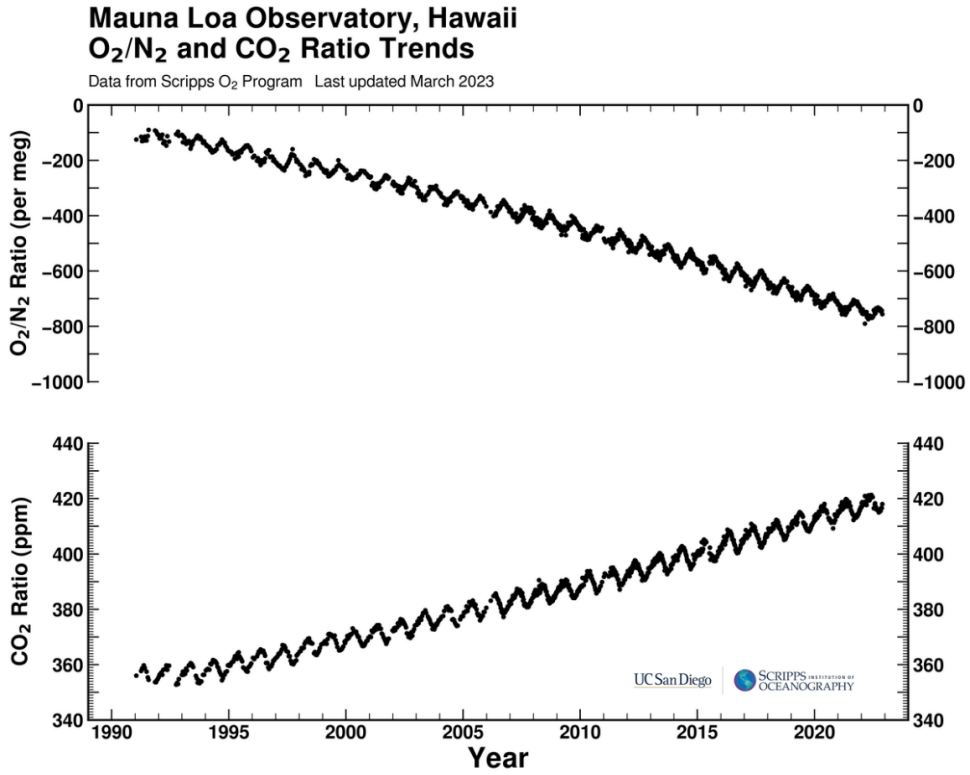

Figure 1.6. The atmospheric O_2/N_2 ratio and CO_2 mole fraction record from flask samples collected at Mauna Loa Observatory, Hawaii, by the Scripps Institution of Oceanography (https://scrippso2.ucsd.edu/graphics-gallery/daily-averages/mlo.html) . Data are from analyses of fortnightly flask samples collected at the station.

Changes in atmospheric O_2 are typically expressed as deviations in the O_2/N_2 ratio, in per meg units (Eq. (1.3)):

$$\delta\left(\frac{O_2}{N_2}\right) = \frac{r_{sample} - r_{ref}}{r_{ref}} \cdot 10^6 \quad (1.3)$$

where r is the O_2/N_2 ratio. Changes in $\delta(O_2/N_2)$ and CO_2 can be compared using a factor of 4.78 per meg/ppm; in other words, 1 ppm change in CO_2 is equivalent to a 4.78 per meg change in $\delta(O_2/N_2)$ (Keeling et al., 1998a). Most organisations measuring $\delta(O_2/N_2)$ report data on the SIO O_2 scale, where 'zero' per meg is arbitrarily defined from an air sample collected in 1988. For this reason, most subsequent $\delta(O_2/N_2)$ measurements are negative.

Using simultaneous measurements of O_2 and CO_2, the atmospheric tracer Atmospheric Potential Oxygen (APO) was derived by Stephens et al. (1998) (Eq. (1.4)):

$$APO = \Delta O_2 + (1.1 \times \Delta CO_2) \quad (1.4)$$

where the factor 1.1 accounts for the previously discussed OR for terrestrial photosynthesis and respiration. APO is therefore, by definition, conservative with respect to all terrestrial biosphere processes. Changes in APO therefore mainly reflect changes in ocean-atmosphere exchange of O_2 and CO_2 (on seasonal and longer timescales). Fossil fuels also have a contribution to the changes in APO, on both short and long timescales (Pickers et al., 2022); this is because fossil fuels have an average OR of 1.4 mol mol^{-1}, which is greater than the 1.1 factor inherent in the APO definition (Keeling and Manning, 2014).

Figure 1.7 shows an APO time series from flask samples collected at the Alert (Canada) and Cape Grim (Australia) stations from the Scripps O_2 programme (Keeling and Graven, 2021). There is a seasonal cycle and long-term downward trend in APO evident at both stations. As APO is conservative with respect to the land biosphere, and fossil fuel combustion has only a very minor seasonal component, the seasonal trend in APO is caused predominantly by air-sea O_2 exchange. This is reflected by the magnitude of the seasonal cycles, where the amplitude is slightly larger in the southern hemisphere due to the presence of more oceans than in the northern hemisphere. The long-term downward trend in APO is driven predominantly by fossil fuel combustion and long-term oceanic uptake of CO_2 (Keeling and Manning, 2014).

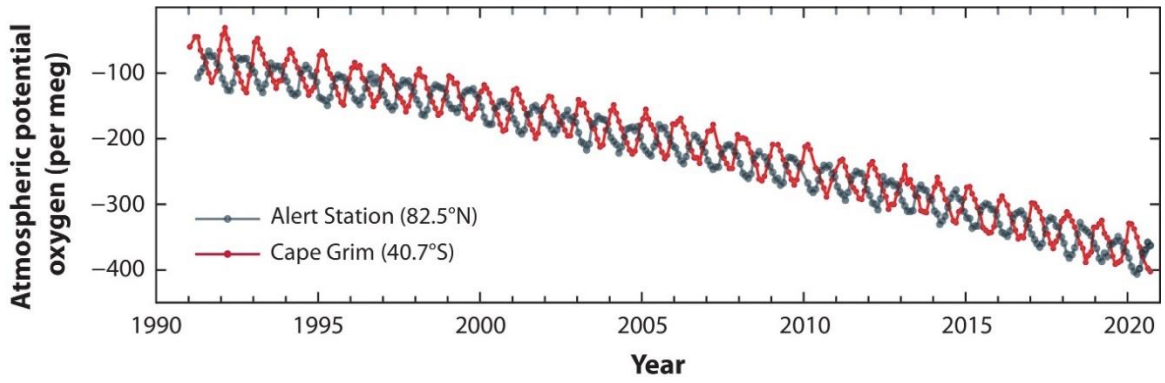

Figure 1.7. APO flask sample measurements collected from Alert Station, Canada in the northern hemisphere and Cape Grim, Australia in the southern hemisphere, from the Scripps O_2 programme (Keeling and Graven, 2021). As for O_2, APO is reported in per meg units.

$\delta(O_2/N_2)$ measurements are now included in a few international measurement programmes. Such measurements of atmospheric $\delta(O_2/N_2)$ alongside CO_2, have a wide number of applications as a tool for supporting carbon cycle studies.

One major application of $\delta(O_2/N_2)$ measurements, is quantification of the global ocean and land carbon sinks (e.g. Keeling and Shertz, 1992; Battle et al., 2000; Manning and Keeling, 2006; Tohjima et al., 2008; Tohjima et al., 2019). In addition, $\delta(O_2/N_2)$ measurements, and APO data derived from these, have been used to improve understanding of ocean processes such as: ocean heat uptake (Resplandy et al., 2019), ocean circulation (Nevison et al., 2020), ocean productivity and outgassing rates (e.g. Jin et al., 2007; Rödenbeck et al., 2008), and spatial and temporal features of air-sea gas exchange (e.g. Keeling et al., 1998b; Eddebbar et al., 2017). More recently, APO has also been demonstrated as a novel tracer for $ffCO_2$ (Pickers et al., 2022).

1.3.2 Radon-222

Radon-222 (^{222}Rn) is a noble gas generated as part of the decay chain of uranium-238 (^{238}U) from the alpha decay of radium-226 (^{226}Ra). As the first gaseous product in this decay chain, ^{222}Rn is emitted from soil and enters the atmosphere, and thus originates predominantly from soil and rock. The ocean, ground-water and natural gas also contribute ^{222}Rn to the atmospheric load, but these contributions are relatively very small (Porstendoerfer, 1994), with an oceanic source two to three orders of magnitude less than the terrestrial source (Zahorowski et al., 2013). As it is a noble gas, ^{222}Rn does not react chemically with other species; it is also poorly soluble in water and does not attach to aerosols, so it is not very susceptible to wet or

dry atmospheric deposition removal processes (Zahorowski et al., 2004). Thus, the only appreciable atmospheric sink of ^{222}Rn is radioactive decay with a half-life of 3.82 days, therefore it does not accumulate in the atmosphere on timescales longer than a month.

Of the radioactive trace elements in the atmosphere, radon has been the most widely researched, initially in the 1950s-1980s due to the health-risk posed from radon emissions in indoor air (Nazaroff, 1988). Environmental levels of radon are typically more than an order of magnitude lower than is typical indoors, but the aforementioned characteristics of radon also make it a reliable indicator of the extent of air mass contact with land, and thus radon observations have many applications as a tracer in atmospheric research.

As radon is emitted predominantly from the soil and rocks, it is an indicator of recent terrestrial influences on air masses (e.g. Liu et al., 1984; Polian et al., 1986; Chambers et al., 2014). Radon has also been used in studies as a background selection technique both in conjunction with other gas species, such as CO (Brunke et al., 2004) and in back trajectory analysis (Chambers et al., 2013), as well as alone (e.g. Chambers et al., 2016; Crawford et al., 2018). Radon is also an excellent tracer for boundary layer mixing processes (e.g. Dörr et al., 1983; Porstendoerfer, 1994); like other species emitted from sources close to the ground, radon accumulates in a shallow nocturnal boundary layer with little vertical mixing. Therefore, if the exhalation rate of radon from the ground is known, the correlation in the overnight increase of radon and gas species of interest (e.g. CO_2) can be used to estimate the flux of this gas; this is known as the radon tracer method (RTM; Levin et al., 1999). This application of radon has been used for GHG emission and sink estimates (e.g. Levin et al., 1999; Hammer and Levin, 2009; Vogel et al., 2012; Wada et al., 2013; Grossi et al., 2018). However, the RTM is reliant on the accuracy of radon flux maps and is limited by the reliability of night-time transport modelling (Levin et al., 2021). Additionally, radon has been used as a tracer in studies of vertical mixing and atmospheric stability (e.g. Chambers et al., 2011; Williams et al., 2013; Chambers et al., 2015).

1.3.3 Isotopologues of CO_2: $\delta^{13}C$, $\delta^{18}O$, $\delta^{17}O$, and $\Delta^{17}O$

Isotopologues are molecules that have the same chemical formula and differ only in their isotopic composition. Measurements of the isotopologues of CO_2 can be used as

tracers to help shed light on carbon cycle processes. The following sections will describe the isotopologues of CO_2 investigated in this thesis.

1.3.3.1 $\delta^{13}C$

Carbon has two stable isotopes: ^{12}C and ^{13}C, with approximately 99% of carbon on Earth present as ^{12}C and 1% as ^{13}C. One source of variation in the $^{13}C/^{12}C$ ratio of atmospheric CO_2 is linked to the exchange between the terrestrial biosphere and the atmosphere. Photosynthesis and respiration impart distinct isotopic signatures to the atmosphere due to isotopic discrimination. During photosynthesis, terrestrial plants preferentially assimilate $^{12}CO_2$ relative to $^{13}CO_2$, thereby enriching the $^{13}C/^{12}C$ ratio of the CO_2 that is left in the atmosphere (Flanagan and Ehleringer, 1998). Respiration reverses this process, thereby increasing atmospheric CO_2 and depleting its $^{13}C/^{12}C$ ratio. A similar effect is produced by fossil fuel combustion. fossil fuels are formed from ancient biological material thus they contain a lower $^{13}C/^{12}C$ ratio compared to the present-day atmosphere. Anthropogenic emissions of CO_2 resulting from the burning of fossil fuels therefore depletes the atmospheric $^{13}C/^{12}C$ ratio (Vardag et al., 2015). The net exchanges of CO_2 across the air-sea interface leaves $^{13}CO_2$ essentially unchanged (Battle et al., 2000). In terms of global carbon sinks, the $^{13}C/^{12}C$ ratio therefore behaves very similarly to O_2 (Section 1.3.1) (Battle et al., 2000).

Figure 1.8 shows $^{13}C/^{12}C$ ratio time series from flask samples collected at the Mauna Loa and South Pole observatories. This figure shows a long-term downward trend mirroring the increasing trend in the atmospheric CO_2 mole fraction, seasonal cycles with a strong hemispheric contrast, and interannual variability associated with El Niño events (Keeling and Graven, 2021).

Variations in the $^{13}C/^{12}C$ ratio are typically expressed in delta notation, in per mil units (Eq. (1.5)).

$$\delta^{13}C = \frac{r_{sample} - r_{ref}}{r_{ref}} \cdot 1000 \quad (1.5)$$

where r is the $^{13}C/^{12}C$ ratio. Most organisations measuring $\delta^{13}C$ report data on the Vienna Pee Dee Belemnite scale (VPDB), where 'zero' per mil is defined from a Pee Dee Belemnite carbonate sample with an anomalously high $^{13}C/^{12}C$ ratio. For this reason, most $\delta^{13}C$ measurements are negative.

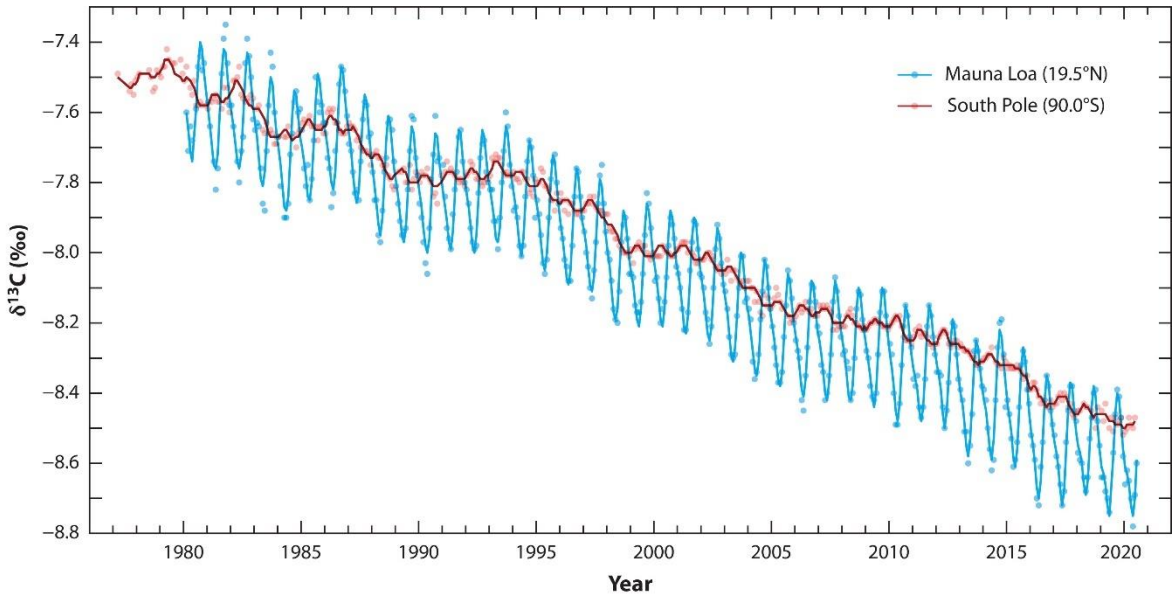

Figure 1.8. Monthly-averaged data for $\delta^{13}C$ of CO_2 from flask samples collected at Mauna Loa, Hawaii and South Pole, Antarctica observatories by the Scripps CO_2 programme (Keeling and Graven, 2021).

Atmospheric CO_2 mole fractions are anti-correlated with the atmospheric $^{13}C/^{12}C$ ratio; so even though variations in $\delta^{13}C$ are typically small, they can provide useful information about the sources and sinks of CO_2 in the atmosphere. An early motivation in $\delta^{13}C$ research was resolving the global land and ocean carbon sinks (e.g. Keeling, 1979; Ciais et al., 1995; Battle et al., 2000). Further, measurements of $\delta^{13}C$ have been widely used for source attribution of atmospheric CO_2, not only between terrestrial and oceanic sources, but also between specific fossil fuel types based on the isotopic source signature (e.g. Miller et al., 2003a; Vardag et al., 2016; Newman et al., 2016; Wang et al., 2022; Pieber et al., 2022). This source attribution can then be used for verification of bottom-up emission estimate methods (e.g. Newman et al., 2016; Wang et al., 2022).

1.3.3.2 $\delta^{18}O$, $\delta^{17}O$ and $\Delta^{17}O$

Oxygen has three stable isotopes, ^{16}O, ^{17}O, and ^{18}O; with the heavier isotopes being rarer on Earth (99.8 % for ^{16}O, 0.2 % for ^{18}O, and 0.04 % for ^{17}O; Affek and Yakir (2014)). It is recognised that the ^{18}O signal in CO_2 reflects a unique coupling between the global hydrological and carbon cycles, and can provide an important tracer of sinks and sources of CO_2, in particular, in the terrestrial biosphere (Affek and Yakir, 2014).

During CO_2 exchange with leaf, soil, and ocean water, the ^{18}O isotopes of CO_2 are exchanged with those of water. Stomatal water in plant leaves is highly enriched

in ^{18}O relative to soil water, due to mass-dependent fractionation during evapotranspiration, which imparts contrasting ^{18}O signatures in CO_2 released into the atmosphere after CO_2-H_2O exchange (e.g. Cuntz et al., 2003; Barthel et al., 2014). Furthermore, the equilibration and isotope exchange of CO_2 with water in stomata is catalysed by the presence of carbon anhydrase, which extensively enriches the CO_2 released from plants with ^{18}O from leaf-water. This isotope exchange process can therefore be directly related to gross primary production as first suggested by Farquhar et al. (1993).

As with $\delta^{13}C$, variations in the $^{18}O/^{16}O$ ratio are typically expressed in delta notation, in per mil units, as $\delta^{18}O$ (Eq. (1.5)). Figure 1.9 shows a $\delta^{18}O$ time series from flask samples collected at the South Pole, Mauna Loa, and Barrow observatories (Keeling and Graven, 2021). This figure shows a seasonal cycle in $\delta^{18}O$ that is larger in the northern hemisphere. In the northern hemisphere the seasonal cycle is dominated by terrestrial exchanges, whereas in the southern hemisphere there is a larger oceanic contribution (Cuntz et al., 2003). This exchange during the summer also leads to the northern hemispheric gradient of mean $\delta^{18}O$ observed in Figure 1.9, with lower values at higher latitudes (Francey and Tans, 1987). There is little evidence of a long-term trend in $\delta^{18}O$, due to the rapid turnover of oxygen atoms with the water reservoirs dominating over other influences. Interannual variability observed in the time-series is associated with El Niño events (Welp et al., 2011).

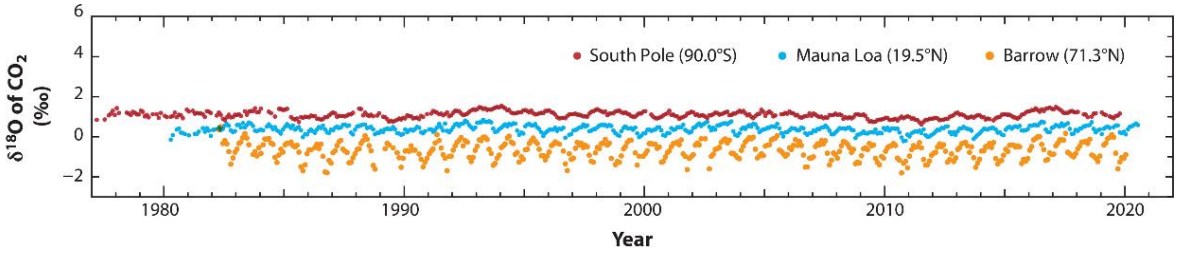

Figure 1.9. Monthly-averaged data for $\delta^{18}O$ of CO_2 from flask samples collected at Barrow, Alaska, Mauna Loa, Hawaii, and the South Pole, Antarctica from the Scripps O_2 programme (Figure adapted from Keeling and Graven, 2021).

As the $\delta^{18}O$ of atmospheric CO_2 is controlled largely by isotopic exchange with water in the leaves of plants, it is an important tool to estimate global gross primary production (GPP; the gross CO_2 uptake of plants from photosynthesis)(Francey and Tans, 1987). Measurements of $\delta^{18}O$ have been widely used to estimate gross carbon fluxes between the atmosphere and the terrestrial biosphere (e.g. Yakir and Wang, 1996; Ciais et al., 1997; Peylin et al., 1999; Cuntz et al., 2003). The response of $\delta^{18}O$ to El Niño events, driven by changes in tropical leaf- and soil-water $\delta^{18}O$ associated with

variable tropical droughts, has also been used to derive estimates of global GPP (Welp et al., 2011).

A challenge with using $\delta^{18}O$ to determine GPP, however, is the requirement for a detailed knowledge of $\delta^{18}O$ values in numerous water reservoirs, which can be highly variable due to the number of processes involved in the hydrological cycle. The addition of ^{17}O in CO_2 measurements can remove this requirement (Hoag et al., 2005). As with $\delta^{18}O$, the $^{17}O/^{16}O$ ratio is typically expressed in delta notation as $\delta^{17}O$. Due to mass-dependent fractionation, variations in ^{17}O are typically strongly correlated to variations in ^{18}O, with any deviation from this correlation (i.e. mass independent fractionation) being expressed as the $\Delta^{17}O$ signature (referred to in the literature as the 'triple oxygen isotope', 'CO_2 excess', or 'O_2 anomaly') (Eq. (1.6)).

$$\Delta^{17}O = \ln(\delta^{17}O + 1) - \lambda_{RL} \times \ln(\delta^{18}O + 1) \quad (1.6)$$

which is usually expressed in per mil (‰) or per meg (0.001‰) units, depending on the magnitude of the $\Delta^{17}O$ signature (Miller, 2002; Young et al., 2002); Very roughly, λ_{RL} is 0.5, representing the fact that the mass difference between the isotopes ^{17}O and ^{16}O is half of the mass difference between the isotopes ^{18}O and ^{16}O.

The processes which affect the isotopic composition of CO_2 usually depend on the mass of the molecules and therefore result in mass-dependent fractionation of the oxygen isotopes. An exception, however, is that compared to tropospheric CO_2, stratospheric CO_2 is anomalously enriched in ^{17}O and ^{18}O (e.g. Thiemens et al., 1991; Lämmerzahl et al., 2002; Yeung et al., 2009). This is linked to mass-independent fractionation of CO_2 during the formation of O_3, which imparts a positive $\Delta^{17}O$ signature (Yung et al., 1991). This enriched stratospheric CO_2 is transported into the upper troposphere (Laskar et al., 2019), where it mixes and eventually comes into contact with water reservoirs in vegetation, soil, and oceans. When CO_2 dissolves in liquid water, there is a mass-dependent exchange of oxygen atoms, meaning that the $\Delta^{17}O$ signature of the CO_2 released back into the atmosphere is reset to around 0 ‰ (Hoag et al., 2005). As a consequence, variations in the tropospheric $\Delta^{17}O$ signature strongly depend on the magnitude of CO_2 exchange with the leaf water reservoir and can therefore be directly related to biospheric activity (Hoag et al., 2005). However, unlike using $\delta^{18}O$ data alone, $\Delta^{17}O$ does not directly depend on the ^{18}O or ^{17}O of soil and leaf water since hydrological cycle processes are largely mass dependent (Hoag et al., 2005). $\Delta^{17}O$ should therefore be a more direct tracer for GPP than variations in $^{18}O/^{16}O$ alone. A schematic summary of the processes affecting the $\Delta^{17}O$ signature of atmospheric CO_2 on a global scale is displayed in Figure 1.10.

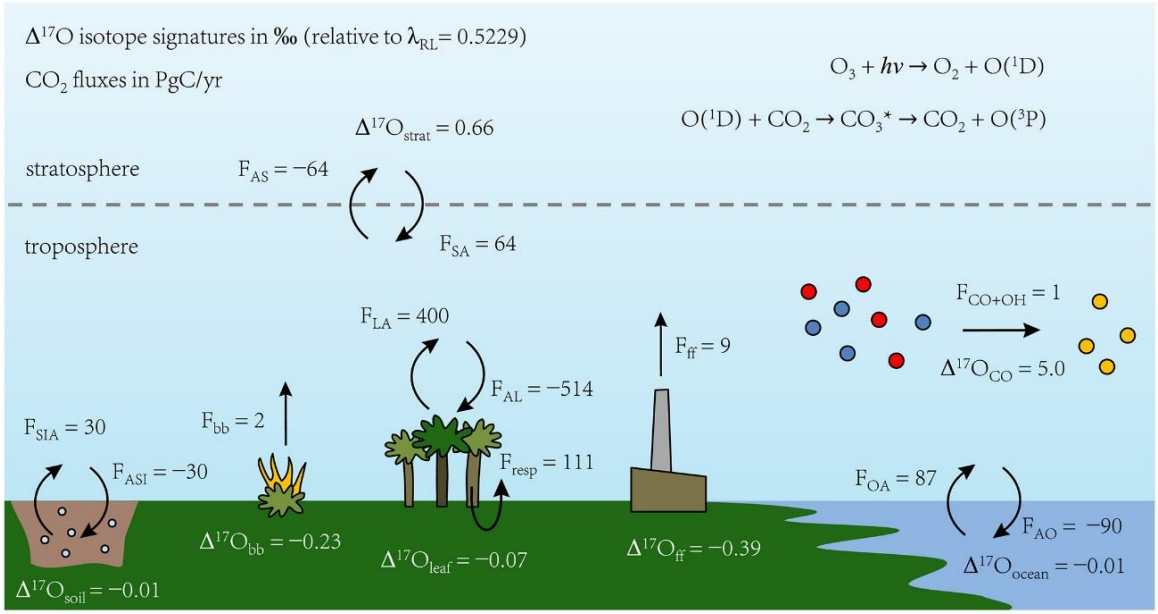

Figure 1.10. Schematic summary of the processes affecting the $\Delta^{17}O$ signature of atmospheric CO_2 as reported by Koren et al. (2019). The CO_2 mass fluxes (F), given in units of PgC/year, are globally integrated values averaged over 2012-2013 and rounded to integers. CO_2 mass fluxes that increase the tropospheric CO_2 mass are expressed as positive numbers. F_{AS}/F_{SA} is atmosphere (troposphere)-stratosphere exchange; F_{AL}/F_{LA} is atmosphere-leaf exchange; $F_{ASI/SIA}$ is atmosphere-soil exchange; F_{OA} is ocean-atmosphere exchange; and F_{bb} is flux from biomass burning. (Koren et al., 2019).

Measurement techniques for $\Delta^{17}O$ in tropospheric CO_2 only became sufficiently accurate for interpreting variations in the 2010s, providing new potential for insights into carbon cycle processes. Using these measurements, numerical models can then simulate atmospheric $\Delta^{17}O$ of CO_2 based on the representation of atmospheric mixing and the exchange processes of CO_2 isotopologues in vegetation. A number of global models for $\Delta^{17}O$ in tropospheric CO_2 have been developed (Hoag et al., 2005; Hofmann et al., 2017; Koren et al., 2019). Koren et al. (2019) presented the first global 3D $\Delta^{17}O$ model, which was used to predict the global signature, seasonal cycle, and vertical and latitudinal gradients. Barkan and Luz (2012) presented the first high-precision data on the $\Delta^{17}O$ composition of tropospheric CO_2 from a limited set of flask samples in Spring 2012 in Jerusalem, Israel. Additionally, Thiemens et al. (2014) presented a decade-long time series of $\Delta^{17}O$ measurements from flask samples collected in La Jolla, California. These measurements identified a stratospheric component in tropospheric CO_2 and discussed the role of El Niño Southern Oscillation indices in tropospheric excursions.

1.4 Weybourne Atmospheric Observatory

The Weybourne Atmospheric Observatory (WAO) is located on the north Norfolk coast of the UK (52.95°N, 01.12°E; see Figure 1.11).The station was established in 1992 by the University of East Anglia (UEA), and is a World Meteorological Organization (WMO) Global Atmosphere Watch (GAW) programme 'Regional' station, a European Union Integrated Carbon Observation System (ICOS) 'class II' station, and a UK National Centre for Atmospheric Science Atmospheric Measurement and Observation Facility (NCAS/AMOF). High-precision in-situ measurements of a very wide range of species are carried out at the station, namely: CO_2, O_2, CO, CH_4, H_2, O_3, N_2O, NO, NO_2, SF_6, ^{222}Rn, PM2.5, PM10, SO_2, NH_3, $\delta^{13}C$-CO_2 and $\delta^{18}O$-CO_2, as well as basic meteorological parameters. The air inlets for the gas species measurements are located 10 m above ground level (a.g.l) and 27 m above sea level (a.s.l), about 50 m from the North Sea coastline (www.weybourne.uea.ac.uk). The station is one hour's drive from UEA.

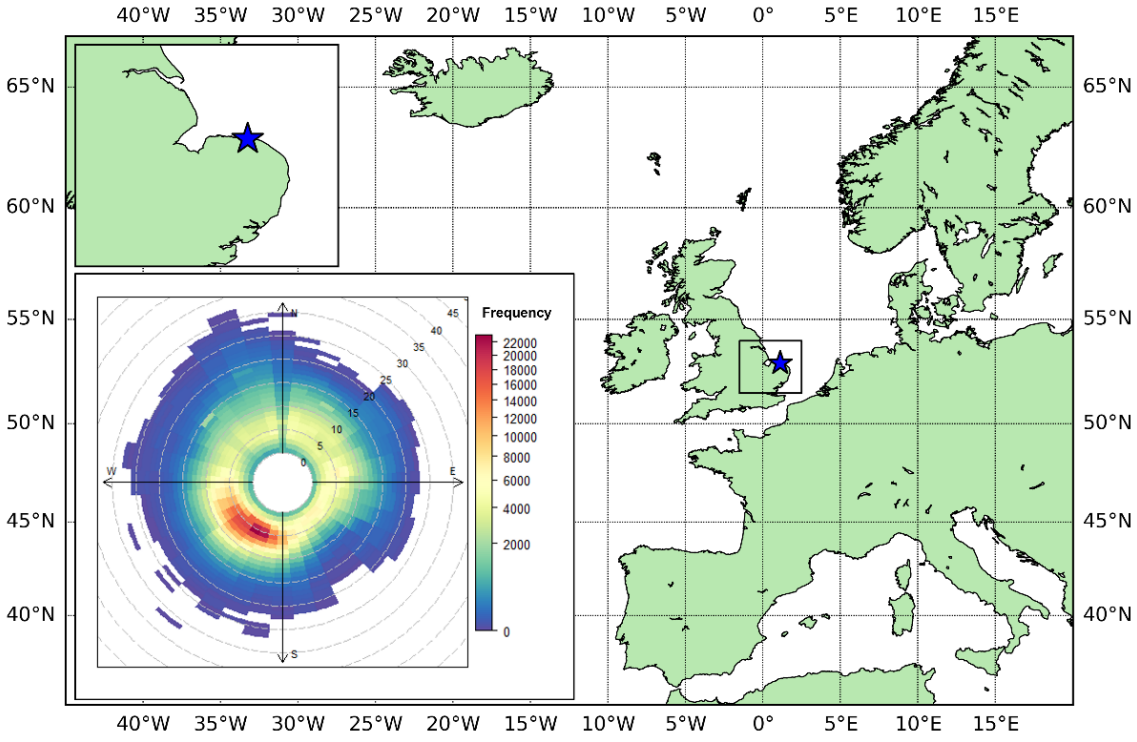

Figure 1.11. Map showing the location of the Weybourne Atmospheric Observatory (blue star), with a polar frequency plot inset showing wind speed (m s^{-1}) and wind direction at WAO averaged over the period 2016-2021 .

The array of species measured at WAO make it an ideal station for analyses of tracer methodologies. Additionally, WAO experiences rapidly changing wind directions, with multiple influences close by, and a number of rapidly changing sources of CO_2; thus, the station is at a strategic location for experiencing a variety of

air masses from a range of sources including relatively clean maritime air from the Atlantic and North Sea, and polluted continental Europe and UK air masses (Fleming et al., 2012).

1.5 Thesis objective and outline

The overarching objective of this thesis is to explore novel measurements of tracers and methods for tracer applications for use in carbon cycle studies, using the Weybourne Atmospheric Observatory as a case study and the common thread woven through my thesis.

The outline of this thesis is as follows. In chapter 2, I evaluate the performance of a Picarro G2207-*i* analyser for high precision atmospheric O_2 measurements, presenting in situ and laboratory tests of its precision and accuracy in comparison to an existing measurement system at WAO. Chapter 3 investigates the use of radon-222 as a tracer for maritime background air masses at WAO and demonstrates its use with multiple gas species in comparison to existing background calculation methodologies. Chapter 4 presents a year-long time series of high-precision CO_2, $\delta^{13}C$, $\delta^{17}O$, $\delta^{18}O$, and $\Delta^{17}O$ measurements at WAO using an Aerodyne dual-laser TILDAS analyser; the different calibration methods and resulting time series are then investigated. Finally, in Chapter 5, I summarise the key findings and conclusions, and outline potential future research.

References

Adcock, K. E., Pickers, P. A., Manning, A. C., Forster, G. L., Fleming, L. S., Barningham, T., Wilson, P. A., Kozlova, E. A., Hewitt, M. C., Etchells, A. J. and Macdonald, A. (2023) '12-years of continuous atmospheric O_2, CO_2 and APO data from Weybourne Atmospheric Observatory in the United Kingdom', *[In Prep]*.

Affek, H. P. and Yakir, D. (2014) '5.7 - The Stable Isotopic Composition of Atmospheric CO_2', in Holland, H.D. & Turekian, K.K. (eds.) *Treatise on Geochemistry (Second Edition)*. Oxford: Elsevier, pp. 179-212.

Ainsworth, E. A. and Long, S. P. (2005) 'What have we learned from 15 years of free-air CO_2 enrichment (FACE)? A meta-analytic review of the responses of photosynthesis, canopy properties and plant production to rising CO_2', *New Phytologist,* 165(2), pp. 351-372.

Baker, T. R., Phillips, O. L., Malhi, Y., Almeida, S., Arroyo, L., Di Fiore, A., Erwin, T., Higuchi, N., Killeen, T. J. and Laurance, S. G. (2004) 'Increasing biomass in Amazonian forest plots', *Philosophical Transactions of the Royal Society of London. Series B: Biological Sciences,* 359(1443), pp. 353-365.

Barkan, E. and Luz, B. (2012) 'High-precision measurements of $^{17}O/^{16}O$ and $^{18}O/^{16}O$ ratios in CO_2', *Rapid Communications in Mass Spectrometry,* 26(23), pp. 2733-2738.

Barthel, M., Sturm, P., Hammerle, A., Buchmann, N., Gentsch, L., Siegwolf, R. and Knohl, A. (2014) 'Soil $H_2{}^{18}O$ labelling reveals the effect of drought on $C^{18}OO$ fluxes to the atmosphere', *Journal of Experimental Botany,* 65(20), pp. 5783-5793.

Bastos, A., O'Sullivan, M., Ciais, P., Makowski, D., Sitch, S., Friedlingstein, P., Chevallier, F., Rödenbeck, C., Pongratz, J., Luijkx, I. T., Patra, P. K., Peylin, P., Canadell, J. G., Lauerwald, R., Li, W., Smith, N. E., Peters, W., Goll, D. S., Jain, A. K., Kato, E., Lienert, S., Lombardozzi, D. L., Haverd, V., Nabel, J. E. M. S., Poulter, B., Tian, H., Walker, A. P. and Zaehle, S. (2020) 'Sources of Uncertainty in Regional and Global Terrestrial CO_2 Exchange Estimates', *Global Biogeochemical Cycles,* 34(2), pp. e2019GB006393.

Battle, M., Bender, M. L., Tans, P. P., White, J. W. C., Ellis, J. T., Conway, T. and Francey, R. J. (2000) 'Global carbon sinks and their variability inferred from atmospheric O_2 and $\delta^{13}C$', *Science,* 287(5462), pp. 2467-2470.

Battle, M. O., Munger, J. W., Conley, M., Sofen, E., Perry, R., Hart, R., Davis, Z., Scheckman, J., Woogerd, J., Graeter, K., Seekins, S., David, S. and Carpenter, J. (2019) 'Atmospheric measurements of the terrestrial $O_2 : CO_2$ exchange ratio of a midlatitude forest', *Atmos. Chem. Phys.,* 19(13), pp. 8687-8701.

Berry, J., Wolf, A., Campbell, J. E., Baker, I., Blake, N., Blake, D., Denning, A. S., Kawa, S. R., Montzka, S. A., Seibt, U., Stimler, K., Yakir, D. and Zhu, Z. (2013) 'A coupled model of the global cycles of carbonyl sulfide and CO_2: A possible new window on the carbon cycle', *Journal of Geophysical Research: Biogeosciences,* 118(2), pp. 842-852.

Bousquet, P., Ciais, P., Peylin, P., Ramonet, M. and Monfray, P. (1999) 'Inverse modeling of annual atmospheric CO_2 sources and sinks: 1. Method and control inversion', *Journal of Geophysical Research: Atmospheres,* 104(D21), pp. 26161-26178.

Brunke, E. G., Labuschagne, C., Parker, B., Scheel, H. E. and Whittlestone, S. (2004) 'Baseline air mass selection at Cape Point, South Africa: application of ^{222}Rn and other filter criteria to CO_2', *Atmospheric Environment,* 38(33), pp. 5693-5702.

Canadell, J. G., Monteiro, P. M. S., Costa, M. H., Cotrim da Cunha, L., Cox, P. M., Eliseev, A. V., Henson, S., Ishii, M., Jaccard, S., Koven, C., Lohila, A., Patra, P. K., Piao, S., Rogelj, J., Syampungani, S., Zaehle, S. and Zickfeld, K. (2021) 'Global Carbon and other Biogeochemical Cycles and Feedbacks', in Masson-Delmotte, V., Zhai, P., Pirani, A., Connors, S.L., Péan, C., Berger, S., Caud, N., Chen, Y., Goldfarb, L., Gomis, M.I., Huang, M., Leitzell, K., Lonnoy, E., Matthews, J.B.R., Maycock, T.K., Waterfield, T., Yelekçi, O., Yu, R. & Zhou, B. (eds.) *Climate Change 2021: The Physical Science Basis. Contribution of Working Group I to the Sixth Assessment Report of the Intergovernmental Panel on Climate Change*. Cambridge, United Kingdom and New York, NY, USA: Cambridge University Press, pp. 673–816.

Chambers, S., Williams, A. G., Zahorowski, W., Griffiths, A. and Crawford, J. (2011) 'Separating remote fetch and local mixing influences on vertical radon measurements in the lower atmosphere', *Tellus B: Chemical and Physical Meteorology,* 63(5), pp. 843-859.

Chambers, S. D., Hong, S. B., Williams, A. G., Crawford, J., Griffiths, A. D. and Park, S. J. (2014) 'Characterising terrestrial influences on Antarctic air masses using Radon-222 measurements at King George Island', *Atmos. Chem. Phys.,* 14(18), pp. 9903-9916.

Chambers, S. D., Williams, A. G., Conen, F., Griffiths, A. D., Reimann, S., Steinbacher, M., Krummel, P. B., Steele, L. P., van der Schoot, M. V., Galbally, I. E., Molloy, S. B. and Barnes, J. E. (2016) 'Towards a Universal "Baseline" Characterisation of Air Masses for High- and Low-Altitude Observing Stations Using Radon-222', *Aerosol and Air Quality Research,* 16(3), pp. 885-899.

Chambers, S. D., Williams, A. G., Crawford, J. and Griffiths, A. D. (2015) 'On the use of radon for quantifying the effects of atmospheric stability on urban emissions', *Atmos. Chem. Phys.,* 15(3), pp. 1175-1190.

Chambers, S. D., Zahorowski, W., Williams, A. G., Crawford, J. and Griffiths, A. D. (2013) 'Identifying tropospheric baseline air masses at Mauna Loa Observatory between 2004 and 2010 using Radon-222 and back trajectories', *Journal of Geophysical Research: Atmospheres,* 118(2), pp. 992-1004.

Ciais, P., Denning, A. S., Tans, P. P., Berry, J. A., Randall, D. A., Collatz, G. J., Sellers, P. J., White, J. W. C., Trolier, M., Meijer, H. A. J., Francey, R. J., Monfray, P. and Heimann, M. (1997) 'A three-dimensional synthesis study of $\delta^{18}O$ in atmospheric CO_2: 1. Surface fluxes', *Journal of Geophysical Research: Atmospheres,* 102(D5), pp. 5857-5872.

Ciais, P., Tans, P. P., White, J. W. C., Trolier, M., Francey, R. J., Berry, J. A., Randall, D. R., Sellers, P. J., Collatz, J. G. and Schimel, D. S. (1995) 'Partitioning of ocean and land uptake of CO_2 as inferred by $\delta^{13}C$ measurements from the NOAA Climate Monitoring and Diagnostics Laboratory Global Air Sampling Network', *Journal of Geophysical Research: Atmospheres,* 100(D3), pp. 5051-5070.

Crawford, J., Chambers, S. D., Cohen, D. D., Williams, A. G. and Atanacio, A. (2018) 'Baseline characterisation of source contributions to daily-integrated PM2. 5 observations at Cape Grim using Radon-222', *Environmental Pollution,* 243, pp. 37-48.

Cuntz, M., Ciais, P., Hoffmann, G., Allison, C. E., Francey, R. J., Knorr, W., Tans, P. P., White, J. W. C. and Levin, I. (2003) 'A comprehensive global three-dimensional model of $\delta^{18}O$ in atmospheric CO_2: 2. Mapping the atmospheric signal', *Journal of Geophysical Research: Atmospheres,* 108(D17).

Djuricin, S., Pataki, D. E. and Xu, X. M. (2010) 'A comparison of tracer methods for quantifying CO_2 sources in an urban region', *Journal of Geophysical Research-Atmospheres,* 115, pp. 13.

Dörr, H., Kromer, B., Levin, I., Münnich, K. O. and Volpp, H. J. (1983) 'CO_2 and radon 222 as tracers for atmospheric transport', *Journal of Geophysical Research: Oceans,* 88(C2), pp. 1309-1313.

Eddebbar, Y. A., Long, M. C., Resplandy, L., Rödenbeck, C., Rodgers, K. B., Manizza, M. and Keeling, R. F. (2017) 'Impacts of ENSO on air-sea oxygen exchange: Observations and mechanisms', *Global Biogeochemical Cycles,* 31(5), pp. 901-921.

Faassen, K. A. P., Nguyen, L. N. T., Broekema, E. R., Kers, B. A. M., Mammarella, I., Vesala, T., Pickers, P. A., Manning, A. C., Vilà-Guerau de Arellano, J., Meijer, H. A. J., Peters, W. and Luijkx, I. T. (2023) 'Diurnal variability of atmospheric O_2, CO_2, and their exchange ratio above a boreal forest in southern Finland', *Atmos. Chem. Phys.,* 23(2), pp. 851-876.

Fang, S. X., Tans, P. P., Steinbacher, M., Zhou, L. X. and Luan, T. (2015) 'Comparison of the regional CO_2 mole fraction filtering approaches at a WMO/GAW regional station in China', *Atmos. Meas. Tech.,* 8(12), pp. 5301-5313.

Farquhar, G. D., Lloyd, J., Taylor, J. A., Flanagan, L. B., Syvertsen, J. P., Hubick, K. T., Wong, S. C. and Ehleringer, J. R. (1993) 'Vegetation effects on the isotope composition of oxygen in atmospheric CO_2', *Nature,* 363(6428), pp. 439-443.

Fernández-Martínez, M., Sardans, J., Chevallier, F., Ciais, P., Obersteiner, M., Vicca, S., Canadell, J. G., Bastos, A., Friedlingstein, P., Sitch, S., Piao, S. L., Janssens, I. A. and Peñuelas, J. (2019) 'Global trends in carbon sinks and their relationships with CO_2 and temperature', *Nature Climate Change,* 9(1), pp. 73-79.

Flanagan, L. B. and Ehleringer, J. R. (1998) 'Ecosystem-atmosphere CO_2 exchange: interpreting signals of change using stable isotope ratios', *Trends in Ecology & Evolution,* 13(1), pp. 10-14.

Fleming, Z. L., Monks, P. S. and Manning, A. J. (2012) 'Review: Untangling the influence of air-mass history in interpreting observed atmospheric composition', *Atmospheric Research,* 104, pp. 1-39.

Forster, P., Storelvmo, T., Armour, K., Collins, W., Dufresne, J. L., Frame, D., Lunt, D. J., Mauritsen, T., Palmer, M. D., Watanabe, M., Wild, M. and Zhang, H. (2021) 'The Earth's Energy Budget, Climate Feedbacks, and Climate Sensitivity', in Masson-Delmotte, V., Zhai, P., Pirani, A., Connors, S.L., Péan, C., Berger, S., Caud, N., Chen, Y., Goldfarb, L., Gomis, M.I., Huang, M., Leitzell, K., Lonnoy, E., Matthews, J.B.R., Maycock, T.K., Waterfield, T., Yelekçi, O., Yu, R. & Zhou, B. (eds.) *Climate Change 2021: The Physical Science Basis. Contribution of Working Group I to the Sixth Assessment Report of the Intergovernmental Panel on Climate Change*. Cambridge, United Kingdom and New York, NY, USA: Cambridge University Press, pp. 923–1054.

Francey, R. J. and Tans, P. P. (1987) 'Latitudinal variation in oxygen-18 of atmospheric CO_2', *Nature,* 327(6122), pp. 495-497.

Friedlingstein, P., Andrew, R. M., Rogelj, J., Peters, G. P., Canadell, J. G., Knutti, R., Luderer, G., Raupach, M. R., Schaeffer, M., van Vuuren, D. P. and Le Quéré, C. (2014) 'Persistent growth of CO2 emissions and implications for reaching climate targets', *Nature Geoscience,* 7(10), pp. 709-715.

Friedlingstein, P., O'Sullivan, M., Jones, M. W., Andrew, R. M., Hauck, J., Olsen, A., Peters, G. P., Peters, W., Pongratz, J., Sitch, S., Le Quéré, C., Canadell, J. G., Ciais, P., Jackson, R. B., Alin, S., Aragão, L. E. O. C., Arneth, A., Arora, V., Bates, N. R., Becker, M., Benoit-Cattin, A., Bittig, H. C., Bopp, L., Bultan, S., Chandra, N., Chevallier, F., Chini, L. P., Evans, W., Florentie, L., Forster, P. M., Gasser, T., Gehlen, M., Gilfillan, D., Gkritzalis, T., Gregor, L., Gruber, N., Harris, I., Hartung, K., Haverd, V., Houghton, R. A., Ilyina, T., Jain, A. K., Joetzjer, E., Kadono, K., Kato, E., Kitidis, V., Korsbakken, J. I., Landschützer, P., Lefèvre, N., Lenton, A., Lienert, S., Liu, Z., Lombardozzi, D., Marland, G., Metzl, N., Munro, D. R., Nabel, J. E. M. S., Nakaoka, S. I., Niwa, Y., O'Brien, K., Ono, T., Palmer, P. I., Pierrot, D., Poulter, B., Resplandy, L., Robertson, E., Rödenbeck, C., Schwinger, J., Séférian, R., Skjelvan, I., Smith, A. J. P., Sutton, A. J., Tanhua, T., Tans, P. P., Tian, H., Tilbrook, B., van der Werf, G., Vuichard, N., Walker, A. P., Wanninkhof, R., Watson, A. J., Willis, D., Wiltshire, A. J., Yuan, W., Yue, X. and Zaehle, S. (2020) 'Global Carbon Budget 2020', *Earth Syst. Sci. Data,* 12(4), pp. 3269-3340.

Gamnitzer, U., Karstens, U., Kromer, B., Neubert, R. E. M., Meijer, H. A. J., Schroeder, H. and Levin, I. (2006) 'Carbon monoxide: A quantitative tracer for fossil fuel CO_2?', *Journal of Geophysical Research-Atmospheres,* 111(D22), pp. 19.

Gillett, N. P., Kirchmeier-Young, M., Ribes, A., Shiogama, H., Hegerl, G. C., Knutti, R., Gastineau, G., John, J. G., Li, L., Nazarenko, L., Rosenbloom, N., Seland, Ø., Wu, T., Yukimoto, S. and Ziehn, T. (2021) 'Constraining human contributions to observed warming since the pre-industrial period', *Nature Climate Change,* 11(3), pp. 207-212.

Graven, H. D. and Gruber, N. (2011) 'Continental-scale enrichment of atmospheric $^{14}CO_2$ from the nuclear power industry: potential impact on the estimation of fossil fuel-derived CO_2', *Atmos. Chem. Phys.,* 11(23), pp. 12339-12349.

Grossi, C., Vogel, F. R., Curcoll, R., Àgueda, A., Vargas, A., Rodó, X. and Morguí, J. A. (2018) 'Study of the daily and seasonal atmospheric CH_4 mixing ratio variability in a rural Spanish region using ^{222}Rn tracer', *Atmos. Chem. Phys.,* 18(8), pp. 5847-5860.

Gruber, N., Bakker, D. C. E., DeVries, T., Gregor, L., Hauck, J., Landschützer, P., McKinley, G. A. and Müller, J. D. (2023) 'Trends and variability in the ocean carbon sink', *Nature Reviews Earth & Environment,* 4(2), pp. 119-134.

Gurney, K. R., Patarasuk, R., Liang, J., Song, Y., O'Keeffe, D., Rao, P., Whetstone, J. R., Duren, R. M., Eldering, A. and Miller, C. (2019) 'The Hestia fossil fuel CO_2 emissions data product for the Los Angeles megacity (Hestia-LA)', *Earth Syst. Sci. Data,* 11(3), pp. 1309-1335.

Hammer, S. and Levin, I. (2009) 'Seasonal variation of the molecular hydrogen uptake by soils inferred from continuous atmospheric observations in Heidelberg, southwest Germany', *Tellus B,* 61(3), pp. 556-565.

Han, P., Zeng, N., Oda, T., Zhang, W., Lin, X., Liu, D., Cai, Q., Ma, X., Meng, W., Wang, G., Wang, R. and Zheng, B. (2020) 'A city-level comparison of fossil-fuel and industry processes-induced CO_2 emissions over the Beijing-Tianjin-Hebei region from eight emission inventories', *Carbon Balance and Management,* 15(1), pp. 25.

Heiskanen, J., Brümmer, C., Buchmann, N., Calfapietra, C., Chen, H., Gielen, B., Gkritzalis, T., Hammer, S., Hartman, S., Herbst, M., Janssens, I. A., Jordan, A., Juurola, E., Karstens, U., Kasurinen, V., Kruijt, B., Lankreijer, H., Levin, I., Linderson, M.-L., Loustau, D., Merbold, L., Myhre, C. L., Papale, D., Pavelka, M., Pilegaard, K., Ramonet, M., Rebmann, C., Rinne, J., Rivier, L., Saltikoff, E., Sanders, R., Steinbacher, M., Steinhoff, T., Watson, A., Vermeulen, A. T., Vesala, T., Vítková, G. and Kutsch, W. (2022) 'The Integrated Carbon Observation System in Europe', *Bulletin of the American Meteorological Society,* 103(3), pp. E855-E872.

Hoag, K. J., Still, C. J., Fung, I. Y. and Boering, K. A. (2005) 'Triple oxygen isotope composition of tropospheric carbon dioxide as a tracer of terrestrial gross carbon fluxes', *Geophysical Research Letters,* 32(2).

Hofmann, M. E. G., Horváth, B., Schneider, L., Peters, W., Schützenmeister, K. and Pack, A. (2017) 'Atmospheric measurements of $\Delta^{17}O$ in CO_2 in Göttingen, Germany reveal a seasonal cycle driven by biospheric uptake', *Geochimica et Cosmochimica Acta,* 199, pp. 143-163.

Humphrey, V., Berg, A., Ciais, P., Gentine, P., Jung, M., Reichstein, M., Seneviratne, S. I. and Frankenberg, C. (2021) 'Soil moisture–atmosphere feedback dominates land carbon uptake variability', *Nature,* 592(7852), pp. 65-69.

Humphrey, V., Zscheischler, J., Ciais, P., Gudmundsson, L., Sitch, S. and Seneviratne, S. I. (2018) 'Sensitivity of atmospheric CO_2 growth rate to observed changes in terrestrial water storage', *Nature,* 560(7720), pp. 628-631.

IPCC (2021a) *Climate Change 2021: The Physical Science Basis. Contribution of Working Group I to the Sixth Assessment Report of the Intergovernmental Panel on Climate Change.* Cambridge, United Kingdom and New York, NY, USA: Cambridge University Press.

IPCC (2021b) 'Summary for Policymakers', in Masson-Delmotte, V., Zhai, P., Pirani, A., Connors, S.L., Péan, C., Berger, S., Caud, N., Chen, Y., Goldfarb, L., Gomis, M.I., Huang, M., Leitzell, K., Lonnoy, E., Matthews, J.B.R., Maycock, T.K., Waterfield, T., Yelekçi, O., Yu, R. & Zhou, B. (eds.) *Climate Change 2021: The Physical Science Basis. Contribution of Working Group I to the Sixth Assessment Report of the Intergovernmental Panel on Climate Change*. Cambridge, United Kingdom and New York, NY, USA: Cambridge University Press, pp. 3−32.

Jin, X., Najjar, R. G., Louanchi, F. and Doney, S. C. (2007) 'A modeling study of the seasonal oxygen budget of the global ocean', *Journal of Geophysical Research: Oceans,* 112(C5).
Keeling, C. D. (1979) 'The Suess effect: ^{13}Carbon-^{14}Carbon interrelations', *Environment International,* 2(4), pp. 229-300.
Keeling, R. F. (1988) 'Measuring correlations between atmospheric oxygen and carbon-dioxide mole fractions - a preliminary-study in urban air', *Journal of Atmospheric Chemistry,* 7(2), pp. 153-176.
Keeling, R. F. and Graven, H. D. (2021) 'Insights from Time Series of Atmospheric Carbon Dioxide and Related Tracers', *Annual Review of Environment and Resources,* 46(1), pp. 85-110.
Keeling, R. F. and Manning, A. C. (2014) '5.15 - Studies of Recent Changes in Atmospheric O_2 Content', in Holland, H.D. & Turekian, K.K. (eds.) *Treatise on Geochemistry (Second Edition)*. Oxford: Elsevier, pp. 385-404; doi: https://doi.org/10.1016/B978-0-08-095975-7.00420-4.
Keeling, R. F., Manning, A. C., McEvoy, E. M. and Shertz, S. R. (1998a) 'Methods for measuring changes in atmospheric O_2 concentration and their application in southern hemisphere air', *Journal of Geophysical Research: Atmospheres,* 103(D3), pp. 3381-3397.
Keeling, R. F. and Shertz, S. R. (1992) 'Seasonal and interannual variations in atmospheric oxygen and implications for the global carbon cycle', *Nature,* 358(6389), pp. 723-727.
Keeling, R. F., Stephens, B. B., Najjar, R. G., Doney, S. C., Archer, D. and Heimann, M. (1998b) 'Seasonal variations in the atmospheric O_2/N_2 ratio in relation to the kinetics of air-sea gas exchange', *Global Biogeochemical Cycles,* 12(1), pp. 141-163.
Koren, G., Schneider, L., van der Velde, I. R., van Schaik, E., Gromov, S. S., Adnew, G. A., Mrozek Martino, D. J., Hofmann, M. E. G., Liang, M.-C., Mahata, S., Bergamaschi, P., van der Laan-Luijkx, I. T., Krol, M. C., Röckmann, T. and Peters, W. (2019) 'Global 3-D Simulations of the Triple Oxygen Isotope Signature $\Delta^{17}O$ in Atmospheric CO_2', *Journal of Geophysical Research: Atmospheres,* 124(15), pp. 8808-8836.
Lämmerzahl, P., Röckmann, T., Brenninkmeijer, C. A. M., Krankowsky, D. and Mauersberger, K. (2002) 'Oxygen isotope composition of stratospheric carbon dioxide', *Geophysical Research Letters,* 29(12), pp. 23-1-23-4.
Laskar, A. H., Mahata, S., Bhattacharya, S. K. and Liang, M.-C. (2019) 'Triple Oxygen and Clumped Isotope Compositions of CO_2 in the Middle Troposphere', *Earth and Space Science,* 6(7), pp. 1205-1219.
Le Quéré, C., Jackson, R. B., Jones, M. W., Smith, A. J. P., Abernethy, S., Andrew, R. M., De-Gol, A. J., Willis, D. R., Shan, Y., Canadell, J. G., Friedlingstein, P., Creutzig, F. and Peters, G. P. (2020) 'Temporary reduction in daily global CO_2 emissions during the COVID-19 forced confinement', *Nature Climate Change,* 10(7), pp. 647-653.
Le Quéré, C., Rödenbeck, C., Buitenhuis, E. T., Conway, T. J., Langenfelds, R., Gomez, A., Labuschagne, C., Ramonet, M., Nakazawa, T., Metzl, N., Gillett, N. and Heimann, M. (2007) 'Saturation of the Southern Ocean CO_2 Sink Due to Recent Climate Change', *Science,* 316(5832), pp. 1735-1738.
Lee, J. Y., Marotzke, J., Bala, G., Cao, L., Corti, S., Dunne, J. P., Engelbrecht, F., Fischer, E., Fyfe, J. C., Jones, C., Maycock, A., Mutemi, J., Ndiaye, O., Panickal, S. and Zhou, T. (2021) 'Future Global Climate: Scenario-Based Projections and Near-Term Information', in Masson-Delmotte, V., Zhai, P., Pirani, A., Connors, S.L., Péan, C., Berger, S., Caud, N., Chen, Y., Goldfarb, L., Gomis, M.I., Huang, M., Leitzell, K.,

Lonnoy, E., Matthews, J.B.R., Maycock, T.K., Waterfield, T., Yelekçi, O., Yu, R. & Zhou, B. (eds.) *Climate Change 2021: The Physical Science Basis. Contribution of Working Group I to the Sixth Assessment Report of the Intergovernmental Panel on Climate Change*. Cambridge, United Kingdom and New York, NY, USA: Cambridge University Press, pp. 553–672.

Levin, I., Glatzel-Mattheier, H., Marik, T., Cuntz, M., Schmidt, M. and Worthy, D. E. (1999) 'Verification of German methane emission inventories and their recent changes based on atmospheric observations', *Journal of Geophysical Research: Atmospheres,* 104(D3), pp. 3447-3456.

Levin, I., Karstens, U., Hammer, S., DellaColetta, J., Maier, F. and Gachkivskyi, M. (2021) 'Limitations of the Radon Tracer Method (RTM) to estimate regional Greenhouse Gases (GHG) emissions – a case study for methane in Heidelberg', *Atmos. Chem. Phys. Discuss.,* 2021, pp. 1-34.

Liu, S. C., McAfee, J. R. and Cicerone, R. J. (1984) 'Radon-222 and tropospheric vertical transport', *Journal of Geophysical Research,* 89(D5), pp. 7291-7297.

Lopez, M., Schmidt, M., Delmotte, M., Colomb, A., Gros, V., Janssen, C., Lehman, S. J., Mondelain, D., Perrussel, O., Ramonet, M., Xueref-Remy, I. and Bousquet, P. (2013) 'CO, NOx and $^{13}CO_2$ as tracers for fossil fuel CO_2: results from a pilot study in Paris during winter 2010', *Atmospheric Chemistry and Physics,* 13(15), pp. 7343-7358.

Manning, A. C. and Keeling, R. F. (2006) 'Global oceanic and land biotic carbon sinks from the Scripps atmospheric oxygen flask sampling network', *Tellus B,* 58(2), pp. 95-116.

Manning, A. C., Nisbet, E. G., Keeling, R. F., Liss, P. S. J. P. T. o. t. R. S. A. M., Physical and Sciences, E. 2011. Greenhouse gases in the Earth system: setting the agenda to 2030. The Royal Society Publishing.

Masiello, C. A., Gallagher, M. E., Randerson, J. T., Deco, R. M. and Chadwick, O. A. (2008) 'Evaluating two experimental approaches for measuring ecosystem carbon oxidation state and oxidative ratio', *Journal of Geophysical Research: Biogeosciences,* 113(G3).

Miller, J. B., Lehman, S. J., Montzka, S. A., Sweeney, C., Miller, B. R., Karion, A., Wolak, C., Dlugokencky, E. J., Southon, J., Turnbull, J. C. and Tans, P. P. (2012) 'Linking emissions of fossil fuel CO_2 and other anthropogenic trace gases using atmospheric $^{14}CO_2$', *Journal of Geophysical Research: Atmospheres,* 117(D8).

Miller, J. B., Tans, P. P., White, J. W. C., Conway, T. J. and Vaughn, B. W. (2003) 'The atmospheric signal of terrestrial carbon isotopic discrimination and its implication for partitioning carbon fluxes', *Tellus Series B-Chemical and Physical Meteorology,* 55(2), pp. 197-206.

Miller, M. F. (2002) 'Isotopic fractionation and the quantification of ^{17}O anomalies in the oxygen three-isotope system: an appraisal and geochemical significance', *Geochimica et Cosmochimica Acta,* 66(11), pp. 1881-1889.

Munassar, S., Monteil, G., Scholze, M., Karstens, U., Rödenbeck, C., Koch, F. T., Totsche, K. U. and Gerbig, C. (2023) 'Why do inverse models disagree? A case study with two European CO_2 inversions', *Atmos. Chem. Phys.,* 23(4), pp. 2813-2828.

Nazaroff, W. W. (1988) *Radon and its decay products in indoor air.* United States: John Wiley and Sons, Incorporated.

Nevison, C. D., Munro, D. R., Lovenduski, N. S., Keeling, R. F., Manizza, M., Morgan, E. J. and Rödenbeck, C. (2020) 'Southern Annular Mode Influence on Wintertime Ventilation of the Southern Ocean Detected in Atmospheric O_2 and CO_2 Measurements', *Geophysical Research Letters,* 47(4), pp. e2019GL085667.

Newman, S., Xu, X., Gurney, K. R., Hsu, Y. K., Li, K. F., Jiang, X., Keeling, R., Feng, S., O'Keefe, D., Patarasuk, R., Wong, K. W., Rao, P., Fischer, M. L. and Yung, Y. L.

(2016) 'Toward consistency between trends in bottom-up CO2 emissions and top-down atmospheric measurements in the Los Angeles megacity', *Atmospheric Chemistry and Physics,* 16(6), pp. 3843-3863.
O'Neill, B. C., Tebaldi, C., van Vuuren, D. P., Eyring, V., Friedlingstein, P., Hurtt, G., Knutti, R., Kriegler, E., Lamarque, J. F., Lowe, J., Meehl, G. A., Moss, R., Riahi, K. and Sanderson, B. M. (2016) 'The Scenario Model Intercomparison Project (ScenarioMIP) for CMIP6', *Geosci. Model Dev.,* 9(9), pp. 3461-3482.
O'Neill, B. C., Kriegler, E., Riahi, K., Ebi, K. L., Hallegatte, S., Carter, T. R., Mathur, R. and van Vuuren, D. P. (2014) 'A new scenario framework for climate change research: the concept of shared socioeconomic pathways', *Climatic Change,* 122(3), pp. 387-400.
Pan, Y., Birdsey, R. A., Fang, J., Houghton, R., Kauppi, P. E., Kurz, W. A., Phillips, O. L., Shvidenko, A., Lewis, S. L., Canadell, J. G., Ciais, P., Jackson, R. B., Pacala, S. W., McGuire, A. D., Piao, S., Rautiainen, A., Sitch, S. and Hayes, D. (2011) 'A Large and Persistent Carbon Sink in the World's Forests', *Science,* 333(6045), pp. 988-993.
Parazoo, N. C., Bowman, K. W., Baier, B. C., Liu, J., Lee, M., Kuai, L., Shiga, Y., Baker, I., Whelan, M. E., Feng, S., Krol, M., Sweeney, C., Runkle, B. R., Tajfar, E. and Davis, K. J. (2021) 'Covariation of Airborne Biogenic Tracers (CO_2, COS, and CO) Supports Stronger Than Expected Growing Season Photosynthetic Uptake in the Southeastern US', *Global Biogeochemical Cycles,* 35(10), pp. e2021GB006956.
Peñuelas, J., Ciais, P., Canadell, J. G., Janssens, I. A., Fernández-Martínez, M., Carnicer, J., Obersteiner, M., Piao, S., Vautard, R. and Sardans, J. (2017) 'Shifting from a fertilization-dominated to a warming-dominated period', *Nature Ecology & Evolution,* 1(10), pp. 1438-1445.
Peylin, P., Ciais, P., Denning, A. S., Tans, P. P., Berry, J. A. and White, J. W. C. (1999) 'A 3-dimensional study of $\delta^{18}O$ in atmospheric CO_2: contribution of different land ecosystems', *Tellus B: Chemical and Physical Meteorology,* 51(3), pp. 642-667.
Peylin, P., Houweling, S., Krol, M. C., Karstens, U., Rodenbeck, C., Geels, C., Vermeulen, A., Badawy, B., Aulagnier, C., Pregger, T., Delage, F., Pieterse, G., Ciais, P. and Heimann, M. (2011) 'Importance of fossil fuel emission uncertainties over Europe for CO_2 modeling: model intercomparison', *Atmospheric Chemistry and Physics,* 11(13), pp. 6607-6622.
Pickers, P. A., Manning, A. C., Quéré, C. L., Forster, G. L., Luijkx, I. T., Gerbig, C., Fleming, L. S. and Sturges, W. T. (2022) 'Novel quantification of regional fossil fuel CO_2 reductions during COVID-19 lockdowns using atmospheric oxygen measurements', 8(16), pp. eabl9250.
Pieber, S. M., Tuzson, B., Henne, S., Karstens, U., Gerbig, C., Koch, F. T., Brunner, D., Steinbacher, M. and Emmenegger, L. (2022) 'Analysis of regional CO_2 contributions at the high Alpine observatory Jungfraujoch by means of atmospheric transport simulations and $\delta^{13}C$', *Atmospheric Chemistry and Physics,* 22(16), pp. 10721-10749.
Polian, G., Lambert, G., Ardouin, B., Jegou, A. J. T. B. C. and Meteorology, P. (1986) 'Long-range transport of continental radon in subantarctic and antarctic areas', 38(3-4), pp. 178-189.
Porstendoerfer, J. (1994) 'Properties and behaviour of radon and thoron and their decay products in the air', *Journal of Aerosol Science,* 25(2), pp. 219-263.
Pu, J.-J., Xu, H.-H., He, J., Fang, S.-X. and Zhou, L.-X. (2014) 'Estimation of regional background concentration of CO_2 at Lin'an Station in Yangtze River Delta, China', *Atmospheric Environment,* 94, pp. 402-408.

Resplandy, L., Keeling, R. F., Eddebbar, Y., Brooks, M., Wang, R., Bopp, L., Long, M. C., Dunne, J. P., Koeve, W. and Oschlies, A. (2019) 'Quantification of ocean heat uptake from changes in atmospheric O_2 and CO_2 composition', *Scientific Reports,* 9(1), pp. 20244.

Riahi, K., van Vuuren, D. P., Kriegler, E., Edmonds, J., O'Neill, B. C., Fujimori, S., Bauer, N., Calvin, K., Dellink, R., Fricko, O., Lutz, W., Popp, A., Cuaresma, J. C., Kc, S., Leimbach, M., Jiang, L., Kram, T., Rao, S., Emmerling, J., Ebi, K., Hasegawa, T., Havlik, P., Humpenöder, F., Da Silva, L. A., Smith, S., Stehfest, E., Bosetti, V., Eom, J., Gernaat, D., Masui, T., Rogelj, J., Strefler, J., Drouet, L., Krey, V., Luderer, G., Harmsen, M., Takahashi, K., Baumstark, L., Doelman, J. C., Kainuma, M., Klimont, Z., Marangoni, G., Lotze-Campen, H., Obersteiner, M., Tabeau, A. and Tavoni, M. (2017) 'The Shared Socioeconomic Pathways and their energy, land use, and greenhouse gas emissions implications: An overview', *Global Environmental Change,* 42, pp. 153-168.

Rödenbeck, C., Houweling, S., Gloor, M. and Heimann, M. (2003) 'CO_2 flux history 1982–2001 inferred from atmospheric data using a global inversion of atmospheric transport', *Atmos. Chem. Phys.,* 3(6), pp. 1919-1964.

Rödenbeck, C., Le Quéré, C., Heimann, M. and Keeling, R. F. (2008) 'Interannual variability in oceanic biogeochemical processes inferred by inversion of atmospheric O_2/N_2 and CO_2 data', *Tellus B,* 60(5), pp. 685-705.

Severinghaus, J. P. (1995) *Studies of the terrestrial O_2 and carbon cycles in sand dune gases and in biosphere 2.* United States [Online] Available at: https://www.osti.gov/servlets/purl/477735 (Accessed: 04/10/2020).

Sitch, S., Friedlingstein, P., Gruber, N., Jones, S. D., Murray-Tortarolo, G., Ahlström, A., Doney, S. C., Graven, H., Heinze, C., Huntingford, C., Levis, S., Levy, P. E., Lomas, M., Poulter, B., Viovy, N., Zaehle, S., Zeng, N., Arneth, A., Bonan, G., Bopp, L., Canadell, J. G., Chevallier, F., Ciais, P., Ellis, R., Gloor, M., Peylin, P., Piao, S. L., Le Quéré, C., Smith, B., Zhu, Z. and Myneni, R. (2015) 'Recent trends and drivers of regional sources and sinks of carbon dioxide', *Biogeosciences,* 12(3), pp. 653-679.

Spielmann, F. M., Wohlfahrt, G., Hammerle, A., Kitz, F., Migliavacca, M., Alberti, G., Ibrom, A., El-Madany, T. S., Gerdel, K., Moreno, G., Kolle, O., Karl, T., Peressotti, A. and Delle Vedove, G. (2019) 'Gross Primary Productivity of Four European Ecosystems Constrained by Joint CO_2 and COS Flux Measurements', *Geophysical Research Letters,* 46(10), pp. 5284-5293.

Steinbach, J., Gerbig, C., Rodenbeck, C., Karstens, U., Minejima, C. and Mukai, H. (2011) 'The CO_2 release and Oxygen uptake from Fossil Fuel Emission Estimate (COFFEE) dataset: effects from varying oxidative ratios', *Atmospheric Chemistry and Physics,* 11(14), pp. 6855-6870.

Stephens, B. B., Gurney, K. R., Tans, P. P., Sweeney, C., Peters, W., Bruhwiler, L., Ciais, P., Ramonet, M., Bousquet, P., Nakazawa, T., Aoki, S., Machida, T., Inoue, G., Vinnichenko, N., Lloyd, J., Jordan, A., Heimann, M., Shibistova, O., Langenfelds, R. L., Steele, L. P., Francey, R. J. and Denning, A. S. (2007) 'Weak Northern and Strong Tropical Land Carbon Uptake from Vertical Profiles of Atmospheric CO_2', *Science,* 316(5832), pp. 1732-1735.

Stephens, B. B., Keeling, R. F., Heimann, M., Six, K. D., Murnane, R. and Caldeira, K. (1998) 'Testing global ocean carbon cycle models using measurements of atmospheric O_2 and CO_2 concentration', *Global Biogeochemical Cycles,* 12(2), pp. 213-230.

Thiemens, M. H., Chakraborty, S. and Jackson, T. L. (2014) 'Decadal $\Delta^{17}O$ record of tropospheric CO_2: Verification of a stratospheric component in the

troposphere', *Journal of Geophysical Research: Atmospheres,* 119(10), pp. 6221-6229.
Thiemens, M. H., Jackson, T., Mauersberger, K., Schueler, B. and Morton, J. (1991) 'Oxygen isotope fractionation in stratospheric CO_2', *Geophysical Research Letters,* 18(4), pp. 669-672.
Tohjima, Y., Mukai, H., Machida, T., Hoshina, Y. and Nakaoka, S. I. (2019) 'Global carbon budgets estimated from atmospheric O_2/N_2 and CO_2 observations in the western Pacific region over a 15-year period', *Atmos. Chem. Phys.,* 19(14), pp. 9269-9285.
Tohjima, Y., Mukai, H., Nojiri, Y., Yamagishi, H. and Machida, T. (2008) 'Atmospheric O_2/N_2 measurements at two Japanese sites: estimation of global oceanic and land biotic carbon sinks and analysis of the variations in atmospheric potential oxygen (APO)', *Tellus B: Chemical and Physical Meteorology,* 60(2), pp. 213-225.
Tolk, L. F., Meesters, A. G. C. A., Dolman, A. J. and Peters, W. (2008) 'Modelling representation errors of atmospheric CO_2 mixing ratios at a regional scale', *Atmos. Chem. Phys.,* 8(22), pp. 6587-6596.
Tsutsumi, Y., Mori, K., Ikegami, M., Tashiro, T. and Tsuboi, K. (2006) 'Long-term trends of greenhouse gases in regional and background events observed during 1998–2004 at Yonagunijima located to the east of the Asian continent', *Atmospheric Environment,* 40(30), pp. 5868-5879.
Turnbull, J. C., Miller, J. B., Lehman, S. J., Hurst, D., Peters, W., Tans, P. P., Southon, J., Montzka, S. A., Elkins, J. W., Mondeel, D. J., Romashkin, P. A., Elansky, N. and Skorokhod, A. (2009) 'Spatial distribution of $\Delta^{14}CO_2$ across Eurasia: measurements from the TROICA-8 expedition', *Atmos. Chem. Phys.,* 9(1), pp. 175-187.
Turnbull, J. C., Miller, J. B., Lehman, S. J., Tans, P. P., Sparks, R. J. and Southon, J. (2006) 'Comparison of $^{14}CO_2$, CO, and SF_6 as tracers for recently added fossil fuel CO_2 in the atmosphere and implications for biological CO_2 exchange', *Geophysical Research Letters,* 33(1).
UNFCCC 2015. Adoption of the Paris agreement, 21st conference of the parties. United Nations Paris.
Vardag, S. N., Gerbig, C., Janssens-Maenhout, G. and Levin, I. (2015) 'Estimation of continuous anthropogenic CO_2: model-based evaluation of CO_2, CO,' *Atmospheric Chemistry and Physics,* 15(22), pp. 12705-12729.
Vardag, S. N., Hammer, S. and Levin, I. (2016) 'Evaluation of 4 years of continuous $\delta^{13}C(CO_2)$ data using a moving Keeling plot method', *Biogeosciences,* 13(14), pp. 4237-4251.
Vogel, F. R., Ishizawa, M., Chan, E., Chan, D., Hammer, S., Levin, I. and Worthy, D. E. J. (2012) 'Regional non-CO_2 greenhouse gas fluxes inferred from atmospheric measurements in Ontario, Canada', *Journal of Integrative Environmental Sciences,* 9(sup1), pp. 41-55.
Vogel, F. R., Levin, I. and Worthy, D. E. J. (2013) 'Implications for Deriving Regional Fossil Fuel CO_2 Estimates from Atmospheric Observations in a Hot Spot of Nuclear Power Plant $^{14}CO_2$ Emissions', *Radiocarbon,* 55(3), pp. 1556-1572.
Wada, A., Matsueda, H., Murayama, S., Taguchi, S., Hirao, S., Yamazawa, H., Moriizumi, J., Tsuboi, K., Niwa, Y. and Sawa, Y. (2013) 'Quantification of emission estimates of CO_2, CH_4 and CO for East Asia derived from atmospheric radon-222 measurements over the western North Pacific', *Tellus B: Chemical and Physical Meteorology,* 65(1), pp. 18037.
Wang, P., Zhou, W., Xiong, X., Wu, S., Niu, Z., Yu, Y., Liu, J., Feng, T., Cheng, P., Du, H., Lu, X., Chen, N. and Hou, Y. (2022) 'Source Attribution of Atmospheric CO2 Using

^{14}C and ^{13}C as Tracers in Two Chinese Megacities During Winter', *Journal of Geophysical Research: Atmospheres,* 127(12).
Weiss, R. F. and Prinn, R. G. (2011) 'Quantifying greenhouse-gas emissions from atmospheric measurements: a critical reality check for climate legislation', *Philosophical Transactions of the Royal Society A: Mathematical, Physical and Engineering Sciences,* 369(1943), pp. 1925-1942.
Welp, L. R., Keeling, R. F., Meijer, H. A. J., Bollenbacher, A. F., Piper, S. C., Yoshimura, K., Francey, R. J., Allison, C. E. and Wahlen, M. (2011) 'Interannual variability in the oxygen isotopes of atmospheric CO2 driven by El Niño', *Nature,* 477(7366), pp. 579-582.
Williams, A. G., Chambers, S. and Griffiths, A. (2013) 'Bulk Mixing and Decoupling of the Nocturnal Stable Boundary Layer Characterized Using a Ubiquitous Natural Tracer', *Boundary-Layer Meteorology,* 149(3), pp. 381-402.
Williams, C. A., Collatz, G. J., Masek, J., Huang, C. and Goward, S. N. (2014) 'Impacts of disturbance history on forest carbon stocks and fluxes: Merging satellite disturbance mapping with forest inventory data in a carbon cycle model framework', *Remote Sensing of Environment,* 151, pp. 57-71.
Worrall, F., Clay, G. D., Masiello, C. A. and Mynheer, G. (2013) 'Estimating the oxidative ratio of the global terrestrial biosphere carbon', *Biogeochemistry,* 115(1), pp. 23-32.
Yakir, D. and Wang, X.-F. (1996) 'Fluxes of CO_2 and water between terrestrial vegetation and the atmosphere estimated from isotope measurements', *Nature,* 380(6574), pp. 515-517.
Yan, Y., Klosterhalfen, A., Moyano, F., Cuntz, M., Manning, A. C. and Knohl, A. (2023) 'A Modeling Approach to Investigate Drivers, Variability and Uncertainties in O_2 Fluxes and the O_2:CO_2 Exchange Ratios in a Temperate Forest', *Biogeosciences Discuss.,* 2023, pp. 1-35.
Yeung, L. Y., Affek, H. P., Hoag, K. J., Guo, W., Wiegel, A. A., Atlas, E. L., Schauffler, S. M., Okumura, M., Boering, K. A. and Eiler, J. M. (2009) 'Large and unexpected enrichment in stratospheric $^{16}O^{13}C^{18}O$ and its meridional variation', *Proceedings of the national academy of sciences,* 106(28), pp. 11496-11501.
Young, E. D., Galy, A. and Nagahara, H. (2002) 'Kinetic and equilibrium mass-dependent isotope fractionation laws in nature and their geochemical and cosmochemical significance', *Geochimica et Cosmochimica Acta,* 66(6), pp. 1095-1104.
Young, H., Turnbull, J. C., Keller, E., Dominfues, L., Parry-Thompson, J., Hilton, T., Brailsford, G. W., Gray, S., Moss, R. and Mikaloff Fletcher, S. E. (2023) 'Urban flask measurements of CO_2ff and CO to identify emission sources at different type sites in Auckland, New Zealand', *Philosophical Transactions of the Royal Society A: Mathematical, Physical and Engineering Sciences,* [Accepted].
Yung, Y. L., DeMore, W. B. and Pinto, J. P. (1991) 'Isotopic exchange between carbon dioxide and ozone via $O(^1D)$ in the stratosphere', *Geophysical Research Letters,* 18(1), pp. 13-16.
Zahorowski, W., Chambers, S. D. and Henderson-Sellers, A. (2004) 'Ground based radon-222 observations and their application to atmospheric studies', *J Environ Radioact,* 76(1-2), pp. 3-33.
Zahorowski, W., Griffiths, A. D., Chambers, S. D., Williams, A. G., Law, R. M., Crawford, J. and Werczynski, S. (2013) 'Constraining annual and seasonal radon-222 flux density from the Southern Ocean using radon-222 concentrations in the boundary layer at Cape Grim', *Tellus B: Chemical and Physical Meteorology,* 65(1), pp. 19622.

Zellweger, C., Forrer, J., Hofer, P., Nyeki, S., Schwarzenbach, B., Weingartner, E., Ammann, M. and Baltensperger, U. (2003) 'Partitioning of reactive nitrogen (NOy) and dependence on meteorological conditions in the lower free troposphere', *Atmos. Chem. Phys.,* 3(3), pp. 779-796.

Chapter 2 Evaluating the performance of a 'Picarro G2207-*i*' analyser for high-precision atmospheric O_2 measurements

Preamble

The work presented in this chapter was originally prepared for publication in the journal 'Atmospheric Measurement Techniques' and was published in 2023 (Fleming et al., 2023). With the exception of some small additions for clarification, this chapter is near identical to the published document. Due to this there are a number of cases where sentences are written in the first person plural i.e., 'We have tested an atmospheric O_2 analyser…'. I wrote this article, and completed the data analysis, but there was contribution to this article from co-authors as detailed below.

LSF, ACM, and PAP developed the measurement methodology, which were conducted by LSF at UEA and WAO. AJE developed the software used to run the analyser. Investigation and visualisation were completed by LSF. Writing was completed by LSF. Review and editing were completed by LSF, ACM, PAP and GLF.

Fleming, L. S., Manning, A. C., Pickers, P. A., Forster, G. L., & Etchells, A. J. (2023). Evaluating the performance of a Picarro G2207-i analyser for high-precision atmospheric O_2 measurements. *Atmospheric Measurement Techniques*, 16(2), 387-401.

Abstract

Fluxes of oxygen (O_2) and carbon dioxide (CO_2) in and out of the atmosphere are strongly coupled for terrestrial biospheric exchange processes and fossil fuel combustion but are uncoupled for oceanic air-sea gas exchange. High-precision measurements of both species can therefore provide constraints on the carbon cycle and can be used to quantify fossil fuel CO_2 ($ffCO_2$) emission estimates. In the case of O_2, however, due to its large atmospheric mole fraction (~20.9 %) it is very challenging to measure small variations to the degree of precision and accuracy required for these applications. We have tested an atmospheric O_2 analyser based on the principle of cavity ring-down spectroscopy (Picarro Inc., model G2207-*i*), both in the laboratory and at the Weybourne Atmospheric Observatory (WAO) field station in the UK, in comparisons to well-established, pre-existing atmospheric O_2 and CO_2 measurement systems.

In laboratory tests analysing air in high-pressure cylinders, from the Allan deviation we found that the precision improved to ± 0.5 ppm (~ ± 2.4 per meg) after 30 minute averaging and a range of hourly averaged values over 24 hours of 1.2 ppm (~5.8 per meg). These results are close to atmospheric O_2 compatibility goals as set by the UN World Meteorological Organization. However, from measurements of ambient air conducted at WAO we found that the built-in water correction of the G2207-*i* does not sufficiently correct for the influence of water vapour on the O_2 mole fraction. When sample air was dried and a 5-hourly baseline correction with a reference gas cylinder was employed, the G2207-*i*'s results showed an average difference from the established O_2 analyser of 13.6 ± 7.5 per meg (over two weeks of continuous measurements). Over the same period, based on measurements of a so-called 'target tank', analysed for 12 minutes every 7 hours, we calculated a repeatability of ± 5.7 ± 5.6 per meg and a compatibility of ± 10.0 ± 6.7 per meg for the G2207-*i* . To further examine the G2207-*i*'s performance in real-world applications we used ambient air measurements of O_2 together with concurrent CO_2 measurements to calculate $ffCO_2$. Due to the imprecision of the G2207-*i*, the $ffCO_2$ calculated showed large differences from that calculated from the established system, and had a large uncertainty of ± 13.0 ppm, which was roughly double that from the established system (± 5.8 ppm).

2.1 Introduction

Oxygen (O_2) is the most abundant molecule in the atmosphere after nitrogen (N_2), with an atmospheric background mole fraction of approximately 20.94 % (Tohjima et al., 2005). Due to this large atmospheric background, O_2 measurements are sensitive to changes in the mole fractions of other atmospheric species, such as carbon dioxide (CO_2), due to dilution effects. O_2 measurements are therefore typically reported on a relative scale calculated as the change in the ratio of O_2 to N_2 relative to a standard O_2/N_2 ratio, as given in Eq. (2.1), and expressed in 'per meg' units.

$$\delta\left(\frac{O_2}{N_2}\right) = \left(\frac{O_2/N_2\ \text{sample} - O_2/N_2\ \text{reference}}{O_2/N_2\ \text{reference}}\right) \times 10^6 \qquad (2.1)$$

In practice, atmospheric N_2 is far less variable than O_2 meaning that changes in the O_2/N_2 ratios can be assumed to be representative of O_2 mole fraction (Keeling and Shertz, 1992). In comparing changes in O_2 to changes in CO_2, on a mole for mole basis, a 1 per meg change in O_2 is equivalent to a 0.2094 ppm (parts per million) change in CO_2 mole fraction (Keeling et al., 1998a).

Over the past 3 decades, atmospheric O_2 has been decreasing at a rate of ~15 per meg per year, primarily owing to fossil fuel combustion (Keeling and Manning, 2014); over the same period, atmospheric CO_2 has been increasing at an average rate of 2 ppm yr^{-1} (Dlugokencky and Tans, 2022), also predominantly due to fossil fuel combustion. For most processes that cause variability in atmospheric O_2, there is an anti-correlated change in atmospheric CO_2; therefore high-precision measurements of atmospheric O_2 play an increasingly important role in our understanding of atmospheric CO_2, carbon cycling, and other biogeochemical processes (e.g. Pickers et al., 2017; Resplandy et al., 2019; Battle et al., 2019; Tohjima et al., 2019). Fluxes of O_2 and CO_2 in and out of the atmosphere are strongly coupled for terrestrial biosphere exchange with a global average oxidative ratio (OR) in the range of 1.03 to 1.10 mol mol^{-1} (Severinghaus, 1995). For fossil fuel combustion, dependent on fuel type, the OR is in the range of 1.17 to 1.95 mol mol^{-1} (Keeling, 1988b). Whereas O_2 and CO_2 fluxes are uncoupled for oceanic air-sea gas exchange primarily due to inorganic reactions in the water involving the carbonate system and not O_2, as well as differences in air-sea equilibration times between the two gases.

The relationship between O_2 and CO_2 fluxes has also allowed for the derivation of the tracer 'atmospheric potential oxygen' (APO), as defined in Eq. (2.2) (Stephens et al., 1998).

$$\text{APO} \approx O_2 + (-1.1 \times CO_2) \qquad (2.2)$$

Where the factor -1.1 represents the mean value of the O_2:CO_2 OR for terrestrial biosphere photosynthesis and respiration (Severinghaus, 1995), and where we have ignored very minor influences from methane and carbon monoxide. APO is therefore, by definition, invariant with respect to the terrestrial biosphere. Changes in APO therefore mainly reflect changes in ocean-atmosphere exchange of O_2 and CO_2 (primarily on seasonal and longer timescales), with a contribution from fossil fuels on both shorter and longer timescales. APO can thus be used to examine oceanic CO_2 fluxes and to quantify fossil fuel CO_2 ($ffCO_2$) emissions (Pickers et al., 2022).

The World Meteorological Organization (WMO) Global Atmospheric Watch (GAW) programme has established a measurement compatibility goal for O_2 of ± 2 per meg (± 0.4 ppm) (Crotwell et al., 2020), where compatibility (which can also be defined as measurement accuracy) refers to the acceptable level of agreement between two field stations or laboratories when measuring the same air sample. This is the scientifically desirable level of compatibility required to resolve latitudinal gradients and long-term trends (Crotwell et al., 2020). There is also an extended goal of ± 10 per meg (± 2 ppm) which is suitable for some specific applications when expected variation are relatively large, such as fossil fuel quantification in large cities (Crotwell et al., 2020). In order to meet the WMO compatibility goals, it is recommended that a measurement system's repeatability should not exceed half of the compatibility goal (i.e., ± 1 per meg, ± 0.2 ppm). Where the repeatability refers to the closeness of agreements between results of measurements of the same measure (which is also sometimes referred to as the measurement systems precision). However, routinely achieving a measurement precision of ± 1 per meg, is not yet achievable for almost any laboratories and field stations making high-precision measurements of atmospheric O_2. The large atmospheric background of O_2 makes it extremely challenging to measure the relatively small variations to the level of repeatability required, since measuring a change of 0.2 ppm against the background (~209400 ppm) requires a relative precision of 0.0001 %.

Presently, there are several different analytical techniques available for measuring atmospheric O_2 to a high precision: interferometry (Keeling, 1988a), isotope ratio mass spectrometry (Bender et al., 1994), paramagnetic techniques (Manning et al., 1999), vacuum ultraviolet absorption (VUV) (Stephens et al., 2011), gas chromatography (Tohjima, 2000), and electrochemical fuel cells (Stephens et al., 2007a). The most precise of these current methods is the VUV absorption technique

however, VUV O_2 analysers are 'homemade' and are not commercially available, thus limiting their widespread applications. None of these techniques are 'off-the-shelf' systems, all of them are complex and time-consuming systems to design, build, and optimise, with very precise pressure, temperature, and flow control needed. All of the techniques also require frequent interruption to sample measurement to carry out calibration procedures (Kozlova and Manning, 2009). The supply of calibration gases for such systems is particularly labour intensive, due to both their relatively rapid consumption rate and the fact that no commercial gas supply company is able to provide suitable gas mixtures for atmospheric O_2 research. Accurate, high-precision atmospheric O_2 measurements therefore remain challenging. An alternative commercially available O_2 analyser with fewer requirements for external gas handling, air-sample drying, and calibration procedures could consequently advance the field of atmospheric O_2 measurements if the required performance could be achieved and if it were relatively easy to operate with low maintenance requirements and a lower rate of calibration gas consumption.

In this paper we present the results from the analysis of a Picarro Inc. G2207-*i* oxygen analyser, which operates on the principle of cavity ring-down spectroscopy technology (CRDS), (hereafter referred to as the G2207-*i*) and evaluate its performance in comparison to established O_2 measurement systems in the University of East Anglia (UEA) Carbon Related Atmospheric Measurements (CRAM) Laboratory and at the Weybourne Atmospheric Observatory (WAO; North Norfolk, UK). Unlike most other analytical techniques used for atmospheric O_2 measurements, it is intended that the G2207-*i* should not require a continuous reference gas supply, and it has built-in pressure and flow control, and the potential for greatly reduced sample drying requirements due to a built-in water measurement and correction procedure. These features make the G2207-*i* a potentially desirable analyser for high-precision atmospheric O_2 research, but we note that it would still require the same rigorous calibration procedures as other analysers (Kozlova and Manning, 2009), albeit possibly at reduced frequency. In this paper we quantify the compatibility, repeatability, and drift rates in the context of WMO/GAW guidelines (Crotwell et al., 2020). In order to further examine the performance of the G2207-*i* in real-world applications, we also calculated $ffCO_2$ from concurrent O_2 and CO_2 measurements made, using the novel methodology presented by Pickers et al. (2022). We compare $ffCO_2$ calculated with O_2 measurements from the G2207-*i* installed at WAO with $ffCO_2$

calculated from the established O_2 system employing a Sable Systems International Inc. 'Oxzilla II' fuel cell analyser.

2.2 Methods

2.2.1 Picarro G2207-*i* analyser

The Picarro G2207-*i* O_2 analyser makes absolute measurements of the mole fractions of the two most abundant atmospheric O_2 isotopologues, $^{16}O^{16}O$ and $^{16}O^{18}O$, through absorption spectra at 7882.18670 cm^{-1} and 7882.050155 cm^{-1}, respectively (Berhanu et al., 2019). The design principles of this analyser have been described in detail by Berhanu et al. (2019). In our study we evaluate only what is called the 'O_2 concentration' mode, measuring only the $^{16}O^{16}O$ isotopologue. In the other mode, called the '$\delta^{18}O$ plus O_2 concentration' mode, O_2 mole fraction values are considerably less precise, as the analyser is not optimised for $^{16}O^{16}O$ measurements (primarily via a different set point for the pressure in the cavity). The analyser reports both 'wet' and 'dry' O_2 mole fraction values. The 'wet' values ($O_{2,NC}$; NC stands for 'not corrected') do not have any correction applied to them, whereas the 'dry' values ($O_{2,WC}$; WC stands for 'water corrected') are corrected for the dilution effect of water vapour on the O_2 mole fraction, as well as spectroscopic interference, using the analyser's parallel water vapour mole fraction measurements. The G2207-*i* datasheet states a measurement precision of 5 ppm + 0.1 % of the reading (1-σ, 5 sec) for the water vapour mole fraction.

2.2.2 CRAM laboratory measurement of cylinder gases

The performance of the G2207-*i* was evaluated in the UEA CRAM Laboratory by measuring a suite of 12 gas cylinders all containing dry natural air with varying O_2 mole fractions. The cylinders were stored horizontally in a thermally insulated 'Blue Box' enclosure in order to prevent gravitational and thermal fractionation of O_2 relative to N_2 (Keeling et al., 2007). Each cylinder was connected to a regulator with a delivery pressure of 1700 mbar and flow rate of ~95 mL min^{-1}, the cylinders were switched between using a multi-position VICI Valco valve. The O_2 composition of each of these cylinders was precisely defined on the Scripps Institution of Oceanography (SIO) O_2 scale (Keeling et al., 2007) using a VUV O_2 analyser, which is also in the

CRAM Laboratory. The CO_2 mole fraction was defined on the 'WMO CO_2 X2007' scale (Zhao and Tans, 2006) using a Siemens Corp. Ultramat model 6F non-dispersive infrared (NDIR) CO_2 analyser. Five of these cylinders were working secondary standards (WSSes) which were used to calibrate the G2207-*i*, one was a reference tank (RT; explained below in section 2.2.3.2), while the other six were treated as cylinders with unknown mole fractions (Table 2.1). The six 'unknown' cylinders were used to evaluate the performance of the analyser with a CO_2 mole fraction range of 375 to 443 ppm and an O_2/N_2 ratio range of -915 to +435 per meg, a much larger range than would typically be observed in ambient air.

The cylinders were run consecutively, starting with the six 'unknowns' and ending with the five WSSes, with the RT run at the beginning and end; this sequence was repeated twice. Each of the gas cylinders was flushed for 20 minutes prior to running on the G2207-*i* to allow for removal of stagnant air and equilibration of the pressure regulators; air from each cylinder was then passed through the analyser for 20 minutes, with the first 8 minutes of data discarded to allow flushing of the previous cylinder's air from the cavity, and to maintain consistency with the flushing time employed in subsequent WAO tests (section 2.2.3.2). The remaining 12 minutes for each cylinder was then averaged to give the 'raw' $O_{2,NC}$ value for each cylinder as measured on the G2207-*i*.

Table 2.1. Declared O_2/N_2 ratios and CO_2 mole fractions with ± 1σ standard deviations of the five WSSes, RT, and six 'unknown' cylinder gases used in the CRAM Laboratory tests of the G2207-*i.*

Cylinder number	Cylinder ID	Declared O_2 (per meg)[a]	Declared CO_2 (ppm)[b]
WSS1	D089507	-565.5 ±1.3	428.741 ±0.018
WSS2	D801299	-486.1 ±3.0	381.230 ±0.016
WSS3	D073409	-658.4 ±2.2	398.875 ±0.018
WSS4	D073419	-926.4 ±5.9	440.355 ±0.072
WSS5	D073418	-782.7 ±5.6	413.662 ±0.057
RT	CC78691	-414.3 ±0.8	384.915 ±0.005
1	D273555	-914.8 ±0.7	443.384 ±0.013
2	D399093	-880.5 ±0.9	415.246 ±0.003
3	ND29112	-582.0 ±1.0	399.976 ±0.004
4	ND29110	-375.0 ±1.3	381.544 ±0.004
5	D273559[c]	411.7 ±2.1	375.122 ±0.007
6	D801298[c]	434.6 ±0.3	412.934 ±0.002

[a] Values declared with a VUV O_2 analyser in the CRAM Laboratory traceable to the SIO O_2 scale
[b] Values declared with a Siemens Ultramat 6F NDIR CO_2 analyser in the CRAM Laboratory traceable to the WMO CO_2 X2007 scale
[c] The O_2 values of these cylinders is far outside the range observed in ambient air, thus are less relevant to the applications of atmospheric observations but have been included in this analysis for completeness of examining the analysers performance.

The G2207-*i* has a linear response to O_2 mole fraction (Eq. (2.3))

$$y = Bx + C \qquad (2.3)$$

where, B and C are the coefficients derived from the slope and intercept of the linear regression calculated from the measurement of the WSSes. Therefore, a minimum of two WSS cylinders are required to determine the B and C coefficients, but by using five we are able to calculate the coefficient of determination (R^2), as well as providing more robustness in the fit. The calibration equation was used to convert the 'raw' $O_{2,NC}$ values taken from the G2207-*i* (x in Eq. (2.3)) into what we call 'ppm equivalent' (ppmEquiv) O_2 units (y in Eq. (2.3)), as described in Kozlova and Manning (2009). A linear interpolation between the RT at the beginning and end of each run was used as a baseline for the run and subtracted from all other cylinder measurements to correct for short-term instrumental variations. The calibration curve (Eq. (2.3)) for the G2207-*i* was also determined relative to the interpolated RT values (WSS - RT); thus, all the unknown cylinder measurements could be converted into ppmEquiv. The ppmEquiv O_2 units were then converted to per meg units, providing a $\delta(O_2/N_2)$ value for each 'unknown cylinder, using Eq. (2.4).

$$\delta\left(\frac{O_2}{N_2}\right) = \frac{\delta O_2 + (CO_2 - 363.29) \times S_{O2}}{S_{O2} \times (1 - S_{O2})} \qquad (2.4)$$

where, δO_2 is the calibrated G2207-*i* $O_{2,NC}$ value in ppmEquiv units, CO_2 is the declared cylinder CO_2 mole fraction from the Siemens analyser in ppm, S_{O2} is 0.2094 which is the standard mole fraction of O_2 molecules in dry air, and 363.29 is an arbitrary CO_2 reference value in ppm, inherent to the SIO O_2 scale (Stephens et al., 2007a).

2.2.3 Weybourne Atmospheric Observatory field tests

Weybourne Atmospheric Observatory (WAO) is located on the north Norfolk coast, UK (52°57'02''N, 1°07'19''E), approximately 35 km north-northwest of Norwich, 170 km northeast of London and 200 km east of Birmingham. It is part of the European Union's Integrated Carbon Observation System (ICOS) and the World Meteorological Organization's (WMO) Global Atmosphere Watch (GAW) programme. High-precision, high-accuracy, continuous measurements of a wide array of atmospheric gas species (including greenhouse gases, isotopes, reactive gases) are

carried out at a fine temporal scale, funded in part through the UK's National Centre for Atmospheric Science (NCAS) long-term measurement programme.

Atmospheric O_2 and CO_2 have been measured continuously at WAO since 2008 (Wilson, 2013). CO_2 is measured with an Ultramat 6E NDIR analyser (Siemens Corp.) and O_2 is measured with a 'Oxzilla II' dual fuel cell O_2 analyser (Sable Systems International Inc.) (hereafter referred to as the 'Oxzilla'). The Oxzilla is a differential analyser which uses two lead fuel cell sensors consisting of a lead anode in an acidic electrolyte solution. O_2 from the air passes through a gas-permeable membrane in the cells and undergoes electrochemical reduction. This reaction then generates a current that is directly proportional to the partial pressure of O_2 at the cell sensing surface. The analysers are arranged in series, with the air sample first passing through the Ultramat 6E and then the Oxzilla, with rigorous gas handling and calibration protocols followed (as in Stephens et al., 2007a).

The G2207-*i* was installed at WAO from 23 October 2019 – 02 November 2019, sampling from a solar shield aspirated air inlet (AAI) at a height of 10 m above ground level (a.g.l.; 20 m above sea level, a.s.l.). The AAI protects the inlet from solar radiation and generates a continuous air flow over the inlet, thus preventing the differential fractionation of O_2 molecules relative to N_2 molecules due to ambient temperature variations (Blaine et al., 2006) and relatively slow inlet flow rates (Manning, 2001). A full plumbing diagram of the gas-handling set-up for the G2207-*i* at WAO is displayed in Figure 2.1.

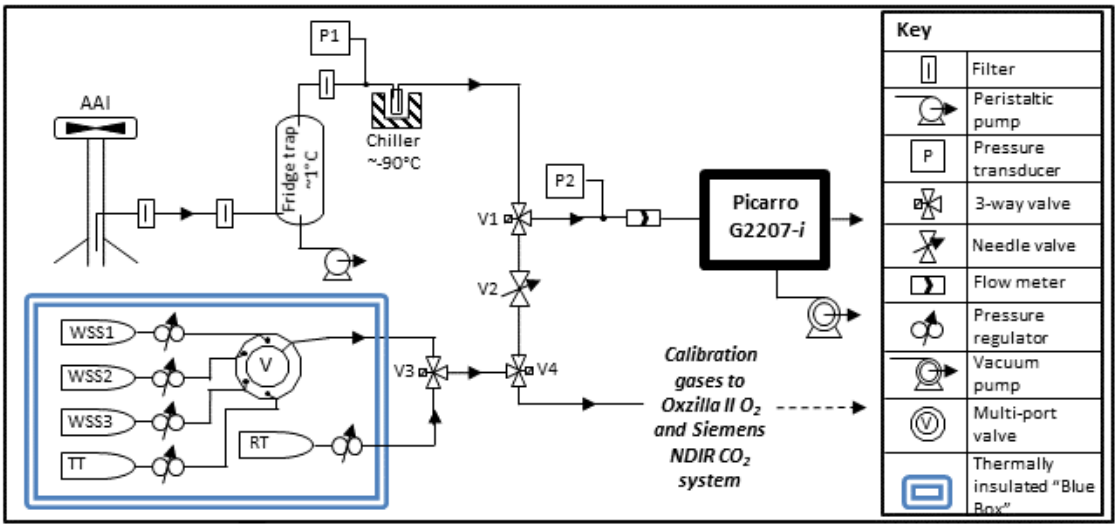

Figure 2.1. Gas handling diagram of the Picarro G2207-*i* installed at WAO. (AAI, aspirated air inlet; WSS, working secondary standard; RT, reference tank; TT, target tank). Calibration gases were shared with the established O_2 and CO_2 system (using V4), but the established system has its own AAI, pump, drying system, and pressure and flow control (not depicted here).

2.2.3.1 Drying

Water vapour mole fractions in the troposphere vary from a few parts per million to a few percent over small temporal and spatial scales. This water vapour has a diluting effect on atmospheric gas measurement. A 1 ppm increase of water vapour will dilute the measured atmospheric O_2 by approximately 1.3 per meg (Stephens et al., 2007a); thus, the existing method for high-precision atmospheric O_2 measurements is to dry the sample air to less than 1 ppm water vapour content before measurement. All calibration and RT gases are also dried to less than 1 ppm water vapour. Furthermore, measurements using spectroscopy techniques are also sensitive to water vapour variability due to changes in the degree of pressure broadening of the spectroscopic lines used to measure the O_2 and $\delta^{18}O_2$. Water vapour correction has previously been successfully implemented for measurements of CO_2 and methane (CH_4) with CRDS analysers (Chen et al., 2010); however, in order to achieve accuracies within the WMO goal of 1% H_2O, custom coefficients must be obtained for each analyser (Rella et al., 2013).

As discussed in section 2.1, O_2 measurements are reported by the G2207-*i* as 'wet' ($O_{2,NC}$) and, after the implementation of water correction, 'dry' ($O_{2,WC}$). In order to evaluate the effectiveness of the built-in water correction procedure for compensating for water vapour dilution, ambient air was sampled with three different drying regimes: no drying, partial drying, and full drying. Under the full drying conditions (which is the current standard practice), the sample air passed through a fridge trap (~1°C) and a cryogenic chiller trap (~-90°C), removing water vapour to < 1 ppm. Under partial drying the chiller was bypassed, so the sample air only passed through the fridge trap, which dries the air to approximately 5000 ppm of water vapour. With no drying, both the chiller and fridge were bypassed. Air was simultaneously sampled through a separate AAI (10 m a.g.l.) into the pre-existing O_2 and CO_2 system with full drying during each of these stages. The time difference between air travelling from the AAIs to each of the two analysers was accounted for. This was done by running ambient air through the G2207-*i* and Oxzilla systems and comparing the high-frequency data with differing time-shifts when there was a lot of variability in the O_2 measurements. We found that no correction was needed for the response time between the two systems.

To evaluate the built-in water correction procedure of the G2207-*i* the $O_{2,WC}$ values were compared with measurements from the Oxzilla (which was continuously

sampling fully dried air) for the no drying and partial drying periods, and the $O_{2,NC}$ and $O_{2,WC}$ G2207-*i* values were compared to the Oxzilla when sampling fully dried air.

2.2.3.2 Calibration procedure

A tailor-made calibration protocol was developed for the G2207-*i* following ICOS atmospheric station specifications (ICOS-RI, 2020). The calibration cylinders were stored horizontally in a thermally insulated 'Blue Box' enclosure in order to prevent gravitational and thermal fractionation of O_2 and N_2. The calibration gases consisted of three WSSes with precisely defined O_2 and CO_2 values which span the unpolluted atmospheric range (traceable to the SIO O_2 and WMO CO_2 X2007 scales) and a reference tank (RT) with O_2 and CO_2 values close to ambient air conditions at the site. The repeatability and compatibility of the analyser were evaluated using a target tank (TT) (sometimes known as a 'surveillance tank') with precisely defined O_2 and CO_2 values. With full drying of the sample air each of the WSSes, the RT, and the TT were run for 20 minutes, the first 8 minutes was discarded due to the sweep-out time of the G2207-*i*, equilibration after valve switching, and surface effects, and the final 12 minutes averaged to determine the cylinder value for the given run. A flushing period of 8 minutes and averaging time of 12 minutes were chosen to match that of the established system. Under partial and no drying, the run-time of the cylinders was increased in order to fully flush the G2207-*i* of water vapour; each cylinder was therefore run for 32 minutes, with the first 20 minutes being discarded and the final 12 minutes averaged.

A full 3-gas WSS calibration of the G2207-*i* was run every 23 hours, this frequency is intentionally not a multiple of 24 hours in order to prevent aliasing the data by calibrating under environmental conditions that may occur at the same time each day. This calibration corrects for drift in the span or non-linearity of the analyser. As in the CRAM laboratory tests (see section 2.2.2), the WSSes were used to define a calibration equation to convert the raw analyser O_2 values into ppmEquiv O_2 units. Eq. (2.3) and the concurrent CO_2 measurement from the Ultramat 6E NDIR were then used to convert this into per meg units.

The RT is used for data correction caused by short-term instrument drift and was run every 5 hours. A linear interpolation between each of the RT run averages was treated as a baseline and subtracted from all subsequent air and cylinder measurements. The calibration curve for the G2207-*i* was also determined relative to

the RT values (WSS- RT) , thus the air measurement differences can be easily converted into per meg units.

Finally, the TT was run every 7 hours, this cylinder is used to quantify the repeatability and compatibility of the analyser. 'Repeatability' is defined as the closeness of agreement between results of successive measurements of the same measure carried out under the same measurement conditions and is considered as a proxy for the precision of a measurement system. 'Compatibility' is defined as the averaged O_2 value of all TT runs over time, compared to the values declared by the VUV, and provides a measure of the compatibility to the SIO scale over time (Kozlova and Manning, 2009). The TT air does not pass through the AAI or drying lines (Figure 2.1) so it is therefore mainly representative of the analyser's repeatability and compatibility only.

2.2.4 Quantifying fossil fuel CO_2 using atmospheric potential oxygen

In order to further assess the G2207-*i*'s performance in real-world applications the hourly-averaged $O_{2,NC}$ observations from the full drying regime period at WAO were used to isolate the fossil fuel component of the concurrent CO_2 observations and then compared to the $ffCO_2$ values calculated from atmospheric potential oxygen (APO) derived from the hourly-averaged Oxzilla O_2 observations following the methodology outlined in Pickers et al. (2022).

The tracer APO, derived by Stephens et al. (1998), was first calculated using Eq. (2.5) (using both G2207-*i* $O_{2,NC}$ and Oxzilla O_2 values); these APO values were then used to calculate $ffCO_2$ using Eq. (2.6).

$$APO = [O_2] + (\left(\frac{-1.1}{0.2094}\right) \times (350 - [CO_2])) \qquad (2.5)$$

where O_2 and CO_2 are in per meg and ppm units, respectively; -1.1 is the global average O_2:CO_2 terrestrial biosphere-atmosphere exchange rate (Severinghaus, 1995), 0.2094 is the mole fraction of O_2 molecules in dry air (Tohjima et al., 2005), and 350 is an arbitrary reference value for CO_2 in ppm. Multiplying CO_2 by -1.1 and dividing by 0.2094 converts the CO_2 data from ppm to per meg units.

$$ffCO_2 = \frac{APO - APO_{bg}}{R_{APO:CO_2}} \qquad (2.6)$$

Where APO is derived from Eq. (5) in per meg units, APO_{bg} is the APO background, or baseline, value determined using a statistical baseline fitting procedure, and $R_{APO:CO2}$ is the APO:CO_2 combustion ratio for fossil fuel emissions. The

APO_{bg} values were determined using the rfbaseline function from the IDPmisc package in R, which implements robust fitting of local regression models, with a smoothing window of 1 week (Ruckstuhl et al., 2012). The APO:CO_2 emission ratio ($R_{APO:CO2}$) used is -0.3 mol mol^{-1}, an approximate mean value for WAO as determined from the COFFEE inventory (a typical value for fossil fuel emissions, given that the APO:CO_2 ratio = O_2:CO_2 + 1.1) (Pickers, 2016; Steinbach et al., 2011). The uncertainty on the ffCO_2 mole fractions was calculated using Eq. (2.6) with the upper and lower uncertainty limit for each variable (where the measurement uncertainty for APO was calculated by summing in quadrature the CO_2 and O_2 measurement uncertainty for each analyser), then taking the standard deviation (SD) of the resultant ffCO_2 value of each combination for each hourly time stamp.

2.3 Results and discussion

2.3.1 Precision and drift

To assess the short-term precision and optimal averaging time of the G2207-*i* the Allan deviation technique (Werle et al., 1993) was used whilst sampling a compressed-air cylinder in the laboratory (50 L, 200 bar). The cylinder was run for 24 hours with a sample flow rate of 94 mL min^{-1} and cavity pressure and temperature of 340 mbar and 45°C, respectively. The results of this Allan deviation analysis are in agreement with those obtained by Berhanu et al. (2019), where a precision of 1 ppm (~4.8 per meg) was achieved after an averaging time of 300 seconds. Precision then continues to improve until around a 30 minute averaging time where a precision of ~0.5 ppm (~2.4 per meg) is reached, and remains around that value for averaging times up to around 1 hour (Figure 2.2). It should be noted that unlike the hourly average and standard deviation obtained from measurement of cylinder air, the hourly averaged atmospheric data also contain natural variability in addition to analyser related noise and drift.

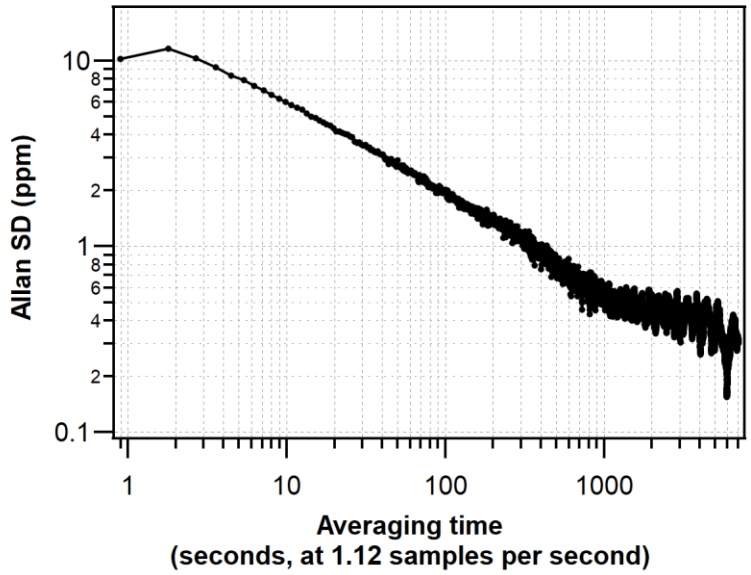

Figure 2.2. Allan deviation plot displaying the precision of the G2207-*i* O_2 mole fraction measured from an ambient compressed-air cylinder. The Allan deviation was calculated using the 'avarn' function from the 'allanvar' R package.

To evaluate the analyser drift (i.e., the changing sensitivity of the analysers response with time), $O_{2,NC}$ values from the G2207-*i* were averaged to 1 hour (Figure 2.3b; reported in ppm where 1 ppm corresponds to a change of 4.8 per meg in the O_2/N_2 ratio). The G2207-*i* datasheet states a maximum drift at STP (standard temperature and pressure) (over 24 hours, peak-to-peak, 1-hour internal average at 21 % O_2) of <6 ppm. We found that over 24 hours, the range of the hourly averages is ~1.2 ppm (approximately 5.8 per meg); this is better than stated by Picarro Inc. but does not meet the WMO compatibility goal of ± 2 per meg, as the internal drift of the analyser is greater than this goal. The standard deviation of each of these hourly averages is ~14.5 ppm (~69.6 per meg) (Figure 2.3a), this is caused by the large amount of analyser noise in the raw 1 second data points, spanning ~100 ppm (~480 per meg) (Figure 2.3c). The overall drift over the 24 hours of raw data however is very small, shown by a linear regression slope of -4.26×10^{-6} ppm s^{-1} (Figure 2.3c).

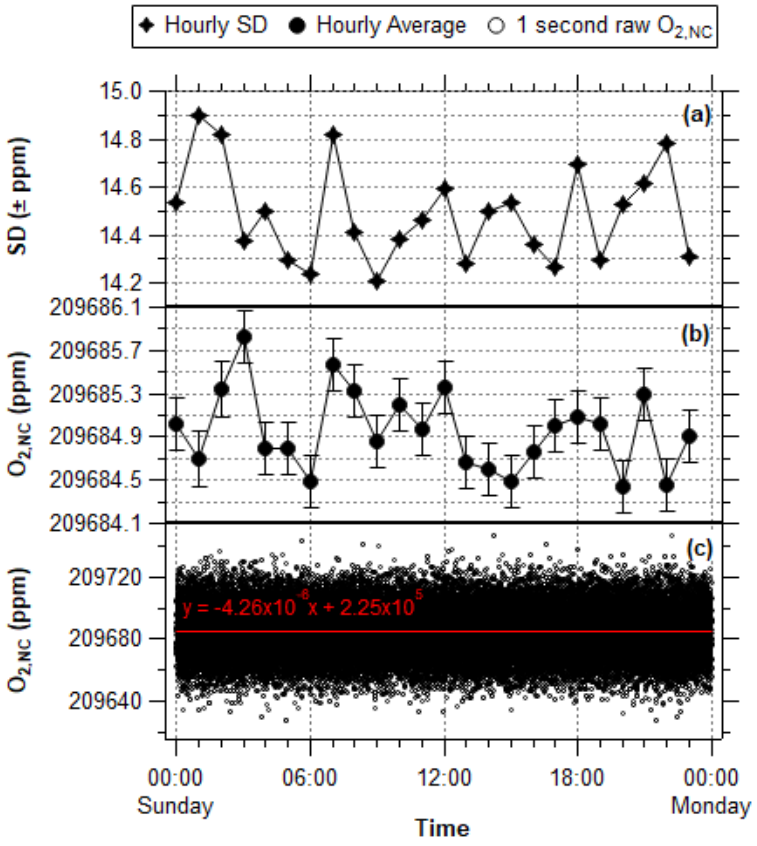

Figure 2.3. $O_{2,NC}$ mole fractions from the G2207-*i* sampling dry compressed cylinder air over 24 hours (reported in ppm, where 1 ppm corresponds to a change of 4.8 per meg in the O_2/N_2 ratio). (a) Standard deviation of the hourly averaged values. (b) Hourly averaged $O_{2,NC}$, with error bars representing standard deviation. (c) Raw 1 second $O_{2,NC}$ values, the red line depicts the linear regression line, with the equation and R^2 value written above.

2.3.2 CRAM laboratory measurement of cylinder gases

The G2207-*i* analyser performance was evaluated by measuring six gas cylinders with precisely defined O_2 and CO_2 values as measured on a VUV O_2 analyser and Siemens Ultramat 6F NDIR CO_2 analyser (Table 2.1). The difference between the $O_{2,NC}$ values (per meg) as measured by the G2207-*i* and the declared values from the VUV are shown in Table 2.2, for runs both with and without the RT interpolation applied. This procedure was carried out twice, referred to as 'Run 1' and 'Run 2' in Table 2.2.

For both sets of runs without the application of the RT interpolation the difference between the VUV declared value and that measured by the G2207-*i* is very large and far outside of an acceptable range (Table 2.2), with an average difference from the declared values for all cylinders of 22.0 ± 10.3 per meg. For all cylinders, except for cylinder 5 and 6, a large improvement in the difference is seen after the

application of the RT correction. Due to the large differences between the declared and measured values without the RT correction applied, only the results with the RT correction will be discussed hereafter.

Table 2.2. The difference between the O_2 value of each cylinder as measured on the G2207-*i* and the VUV analyser (G2207-*i* - VUV), for two runs on the G2207-*i* with and without RT correction applied.

		Without RT correction			With RT correction		
Cyl no.	**Declared O_2 (per meg)**	**Run 1 difference from declared (per meg)[a]**	**Run 2 difference from declared (per meg)[a]**	**Mean of absolute difference of both runs (per meg)[b]**	**Run 1 difference from declared (per meg)[a]**	**Run 2 difference from declared (per meg)[a]**	**Mean of absolute differences of both runs (per meg)[b]**
1	-914.8 ±0.7	9.9±8.4	21.4±8.2	15.7± 8.1	0.4±8.5	2.4±8.1	1.4±1.4
2	-880.5 ±0.9	13.7±8.7	26.5±8.3	20.1±9.1	6.1±8.4	7.6±8.2	6.9±1.1
3	-582.0 ±1.0	8.1±8.5	22.4±11.3	15.3±10.1	0.7± 8.0	3.1±11.2	1.9±1.7
4	-375.0 ±1.3	12.4±11.6	18.4±9.5	15.4±4.2	5.8±11.3	-1.1±9.5	3.5±3.3
5	411.7 ±2.1	44.0±12.6	-3.6±11.5	23.8±28.6	19.0±12.4	-40.1±10.2	29.6±14.9
6	434.6 ±0.3	44.6±5.4	-39.1±10.2	41.9±3.9	22.2±5.1	-49.8±11.5	36.0±19.5

[a] ±1σ standard deviation of the 12-minute G2207-*i* average.
[b] ±1σ standard deviation of the average of the run 1 and run 2 G2207-*i* – VUV absolute differences.

Cylinders 5 and 6 contain O_2 values far higher than that found in ambient air (411.7 and 432.6 and per meg, respectively) and outside of the range spanned by the WSSes used for calibration. For these two cylinders, the difference between the declared value and that measured by the G2207-*i* is far larger than the other cylinders and also more variable between the two runs with a standard deviation of the absolute values between the two runs of ± 14.9 and ± 19.5 per meg, respectively (Table 2.2). Berhanu et al. (2019) found that the accuracy of the G2207-*i* was reduced when the CO_2 mixing ratio was much higher than that of ambient air but did not observe the same reduction in accuracy with high O_2 mixing ratios. Ignoring the two cylinders with positive O_2, the average absolute difference between the remaining 4 unknown cylinders and the declared values over the two runs is 3.4 ± 2.5 per meg, this is slightly greater than the WMO compatibility goal of ± 2 per meg but does fall within the extended goal of ± 10 per meg and is similar to what can be achieved with an Oxzilla II (Pickers et al., 2017). There is also no correlation between the accuracy

and the declared O_2 value excluding the two cylinders with positive O_2 (R^2 = 0.07 for run 1, R^2 = 0.53 for run 2).

Although the accuracy of the O_2 values measured by the G2207-*i* for these cylinders is variable, particularly for the cylinders with high O_2, the standard deviation of the 2-minute data points used to calculate the final cylinder O_2 value as defined by the G2207-*i* within each run is more consistent. However, the repeatability, used as a proxy for precision, and defined here as the ± 1σ standard deviation of the average of the two measurements of each cylinder are variable. For the two cylinders with high O_2 (cylinders 5 and 6) the repeatability is more than 5 times greater than the WMO extended repeatability goal of ± 5 per meg. For the remaining four cylinder the repeatability is far lower, with cylinder 1 and cylinder 3 both falling within the extended repeatability goal.

2.3.3 Weybourne Atmospheric Observatory field tests

2.3.3.1 Partial and no drying of ambient air measurements

The results from no drying and partial drying of the sample air into the G2207-*i* at WAO are displayed in Figure 2.4 and Figure 2.5, respectively. The O_2 mole fractions reported in ppm units by the G2207-*i* were converted to per meg units using the calibration equations produced through the measurement of the three WSS cylinders every 23 hours, and the concurrent CO_2 observations from the Ultramat 6E analyser.

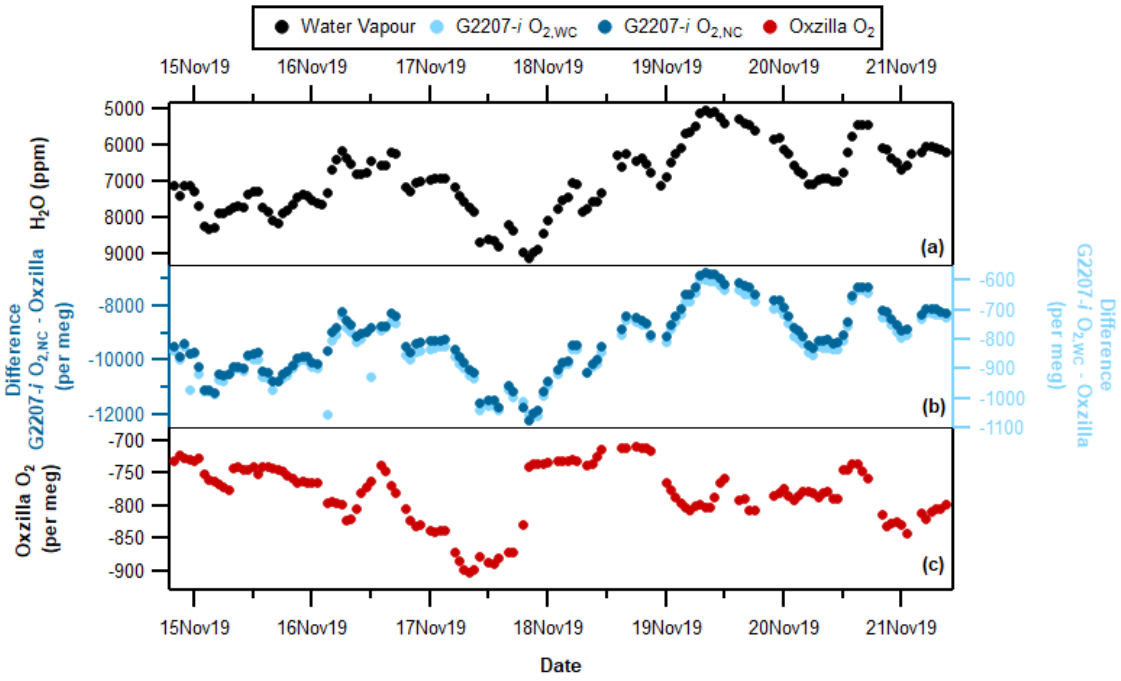

Figure 2.4. With no drying of the sample air through the G2207-*i* (a) Hourly averaged water vapour, (b) G2207-*i* – Oxzilla difference for $O_{2,NC}$ (dark blue) and $O_{2,WC}$ (light blue), and (c) Oxzilla O_2 with no drying of the sample air through the G2207-*i*. Note the reversed water vapour axis and different axis scales for $O_{2,NC}$ and $O_{2,WC}$.

During the period where there was no drying of the G2207-*i* air sample there is a significant difference between the O_2 values reported by the Oxzilla (dried air) and the G2207-*i* $O_{2,NC}$ values (Figure 2.4b), this is to be expected due to the diluting effect of water vapour; however, there is also a significant difference between the Oxzilla O_2 and the G2207-*i* $O_{2,WC}$ values. Over the entire no drying period the average difference between the Oxzilla observations and the G2207-*i* $O_{2,NC}$ is -9654.4 ± 272.8 per meg. The average difference between the Oxzilla and the G2207-*i* $O_{2,WC}$ values is -849.8 ± 31.1 per meg. Although the difference is substantially smaller with the application of the G2207-*i* built-in water correction procedure, it is still unusably large, with no similarity in the Oxzilla and G2207-*i* signals and both the $O_{2,NC}$ and $O_{2,WC}$ G2207-*i* values correlating with the H_2O variability (Figure 2.6a and b). This demonstrates that the algorithm currently applied for water correction is unsuitable for precise O_2 measurement.

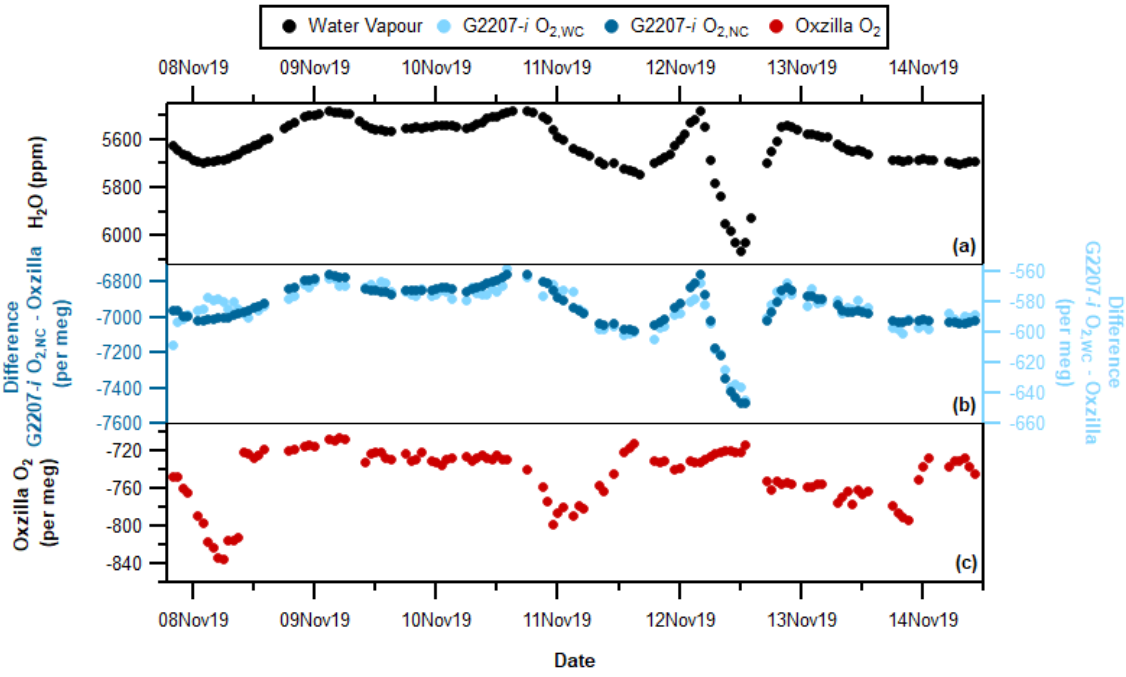

Figure 2.5. With partial drying of the sample air through the G2207-*i* (a) Hourly averaged Water vapour (top), (b) G2207-*i* – Oxzilla difference for $O_{2,NC}$ (dark blue) and $O_{2,WC}$ (light blue), and (c) Oxzilla O_2 (bottom) with partial drying of the sample air through the G2207-*i* (Oxzilla sample air is fully dried). Note the reversed water vapour axis, and different axis scales for $O_{2,NC}$ and $O_{2,WC}$. The spike in water vapour on 12 November 2019 is due to a temporary increase in the temperature of the fridge.

As seen during the no-drying period of the sample air, there is also a significant difference between the reported O_2 values of the Oxzilla and G2207-*i* under the partial drying regime for both $O_{2,NC}$ and $O_{2,WC}$ (Figure 2.5). With partial drying, the time-series of the difference between the O_2 values of the two analysers is a lot smoother than with no drying, this is due to the fridge trap removing some of the natural variability in the water vapour mole fraction. Over the entire partial drying period the average difference between the Oxzilla observations and the G2207-*i* $O_{2,NC}$ is -7144.1 ± 258.6 per meg. The average difference between the Oxzilla and the G2207-*i* $O_{2,WC}$ values is -612.7 ± 31.8 per meg. There is a large improvement with the application of the water correction procedure; however, as with the no-drying results, the difference in O_2 values between the Oxzilla and G2207-*i* $O_{2,WC}$ are too large to be usable for any application, with the $O_{2,NC}$ and $O_{2,WC}$ values correlating with the H_2O variability (Figure 2.6c and d).

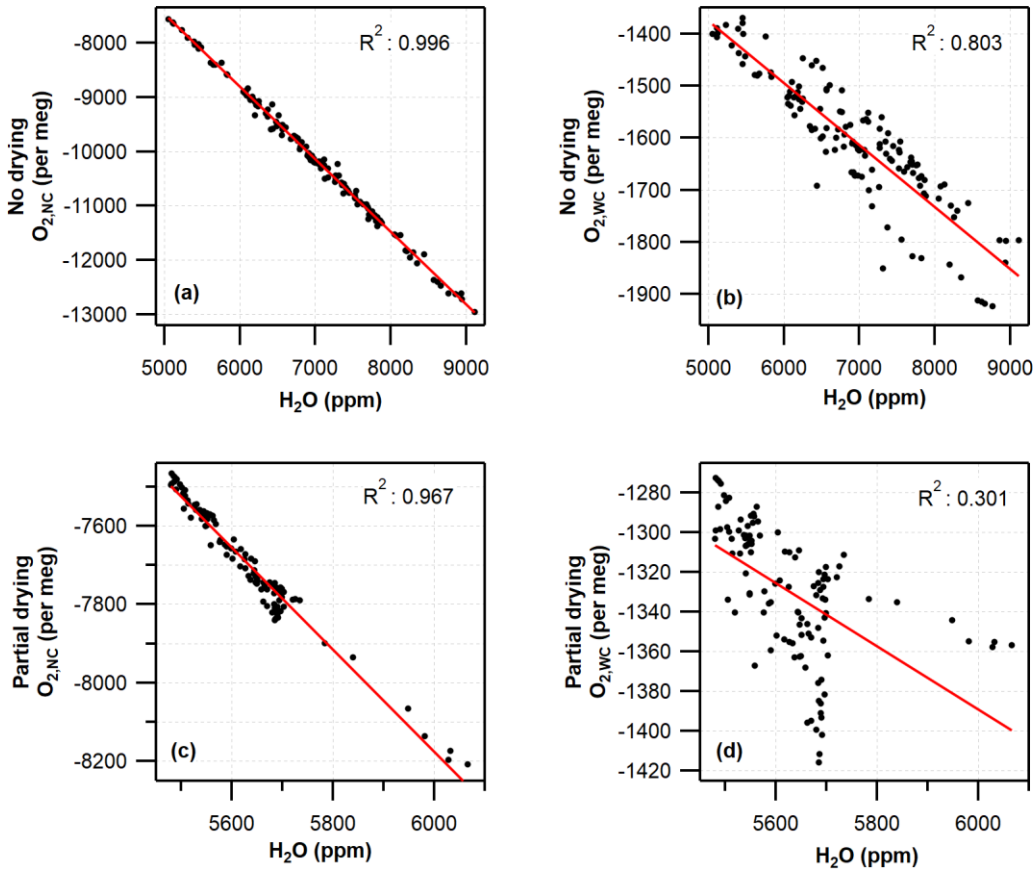

Figure 2.6. Correlation between water vapour mole fraction and hourly averaged G2207-*i* O_2 for (a) no drying $O_{2,NC}$, (b) no drying $O_{2,WC}$, (c) partial drying $O_{2,NC}$, and (d) partial drying $O_{2,WC}$. Red lines show linear regression.

Under both partial drying and no-drying regimes, the difference between the Oxzilla and G2207-*i* values is strongly correlated with the water vapour mole fraction but decreases with the application of the built-in water correction procedure (Figure 2.6). The R^2 value decreases from 0.996 to 0.803 for no drying and from 0.967 to 0.301 for partial drying once the water correction has been applied. Given the correlation between the water vapour mole fraction and the $O_{2,WC}$ reported by the G2207-*i* these values are not usable without significant improvements to the water correction procedure by Picarro Inc..

Due to the large differences observed between the Oxzilla and G2207-*i* reported O_2 values under no drying and partial drying, no further investigation was undertaken, thus only the fully dried sample air is considered hereafter.

2.3.3.2 Full drying of ambient air measurements

The results from fully drying the sample air between 24 October 2019 and 7 November 2019 are displayed in Figure 2.7. The O_2 mole fractions reported in ppm

units by the G2207-*i* were converted to per meg units using the calibration equations produced through the measurement of the three WSS cylinders every 23 hours, and the concurrent CO_2 observations.

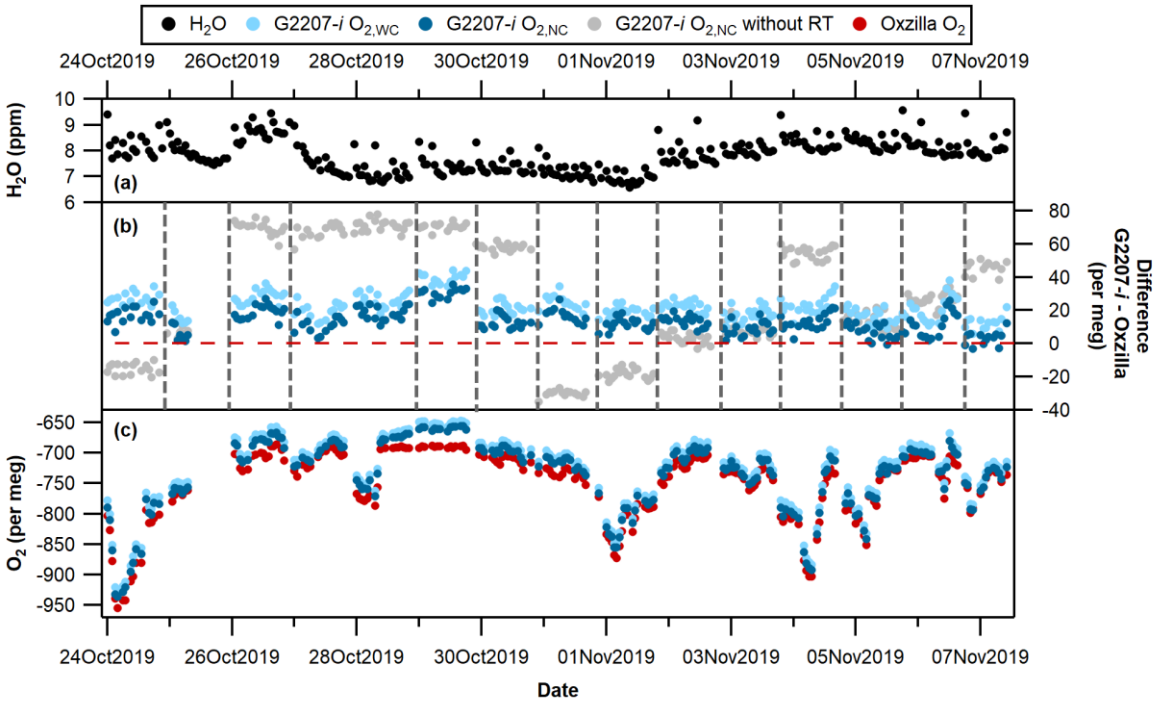

Figure 2.7. Time series with full drying of the air sample. (a) Hourly averaged water vapour, spikes are due to equilibration after valve switching from cylinder air to sample air. (b) G2207-*i* – Oxzilla difference for $O_{2,WC}$ (light blue), $O_{2,NC}$ (dark blue), and $O_{2,NC}$ without the RT interpolation applied (grey); vertical dashed lines indicated a full 3-gas WSS calibration on the G2207-*i*, and the red horizontal line indicates zero difference from the Oxzilla. (c) Hourly averaged Oxzilla O_2 (red), $O_{2,WC}$ (light blue) and $O_{2,NC}$ (dark blue). Note, there was no WSS calibration on 27 October 2019 due to a macro error which prevented valve switching to calibration gases, therefore the calibration from 26 October 2019 was applied for 46 hours.

There is a greater difference between the Oxzilla and G2207-*i* $O_{2,WC}$ values than the $O_{2,NC}$ values, with an average difference over the entire full drying period of 22.6 ± 7.4 per meg compared to 13.6 ± 7.5 per meg, respectively. This may be due to overcorrection of the $O_{2,NC}$ values as the water vapour mole fraction is below the G2207-*i*'s lower detection limit and precision i.e. the G2207-*i* is reporting H_2O mole fractions of approximately 7 ppm (Figure 2.7a) (with frequent spikes due to equilibration after switching of V1 (Figure 2.1) from cylinder to sample air); however, when the air sample is fully dried by passing through the chiller and fridge trap, the water vapour is reduced to below 1 ppm. This overestimated water correction whilst sampling fully dried air was also found by Berhanu et al. (2019). We therefore only refer to the $O_{2,NC}$ values, which we believe to be more accurate, in the analysis from now onwards.

The large jumps in the G2207-*i* $O_{2,NC}$ values following WSS calibrations (see Figure 2.7b, grey points) are caused by a drift in the instruments baseline, which only becomes applied to the data after each calibration step is applied. These jumps were reduced through the application of the 5-hour RT interpolation procedure (see Figure 2.7b, blue points) which constrained the baseline drift (refer to section 2.2.3.2). After the application of the RT interpolation the jumps between WSS calibrations were vastly reduced (see Figure 2.7).

2.3.3.3 Repeatability and compatibility

The repeatability and compatibility of the analyser were evaluated through the running of a TT every 7 hours during the full drying period using $O_{2,NC}$ values, the results of which are presented in Figure 2.8 and Table 2.3. For O_2 the WMO repeatability goal is ± 1 per meg (with an extended goal of ± 5 per meg) and the compatibility goal is ± 2 per meg (with an extended goal of ± 10 per meg; indicated by the dashed lines in Figure 2.8; (Crotwell et al., 2020)).

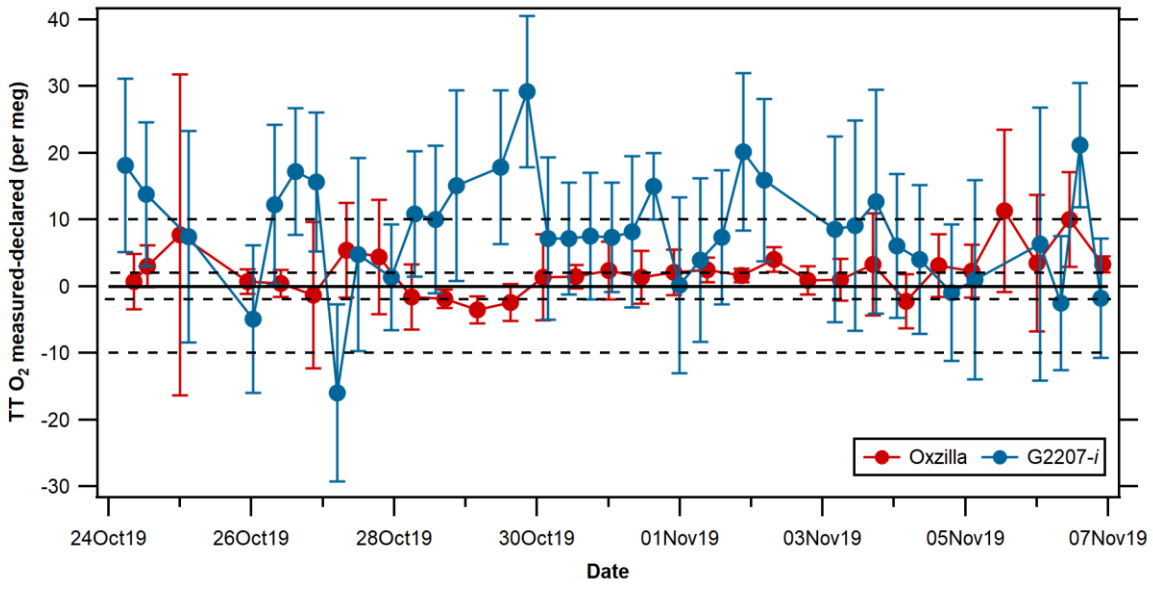

Figure 2.8. TT differences from declared values (measured - declared) (± 1σ standard deviation) for the Oxzilla (red) and G2207-*i* $O_{2,NC}$ (blue) . The solid line indicates zero difference from the declared O_2 value of the TT, and the dashed lines indicate the WMO compatibility goal of ± 2 per meg and the extended goal of ± 10 per meg.

The repeatability is determined from the mean ± 1σ standard deviations of the average of two consecutive measurements of the TT. For the G2207-*i* this is equal to ± 5.7 ± 5.6 per meg, compared to ± 2.2 ± 2.0 per meg on the Oxzilla. Prior to applying the RT interpolation to the G2207-*i* data, the repeatability of the G2207-*i* was ± 11.9 ±

13.8 per meg, twice as bad as after the RT application; this is because after the RT interpolation was applied the large jumps in the TT value after a WSS calibration were removed. In the context of the WMO repeatability goals, neither the Oxzilla nor the G2207-*i* meet the goal of ± 1 per meg. For O_2, the WMO the goals are very ambitious and not currently achievable by the O_2 measurement community; hence, the 'extended' O_2 repeatability goal of ± 5 per meg (Crotwell et al., 2020). The Oxzilla TT results lie within this extended goal, however the G2207-*i* does not, even after the application of the RT.

Table 2.3. Repeatability and compatibility goals and achievements for each analyser.

	Repeatability (per meg)[a]	**Compatibility (per meg)[b]**
WMO compatibility goal	± 1 (± 5)[c]	± 2 (± 10)[c]
Oxzilla	± 2.21 ± 1.96	± 3.03 ± 2.59
G2207-*i* $O_{2,NC}$ without RT interpolation	± 11.86 ± 13.83	± 22.88 ± 34.11
G2207-*i* $O_{2,NC}$	± 5.69 ± 5.61	± 9.97 ± 6.71

[a] Values are calculated using the method in Kozlova and Manning (2009) and Pickers et al. (2017). Mean ± 1σ standard deviations of the average of two consecutive measurements of the TT, determined from 30 TT measurements for the Oxzilla and 37 TT measurements for the G2207-*i*, where one run is the average of 12 minutes of data. Uncertainties are given on these mean standard deviations, illustrating that the analytical repeatability is variable over time.

[b] Mean differences between the measured TT O_2/N_2 ratio, and the declared values determined on the VUV analyser against primary calibration standards on the SIO O_2 scale.

[c] WMO repeatability and compatibility goals, where the repeatability of a measurement should be at most half of the value of the compatibility goal. For O_2, the WMO the goals are very ambitious and not currently achievable by the O_2 measurement community; hence the 'extended' O_2 goals, which are suitable for some O_2 applications, shown in parenthesis.

The compatibility of the analyser, which is here used as a proxy for accuracy, is determined by calculating the mean difference between the TT O_2 as measured by the G2207-*i* and the VUV declared value (-718 per meg). The mean absolute difference from the declared value on the VUV for the Oxzilla is 3.0 ± 2.6 per meg, this is well within the extended WMO compatibility goal of ± 10 per meg and is quite close to more stringent goal of ± 2 per meg. The compatibility of the G2207-*i* prior to the application of the RT is 22.9 ± 34.1 per meg, which is far greater than even the extended compatibility goal of ± 10 per meg. After the application of the RT interpolation the compatibility of the G2207-*i* $O_{2,NC}$ was calculated as 10.0 ± 6.71 per meg, although this is not within the WMO compatibility goal, it is just within the extended goal, which is deemed suitable for some applications in specific circumstances, such as where the signals are very large as such that reduced

repeatability and compatibility does not preclude useful information from the measurements.

The compatibility and repeatability of the G2207-*i* measurements were vastly improved after the application of a 5-hourly RT, however if one ignores the TT results immediately after a new WSS calibration (i.e., after the large jumps when the RT was not applied), the repeatability without the RT interpolation is 5.2 ± 4.5 per meg, improving to 4.3 ± 4.6 per meg when the RT is applied. This is because the RT corrected for baseline drift between WSS calibrations, but it does not correct for drift within the calibration period. However, as the TT results are imprecise (as illustrated by the large error bars in Figure 2.8), even if any baseline drift within a calibration period were corrected for there would likely be little improvement in the final TT results as the noise in the RT-corrected TT values is primarily caused by imprecision rather than baseline drift.

2.3.4 Applications of the G2207-*i* O_2 measurements in the calculation of fossil fuel CO_2

In order to further assess the G2207-*i*'s performance in real-world applications the fully dried, RT corrected, $O_{2,NC}$ observations from WAO were used to isolate the fossil fuel component of the concurrent CO_2 observations and then compared to the $ffCO_2$ values calculated from the Oxzilla O_2 observations following the APO methodology outlined in Pickers et al. (2022). The resultant $ffCO_2$ values calculated from each analyser are displayed in Figure 2.9.

The measurement uncertainty was calculated as the average hourly SD on 30 October 2019, this date was chosen as it was a particularly stable period with little variation in the TT results for both analysers (Figure 2.8); the resultant uncertainty for the G2207-*i* is **±** 11.2 per meg compared to **±** 4.9 per meg for the Oxzilla. The uncertainty in the baseline (± 28 %), and the emission ratio uncertainty (± 22 %) are significantly larger than these measurement uncertainties (Pickers et al., 2022), but as these are the same for both analysers the additional measurement uncertainty for the G2207-*i* caused by analyser noise increases the uncertainty of the calculated $ffCO_2$ values. The average final calculated uncertainty on the $ffCO_2$ values calculated from the Oxzilla measurements is 5.8 ppm, compared to 13.0 ppm on the G2207-*i* .

The average $ffCO_2$ value over the entire full drying period for the Oxzilla is 5.1 ppm, compared to 7.9 ppm on the G2207-*i* (Table 2.4); the calculated $ffCO_2$ from the

G2207-*i* is higher than that of the Oxzilla 73 % of the time. This difference is predominantly due to the higher O_2 values reported by the G2207-*i* as discussed in section 2.3.3.2; some of this difference also comes from the jumps in the G2207-*i* O_2 values which mean that the calculated baselines used for each analyser follow different trends. For example, on the 27 October 2019 and 30 October 2019 the largest difference between the calculated $ffCO_2$ values is observed (Figure 2.9), on both of these dates there is a large jump in O_2 values from the previous day measured by the G2207-*i* following a WSS calibration (Figure 2.7). Although the O_2 difference between the two analysers on these days are low, there was a large difference the preceding day. Days with the larger differences (due to a higher O_2 value reported by the G2207-*i*) in observed values pull the baseline to become more positive, thus making the difference between the $ffCO_2$ calculated from the two analysers larger on days where the actual observed O_2 difference is smaller.

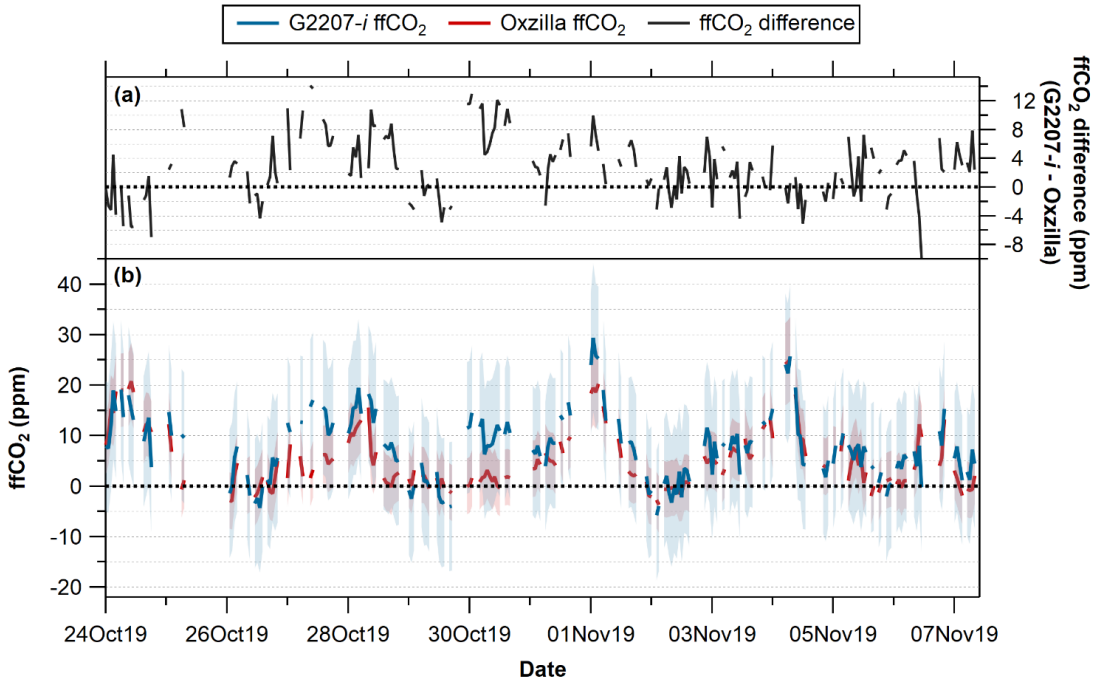

Figure 2.9. (a) Difference between the $ffCO_2$ calculated using the G2207-*i* and the Oxzilla O_2 (G2207-*i* – Oxzilla). (b) Calculated $ffCO_2$ from the G2207-*i* (red) and the Oxzilla (blue), blue and red shaded areas indicate uncertainty of the calculated $ffCO_2$. Dashed black lines indicates 0 ppm. Negative $ffCO_2$ values occur when O_2 observations are above (more negative) the calculated O_2 baseline. Note the gaps are due to threshold requirement of a minimum of 20 minutes of data for hourly averages.

Although the G2207-*i* calculated $ffCO_2$ values are often higher than those from the Oxzilla, it still follows the same trend (with some jumps in the G2207-*i* values); however, the maximum and minimum values occur at different times. The differences

in $ffCO_2$ calculated from the G2207-*i* and the Oxzilla will become problematic if using the G2207-*i* analyser for top-down $ffCO_2$ quantification on an hourly basis.

Table 2.4. Comparison of $ffCO_2$ values calculated from the Oxzilla and G2207-*i* O_2 measurements. Average values given ±1σ standard deviation.

	Oxzilla $ffCO_2$ (ppm)	**G2207-*i* $ffCO_2$ (ppm)**
Average	5.1 ± 5.9	7.9 ± 6.6
Maximum	25.2	29.4
Minimum	-3.7	-6.5

2.4 Conclusions

The performance of the Picarro G2207-*i* under both laboratory and field conditions has been thoroughly evaluated. When running a cylinder on the G2207-*i* over 24 hours in the laboratory, we observed a large amount of noise in the raw 1 second data, resulting in a large standard deviation in averaged data. This standard deviation is reduced over longer averaging times. During the laboratory measurement of cylinder gases with declared O_2 values, the G2207-*i* performed within the WMO extended compatibility goal of ± 10 per meg when measuring cylinders with a negative O_2 per meg value. When measuring cylinders with a positive O_2 value, the precision and accuracy of the result worsened, thus the G2207-*i* is not recommended for use in this range.

When sampling ambient air, we found that the G2207-*i*'s built-in water correction does not, at present, sufficiently correct for the influence of water vapour even when the sample air is partially dried, and we therefore recommend full drying (<1 ppm H_2O) of air samples. When sampling fully dried air, large step-changes in the reported O_2 values from the G2207-*i* were observed after each WSS calibration; the addition of a RT every 5-hours vastly reduced these jumps however they were still observable. When the RT routine was applied the repeatability of the G2207-*i* was ± 5.7 ± 5.6 per meg, falling just outside of the WMO extended goal of ± 5 per meg, it is possible that with a more frequent RT routine this repeatability will improve. The compatibility was ± 10.0 ± 6.7 per meg, falling within the WMO extended compatibility goal for O_2 of ± 10 per meg. In the future, investigation into whether increasing the frequency of the running of a RT to reduce jumps in the observed O_2 values after a WSS calibration may improve both the repeatability and compatibility of the analyser. A key benefit of CRDS analysers is that they do not, in principle,

require drying of the air sample. However, this is not currently the case with the G2207-*i* for O_2 measurements.

References

Battle, M. O., Munger, J. W., Conley, M., Sofen, E., Perry, R., Hart, R., Davis, Z., Scheckman, J., Woogerd, J., Graeter, K., Seekins, S., David, S. and Carpenter, J. (2019) 'Atmospheric measurements of the terrestrial O_2 : CO_2 exchange ratio of a midlatitude forest', *Atmos. Chem. Phys.,* 19(13), pp. 8687-8701.

Bender, M. L., Tans, P. P., Ellis, J. T., Orchardo, J. and Habfast, K. (1994) 'A high precision isotope ratio mass spectrometry method for measuring the O_2/N_2 ratio of air', *Geochimica et Cosmochimica Acta,* 58(21), pp. 4751-4758.

Berhanu, T. A., Hoffnagle, J., Rella, C., Kimhak, D., Nyfeler, P. and Leuenberger, M. (2019) 'High-precision atmospheric oxygen measurement comparisons between a newly built CRDS analyzer and existing measurement techniques', *Atmos. Meas. Tech.,* 12(12), pp. 6803-6826.

Blaine, T. W., Keeling, R. F. and Paplawsky, W. J. (2006) 'An improved inlet for precisely measuring the atmospheric Ar/N_2 ratio', *Atmospheric Chemistry and Physics,* 6(5), pp. 1181-1184.

Chen, H., Winderlich, J., Gerbig, C., Hoefer, A., Rella, C. W., Crosson, E. R., Van Pelt, A. D., Steinbach, J., Kolle, O., Beck, V., Daube, B. C., Gottlieb, E. W., Chow, V. Y., Santoni, G. W. and Wofsy, S. C. (2010) 'High-accuracy continuous airborne measurements of greenhouse gases (CO_2 and CH_4) using the cavity ring-down spectroscopy (CRDS) technique', *Atmos. Meas. Tech.,* 3(2), pp. 375-386.

Crotwell, A., Lee, H. and Steinbacher, M. (2020) *Report of the 20th WMO/IAEA Meeting on Carbon Dioxide, Other Greenhouse Gases and Related Measurement Techniques (GGMT-2019)*, Jeju Island, South Korea: World Meteorological Organization Global Atmospheric Watch (Report Series #255. Available at: https://library.wmo.int/

Dlugokencky, E. J. and Tans, P. P. (2022) 'Trends in Atmospheric Carbon Dioxide. National Oceanic and Atmospheric Administration, Earth System Research Laboratory (NOAA/ESRL)'.

Fleming, L. S., Manning, A. C., Pickers, P. A., Forster, G. L. and Etchells, A. J. (2023) 'Evaluating the performance of a Picarro G2207-i analyser for high-precision atmospheric O_2 measurements', *Atmos. Meas. Tech.,* 16(2), pp. 387-401.

ICOS-RI (2020) *ICOS Atmosphere Station Specifications V2.0*: ICOS ERIC.

Keeling, R. F. (1988a) 'Development of an Interferometric Oxygen Analyzer for Precise Measurement of the Atmospheric O_2 Mole Fraction', *UMI*.

Keeling, R. F. (1988b) 'Measuring correlations between atmospheric oxygen and carbon-dioxide mole fractions - a preliminary-study in urban air', *Journal of Atmospheric Chemistry,* 7(2), pp. 153-176.

Keeling, R. F. and Manning, A. C. (2014) '5.15 - Studies of Recent Changes in Atmospheric O_2 Content', in Holland, H.D. & Turekian, K.K. (eds.) *Treatise on Geochemistry (Second Edition)*. Oxford: Elsevier, pp. 385-404; doi: https://doi.org/10.1016/B978-0-08-095975-7.00420-4.

Keeling, R. F., Manning, A. C., McEvoy, E. M. and Shertz, S. R. (1998) 'Methods for measuring changes in atmospheric O_2 concentration and their application in southern hemisphere air', *Journal of Geophysical Research: Atmospheres,* 103(D3), pp. 3381-3397.

Keeling, R. F., Manning, A. C., Paplawsky, W. J. and Cox, A. C. (2007) 'On the long-term stability of reference gases for atmospheric O_2/N_2 and CO_2 measurements', *Tellus B,* 59(1), pp. 3-14.

Keeling, R. F. and Shertz, S. R. (1992) 'Seasonal and interannual variations in atmospheric oxygen and implications for the global carbon cycle', *Nature,* 358(6389), pp. 723-727.

Kozlova, E. A. and Manning, A. C. (2009) 'Methodology and calibration for continuous measurements of biogeochemical trace gas and O_2 concentrations from a 300-m tall tower in central Siberia', *Atmos. Meas. Tech.,* 2(1), pp. 205-220.

Manning, A. C. (2001) *Temporal variability of atmospheric oxygen from both continuous measurements and a flask sampling network: Tools for studying the global carbon cycle.* Ph.D., University of California, San Diego, La Jolla, California, U.S.A.

Manning, A. C., Keeling, R. F. and Severinghaus, J. P. (1999) 'Precise atmospheric oxygen measurements with a paramagnetic oxygen analyzer', *Global Biogeochemical Cycles,* 13(4), pp. 1107-1115.

Pickers, P. A. (2016) *New applications of continuous atmospheric O_2 measurements: Meridional transects across the Atlantic Ocean, and improved quantification of fossil fuel-derived CO_2.* Ph.D., University of East Anglia, Norwich, UK [Online] Available at: http://cramlab.uea.ac.uk/Publications.htm (Accessed: 15/02/2019).

Pickers, P. A., Manning, A. C., Quéré, C. L., Forster, G. L., Luijkx, I. T., Gerbig, C., Fleming, L. S. and Sturges, W. T. (2022) 'Novel quantification of regional fossil fuel CO_2 reductions during COVID-19 lockdowns using atmospheric oxygen measurements', 8(16), pp. eabl9250.

Pickers, P. A., Manning, A. C., Sturges, W. T., Le Quéré, C., Mikaloff Fletcher, S. E., Wilson, P. A. and Etchells, A. J. (2017) 'In situ measurements of atmospheric O_2 and CO_2 reveal an unexpected O_2 signal over the tropical Atlantic Ocean', *Global Biogeochemical Cycles*.

Rella, C. W., Chen, H., Andrews, A. E., Filges, A., Gerbig, C., Hatakka, J., Karion, A., Miles, N. L., Richardson, S. J., Steinbacher, M., Sweeney, C., Wastine, B. and Zellweger, C. (2013) 'High accuracy measurements of dry mole fractions of carbon dioxide and methane in humid air', *Atmos. Meas. Tech.,* 6(3), pp. 837-860.

Resplandy, L., Keeling, R. F., Eddebbar, Y., Brooks, M., Wang, R., Bopp, L., Long, M. C., Dunne, J. P., Koeve, W. and Oschlies, A. (2019) 'Quantification of ocean heat uptake from changes in atmospheric O_2 and CO_2 composition', *Scientific Reports,* 9(1), pp. 20244.

Ruckstuhl, A. F., Henne, S., Reimann, S., Steinbacher, M., Vollmer, M. K., O'Doherty, S., Buchmann, B. and Hueglin, C. (2012) 'Robust extraction of baseline signal of atmospheric trace species using local regression', *Atmos. Meas. Tech.,* 5(11), pp. 2613-2624.

Severinghaus, J. P. (1995) *Studies of the terrestrial O_2 and carbon cycles in sand dune gases and in biosphere 2.* United States [Online] Available at: https://www.osti.gov/servlets/purl/477735 (Accessed: 04/10/2020).

Steinbach, J., Gerbig, C., Rodenbeck, C., Karstens, U., Minejima, C. and Mukai, H. (2011) 'The CO_2 release and Oxygen uptake from Fossil Fuel Emission Estimate (COFFEE) dataset: effects from varying oxidative ratios', *Atmospheric Chemistry and Physics,* 11(14), pp. 6855-6870.

Stephens, B. B., Bakwin, P. S., Tans, P. P., Teclaw, R. M. and Baumann, D. D. (2007) 'Application of a Differential Fuel-Cell Analyzer for Measuring Atmospheric Oxygen Variations', *Journal of Atmospheric and Oceanic Technology,* 24(1), pp. 82-94.

Stephens, B. B., Keeling, R. F., Heimann, M., Six, K. D., Murnane, R. and Caldeira, K. (1998) 'Testing global ocean carbon cycle models using measurements of atmospheric O_2 and CO_2 concentration', *Global Biogeochemical Cycles,* 12(2), pp. 213-230.

Stephens, B. B., Keeling, R. F. and Paplawsky, W. J. (2011) 'Shipboard measurements of atmospheric oxygen using a vacuum-ultraviolet absorption technique', *Tellus B: Chemical and Physical Meteorology,* 55(4), pp. 857-878.

Tohjima, Y. (2000) 'Method for measuring changes in the atmospheric O_2/N_2 ratio by a gas chromatograph equipped with a thermal conductivity detector', *Journal of Geophysical Research: Atmospheres,* 105(D11), pp. 14575-14584.

Tohjima, Y., Machida, T., Watai, T., Akama, I., Amari, T. and Moriwaki, Y. (2005) 'Preparation of gravimetric standards for measurements of atmospheric oxygen and reevaluation of atmospheric oxygen concentration', *Journal of Geophysical Research: Atmospheres,* 110(D11).

Tohjima, Y., Mukai, H., Machida, T., Hoshina, Y. and Nakaoka, S. I. (2019) 'Global carbon budgets estimated from atmospheric O_2/N_2 and CO_2 observations in the western Pacific region over a 15-year period', *Atmos. Chem. Phys.,* 19(14), pp. 9269-9285.

Werle, P., Mücke, R. and Slemr, F. (1993) 'The limits of signal averaging in atmospheric trace-gas monitoring by tunable diode-laser absorption spectroscopy (TDLAS)', *Applied Physics B,* 57(2), pp. 131-139.

Wilson, P. A. (2013) *Insight into the Carbon Cycle from Continuous Measurements of Oxygen and Carbon Dioxide at Weybourne Atmospheric Observatory, UK.* Ph.D., University of East Anglia, Norwich, UK [Online] Available at: https://www.cramlab.uea.ac.uk/Publications.php (Accessed: 23/02/2019).

Zhao, C. L. and Tans, P. P. (2006) 'Estimating uncertainty of the WMO mole fraction scale for carbon dioxide in air', *Journal of Geophysical Research: Atmospheres,* 111(D8).

Chapter 3 Using radon-222 to determine 'background' mole fractions of trace gases at Weybourne Atmospheric Observatory

3.1 Introduction

The atmospheric mole fraction and lifetime of a gas species is the result of a complex combination of emissions from sources and losses to sinks, and characteristics of the atmospheric volume into which they mix, on a local, regional, and global scale. To interpret the time series of atmospheric gas measurements and to understand the processes that affect them, it is necessary to separate and quantify the contribution from each of the sources and sinks to the measured mole fractions. However, this is a complicated task. For gases that have multiple sources and sinks, measurements of the atmospheric mole fractions alone are inadequate to precisely differentiate the contribution of these different sources and sinks to the total atmospheric abundance (Weiss and Prinn, 2011; Vardag et al., 2015; Pickers et al., 2022). The ability to predict the impact of gases in the atmosphere on climate depends critically on this ability to accurately represent these key processes in a range of models. The understanding of which processes are involved is also of vital importance to predict how sources and sinks may change under future climate scenarios.

Gas species with long lifetimes reside in the atmosphere leading to a 'background' mole fraction that is dictated by sources and sinks; new pollution events then occur on top of this background. The quantification of the different components of the measured mole fraction therefore first requires a separation of 'background' and 'non-background' signals ('background' is sometimes also referred to as 'baseline'). The combination of above-background pollution events with inverse modelling and atmospheric transport and chemistry models can then be used to map and quantify emissions and provide further understanding of the processes contributing to global atmospheric mole fractions. The background mole fraction of an atmospheric species can be defined as 'the concentration [mole fraction] of a gas species in a pristine air mass in which atmospheric impurities of a relatively short lifetime are not present' (IUPAC, 1997). For example, well-mixed air masses that contain constituent gas species at mole fractions considered representative of regional or hemispheric background value due to having little influence from localised sources of the constituent species. In order to identify an atmospheric background, it is therefore necessary to remove continental and local anthropogenic effects, which can cause either increases or decreases in the background mole fraction (Brunke et al., 2004).

To accurately assess long-term natural and anthropogenic emissions influences and short-term pollution events on the atmosphere, it is first necessary to identify these background atmospheric conditions. The comparison of time series from different sampling sites also requires the separation of well-mixed background air masses from those that have been subject to recent pollution events from localised sources. However, the determination of background conditions is subjective as there is no standardised methodology for determining backgrounds within the scientific atmospheric community. A consistent definition of background conditions across WMO GAW (World Meteorological Organization Global Atmosphere Watch) stations has historically been problematic as they represent a mixture of contrasting settings. Very few monitoring stations are remote enough to be permanently exposed to pristine air masses, and many GAW stations are frequently affected by local sources or sinks, meaning that all stations do not provide the same opportunities for observing air masses that have been minimally perturbed by terrestrial contact on diurnal, synoptic, or seasonal timescales (Chambers et al., 2016). Ultimately, the choice of method for determining the background in different studies is dependent on the local conditions at the given measurements station and the scientific question being asked.

In recent years, several methods have been used to estimate the background composition for a range of atmospheric gas species. These methods, in brief, are as follows: criteria based on meteorological conditions using either measured meteorology from the station being investigated (e.g. Brailsford et al., 2012), evaluation of the air mass origin using back trajectory analysis (e.g. Cui et al., 2011), or by using a Lagrangian particle atmospheric dispersion model (e.g. Manning et al., 2021); criteria based on statistical methods, including curve fitting (e.g. Ruckstuhl et al., 2012; Apadula et al., 2019); and criteria based on chemical parameters, such as trace gas mole fractions or the ratio of trace gases (e.g. Tsutsumi et al., 2006; Pu et al., 2014). Many studies use a combination of two or more of the aforementioned methods in order to identify the background mole fractions (e.g. Brailsford et al., 2012; Pu et al., 2014).

For remote coastal locations, the 'background' can also be referred to as the 'clean maritime air sector', for which wind direction can often be a good proxy to define a sector that has been subject to limited terrestrial contact. However, this is often complicated by local circulation that can impact upon this 'clean air sector'.

Furthermore, wind direction alone is not necessarily a robust indicator of air mass history as the wind direction measured at a given location is not always representative of the larger scale synoptic flow due to local circulation e.g., sea breeze effects (Fleming et al., 2012). Air masses arriving from the 'clean maritime air sector' could have also mixed with polluted air before arriving at the measurement station (Fleming et al., 2012). This approach is therefore frequently used in conjunction with filtering of the time series in order to identify stable periods of air, that are representative of the 'clean maritime air sector' (Schuepbach et al., 2001; e.g. Brailsford et al., 2012; Chambers et al., 2016).

Air mass back trajectories offer a more reliable method for estimating background conditions than use of the wind direction alone, as they provide information about the long-range air-mass history before arrival at the measurement point; however, their accuracy is affected by the resolution of the meteorological data used. Back trajectory models follow the path of a single parcel of air backwards through time from the receptor site. Back trajectories are used to determine a background by partitioning the trajectories into different source regions, and rejecting data that originates or passes over the defined 'non-background' regions (e.g. Balzani Lööv et al., 2008; Cui et al., 2011). Trajectory analysis also has its limitations: the meteorological reanalysis data are not immediately available so they cannot be used to operate conditional samplers which can be set to sample when specified criterion are met, e.g. when air is arriving from the clean air sector. Additionally, the resolution is generally not better than a few hours, and, most importantly, even though the trajectory may indicate that an air mass may have passed over land it may not have mixed with polluted air close to the surface (Gras and Whittlestone, 1992). In the boundary layer, the analysis of a single back trajectory is also not sufficient to fully describe the transport of an air mass due to turbulent mixing processes; these processes can be captured by the addition of dispersion modelling (Stohl, 1998).

Atmospheric Particle Dispersion Models (e.g., NAME (Jones et al., 2007)) can be used to better understand the history of the air mass being sampled through the simulated release of a large number of particles backwards in time from the receptor site to produce a 'footprint' of the air mass history, thus providing an improvement to back trajectory models which only follow a single parcel of air. Using this method, background composition is estimated using measurements in air masses that have

not been influenced by significant local sources or sinks (e.g. Ebinghaus et al., 2011; Manning et al., 2021). However, particle dispersion models are also limited by the frequency of runs (usually every few hours), the resolution of the meteorological data used as an input, and the delay in the availability of the input data meaning it cannot be computed in real-time.

Purely statistical methodologies have also been used for the estimation of background composition. This approach commonly relies on a comparison of the standard deviation of the mole fraction data and the identification of measurements that deviate significantly from a smooth curve fit to the data; Thoning et al. (1989) presented an early statistical method for determining the carbon dioxide (CO_2) background at Mauna Loa Observatory, and is the basis for many other statistical background methods. Examples of other statistical methods developed include: robust extraction of baseline signal (REBS) (Ruckstuhl et al., 2012), background data selection (BaDS) (Apadula et al., 2019; Trisolino et al., 2021), HPspline (Keeling et al., 1989), coefficient of variation (COV) (Hagler et al., 2010; Brantley et al., 2014), standard deviation method (Drewnick et al., 2012) and anomaly detection algorithm (ADA) (Resovsky et al., 2021). Statistical filters are particularly appropriate for trace gases such as CO_2, methane (CH_4), and carbon monoxide (CO), where the key indicator of non-background influence is variability that is primarily caused by different sources and variable transport patterns (Brunke et al., 2004). A benefit of using statistical methods is that they do not have to be adapted to the conditions at an individual measurement station, so can be quicker and easier to implement, meaning they can be performed in near real-time, and they allow for easier comparison of multiple stations across large spatial scales. However, as these methods are based purely on the input dataset, with no additional information, the produced background estimation can be easily skewed by any inconsistencies or large gaps in the dataset.

Finally, the presence of concurrently measured atmospheric constituents, or ratios to other atmospheric constituents have been used as 'tracers' to select for background air masses. For example, CO (e.g. Parrish et al., 1991; Tsutsumi et al., 2006), NO_y (e.g. Zellweger et al., 2003; Zanis et al., 2007), and black carbon (Pu et al., 2014; Fang et al., 2015). Tracers offer an objective, real-time criterion for background selection provided that they can be measured in parallel and provide a strong indication that the air being sampled has not been influenced recently by passage over land or a pollution source.

One such tracer with the ability to act as a proxy for recent influence from land surface contact is atmospheric radon-222 (^{222}Rn). Radon-222 is a noble gas generated as part of the decay chain of uranium-238 (^{238}U) from the alpha decay of radium-226 (^{226}Ra). As the first gaseous product in this decay chain, ^{222}Rn is emitted from soil and enters the atmosphere, and thus originates predominantly from soil and rock. The ocean, ground-water and natural gas also contribute ^{222}Rn to the atmospheric load, but these contributions are relatively very small (Porstendoerfer, 1994), with an oceanic source two to three orders of magnitude less than the terrestrial source (Zahorowski et al., 2013). As it is a noble gas, ^{222}Rn does not react chemically with other species. It is also poorly soluble in water and does not attach to aerosols, so is not highly susceptible to wet or dry atmospheric deposition removal processes (Zahorowski et al., 2004). Thus, the only atmospheric sink of ^{222}Rn is radioactive decay with a half-life of approximately 3.82 days. Therefore, it does not accumulate in the atmosphere on timescales longer than a month. This half-life is also comparable to that of other short-lived atmospheric pollutants (e.g. NOx, CO, O_3), and to the timescale of many important aspects of atmospheric dynamics, making radon a useful tracer at local, regional, and global scales (Zahorowski et al., 2004). As ^{222}Rn emissions are predominantly land based, *in situ* atmospheric ^{222}Rn measurements can act as a powerful tracer to identify background air masses that have had limited recent interaction with terrestrial sources and sinks.

Unlike other background estimation methods, ^{222}Rn is based on continuous observations, and therefore does not rely on complex meteorological or statistical models that can introduce further uncertainties and require large amounts of computer processing power. ^{222}Rn has been widely used as an indicator of recent terrestrial influences in air masses (e.g. Liu et al., 1984; Polian et al., 1986; Chambers et al., 2014), and of vertical mixing and atmospheric stability (e.g. Chambers et al., 2011; Williams et al., 2013; Chambers et al., 2015). Radon has also been used in studies as a background selection technique both in conjunction with other gas species, such as CO (Brunke et al., 2004) and in back trajectory analysis (Chambers et al., 2013), as well as alone (e.g. Chambers et al., 2016; Crawford et al., 2018). All of these studies using ^{222}Rn alone as a background selection methodology were either conducted at southern hemisphere or at high-altitude monitoring stations.

Despite the importance of defining the background for scientific understanding and interpretation of atmospheric gas species measurements, there is

no internationally agreed method to calculate, or even define it. In different contexts, the background is defined to mean different things. In this chapter, I evaluate the potential of ^{222}Rn as a proxy for regional maritime air masses and use these air masses to define a Regional Maritime Background (RMB) for several gas species routinely measured at the Weybourne Atmospheric Observatory (WAO; a northern hemisphere coastal station) and compare the resultant RMBs to those calculated using other methodologies. The six species that will be used to investigate the use of ^{222}Rn for calculating RMB values are CO_2, oxygen (O_2), hydrogen (H_2), CH_4, CO, and nitrous oxide (N_2O). These ^{222}Rn derived RMBs are then compared to backgrounds produced using a statistical method, a particle dispersion model, a back trajectory analysis, and meteorological and standard deviation (SD) filtering.

3.1.1 Aims

(i) Use the 3-year ^{222}Rn in situ time series at WAO to calculate monthly regional maritime backgrounds of 6 gas species: CO_2, O_2, H_2, CH_4, CO, and N_2O.

(ii) Quantitively compare the ^{222}Rn method presented here to a range of other methods used to calculate atmospheric backgrounds to assess the robustness and compatibility compared to other methods.

3.2 Weybourne Atmospheric Observatory and datasets

The Weybourne Atmospheric Observatory (WAO) is located on the north Norfolk coast, UK (52°57'02''N, 1°07'19''E), approximately 35 km north-northwest of the city of Norwich, 170 km northeast of London and 200 km east of Birmingham. WAO experiences rapidly changing wind direction and is thus at a strategic location for sampling a variety of air masses including relatively clean ocean air from the North Atlantic Ocean and North Sea, as well as polluted European and UK air masses (Fleming et al., 2012). WAO is part of the European Union's Integrated Carbon Observation System (ICOS) as an approved 'Class 2' station and is also a member of the World Meteorological Organization's (WMO) Global Atmosphere Watch (GAW) programme. High-precision, high-accuracy, continuous measurements of a wide array of atmospheric gas species (including greenhouse gases, isotopes, and reactive gases)

are carried out at fine temporal scales. For a full station description, refer to Chapter 1.

3.2.1 Radon data

Radon has been measured at the WAO since March 2018 using an ANSTO (Australian Nuclear Science and Technology) 1500 L dual-flow-loop two-filter atmospheric radon detector (Whittlestone and Zahorowski, 1998; Chambers et al., 2011). Unlike proxy techniques that use radon progeny measurements, the dual-flow-loop two-filter radon detectors provide a direct measurement of ambient radon activity. Air is drawn from a height of 10 m a.g.l. at approximately 85 L min^{-1} through an inlet system and a delay volume to allow for thoron (^{220}Rn) decay (T1/2 = 56 s). This then passes through a filter to remove all ambient aerosols, as well as ^{222}Rn and ^{220}Rn progeny. This filtered air then passes into the main delay volume (1500 L) where new radon progeny form and the alpha-decays are counted on a second filter. The only source of progeny on the second filter is from the radioactive decay of ^{222}Rn in the delay chamber, thus the alpha-decay (α) count rate is proportional to the ambient ^{222}Rn activity concentration. Atmospheric ^{222}Rn activity concentrations are then determined from the α count rate and air flow rate into the delay volume with a data point produced every 30-minutes. Air flows continuously through the analyser with a response time of 45 minutes due to the large delay volume. For a full description of the detector operating principles see Whittlestone and Zahorowski (1998) and Griffiths et al. (2016).

Calibration of the detector is performed monthly (which is corrected for in post-processing; see Griffiths et al. (2016)) by the injection of radon from a well-characterised ^{226}Ra source (Pylon Electronics Inc.), with a source activity of 50 kilobecquerel (kBq) at a flow rate of approximately 80 mL min^{-1}. The detector's signal is affected by a slow build-up of lead-210 (^{210}Pb; $t_{1/2}$ = 22.3 yr) on the second filter, therefore instrumental baseline drift checks are performed approximately every three months, from which a linear model of ^{210}Pb accumulation on the second filter is derived and removed from the raw α counts. The net counts are then calibrated to atmospheric radon activity concentration (Schmithüsen et al., 2017). The accurate identification and removal of the detector's baseline drift is particularly important for

coastal stations, such as WAO, where radon activity concentrations can vary over several orders of magnitude (Chambers et al., 2011).

The raw ^{222}Rn data were quality-checked and averaged to one hour. The timestamps of the ^{222}Rn data were shifted backwards in time by two hours to account for the lag caused by the delay volume and instrument response time of the radon detector. The two-hour shift was determined by calculating the lagged covariance of radon with hourly lag intervals from -5 to +2 hours, with the resultant covariances (normalised to the -5 hours results) shown in Figure 3.1; a time lag of -2 hours produced the highest covariance between ^{222}Rn and each species. The optimum time-lag of two hours is likely attributable to a combination of the 45 minute detector response time (Griffiths et al., 2016) and that the convention for radon observations is for the timestamp to mark the end of the sampling period, whereas the averaging of other gas species normally marks the beginning of the hour. The widely used approach to account for the delayed detector response is to implement a time-deconvolution to the raw observations (Griffiths et al., 2016); however, this was not able to be completed in the timeframe required here.

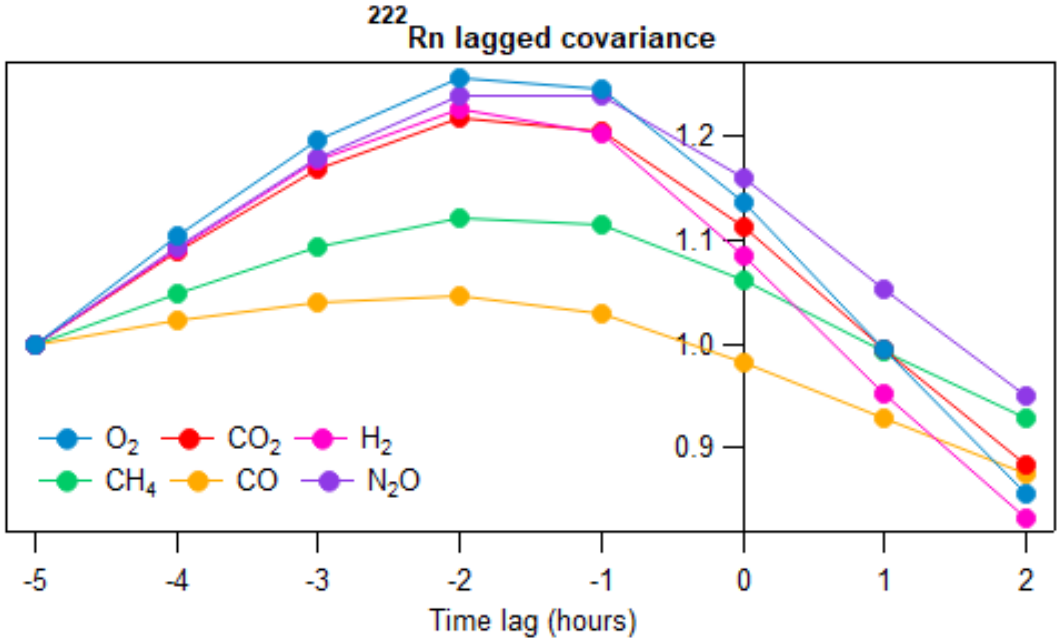

Figure 3.1. Covariance of ^{222}Rn with O_2, CO_2, H_2, CH_4, CO, and N_2O, with a time-lag applied to the ^{222}Rn data between -5 and +2 hours, normalised so that -5 hours = 1.

3.2.2 Other datasets

A range of atmospheric gas species are measured routinely at the WAO; for the purposes of this study, to evaluate the potential of ^{222}Rn as a tracer for regional maritime background (RMB) air masses, six species have been investigated: CO_2, O_2 (reported as O_2/N_2 ratios), H_2, CH_4, N_2O, and CO. This choice of species allows for the comparison of different background calculation methods for a number of gases with differing source and sink processes.

The six gas species are measured at WAO using a variety of instruments, as explained here in brief. O_2/N_2 ratios and CO_2 mole fractions have been measured continuously at WAO since 2008 (Adcock et al., 2023). The O_2/N_2 ratio (hereafter referred to as O_2 for simplicity) is measured with a Sable Systems International Inc. 'Oxzilla II' differential fuel cell analyser and reported on the Scripps Institution of Oceanography (SIO) O_2/N_2 scale (Keeling et al., 2007). CO_2 is measured using a Siemens Corporation 'Ultramat 6E' non-dispersive infrared (NDIR) analyser and the time series used in this chapter is reported on the WMO-X2007 scale (Zhao and Tans, 2006).

CH_4, records at WAO began in 2013, and N_2O and CO records began in 2008; since 2018 they have been measured on a Fourier Transform Infrared gas and isotope analyser (FTIR, Ecotech Spectronus™) (Griffith et al., 2012). The CH_4 mole fraction is reported on the WMO-X2004A scale (Dlugokencky et al., 2005), the N_2O mole fraction on the WMO-X2006A scale (Hall et al., 2007) and the CO mole fraction is reported on the WMO-X2014A scale.

Molecular hydrogen (H_2) has been measured since 2008 on a modified Reduction Gas Analyser (Forster et al., 2012) (RGA3, Trace Analytical, Inc., California, USA), which includes gas chromatography followed by the reduction of mercuric oxide, and the H_2 mole fraction is reported on the Max Planck Institute for Biogeochemistry (MPI-BGC)-2009 scale (Jordan and Steinberg, 2011).

The three-year time series (01Apr2018 – 31Mar2021) of ^{222}Rn, O_2, CO_2, CH_4, CO, N_2O, and H_2 used in this analysis are displayed in Figure 3.2, averaged to one-hour for each species. The small gaps present in the time series are due to flushing and calibration periods, and the longer gaps (particularly in CO_2 and O_2) are due to periods of instrument down-time or maintenance.

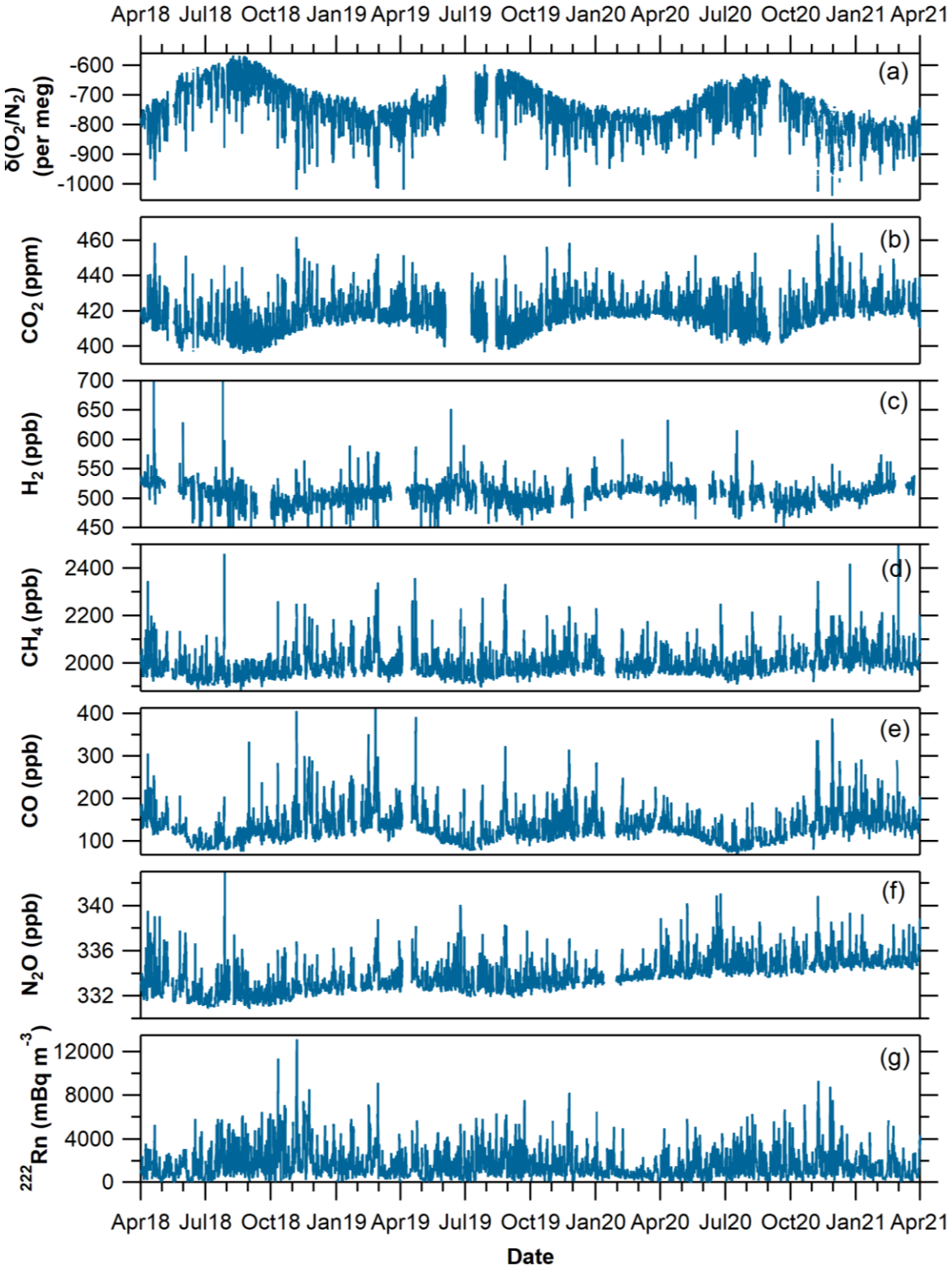

Figure 3.2. Time series of (a) O_2, (b) CO_2, (c) CH_4, (d) CO, (e) N_2O, (f) H_2, and (g) ^{222}Rn from WAO between 1st April 2018 - 31st May 2021, observations averaged to 1-hour for each species.

3.3 Radon regional maritime background estimation

3.3.1 Methods

3.3.1.1 Identifying a Radon threshold

To identify air masses representative of a regional maritime background, a radon lower threshold limit needs to be determined to limit any potential terrestrial influences (e.g. land based CO2 emissions). Previous studies in the Southern Hemisphere have used a threshold of 50-100 mBq m^{-3}, which can be confidently determined due to the lack of land masses (Brunke et al., 2004; Molloy and Galbally, 2014; e.g. Chambers et al., 2016; Crawford et al., 2018). In the Northern Hemisphere there is a larger amount of residual terrestrial influence on the radon activity concentration, thus a new threshold needs to be defined.

In order to determine this threshold, the deviations of hourly mole fractions of the gas species being investigated from the mean or minimum value were first investigated. In the case of species with predominantly surface sources (e.g.,CH4, N_2O, CO), the 14-day running minimum value was taken and subtracted from the hourly observations and then these results were divided into 100 mBq m^{-3} Rn bins for each month. For species with both surface sources and sinks, the 14-day running mean was taken and subsequently subtracted from the hourly observations, and then divided into 100 mBq m^{-3} Rn bins. For each of the ^{222}Rn bins the 10^{th}, 50^{th}, and 90^{th} percentile values were then calculated; when the spread of the distribution (i.e. 90^{th} – 10^{th} percentile values) is small, this means that the hourly observed values of the species are close to that of the seasonal trend (fortnightly mean/minimum value), whereas when the deviation distributions are broader this indicates that the hourly values are diverging more from the monthly mean/minimum values, as a result of surface source contributions.

As an example, Figure 3.3 displays the results of the CH_4 hourly deviation distributions from the 14-day running mean for each month in 2020 in 100 mBq m^{-3} bins between 0-2000 mBq m^{-3}. The higher radon activity concentrations have not been included here to focus on the clean air end of the radon concentrations. It is immediately clear that for the lowest radon activity concentration bins (<200 mBq m^{-3}), the deviation in the hourly CH_4 mole fractions from the fortnightly mean is small.

As radon activity concentrations increase, indicative of terrestrial influence, the deviation in the CH4 distributions become larger, indicating that the hourly values are diverging from the monthly mean value due to influence from terrestrial sources and sinks. Gas species RMB estimates calculated from radon concentrations below 200 mBq/m^3 should therefore be fairly representative of an RMB, whereas those generated from radon activity concentrations ≤ 500 mBq m^{-3} would be more representative of regional background values.

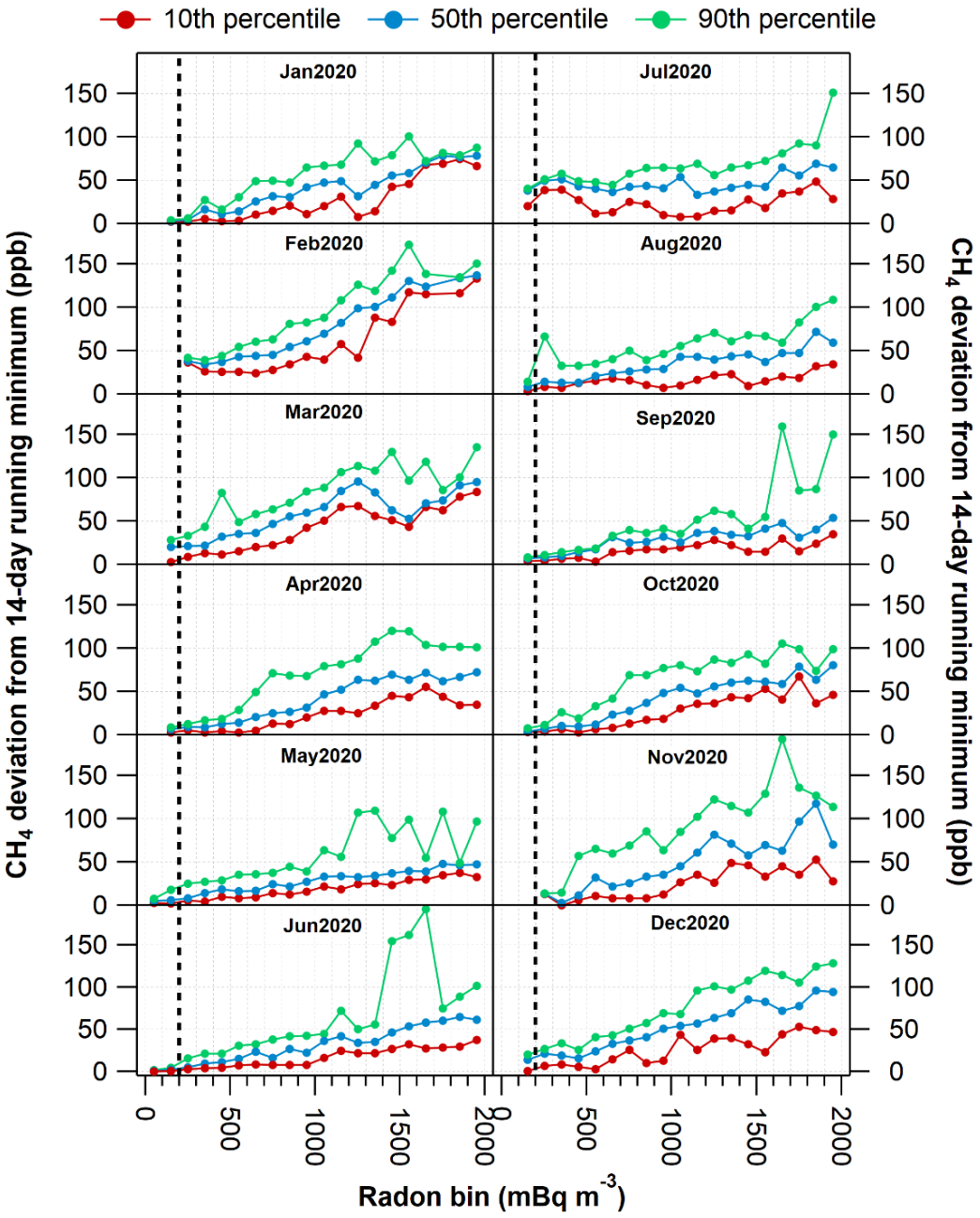

Figure 3.3. CH_4 10th, 50th and 90th percentiles of the hourly deviations from the 14-day running minimum for 100 mBq m^{-3} Rn bins from 0-2000 mBq m^{-3}. The dotted vertical line indicates 200 mBq m^{-3}.

In order to further investigate the degree of interaction with the land surface for varying activity concentrations of radon, back trajectory analysis using the Hybrid Single-Particle Lagrangian Integrated Trajectory (HYSPLIT) model has been used to produce maps indicating the percentage of trajectories passing over each grid cell for varying radon thresholds. HYSPLIT back trajectory analyses are displayed in Figure 3.4 for $^{222}Rn \leq 100$ mBq m^{-3}, $^{222}Rn \leq 200$mBq m^{-3}, and $^{222}Rn \leq 500$ mBq m^{-3}, based on concurrent radon activity concentrations for the HYSPLIT run timestamp. It is worth noting that this threshold value does not play as much of a role in selecting which observations are used in the RMB calculation as the ^{222}Rn percentile used in step 1 (see section 3.3.1.2 below), but it is used mainly to flag potential terrestrial influence on the final determined monthly RMB values for each species.

Figure 3.4 shows the percentage of HYPLIT back trajectories run from WAO that passed over each grid cell when the radon activity concentration was less than 100 mBq m^{-3}, 200 mBq m^{-3}, and 500 mBq m^{-3}. These results indicate, that when the air mass arriving at WAO contains an activity concentration of less than 100 mBq m^{-3} (Figure 3.4a), there has been very little interaction with the land surface (at least within the preceding 96 hours). However, there are also very few hourly observations in which the radon activity concentration is below 100 mBq m^{-3}, only 141 within the three year time series, this is not enough data to use this threshold to produce a reliable RMB value. When looking at radon activity concentrations less than 200 mBq m^{-3} (Figure 3.4b), there is minimal terrestrial influence, with the highest percentage of trajectories passing over the North Sea and should therefore be representative of RMB conditions. There are also a larger number of datapoints (1106) that fall below this threshold. Finally, for the 500 mBq m^{-3} (Figure 3.4c) there is a far greater number of observations (3351); however, there is also a much greater interaction with European and UK land masses over the HYSPLIT trajectory period. This again shows that a threshold of 500 mBq m^{-3} would be more representative of a regional background, as discussed above. 200 mBq m^{-3} threshold is therefore a balance between obtaining enough data to represent the RMB and avoiding the adverse effects of terrestrial influences.

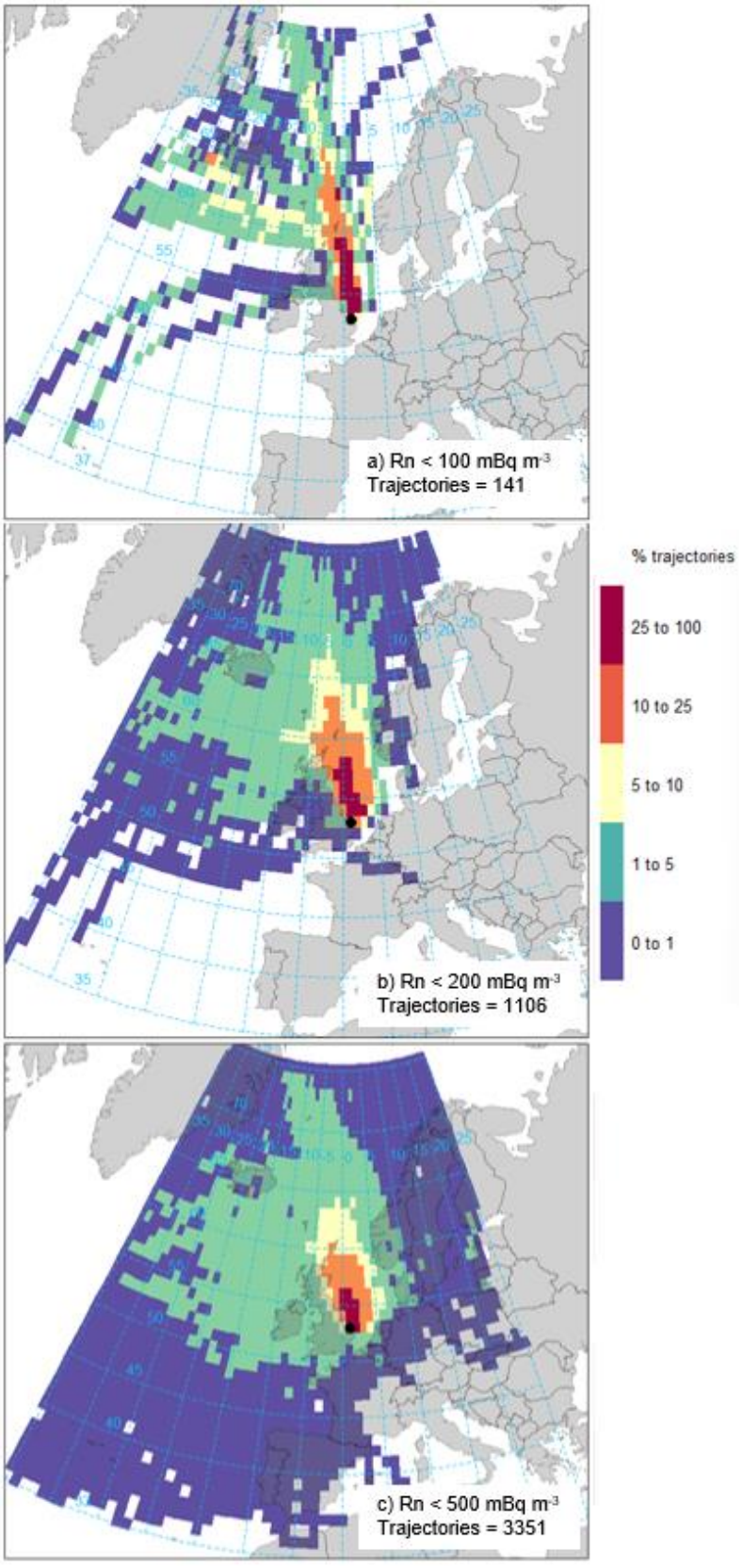

Figure 3.4. Percentage of HYSPLIT back trajectories from WAO over the entire measurement period which passed over each grid cell with radon activity concentrations less than (a) 100 mBq m^{-3} (b) 200 mBq m^{-3} and (c) 500 mBq m^{-3}. Plots produced using HYSPLIT run through the 'openair' package in R (Carslaw and Ropkins, 2012).

3.3.1.2 Implementing the Radon method

In order to calculate the monthly RMB values for the gas species the threshold calculated above is implemented using the following method for each month (adapted from Chambers et al., 2017) (Figure 3.5):

Step 1: Selection of hourly samples of each gas species from each month that are concurrent with 'low radon'.

a) Calculate the 1st and 3rd percentile ^{222}Rn activity concentration for the month.
b) If the 3rd percentile is less than the 200 mBq m^{-3} threshold retain the concurrent observations of the gas species being investigated and move to step 2.
c) If the monthly ^{222}Rn 3rd percentile is greater than the 200 mBq m^{-3} threshold, then only retain gas samples with a concurrent ^{222}Rn activity concentration less than 200 mBq m^{-3} (if there are at least 7 observations that fit this criteria).
d) If there are not at least 7 hourly observations within a month with a ^{222}Rn activity concentration less than the 200 mBq m^{-3} threshold, then keep only the observations that are concurrent with the lowest 1st percentile of ^{222}Rn activity concentrations for that month. For this situation, the month in question should be flagged to indicate that values may be slightly contaminated by local terrestrial influences.

Step 2: For species that are expected to have *mainly sources* over the terrestrial measurement fetch remove extreme low values

a) Calculate the monthly 25th percentile (P25), median (P50), and 75th percentile (P75) of the values retained in step 1.
b) Calculate the P75 – P50 and P50 – P25 difference for each month
c) If the P50 – P25 difference is larger than 10 times the P75 – P50 difference, then remove any values less than P50 – (0.5 * (P50 -P25)).

Step 3: Make a monthly RMB estimation for each trace gas (whether step a or b is used below will depend on the gas species being investigated).

a) For atmospheric species that have *both sources and sinks* over the measurement fetch in recent days (e.g., CO_2, O_2, H_2), calculate the median activity concentration or mole fraction of the samples retained in step 1 (this is the monthly RMB estimate) .

b) For species that are expected to have *mainly sources* over the measurement fetch (e.g., CH_4, CO, N_2O), then select only the lowest 25%-33% of observations from the values retained in step 2 (e.g., if 20 samples were available choose the lowest 5 mole fractions, if only 7 samples were available, choose the lowest 3 mole fractions) then calculate the average monthly mole fraction from these retained values.

For species which are expected to have primarily terrestrial sources (i.e. few terrestrial sinks) outlier removal may be required after step 1 in order to prevent skew in the final monthly RMB estimates from anomalously low values (step 2). This additional step is not required for species with sources and sinks as in step 3 we take the median, which acts as a type of extreme outlier removal, whereas for species with only sources we take the average of the lowest values, meaning this method is very susceptible to skewing from low values. A large skew in the opposite direction (i.e. if is P75-P50 is larger than P50-P25) is not considered, as we are taking the average of the lowest values anyway.

In many applications of background values, an hourly value is required to match the timestamp of the species being investigated. As this radon method produced monthly values (where the timestamp of the final background estimate is set as the 15th of the month), these were then interpolated to hourly timestamps.

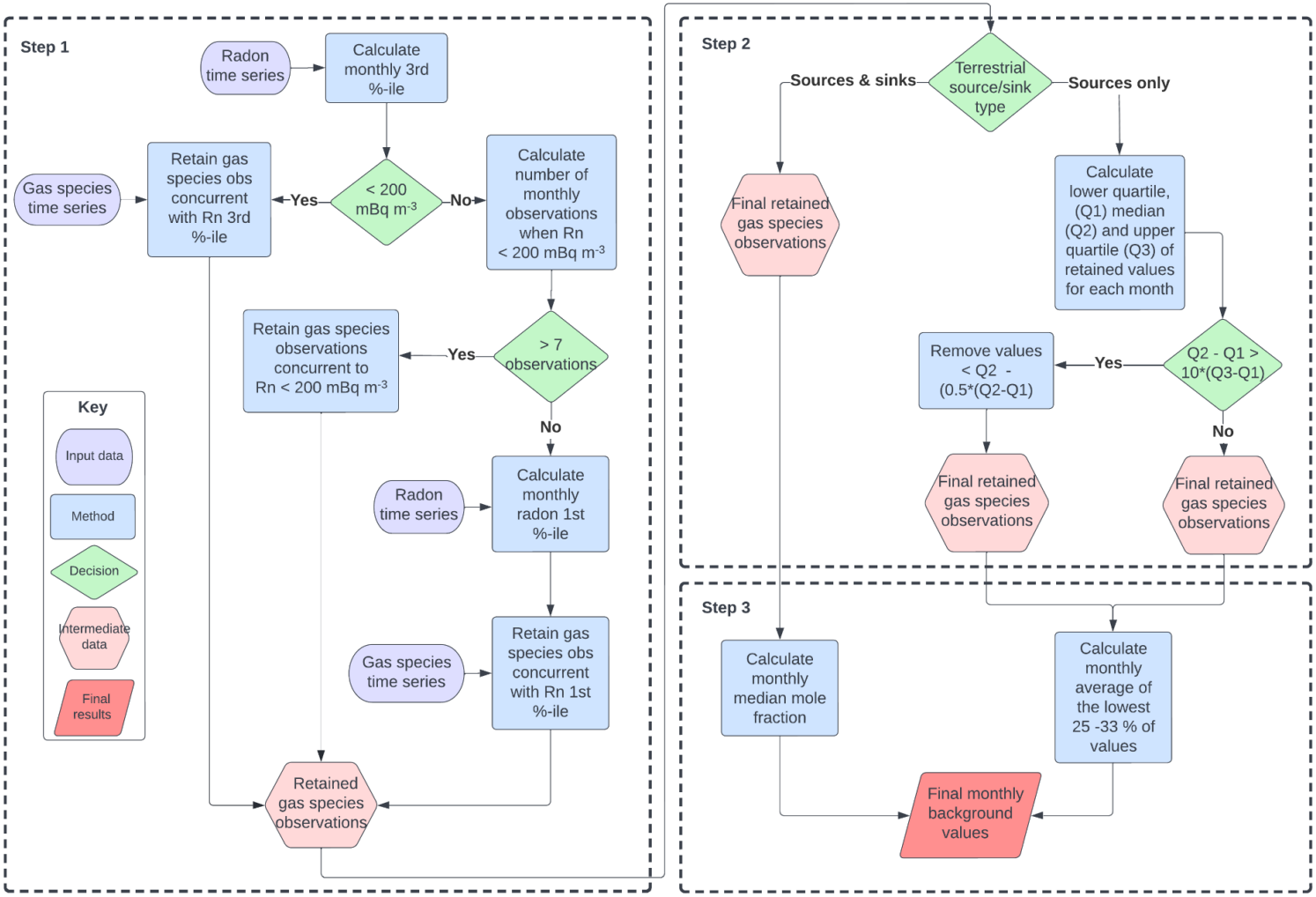

Figure 3.5. Flow chart detailing the radon derived RMB calculation methodology

3.3.1.3 NAME composite footprints

In order to investigate the origins of the air masses used to calculate the RMB estimate in the radon method, monthly NAME composite footprints for the air masses arriving at WAO were produced for the observations retained after step 1 of the methodology (for April 2018 – December 2021). These NAME footprints are used qualitatively to evaluate the data selected during each month's RMB estimation.

The UK Met Office's NAME (Jones et al., 2007) is a Lagrangian particle dispersion model that calculates dispersion by tracking the path-line of individual 'particles' through time as it follows the average atmospheric motion within a specific period of time. The particles motion also have a random component to represent the effects of atmospheric turbulence. NAME uses the Met Office's Unified Model and European Centre for Medium-Range Weather Forecasts Numerical Weather Prediction (ECMWF NWP) meteorological data (Jones et al., 2007).

NAME was run each hour from WAO with 20000 inert, theoretical, particles are released from a height of 10 m a.g.l from WAO, with a unit release rate of 1 g s^{-1}, backwards in time for 30 days or until they leave the computational domain. For each month, the NAME run for each hour that was used in the radon method RMB estimate was then combined into a 'footprint'. These footprints are created by summing the NAME runs for each grid cell (0.325° longitude x 0.234° latitude) when the NAME particles had passed within 40 m of the surface. Thus, providing an indication of a grid cells influence to the air mass being measured at WAO for any given hour.

The timestamps used to create the NAME composite footprints represent those retained after step 1 of the method in section 3.3.1.2, so for species with both sources and sinks the mean of these timestamps was taken, whereas for species with predominantly surface sources the average of the lowest 25 - 33% of these timestamps was taken.

3.3.2 Results and discussion

3.3.2.1 Radon data

The hourly radon data time series from 1st April 2018 – 31st March 2021 is displayed in Figure 3.6a. Radon levels at WAO during this period range from around 40 to 13200 mBq m^{-3}, with the former being indicative of long-range transport over ^{222}Rn devoid regions, and the latter indicating interaction with terrestrial sources. Activity concentrations below 200 mBq m^{-3} occur more frequently during the late spring and summer months (i.e., May – August) each year; thus, indicating less terrestrial influence on air masses during these periods. Within Figure 3.6, months in which both the 1st and 3rd percentile radon activity concentrations are above the 200 mBq m^{-3} threshold are those that will be flagged for 'potential terrestrial influence'. For some months the 3rd percentile radon does not fall below the 200 mBq m^{-3} threshold, but the 1st percentile does; for these months the calculated RMB s will not contain data where radon is greater than the threshold, but the monthly RMB estimate will be calculated from fewer hourly data points, and therefore may not be as robust.

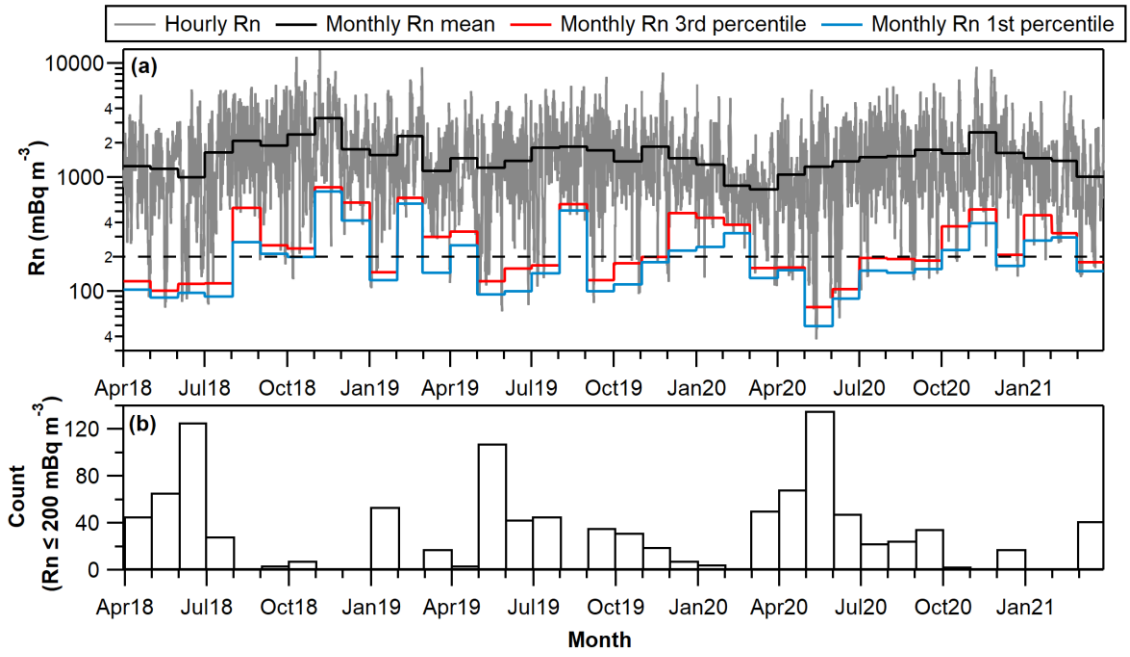

Figure 3.6. (a) Hourly radon activity concentrations at WAO from April 2018 – March 2021 (grey), with monthly mean (black), 3rd percentile (red) and 1st percentile (blue) overlayed. Dashed line indicates 200 mBq m^{-3} radon threshold. Note the logarithmic y-axis scale. (b) Number of monthly radon values below 200 mBq m^{-3}.

The number of hourly radon data points below the 200 mBq m^{-3} threshold each month is highly variable (Figure 3.6b). Seasonally, the radon activity concentration is higher over the autumn and winter months than the spring and summer. Three months have over 100 hourly radon data points below 200 mBq m^{-3}: May 2020 has the most with 136 hours below the threshold, followed by June 2018 with 126 points and May 2019 with 108. Seven months don't have any hourly values below the 200 mBq m^{-3} threshold (November 2018, December 2018, February 2018, August 2019, February 2020, November 2020, and February 2021), therefore the RMB estimate during these months is more likely to have more influence from terrestrial sources and sinks, and thus will require further investigation into how suitable the radon method is during these scenarios for producing an RMB estimate. These months, with the exception of August 2019, are all during the late autumn to winter period, which corresponds with the higher radon activity concentration observed. The decrease in radon activity concentration excursions below the 200 mBq m^{-3} threshold observed over winter may be due to fewer air masses arriving at WAO from the maritime sector (N – NE). Figure 3.7 displays a wind rose for each season. During the spring and summer months the wind direction was more frequently N/NE (i.e., from the direction of the North Sea) than during the winter, when this wind direction occurred infrequently. During autumn and winter the wind direction was predominantly from the SE, thus passing over the UK mainland before arriving at the WAO, with fewer observations from other wind directions. This means that during this period WAO may not be experiencing many air masses that can be considered as representative of the RMB and can explain why the number of monthly radon data point below the 200 mBq m^{-3} threshold is much lower during the winter months. The implication of this is that the RMB calculation method described in this chapter may be less successful over the winter; this will be explored in the following sections.

To further qualitatively investigate the origins of air masses used to calculate the monthly radon RMB estimates, NAME composite footprints were produced. These footprints display the origins of air masses corresponding to observations retained after 'step 1' of the radon RMB calculation methodology. For species with 'sources and sinks' the median of these values was taken, whereas for

species with 'primarily sources' the mean of the lowest 25 – 33% of these values was taken.

Figure 3.8 shows the composite footprints of data retained after step 1 for 2018, 2019, and 2020. Generally, the largest density of air masses arrive at WAO from over the North Sea, as would be expected from a clean maritime air mass. For the air masses that have passed over the UK mainland, it is likely that these air masses occur during months which were flagged for 'potential terrestrial influence'. There is very little interaction seen with mainland Europe.

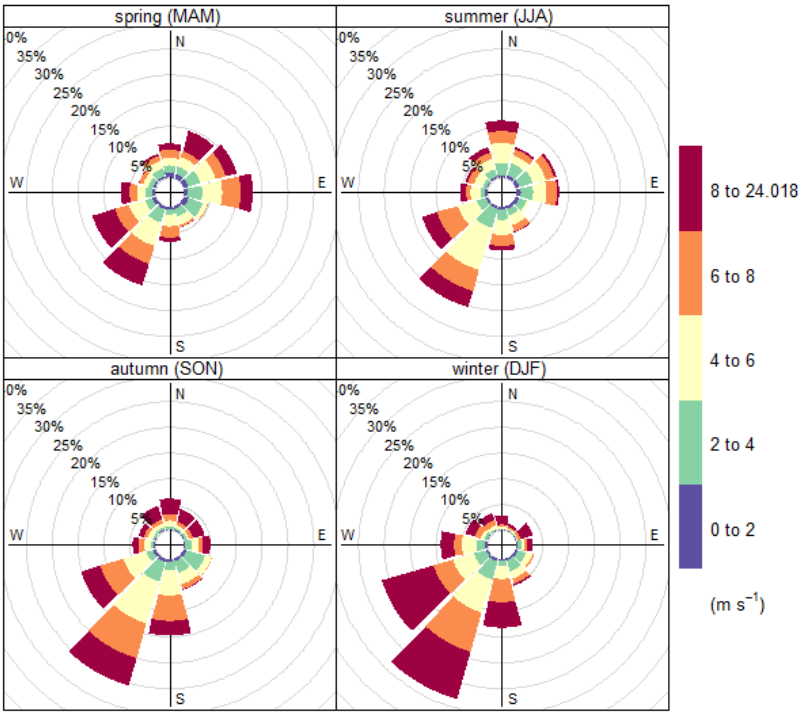

Figure 3.7. Seasonal wind roses for WAO. Produced using the 'openair' package in R and meteorological data between 01Apr2018 – 31Mar2021.

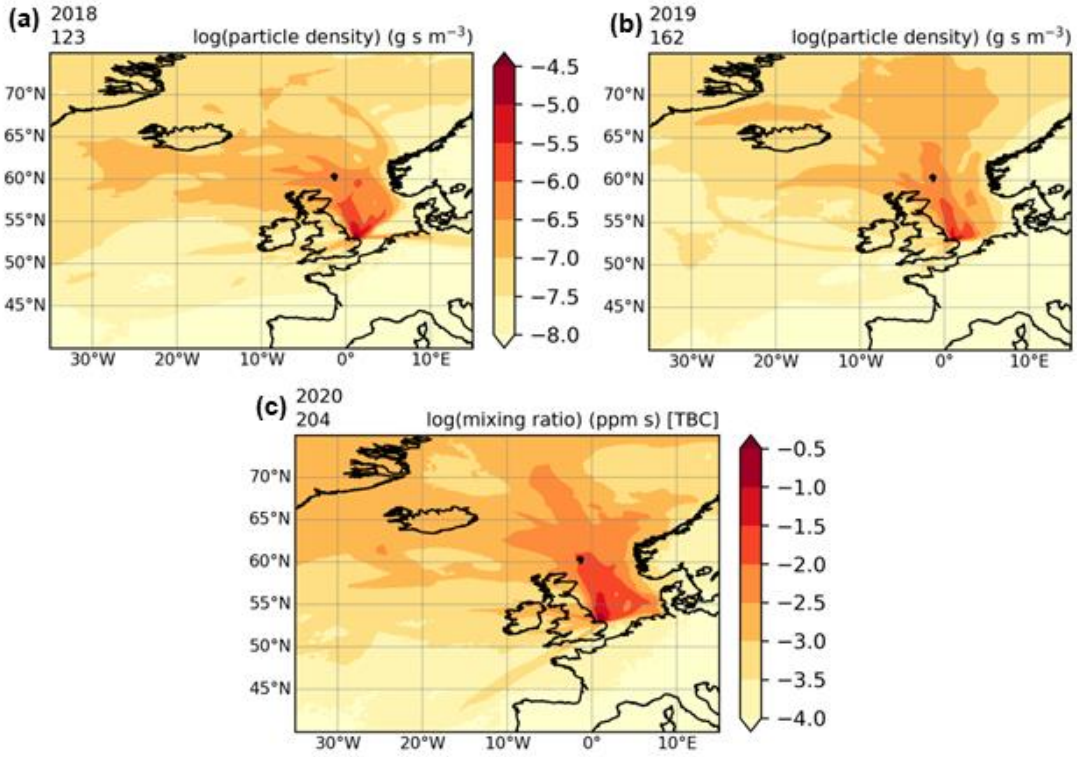

Figure 3.8. NAME composite footprints for 30-day backwards runs for (a) 2018, (b) 2019, and (c) 2020 displaying grid cell contribution to air masses arriving at WAO corresponding to timestamps of observations retained after step 1 of the radon RMB calculation methodology. Note, the unit change for the 2020 footprint to ppm s [TBC], which are to be confirmed. As these footprints are only being used for a qualitative analysis the unit is not as relevant as the scale.

3.3.2.2 Radon-derived regional maritime background estimates

In this section the final RMB estimates for each species using the radon method are presented in Figure 3.9; these results are calculated using a ^{222}Rn threshold of 200 mBq m^{-3}, the 3rd percentile as the upper percentile limit and the 1st percentile as the lower percentile limit. Months in which the RMB estimate is coloured in red in Figure 3.9 are flagged for potential terrestrial influence as the method used to compute these values retained the lowest 1st percentile of observations for the month and may be concurrent with radon activity concentrations above the 200 mBq m^{-3} threshold. In total, 14 of the 36 months are flagged for potential terrestrial influence, which is a significant number, these months will be further investigated in the method comparison (section 3.5) to determine the validity of using radon as an RMB selection method under these conditions. Most of these months fall within the late autumn – winter period, which is caused by the higher radon activity concentrations observed at WAO during this period thus resulting in

fewer data points below the 200 mBq m^{-3} threshold (as discussed in section 3.3.2.1).

Any month that is missing an RMB estimate for any species is due to gaps in the time series corresponding to times where the radon activity concentration meets the selection criteria. This is a drawback of this method as in some months less than 10 hourly radon points meet the given criteria, so if another analyser is down for any reason during this short period an RMB estimate will not be calculated for that entire month. This can particularly be seen in August and September 2018 for the H_2 estimates as the data gaps are small (Figure 3.9), but no RMB estimate is produced for either month; whereas, for June and July 2019 there is no RMB estimate for CO_2 or O_2, but the gap in the data covers the majority of this period so this missing RMB value is not as surprising. Gaps in the datasets not only mean that an RMB estimate may not be produced for the given month but, possibly more importantly, mean that an estimate may be produced from only one value which can significantly bias the monthly estimate. This highlights the need to manually check the underlying data that has been used to calculate each month's estimate. For the RMB estimate produced by radon in this chapter, there is only one month in which a single value was used to produce the RMB estimates. In August 2019 the monthly radon RMB estimate for all species, except H_2, is based on a single hourly data point. This is because the O_2 and CO_2, and N_2O, CH_4 and CO analysers were not running between 01/08/2019 and 13/08/2019, 10/08/2019 and 13/08/2019, respectively. This is the period in which the radon values met the criteria for the observations to be used in the monthly RMB calculation. As only a single value is used to calculate this month's RMB, it will be removed from all further analysis as it is not reliable to define an entire month's RMB mole fraction based on a single hourly observation.

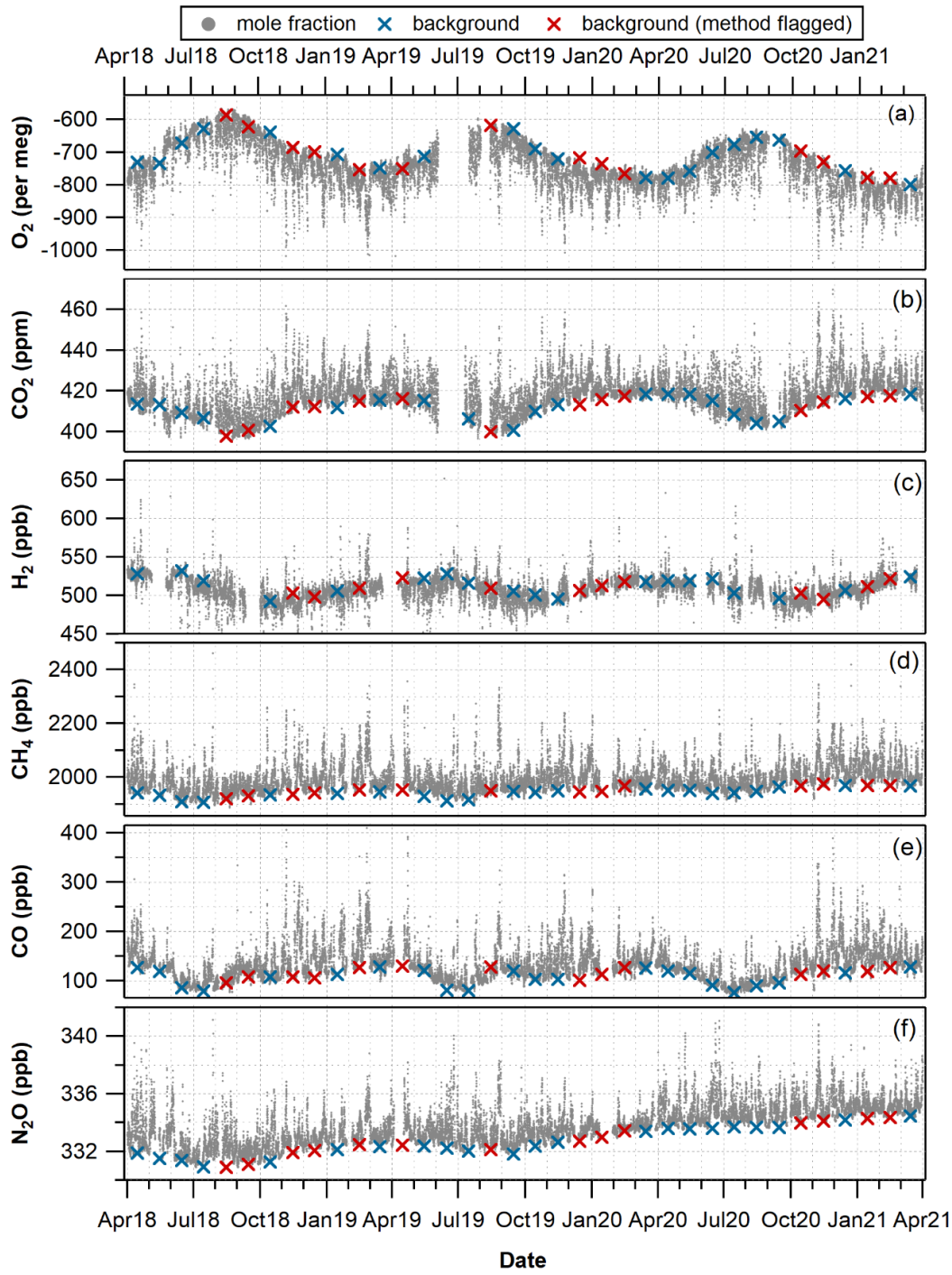

Figure 3.9. Hourly averaged time series (grey), and monthly RMB estimates using ^{222}Rn (blue and red crosses), where the red crosses are for months in which the method was flagged, for each species.

For species with primarily sources (i.e., few sinks) over the terrestrial fetch, an additional method step of 'outlier removal' was also completed in order to prevent the monthly RMB estimates from being skewed by anomalously low values. The outlier removal only affected the values retained for CH_4 in Nov2020, and in Apr2019, Jun2019 and Nov2020 for CO. As an example, box plots showing

the monthly RMB values retained after 'step 1' and 'step 2' (outlier removal), are displayed in Figure 3.10a and b, respectively.

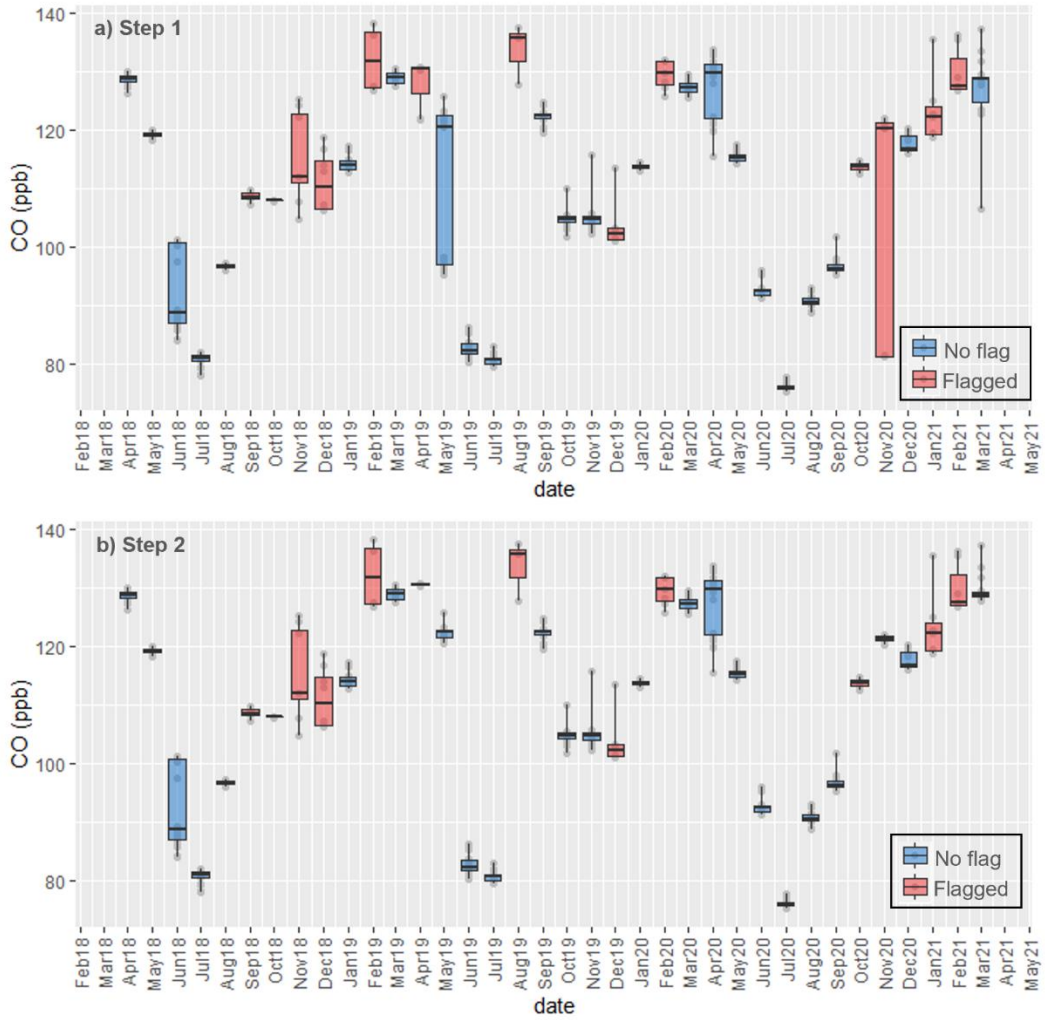

Figure 3.10. Box plots of the monthly CO values retained after (a) step 1 and (b) step 2 of the radon RMB calculation method.

Comparing the NAME footprints for the flagged vs. non-flagged months, there is a distinct difference in the source regions. As would be expected, the non-flagged months have little recent interaction with any land surface (e.g. Figure 3.11a and b), whereas during the flagged months observations used in the RMB calculation are frequently from air masses which have recently passed over the UK (e.g. Figure 3.11c and d). This indicates that the radon methodology is correctly identifying months in which the RMB estimate may have some terrestrial influence, and that in non-flagged months the air masses are representative of the RMB.

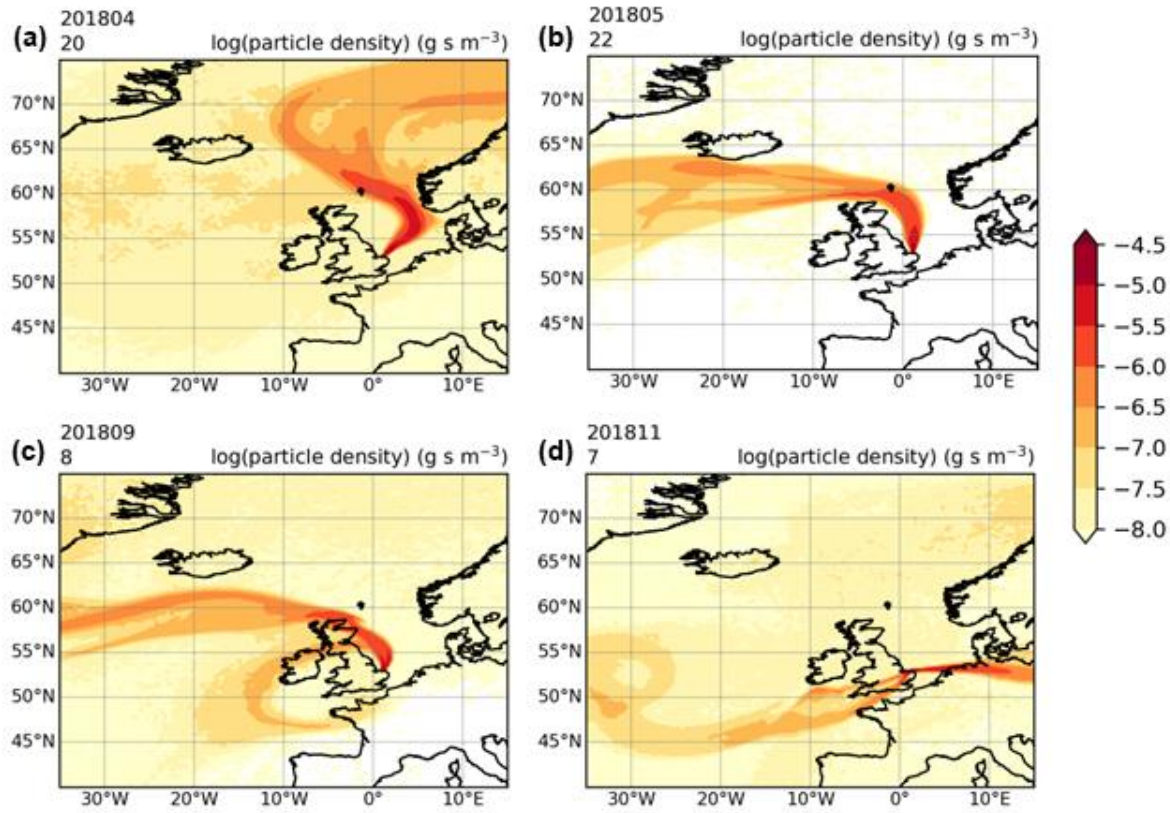

Figure 3.11. NAME composite footprints for 30-day backwards runs for (a) Apr2018, (b) May2018, (c) Sep2018, and (d) Nov2018. Apr2018 and May2018 are not flagged, and Sep2018 and Nov18 are method flagged for potential terrestrial interaction.

3.3.2.3 Threshold sensitivity analysis

The thresholds set in the RMB selection method described in section 3.3.1.2, are based on the investigation described in section 3.3.1.1. In order to determine the robustness of the resulting estimates with these threshold values, a threshold sensitivity analysis was completed. Radon thresholds of 100, 200 and 500 mBq m^{-3} were investigated, with upper percentile values of 0.1, 0.05 and 0.03 (step 1b/c), and lower percentile values (step 1d) of 0.05, 0.03 and 0.01 (Table 3.1). In total 18 different variations of the threshold limits were run for each gas species.

For each species, 18 RMB estimates were therefore produced for each month; the mean, SD, maximum, and minimum RMB estimate of the 18 threshold variations for each month were calculated. The mean and SD over all 36 months, RMB estimates for each species were then also calculated. If the SD on the mean of any given month is greater than 5 times larger than the SD of all the months, that month's final RMB estimate should be flagged as less robust.

Table 3.1. Variations of radon threshold and upper and lower percentile values used in threshold selection analysis of RMB estimation method

Threshold combination #	Rn threshold (mBq m^{-3})	Upper percentile	Lower percentile
1	100	0.03	0.01
2	100	0.05	0.01
3	100	0.05	0.03
4	100	0.1	0.01
5	100	0.1	0.03
6	100	0.1	0.05
7	200	0.03	0.01
8	200	0.05	0.01
9	200	0.05	0.03
10	200	0.1	0.01
11	200	0.1	0.03
12	200	0.1	0.05
13	500	0.03	0.01
14	500	0.05	0.01
15	500	0.05	0.03
16	500	0.1	0.01
17	500	0.1	0.03
18	500	0.1	0.05

The results of the threshold sensitivity analyses are summarised in Figure 3.12. Each of the combinations of threshold values does not produce a unique value for each monthly RMB estimate but are grouped into three to five unique values repeated within the 18 combinations. For example, the estimate produced for CO_2 in April 2018 using the thresholds of: 'Rn < 100 mBq m^{-3}, upper percentile 0.05, and lower percentile 0.03' and 'Rn < 200 mBq m^{-3}, upper percentile 0.03, and lower percentile 0.01', both give a monthly RMB value of 413.56 ppm, with the former combination being method flagged for potential terrestrial influence. These groupings are due to the different threshold combinations often selecting the same hourly values for each species for the final RMB calculation and explain the low standard deviations between the different threshold combinations displayed in Figure 3.12.

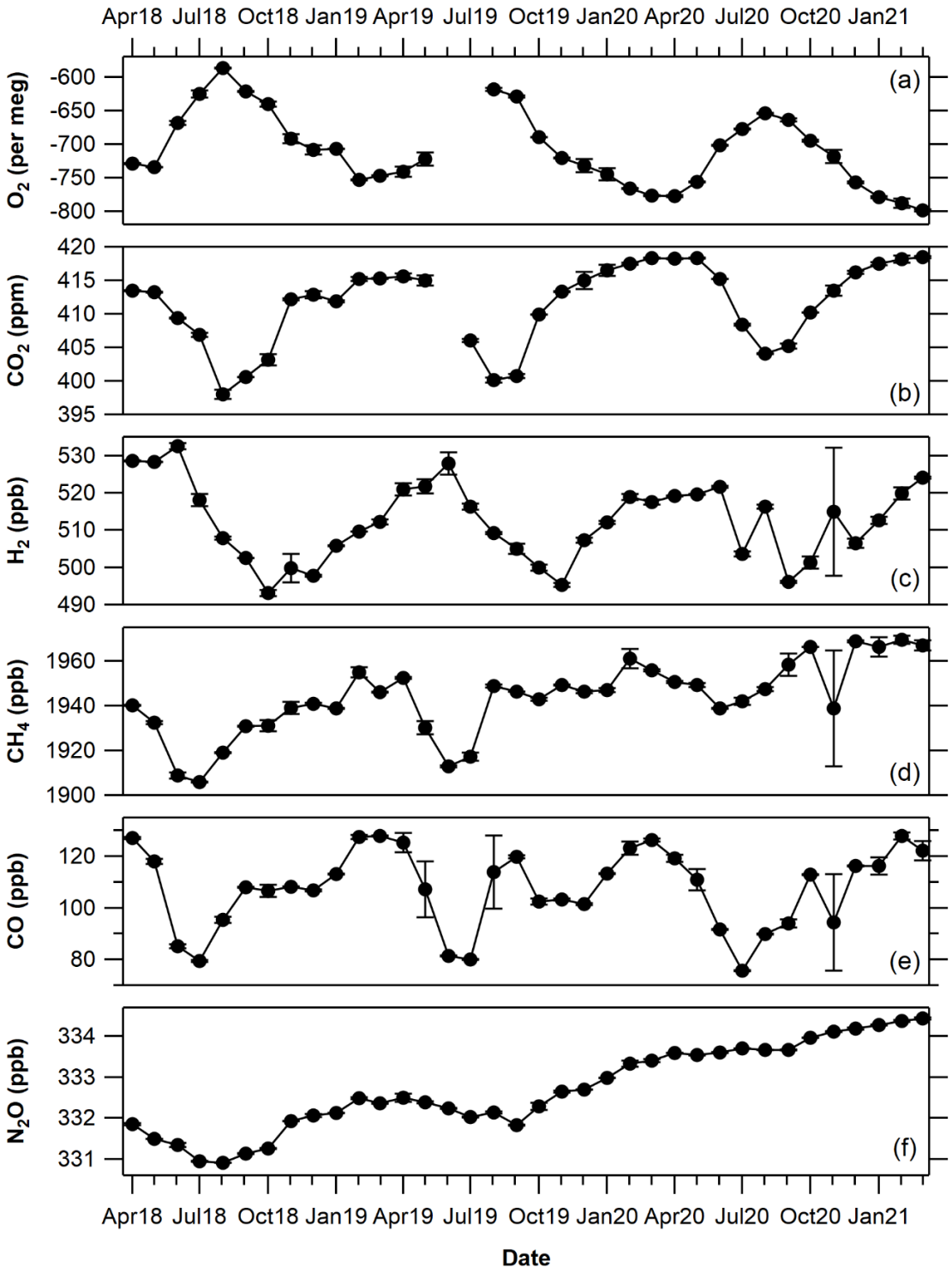

Figure 3.12. Threshold analysis results. Mean ± 1σ SD monthly RMB estimate of the 18 threshold selection analysis threshold combinations for (a) O_2, (b) CO_2, (c) H_2, (d) CH_4, (e) CO, and (f) N_2O.

Table 3.2. Average monthly SD for each species, flagging threshold (5x average SD) and average SD with flagged value removed.

	CO_2 (ppm)	O_2 (per meg)	CH_4 (ppb)	CO (ppb)	N_2O (ppb)	H_2 (ppb)
Average SD ± 1σ SD	0.30±0.31	3.00±3.22	1.91±4.32	2.18±4.08	0.02±0.02	1.30±2.84
Flagging threshold (5x average SD)	1.54	16.12	9.58	10.88	0.11	14.19
Average SD ± 1σ SD with flagged months removed	0.30±0.31	3.00±3.22	1.23±1.32	1.05±1.20	0.02±0.02	0.85±0.85

Table 3.2 shows the average SD over all months for each species, this was calculated by taking the SD of the RMB estimates produced for each month (i.e., the error bars in Figure 3.12) then averaging these values. Any individual month where the SD exceeded the average multiplied by a factor of five was then removed. When flagged months are removed from the average SD, the lower uncertainty limits for each species overlap with (Table 3.2), thus indicating a robust result. The months with a considerably higher SD (over 5x the average SD) are the same months in which outliers were removed for CO and CH_4 in 'step 2' (section 3.3.2.1); this is because when using some combinations of threshold values, outliers are not removed. Additionally, November 2020 is flagged for H_2; for this month the results are still grouped into a few values, but there is a large spread between the values.

For all species, except H_2, an RMB estimate is produced for every threshold combination for each month an estimate is produced. For H_2 there are six months for which some threshold combinations did not produce a result (May2018, Aug2018, Sep2018, Mar2019, Aug 2020, Mar2021). This is because during these months there are gaps in the H_2 time series (Figure 3.2), so when both the ^{222}Rn and percentile thresholds are lower, there are not enough available data points to produce an estimate.

3.4 Method comparison

3.4.1 Calculation of background using established methodologies

To contextualise the regional maritime backgrounds derived in section 3.3.2.2, I have compared my results to backgrounds derived using four different methods: atmospheric transport models (NAME and STILT), a statistical method known as robust extraction of baseline signal (REBS), and a meteorologically derived background (MET). There are a few important considerations to be taken into account throughout this section and the following discussion: (1) none of these background methods or results are inherently 'correct' or 'incorrect', (2) REBS is not defining an RMB as it is not based on any met/transport data, but is instead defining a statistical background based on the observations, (3) the NAME background is representative of the background at Mace Head, Ireland (MHD), not an RMB at WAO.

Table 3 shows the frequency and availability of data for each background method. For the purposes of this comparison, all of the background estimates were interpolated to hourly values.

Table 3.3. Frequency and data availability for each background estimation method and gas species.

	Background method				
	Radon	**REBS**	**NAME (MHD)**	**STILT**	**MET**
Frequency	Monthly	Hourly	Monthly	3-hours	Monthly
O_2	15Apr18-15Mar21	01Apr18-31Mar21			15Apr18-15Mar21
CO_2	15Apr18-15Mar21	01Apr18-31Mar21	15Apr18-15Mar21	01Apr18-31Dec20	15Apr18-15Mar21
H_2	15Apr18-15Mar21	01Apr18-23Mar21	15Apr18-15Mar21		15Apr18-15Mar21
CH_4	15Apr18-15Mar21	01Apr18-31Mar21	15Apr18-15Mar21		15Apr18-15Mar21
CO	15Apr18-15Mar21	01Apr18-31Mar21	15Apr18-15Mar21		15Apr18-15Mar21
N_2O	15Apr18-15Mar21	01Apr18-31Mar21	15Apr18-15Mar21		15Apr18-15Mar21

3.4.1.1 Robust Extraction of Baseline Signal

The robust extraction of baseline signal (REBS) method was developed by Ruckstuhl et al. (2012) and can be implemented using the 'rfbaseline' function from the 'IDPmisc' package in R (Ruckstuhl et al., 2020). This function uses a statistical approach, based on local regression of the time series, over a moving time window ('span'). The asymmetrical weighting of the REBS function is particularly appropriate for species where the excursion events are all in the same direction i.e. either mostly positive or mostly negative. Ruckstuhl et al. (2012) state that this method can be applied at any background station to time series of trace gases without significant surface sinks and latitudinal concentration gradient. This methodology of background selection is highly subjective, and dependent on a somewhat arbitrary selection of input variables; nevertheless, it is a tool often used in atmospheric research, thus its inclusion in this chapter is valuable.

The rfbaseline function has three user definable input variables: 'maxit', 'span', and 'B'. The span influences the amount of smoothing by specifying the fraction of points used to compute each fitted value, maxit specifies the number of iterations in the robust fit using an asymmetric biweight function, and B is the tuning constant in the biweight function that represents the standard deviation of data below the baseline curve and thus determines how much the function ignores higher values, where a higher B value results in a higher baseline.

The B and span input parameters have the most influence on the resultant baseline, in order to determine the optimum values for these two parameters rfbaseline was run multiple times for each species with varying span and B inputs. The span was run using 2 week intervals from 2 weeks to 12 weeks, whilst B was held at 1.5. The B value was then run as the following: 0.01, 0.05, 0.1, 0.5, 1, 2, and 4, whilst the span was held at 8 weeks. This was completed for each of the six species; the results of these runs for CH_4, CO_2, and H_2 are displayed in Figure 3.13, Figure 3.14, and Figure 3.15, respectively. It should be noted that the parameters chosen in the following discussion are chosen subjectively, which is an intrinsic negative feature of the REBS background calculation method.

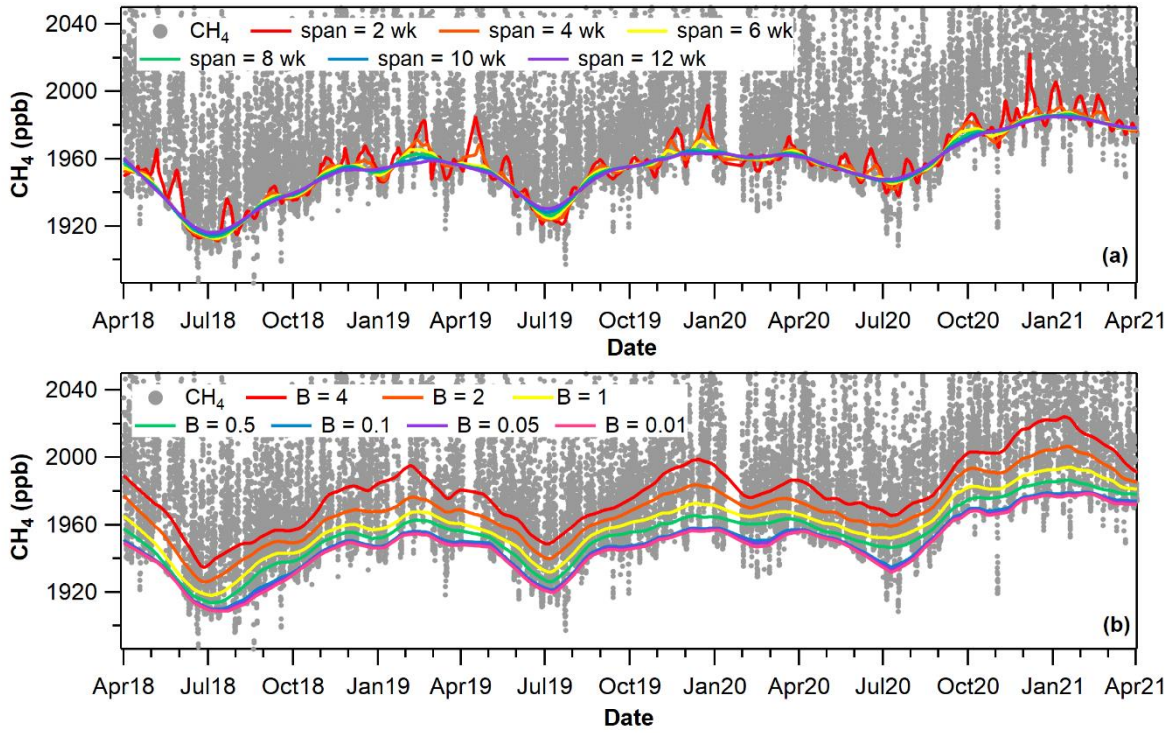

Figure 3.13. (a) REBS background results for CH_4 when varying span between 2 and 12 weeks, when B is held at 1.5. (b) REBS background results for CH_4 when varying B between 0.01 and 4, when span is held at 8 weeks. Note: the y-axis scale does not span the entire CH_4 concentration range in order to better display the differences between the REBS baselines.

For CH_4, when the span is set at 2, 4, or 6 weeks, the background picks up too much of the short-term variation (Figure 3.13a). When the span is set at 8, 10 and 12 weeks the background is much smoother and follows the longer-term trends (Figure 3.13a). The baselines with 10 and 12 week spans have higher annual cycle minima, therefore the 8 week span was chosen for calculating CH_4, N_2O and CO backgrounds. The B value changes the height at which the baseline sits on the data. For CH_4, CO and N_2O, (species that do not have many land-based sinks) the background would be expected to sit lower on the observations. The B values of 0.5 – 4 all produce a baseline that appears too high. The B values of 0.01 – 0.1 all produce very similar baselines, therefore the middle value of 0.05 was selected to produce the REBS background estimates for CH_4, CO and N_2O.

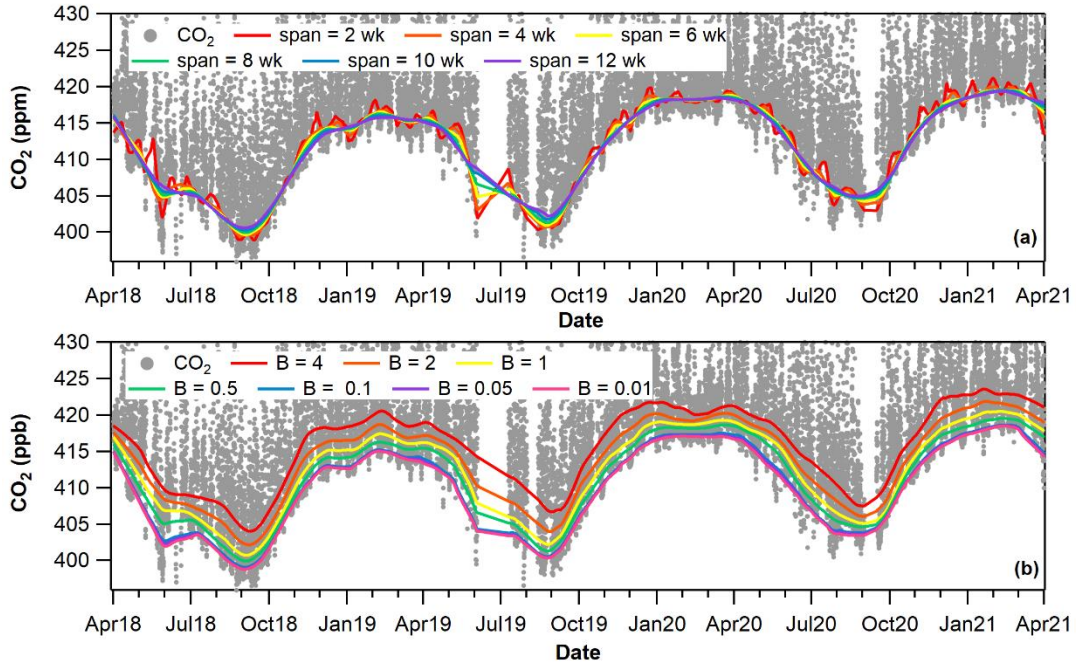

Figure 3.14. (a) REBS background results for CO_2 when varying span between 2 and 12 weeks, when B is held at 1.5. (b) REBS background results for CO_2 when varying B between 0.01 and 4, when span is held at 8 weeks.

For CO_2 (and O_2), as with CH_4, the span lengths below 8 weeks are strongly influenced by short-term variation in the observations, whereas a span of 8 weeks or above produces a much smoother baseline (Figure 3.14a). There is very little difference between the results of the 8, 10 and 12 week spans for the majority of the timeseries, but again the 10 and 12 week inputs produce baselines that sit higher in the data minima; therefore, 8 weeks was selected as the span value for CO_2 and O_2. It is also logical for the same span value to be used for all species, as this period relates directly to the length of observations input and thus to atmospheric mixing time, whereas the B value is a purely statistical parameter.

The B values between 1 and 4 again produced baselines that sit too high on the dataset (Figure 3.14b). As CO_2 (and O_2) have significant land-based sinks the baseline should not sit at the bottom of the dataset (as was the case with CH_4) therefore, the B values of 0.1, 0.05 and 0.01 sit too low. A B value of 0.5 was therefore selected to produce the REBS background estimates for CO_2 and O_2.

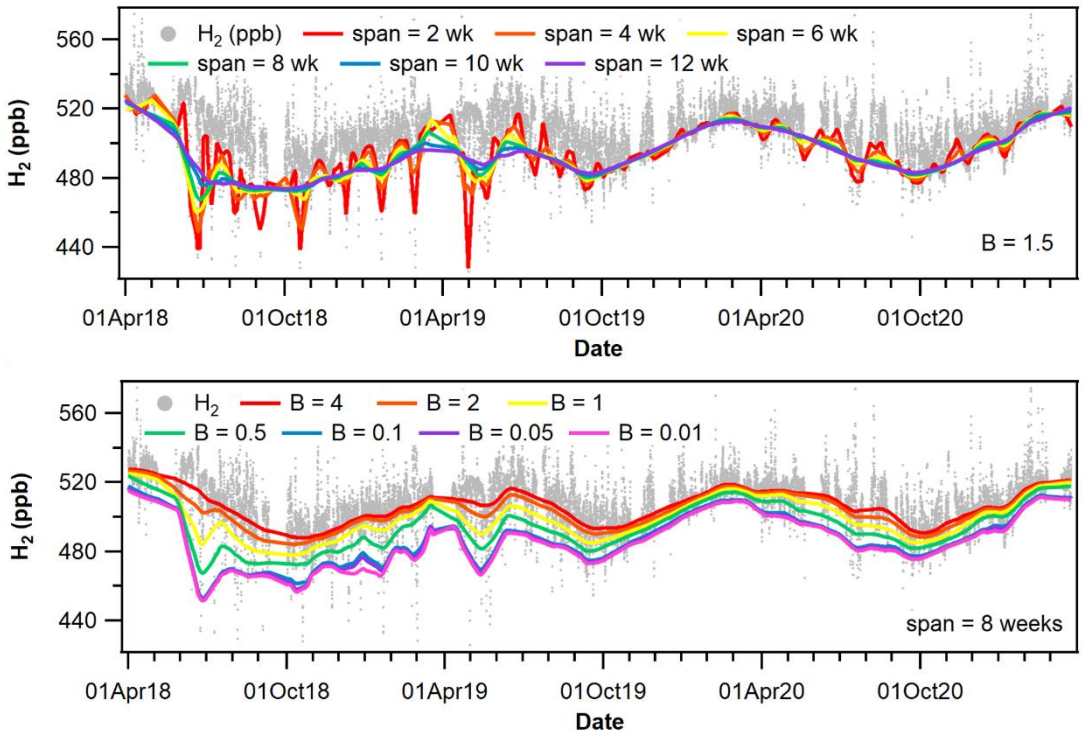

Figure 3.15. (a) REBS background results for H_2 when varying span between 2 and 12 weeks, when B is held at 1.5. (b) REBS background results for H_2 when varying B between 0.01 and 4, when span is held at 8 weeks.

As discussed above, the input span value should remain the same for all species, therefore 8 weeks was again selected for H_2. For H_2, as there are significant land-based sources and sinks, the lower B values are significantly skewed to the lower data points (Figure 3.15b). Even when increased to 2, the lower datapoints are having a large impact on the resultant baseline; therefore, a B value of 4 was selected to produce the H_2 REBS background estimate. The large skew towards the drawdowns in the H_2 time series when setting the B value is not unexpected, as Ruckstuhl et al. (2012) state that this method can 'be applied to any background station to time series of trace gases without significant surface sinks'. As the main sink of H_2 is soil deposition (Ehhalt and Rohrer, 2009), REBS is not the most appropriate method for selection of H_2 background values, however it is still being included in this comparison for completeness, and a B value which reduced the biasing from the large deposition events was selected accordingly.

The REBS output are produced on the same timestamp as the input data, but a datapoint is not created for any gaps in the input data. This output was then interpolated to hourly cover any gaps in the input data for the purpose of comparison to the radon background.

3.4.1.2 NAME particle dispersion model (Mace Head)

The UK Met. Office's NAME (Jones et al., 2007) is a Lagrangian particle dispersion model that calculates dispersion by tracking the path-line of individual 'particles' through time as it follows the average atmospheric motion within a specific period of time. The particles' motion also have a random component to represent the effects of atmospheric turbulence. NAME uses the Met Office's Unified Model and European Centre for Medium-Range Weather Forecasts Numerical Weather Prediction (ECMWF NWP) meteorological data (Jones et al., 2007).

The methodology used to compute the NAME derived time-varying background mole fractions is described in full in Manning et al. (2021), but can be briefly summarised as the following: 20000 inert, theoretical, particles are released from a height of 10 m a.g.l each hour from MHD, with a unit release rate of 1 g s^{-1}, backwards in time for 30 days or until they leave the computational domain (98.1° W to 39.6°E, 10.6 ° to 79.2°N). Thus, NAME generates a modelled mole fraction contribution to MHD for each grid cell over the 30 days for each 4-hour period. The background times are then defined as periods where the 30-day air history from NAME is dominated (> 80 % of particles) by air from the Atlantic that entered the NAME domain from the western or northern edges and when the amount of land crossed within 62.5 km of the MHD station is small. Using these background times, a polynomial is then fitted to the mole fractions; any background times that are significantly different to the fitted background are identified and removed from the set of background times and another polynomial is then fitted with the new set of background times to produce the final background mole fraction for MHD.

The NAME modelled backgrounds in this chapter are derived from, and therefore represent, in situ observations at Mace Head (MHD), located on the west coast of Ireland (53°33'N, 9°904'W) (Figure 3.16) and were provided by Alistair Manning from the UK MetOffice. Mace Head is considered a background station in the World Meteorological Organisation (WMO) Global Atmosphere Watch (GAW) programme and is representative of mid-latitude northern hemispheric background air masses with, on average, over 50% of the air masses arriving at MHD recently having passed over the North Atlantic Ocean (Ebinghaus et al., 2011). For this reason, it is used by the DECC UK emissions verification

programme network as a baseline upon which UK emissions are estimated (Stanley et al., 2018).

Figure 3.16. Map of the UK and Ireland displaying the location of MHD (blue) and WAO (red).

The baseline estimates from MHD were provided for CO_2, CH_4, CO, N_2O, and H_2. However, as O_2 is not routinely measured at MHD , no NAME background estimate is available for this species for the purposes of comparison. Greenhouse gas measurement networks in the UK have evolved independently over the years depending upon funding sources, as a result MHD and WAO do not use the same primary reference scales for some species. At MHD, CO_2, CO, and H_2 are reported on the same scales as at WAO: WMO-X2007, WMO-X2014A, and MPI-2009, respectively. Methane is reported on the TU-1987 scale at MHD, whereas it is reported on the WMO-X2004A scale at WAO. N_2O at MHD is reported to the SIO-16 scale, whereas it is reported to the WMO-X2006A scale at WAO. The NAME backgrounds calculated for MHD for CH_4 and N_2O have still been included in this comparison despite the differing scales, but this has been taken into consideration in the discussion of these results. The NAME derived background estimates are produced on daily, monthly, and annual timestamps. For this study I have used the monthly estimates (timestamp on the 15th of the month) in order to match the timestamp of the radon calculated backgrounds. These monthly estimates were

then interpolated to hourly for consistency in the comparisons with the other methodologies.

3.4.1.3 STILT back trajectory model

The STILT (Stochastic Time-Inverted Lagrangian Transport) model (Lin et al., 2003) is a Lagrangian particle dispersion model for atmospheric transport. STILT simulates atmospheric transport by following a particle ensemble backward in time from its release at the measurement site, and the footprints that represent the sensitivity of tracer concentrations at the site to surface fluxes upstream are calculated. The STILT footprints for WAO are produced by the ICOS Carbon Portal (https://stilt.icos-cp.eu/viewer/) driven by a 3-hourly analysis of the ECMWF-IFS (Integrated Forecasting System) atmospheric circulation model at a 0.25° x 0.25° resolution and mapped onto a 1/12° latitude x 1/8° longitude grid. The footprints are then coupled to the biosphere model VPRM (Vegetation Photosynthesis and Respiration Model) (Mahadevan et al., 2008) and anthropogenic emissions from the EDGAR v4.3 emission inventory (Janssens-Maenhout et al., 2019) to simulate atmospheric CO_2 mole fractions. The background mole fraction produced from STILT represents the influence from sources and sinks outside the STILT model domain and prior to the start of the model run. These initial and lateral boundary conditions are taken from the Jena CarboScope global 3D atmospheric CO_2 mixing ratio fields (http://www.bgc-jena.mpg.de/CarboScope/).

The STILT runs from the ICOS Carbon Portal produce a CO_2 background mole fraction for WAO every 3-hours; for the purpose of comparison to the other background methods, the data was interpolated to every hour.

3.4.1.4 Meteorologically and standard deviation filtering

Background estimates for each species were determined through a filtering process taking into account the variability in the species mole fractions and meteorological conditions that indicate the site is sampling air that has recently passed over the North Sea (e.g. Brailsford et al., 2012). First, the 5-hour running SD of each gas species time series was calculated in order to identify periods of stable data. Hourly averaged wind speed and wind direction data were then used to further filter the data to a 'maritime air sector'. In order to exclude measurements

potentially influenced by local sources during low wind speeds, only measurements concurrent with wind speeds greater than 5 m s^{-1} were selected (Schuepbach et al., 2001). Next, the wind direction of between 340° and 45° filter was applied, in order to only include air masses from the maritime sector.

After the meteorological filters were applied, the remaining data was further filtered using the previously calculated 5-hour running SD. The gas species data points corresponding to the lowest 50% of the remaining 5-hour running SD values were then retained and averaged to produce a monthly background estimate for each gas. These monthly estimates were then interpolated to hourly values for comparison with the other background methods; if there was a gap in the met estimates of 3 months or greater, the months either side of the gap were not interpolated between.

3.4.2 Results and discussion

The results of the comparison of each background method described above with the radon derived backgrounds are described and discussed in the following section. For comparison, each of the background estimates have been interpolated to hourly values. If there is a gap of 3 or more months, this gap was not interpolated over.

3.4.2.1 CO_2

The method comparison of the CO_2 backgrounds calculated using radon, REBS, NAME, STILT, and the MET methods are displayed in Figure 3.17. Over the entire time period, the average of the absolute difference between the radon background and REBS is 2.02 ± 2.05 ppm, for the NAME background the average absolute difference is 0.77 ± 0.66 ppm. The average absolute difference from the radon background is 1.08 ± 0.90 ppm and 0.98 ± 1.09 ppm for the STILT and MET methods, respectively.

Compared to the radon, NAME, and MET derived estimates, the STILT estimate is far more variable (Figure 3.17), this is due to the timestamp of the original STILT background estimate before it was interpolated to hourly values. The STILT estimate is produced for every 3-hour time-step and then interpolated to hourly, whereas the radon, NAME, and MET backgrounds were produced on a

monthly timestamp and then interpolated to hourly values thus producing a smoother curve. Other than the more variable STILT background, STILT and NAME both produced similar background estimates, with the STILT background following similar trends than NAME but with more noise. The average NAME – STILT absolute difference over the entire time series is 0.86 ± 0.74 ppm. These background methods are both produced using Lagrangian particle distribution models and use the ECMWF circulation data; however, the NAME background values are calculated using CO_2 observations from MHD, whereas STILT uses Jena CarboScope global 3D atmospheric CO_2 mixing ratio fields.

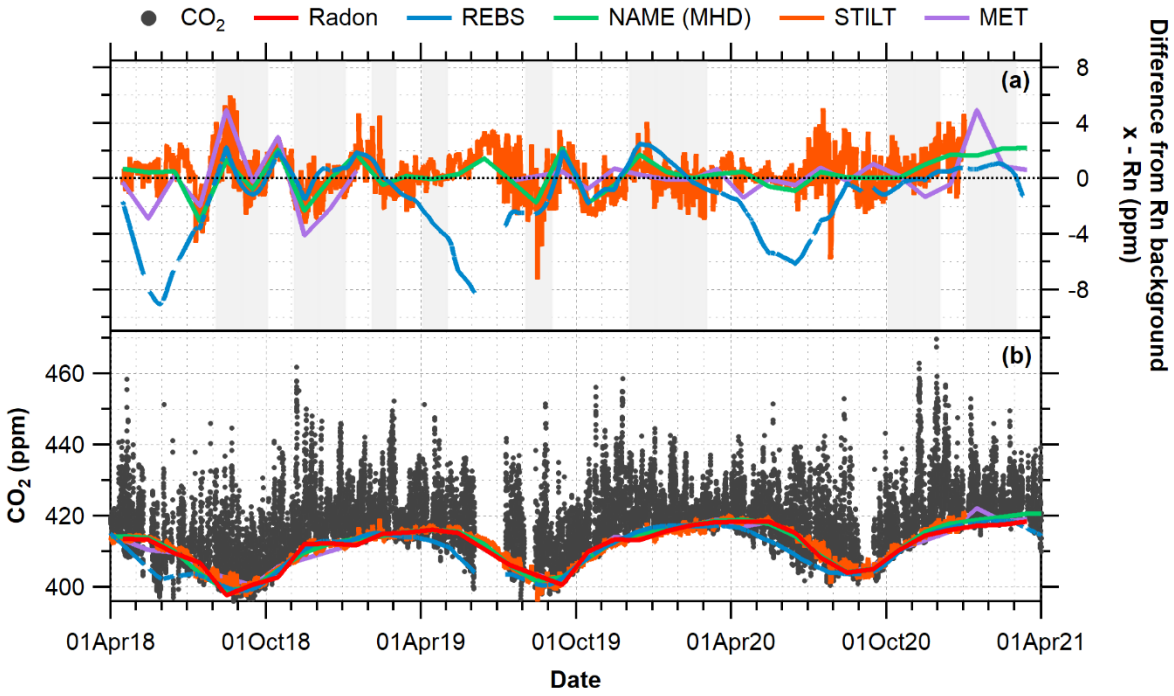

Figure 3.17. (a) Difference from radon background estimate, where the radon estimate is subtracted from the named method. Shaded areas indicate months when the radon methodology was flagged. (b) CO_2 time series and background estimates using radon, REBS, NAME, STILT, and MET methods.

The average absolute difference between the NAME and the radon backgrounds is 0.28 ± 0.98 ppm; however, the error given on the NAME CO_2 monthly estimates varies between 0.523 and 0.9825 ppm. The agreement between the NAME and radon methods is good, particularly as the NAME background was calculated using data from MHD which receives predominantly maritime air masses from the North Atlantic Ocean with very little, if any, terrestrial or pollution sources or sinks, and thus is a good site for determining background signals; thus the radon method is appropriately filtering out air masses with recent terrestrial influence. The similarity in these estimates also indicates that even

though NAME was not run for the study field station, MHD observations can provide a suitable background estimate for CO_2 at WAO when using NAME. The average difference between the NAME and MET methods is very small, 0.09 ± 1.47 ppm, however this difference does vary between a maximum of 4.96 and -4.11 ppm. The small average difference shows that the MET method is filtering out terrestrial air masses with influence from localised sources and sinks. Additionally, the general variability is similar to that of the STILT methodology which is based on more complex meteorological fields of atmospheric transport.

In Figure 3.17 there are a number of months in which the radon method differs from all four of the other methodologies, the majority of these months are those that were flagged for 'potential terrestrial influence'. Of the 35 months that the ^{222}Rn method produced a background estimate, 14 of these were flagged for potential terrestrial influence, due to the data selection method used (grey shaded months in Figure 3.17). The average difference of the REBS, NAME, STILT, and MET estimates for the 14 flagged and 21 non-flagged monthly estimates are shown in Table 3.4,. For each background calculation method, with the exception of REBS, the average absolute difference from the ^{222}Rn estimate is smaller in the unflagged months; however, this difference is not significant and for each method the errors (±SD) between the flagged and non-flagged months overlap. For the REBS method, the flagged months are closer to the radon background value than the non-flagged months. However, the controlling factor in this is that the REBS estimate differs largely from the radon estimates during the spring/summer months, and these months also happen to be the months in which the radon method is most commonly not flagged. Where the absence of flags on the radon method during the spring/summer is caused by a higher frequency of air masses passing over the maritime sector before arrival at WAO than during the autumn/winter, as discussed in section 3.3.2.1.

Table 3.4. Average of the absolute difference from the ^{222}Rn method background estimate for flagged and non-flagged months for REBS, NAME, STILT, and MET background estimates.

	Non-flagged months (average ± SD) (ppm)	Flagged months (average ± SD) (ppm)
REBS – Rn	3.00 ± 2.37	1.12 ± 0.98
NAME – Rn	0.97 ± 0.89	0.99 ± 0.93
STILT – Rn	1.00 ± 0.8	1.12 ± 0.98
MET - Rn	0.88 ± 0.86	0.95 ± 1.78

The CO_2 background estimates in Figure 3.17b display an evident seasonal cycle, with an annual maximum during the late winter months, minimum during the late summer, and a seasonal cycle amplitude of around 15 ppm. Over the spring months, during the Northern hemisphere growing season, there are more localised terrestrial CO_2 sinks, therefore the background should sit higher on the observations during the spring. This background characteristic can be seen in the ^{222}Rn, NAME, and STILT background estimates, but not in the REBS estimate (Figure 3.17b). The difference between the REBS background estimate and the radon estimate therefore has a seasonal cycle due to this discrepancy, which cannot be seen with the NAME and STILT differences from the radon method (Figure 3.18). The opposite is the case over the winter months, where the local terrestrial CO_2 source is larger than the sinks so the background should be lower; again, the REBS estimate does not produce this trend and is therefore higher than the radon estimates over the winter months (DJF) (Figure 3.18). The terrestrial drawdown of CO_2 that occurs during the spring and summer months, and emission during the autumn and winter are not representative of the wider background, whereas the REBS method is assigning these localised fluxes into the background component. As the REBS estimate disagrees with all the other methodologies during this period, there is confidence that it is the REBS estimate that is not producing a representative RMB, not the radon; additionally, the asymmetrical weighting of the REBS function mean that it is not a particularly applicable species in which the deviations are not either mostly positive or mostly negative. REBS is a purely statistical background estimate method, and thus has no prior information other than the CO_2 mole fraction time series causing the discrepancy in the seasonality of this background estimate in comparison to radon. Conversely, both

the NAME and STILT background estimates have inputs of CO_2 mole fractions and atmospheric circulation data. As the input parameters to the REBS code are user defined, changing these could improve the agreement between the radon and REBS estimates seasonally. Increasing the B value used as an input would decrease the difference between the radon and REBS estimate during the spring months, however this would then increase the difference during winter. Further, if REBS were to be run as the sole background estimation method, this information regarding the seasonal differences would not be available.

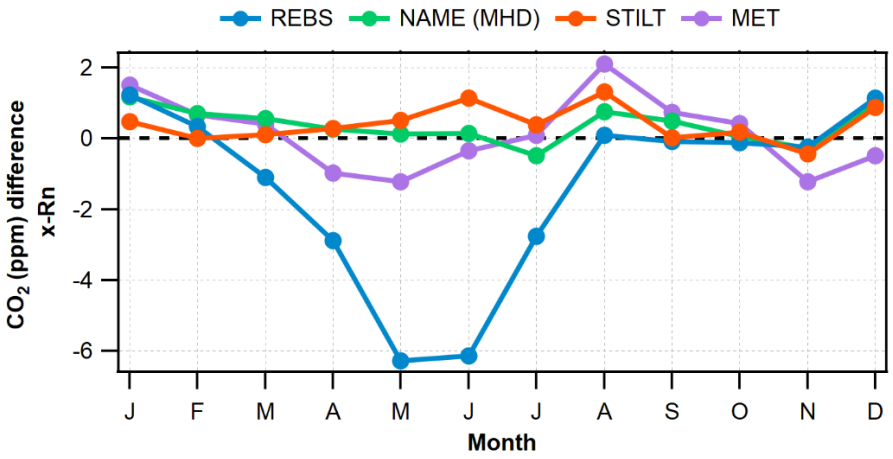

Figure 3.18. Mean monthly difference between REBS (blue), NAME (green), STILT (orange), and MET (purple) derived backgrounds compared to the radon background calculation.

3.4.2.2 O_2

The O_2 time series and method comparison of the O_2 backgrounds calculated using radon, REBS, and MET methods are displayed in Figure 3.19. Over the entire time period, the average difference between the radon background and REBS is 13.86 ± 12.30 per meg, for the MET derived background the average difference is 6.48 ± 6.44 per meg.

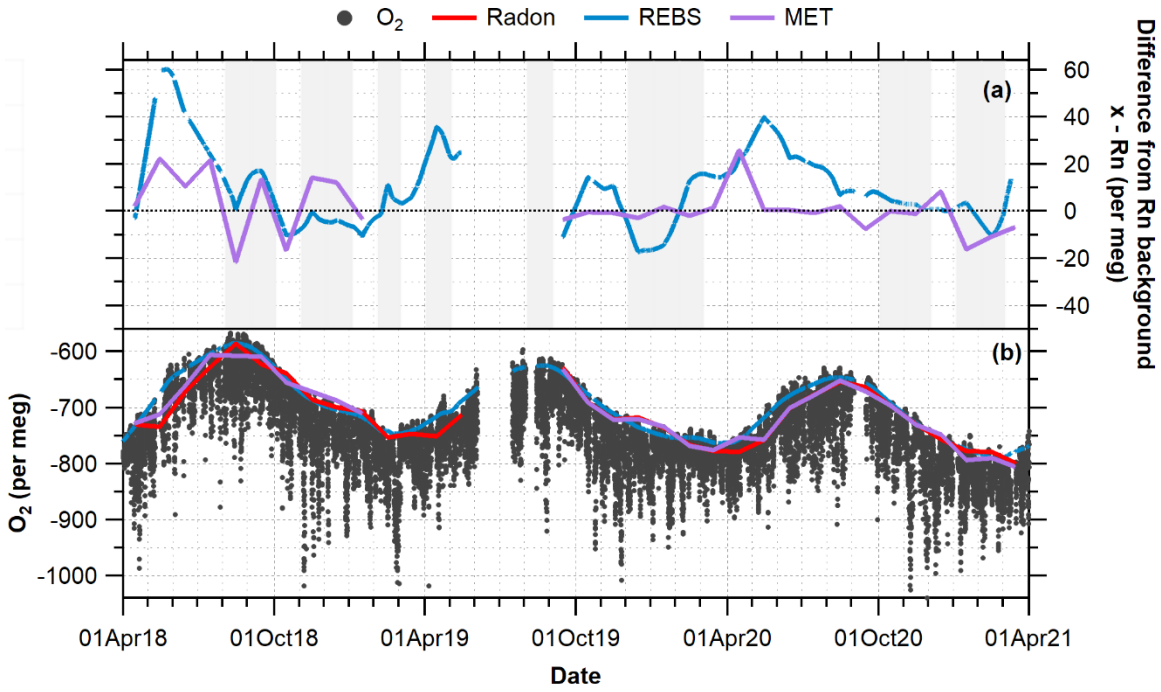

Figure 3.19. (a) Difference from radon background estimate, where radon estimate is subtracted from the named method. Shaded areas indicate months when the radon methodology was flagged. (b) O_2 time series and background estimates using radon, REBS, and MET methods.

The O_2 background estimates display a distinct seasonal cycle, with the maxima in late summer (August) and minima during late winter (February), with a seasonal cycle amplitude of around 150 per meg (Figure 3.19b). The difference between the REBS and ^{222}Rn background estimates also displays a seasonal cycle, with the REBS estimate being higher than the ^{222}Rn estimate in spring/summer, and lower in autumn/winter. During spring-summer in the northern hemisphere, there is an increase in photosynthesis, thus an increase in localised land sources of O_2, whereas in the autumn-winter there is an increase in localised land sinks of O_2. Due to this seasonal cycle in the sources and sinks of O_2, it would be expected that the background would be higher during the spring-summer months, and lower in the autumn-winter. This seasonal difference can be seen in the ^{222}Rn background estimate, but is not apparent in the REBS estimate. This is the cause of the seasonal difference between the REBS and ^{222}Rn estimates in Figure 3.19a. This is due to the same reasons discussed in section 3.4.2.1 for CO_2, where the terrestrial emission of O_2 that occurs during the spring/summer months, and drawdown during the autumn/winter are not representative of the wider background, whereas the REBS method is assigning these localised fluxes into the background component. As with CO_2, the input parameters of the REBS function could be tweaked to correct for the

large spring/summer difference from the radon background estimate; however, this would cause an increase in the difference during the autumn/winter, and again, if REBS were being used as the only background estimation method this seasonal discrepancy would be unknown to the user. There is also a seasonal difference observed between the MET and radon methods in Figure 3.20; however, this is less pronounced than the REBS-radon difference, and rather than being caused by a consistent difference, it is due to a few spikes in the MET background (Figure 3.19).

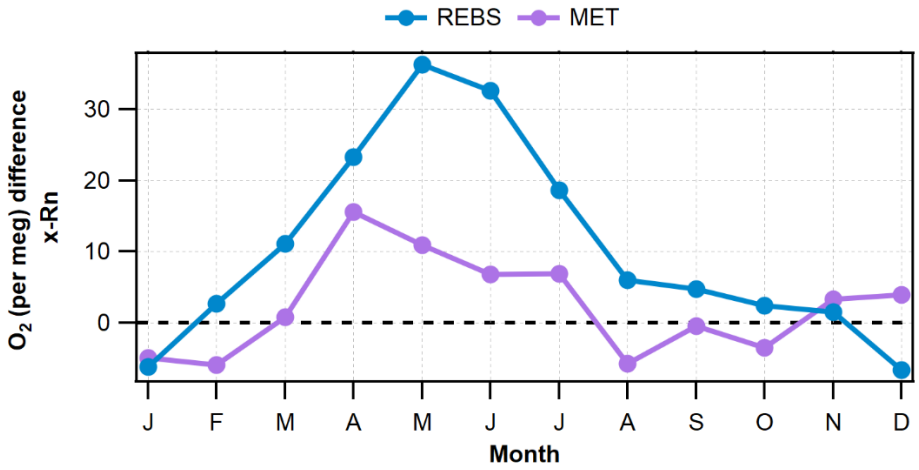

Figure 3.20. Mean monthly difference from the radon background for REBS (blue) and MET (purple).

3.4.2.3 H_2

The method comparison of H_2 backgrounds calculated using radon, REBS, NAME, and the MET methodologies are displayed in Figure 3.21. Over the entire time period, the average of the difference of the absolute values between the radon background and REBS is 6.27 ± 4.53 ppb, for the NAME background the average absolute difference is 11.95 ± 4.24 ppb. The average absolute difference from the radon background is 11.96 ± 4.40 ppb for the MET method.

The H_2 observations and associated background estimates all display a distinct seasonal cycle, with spring maxima and autumn minima and a seasonal cycle amplitude in the background estimates of around 50 ppb. All four methods pick up the seasonal cycle in the H_2 data, with peaks in early autumn attributed to higher loss rates by the OH radical and stronger rates of soil deposition with drier soil conditions (e.g. Steinbacher et al., 2007; Lallo et al., 2008). The radon RMB background estimate generally sits higher on the H_2 data during the summer

months, which could be reflective of the larger flux of atmospheric H_2 into soil during the summer (e.g. Bartyzel et al., 2013).

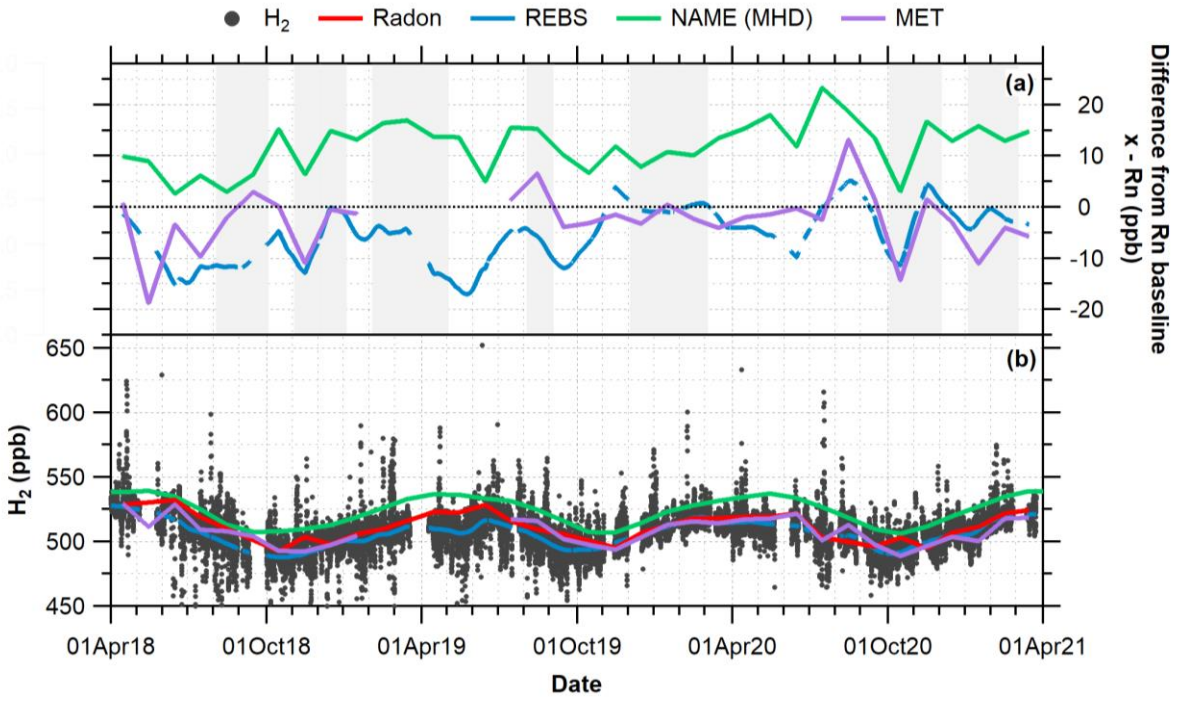

Figure 3.21. (a) Difference from radon background estimate, where radon estimate is subtracted from the named method. Shaded areas indicate months when the radon methodology was flagged. (b) H_2 time series and background estimates using radon, REBS, NAME, and MET methods.

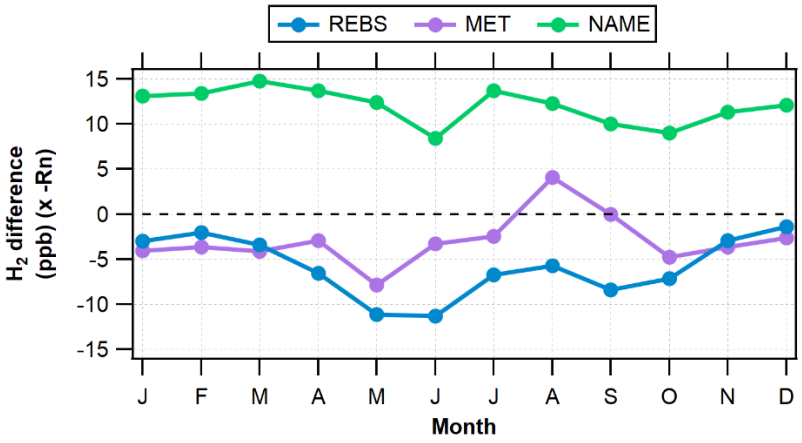

Figure 3.22. Mean monthly difference from the radon background for REBS (blue), MET (purple), and NAME (green) derived backgrounds.

In contrast to the other species examined in this chapter, the difference between the NAME method and the radon method does not vary around the zero line but instead has a significant positive offset of ~10-15 ppb, i.e., the NAME estimate is consistently higher than the radon estimate (Figure 3.21a). For the NAME monthly background estimates, the standard deviation varies between 3.31 and 8.54 ppb. The offset between the NAME and radon background estimates may

be due to the NAME background estimate being produced with MHD H_2 observations, not WAO. The main sink of H_2 is soil deposition, accounting for around 75% of the total sinks (Ehhalt and Rohrer, 2009), the background air at MHD has spent a lot of time over the open ocean, and is therefore less affected by the H_2 soil sink; whereas WAO is measuring a maritime background which is surrounded by land masses (i.e. the UK and Europe). Therefore, it is much more probable that the air masses observed at WAO have experienced more sink activity. Another possible cause of the higher NAME background estimate for H_2 is that 'tropical maritime' North Atlantic air masses (below 40°S) are associated with higher H_2 mole fractions (Simmonds et al., 2000; Forster et al., 2012). It is likely that MHD experiences these air masses during their background periods, whereas the WAO RMB air is missing this southerly component due to its location on the east of the UK land mass. Looking at the monthly NAME composite footprints (refer to section 3.3.1.3), there is only one month (July 2019) over the 3-years in which there is a significant contribution from < 45°N, without the air mass passing over land, to the air masses observed at WAO used in the radon RMB calculation method (Figure 3.23). For this month, the NAME and radon background estimates are closer than during the surrounding months (Figure 3.21a). Finally, even though H_2 at WAO and MHD are reported to the same scale, the H_2 mole fraction is known to drift in calibration standards. Thus to be more conclusive a scale intercomparison between WAO and MHD would need to be performed.

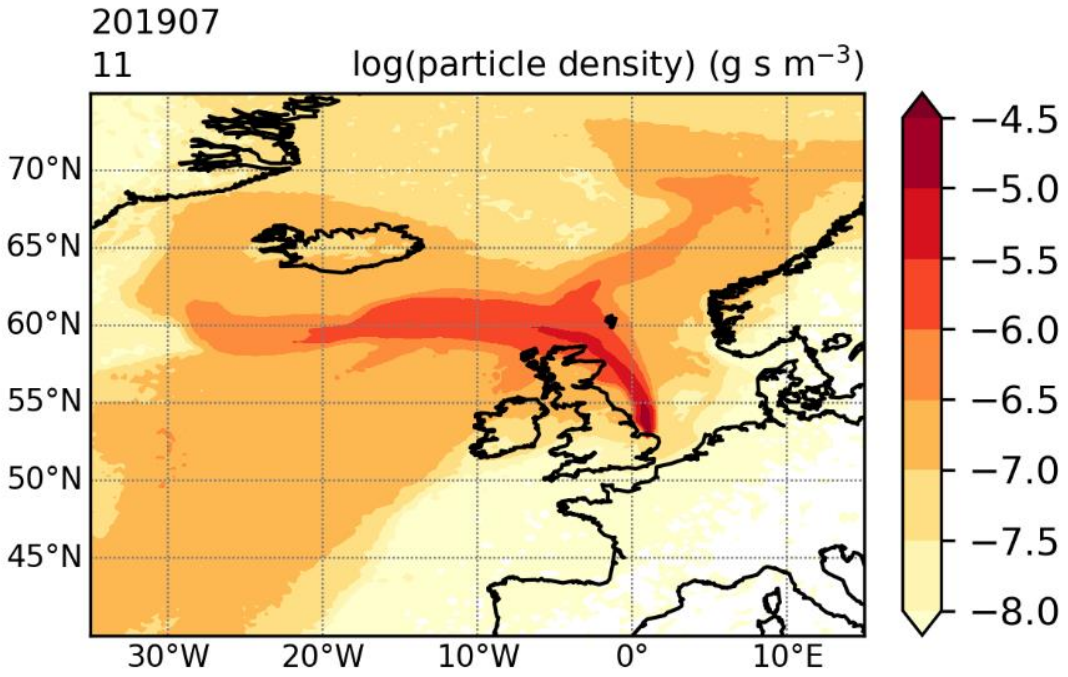

Figure 3.23. NAME 30-day composite footprint for air masses corresponding to data points used in the radon background method estimate for July 2019.

In the case of H_2, the MHD NAME derived background is not suitable for use as a background at WAO. However, the latitudinal gradient of H_2 in the northern hemisphere (Figure 3.24; Ehhalt and Rohrer (2009)) also means that air masses that arrive at WAO which have experienced rapid latitudinal transport may not be representative for the station's latitude. The removal of air masses which have been transported from other latitudes before the calculation of the radon derived background for species such as H_2 should be further investigated in future work but is beyond the scope of this chapter.

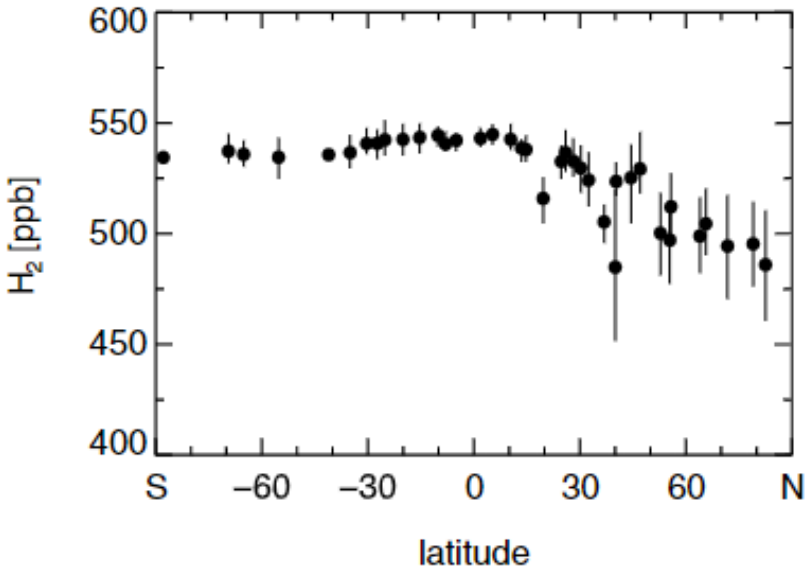

Figure 3.24. Average latitudinal distribution of the H_2 mixing ratio from 1994-2003 (± SD) (Ehhalt and Rohrer, 2009).

3.4.2.4 CH_4

The method comparison of CH_4 backgrounds calculated using radon, REBS, NAME, and the MET methods are displayed in Figure 3.25. Over the entire time period, the average absolute difference between the radon background and REBS is 10.68 ± 4.62 ppb, for the NAME background the average absolute difference is 3.17 ± 2.68 ppb. The average of the absolute difference from the radon background is 6.21 ± 4.06 ppb for the MET method.

In general, the NAME-Rn difference is centred around zero whereas there is a positive offset in the REBS-Rn and MET-Rn difference i.e., the REBS and MET backgrounds are consistently higher than the Rn background (Figure 3.25a). As discussed with the other species, the REBS background can be adjusted to sit higher or lower on the CH_4 observations by tweaking the input values used in the function; however, if REBS were used as the sole method for background estimation there would be no other methods for comparison to know whether this resultant background values need adjusting.

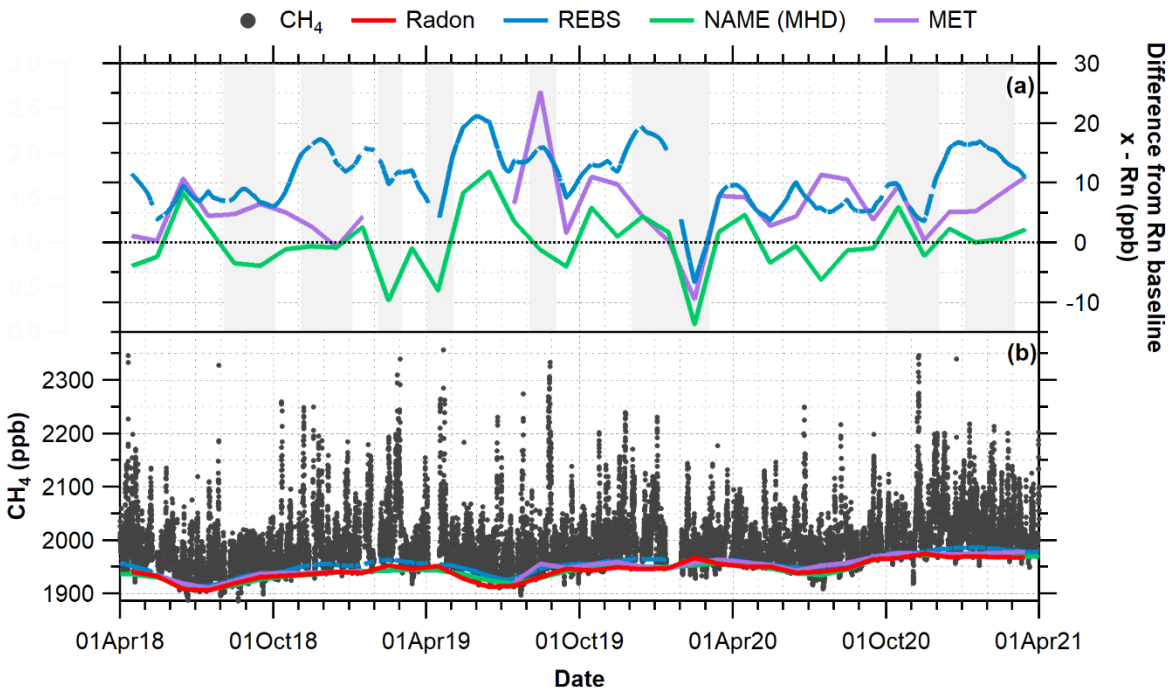

Figure 3.25. (a) Difference from radon background estimate, where radon estimate is subtracted from the named method. Shaded areas indicate months when the radon methodology was flagged. (b) CH_4 time series and background estimates using radon, REBS, NAME, and MET methods.

Although the NAME-Rn difference is centred around zero, CH_4 is not reported to the same scale at MHD and WAO. MHD report CH_4 to the TU-1986 scale, whereas it is reported on the WMO-X2004a scale at WAO. The TU-1986 values can be converted to WMO-X2004A scale by multiplication of a factor of 1.0001 (Prinn et al., 2018). When this conversion factor is applied to the NAME background estimate the average absolute difference from the radon background only decreases by 0.004 ppb and the average difference increases from 0.02 ppb to 0.22 ppb and is still centred around zero. The standard deviation given on the monthly MHD NAME background estimates vary between 4.55 and 6.87 ppb, which is larger than the average absolute difference between the NAME and radon estimates.

There are two months in which the difference from the radon background is similar for all three other methods but different from the radon estimate: June 2018 and February 2020. In June 2018 the radon estimate is lower than the other three methods, whereas in February 2020 the other three methods are all lower than the radon background estimate. The estimate for February 2020 is flagged for the radon method, indicating that there is potential terrestrial influence on the radon background estimate, therefore it is likely that the air masses used to

calculate the radon background had been in recent contact with CH_4 sources thus the higher background result. This can be seen in the NAME composite footprint corresponding to the observations retained after step 1 to calculate the February 2020 radon background estimate Figure 3.26.

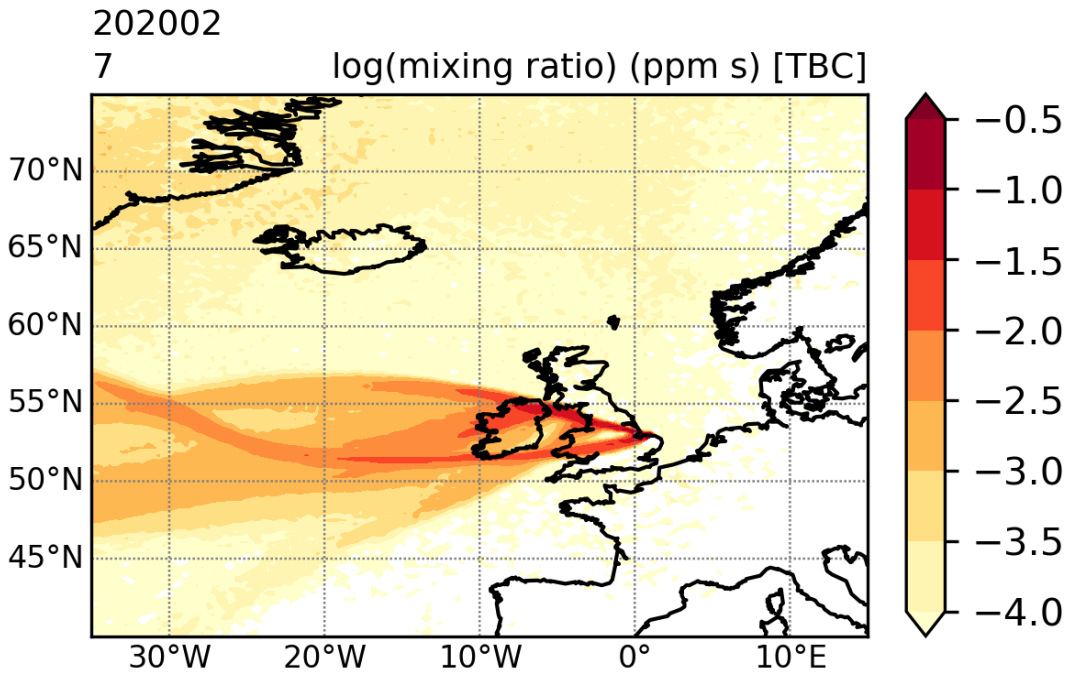

Figure 3.26. NAME 30-day composite footprint for air masses corresponding to data points used in the radon RMB method estimate for February 2020.

The RMB methodology assumes that when an air mass has not been in recent contact with the land surface that it has not been in contact with anthropogenic CH_4 sources, however, this is not always the case. One potential source of methane emissions is leakage from offshore oil or gas production in the North Sea (Riddick et al., 2019); this source would not be filtered out by the radon background methodology as air mass contact with offshore oil and gas platforms would not cause an elevation in the radon concentration. However, although there are a number of oil and gas platforms in the North Sea (Figure 3.27), which the air masses being used to calculate the CH_4 background in the radon methodology frequently pass over (as shown in the NAME footprints in section 3.3.2.3), there does not appear to be an enhancement in the CH_4 background estimation using radon, in comparison to NAME which is based on MHD which does not experience equivalent CH_4 sources over the ocean. This is likely due to the radon methodology using the lowest 25 – 33% of CH_4 values retained when radon is below the

thresholds, therefore this filters any positive excursions which would be caused by CH_4 release from oil and gas platforms.

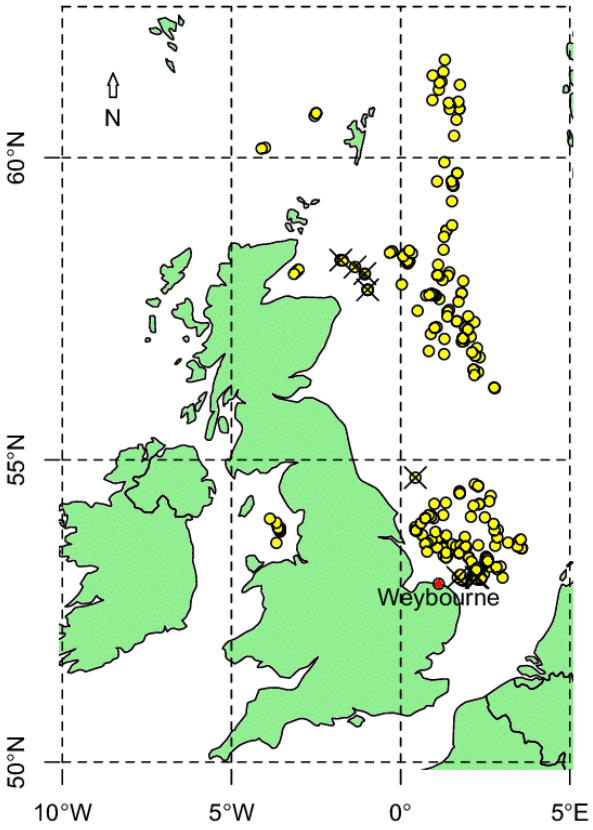

Figure 3.27. Map of the North Sea showing the locations of all UK offshore oil and gas platforms (filled yellow circles) Riddick et al. (2019). The black crosses indicate platforms measured by Riddick et al. (2019), so can be ignored in the context of this chapter.

3.4.2.5 CO

The method comparison of CO backgrounds calculated using the radon, REBS, NAME, and MET methods are displayed in Figure 3.28. Over the entire time period, the average absolute difference between the radon background and REBS is 3.84 ± 2.75 ppb, for the NAME background the average absolute difference is 3.19 ± 2.24 ppb. The average absolute difference from the radon background is 3.39 ± 1.76 ppb for the MET method.

Although the absolute average difference from the radon value is similar for all three methods, the NAME difference is centred around zero, whereas there is a positive offset with the meteorological and REBS methods. In other words, the average of the real difference values compared to the radon method for the NAME background is -0.42 ± 3.87 ppb, whereas this difference is 3.05 ± 2.29 ppb and 2.60

± 3.94 ppb for the MET and REBS methods, respectively. The standard deviation on the monthly MHD NAME background estimates varies between 3.23 and 7.07 ppb; again this is greater than the average absolute difference between the NAME and radon backgrounds.

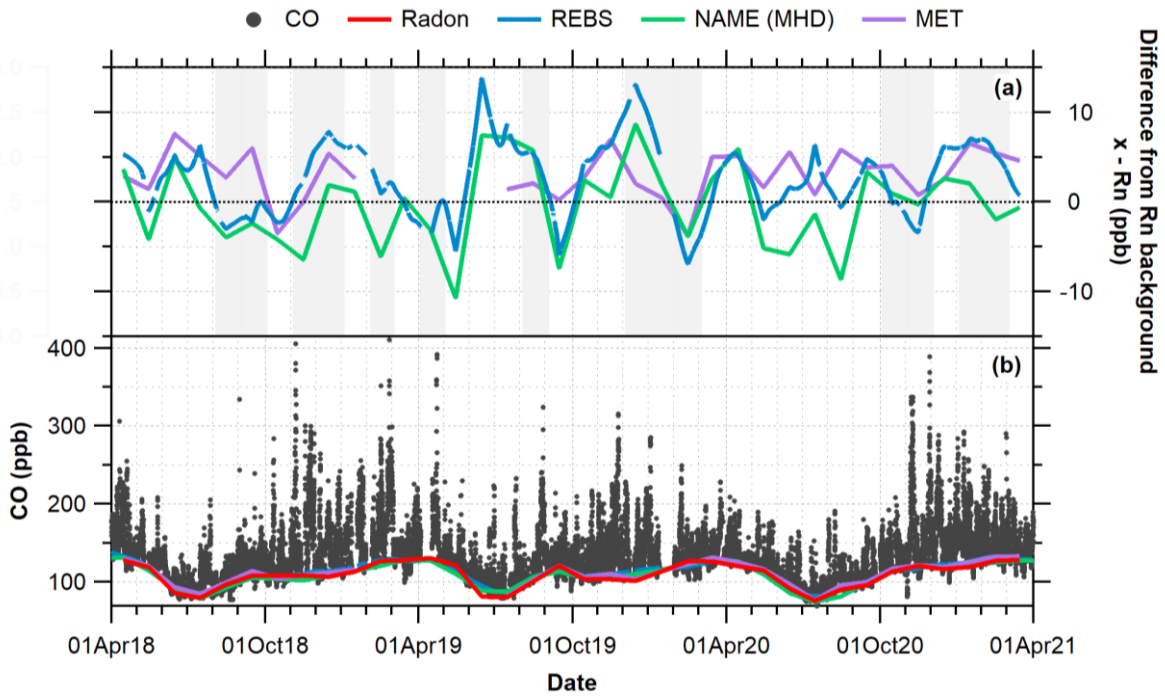

Figure 3.28. (a) Difference from radon background estimate, where radon estimate is subtracted from the named method. Shaded areas indicate months when the radon methodology was flagged. (b) CO time series and background estimates using radon, REBS, NAME, and MET methods.

As with H_2, CO has a latitudinal gradient (e.g. Piotrowicz et al., 1990). Low CO can be attributed to 'tropical maritime' air masses from the North Atlantic, which would be experienced at MHD. This latitudinal gradient could be seen in the consistent offset between the NAME and radon background estimates for H_2, but this is not the case for CO. However, due to the latitudinal gradient of CO, the removal of air masses which have been transported from other latitudes before the calculation of the radon derived background for species such as CO should be further investigated in future work but is beyond the scope of this chapter.

The average difference between the REBS and radon methods has a positive offset. This could be accounted for by tweaking the variables input into the calculation; however, if REBS were to be used alone there would be nothing to compare this background against, so one would not know that these variables needed to be changed. Ignoring this offset, the variability in the difference between the REBS and radon method shows a similar pattern to the difference between the

NAME and radon methods (Figure 3.28a); this indicates that the radon method may not be correctly picking up the monthly variability in the CO background. The MET method also displays an offset from the radon method, with the MET background being higher than that estimated using radon. As the MET method is supposedly also filtering out terrestrial influence through use of wind speed and wind direction, it would be expected that these two backgrounds should be more similar. The difference in the MET and radon methods here could be due to the effects of local circulation, such as sea breeze effects, not being filtered for in the MET method.

3.4.2.6 N_2O

The method comparison of the N_2O backgrounds calculated using radon, REBS, NAME, and the MET methods are displayed in Figure 3.29. Over the entire time period, the average absolute difference between the radon background and REBS is 0.31 ± 0.12 ppb, for the NAME background the average absolute difference is 0.37 ± 0.09 ppb. The average absolute difference from the radon background is 0.25 ± 0.22 ppb for the MET method.

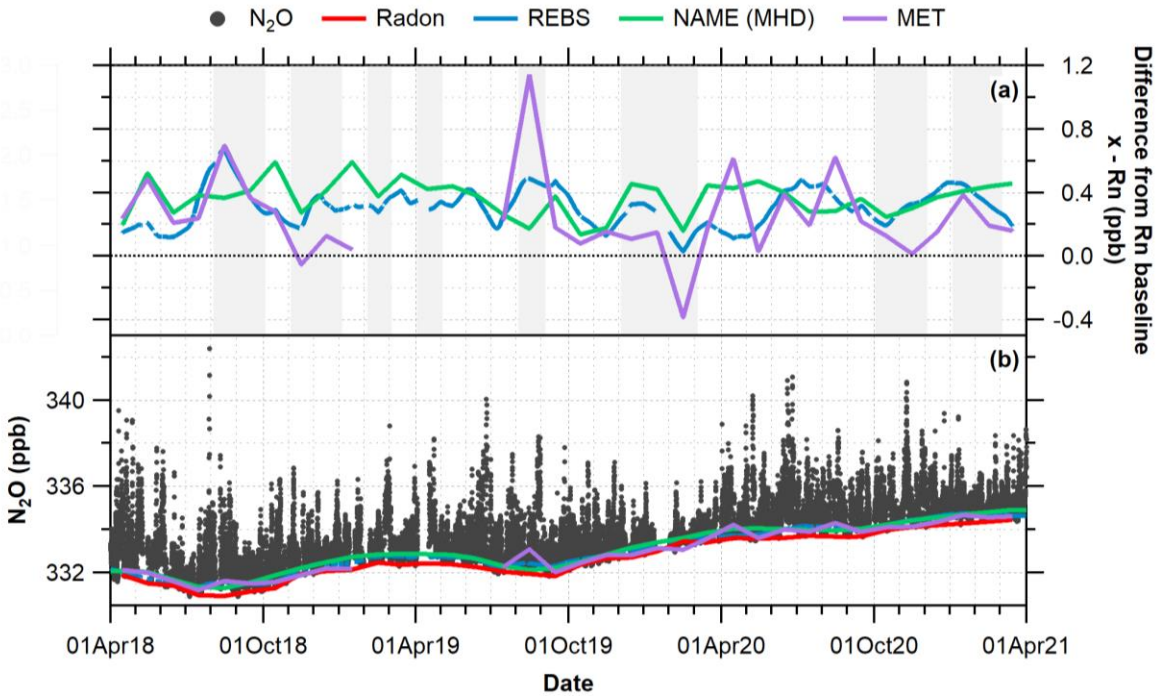

Figure 3.29. (a) Difference from radon background estimate, where radon estimate is subtracted from the named method. Shaded areas indicate months when the radon methodology was flagged. (b) N_2O time series and background estimates using radon, REBS, NAME, and MET methods.

There is a positive offset in the difference of the radon method with all three other methodologies. As with the other species the difference from the REBS estimate is due to the input variables used in the function. Although these input variables were tested through trying a variation of values, the subjective nature of this statistical method has a large effect on the output. The difference between the REBS and radon methods for N_2O is highly variable; additionally, this difference is not consistent with the difference seen between the radon and the other two methods.

The consistent positive offset in the difference between the radon and NAME methods could be partially explained by the scale differences, at WAO N_2O is reported on the WMO X2006A scale, whereas the MHD N_2O measurements are reported in the SIO-16 scale. SIO-16 scale values can be converted to WMO X2006A via multiplication by a factor of 0.9983 (Prinn et al., 2018). When this conversion factor is applied, the average absolute difference between the NAME and ^{222}Rn background estimates is reduced from 0.37 ± 0.09 ppb to 0.19 ppb ± 0.09 ppb (Figure 3.30). However, the offset of the difference changes from a positive to a negative offset i.e., the average of the difference from the radon background before the scale correction is applied is 0.37 ± 0.09 ppb, which changes to -0.19 ± 0.09 ppb after the correction. The standard deviation given on the monthly MHD NAME background estimate varies between 0.0819 and 0.138 ppb.

After the scale correction to allow for a more direct comparison between the MHD NAME modelled background and the WAO 222Rn RMB, the lower values observed in the NAME background could be due to the latitudinal gradient of N2O. N2O displays a strong latitudinal gradient due to the disproportionately higher emissions in the Northern Hemisphere (Figure 3.31) (Jiang et al., 2007). As MHD has a Southerly component to its background it could be observing air masses with lower N2O from these lower latitudes, whereas the WAO RMB air is missing this southerly component due to its location on the east of the UK land mass.

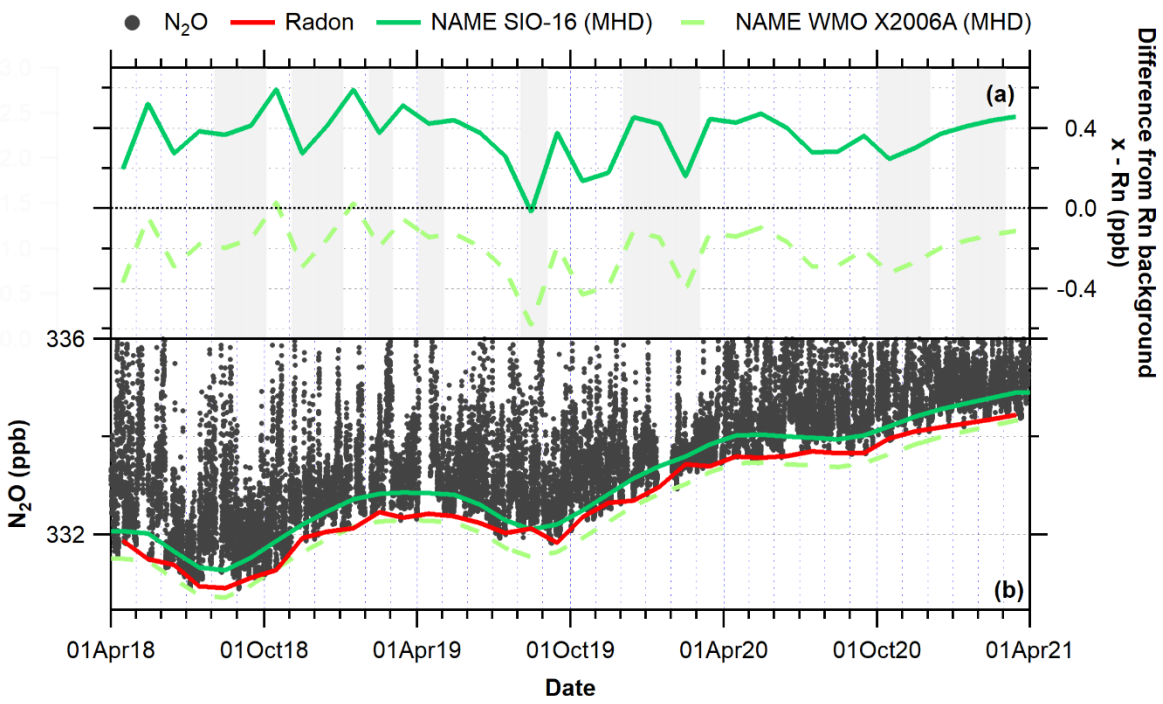

Figure 3.30. (a) Difference from radon background estimate, where radon estimate is subtracted from the NAME method. Shaded areas indicate months when the radon methodology was flagged. (b) N_2O time series and background estimates using radon, NAME on the SIO-16 scale used at MHD, and NAME converted to the WMO X2006A scale to be comparable to WAO.

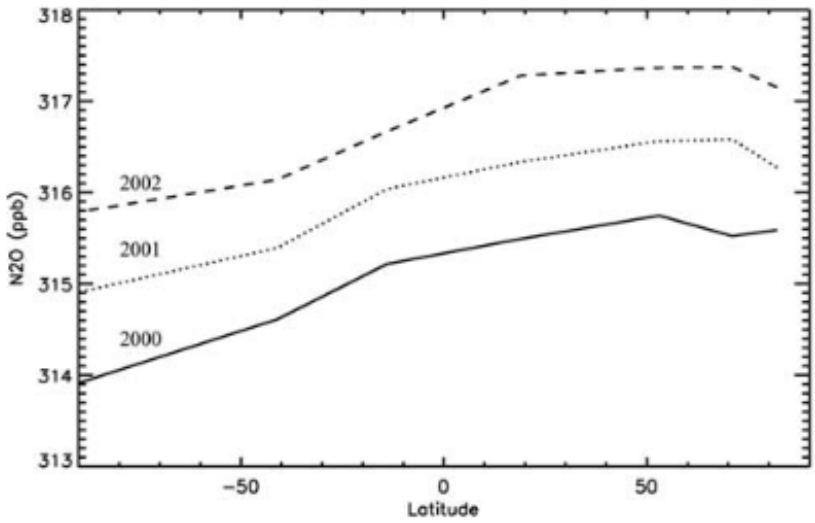

Figure 3.31. N_2O variation with latitude in 2000 (solid line), 2001 (dotted line), and 2002 (dashed line) (Jiang et al., 2007).

Another possible reason for the higher N_2O background for the ^{222}Rn method than the MHD NAME method is a greater influence from European and UK land masses on the ^{222}Rn method background values. The two months with the best agreement between the Rn and NAME methods are October 2018 and January

2019, both have a scale adjusted NAME-Rn difference of -0.03 ppb. The two non-flagged months with the largest scale adjusted NAME-Rn difference are October 2019 and November 2019, with a difference of -0.43 and -0.93 ppb, respectively. The NAME footprints for the air masses used in October 2018 and January 2019 ^{222}Rn RMB estimates show almost no interaction with the UK and Europe (Figure 3.32(a) and (B)). Conversely, for the months with the largest difference between the ^{222}Rn and NAME backgrounds, October 2019 and November 2019, the air masses used in the calculation of the ^{222}Rn RMB display a greater degree of interaction with the UK and European land masses (Figure 3.32(c) and (d)). This indicates that the higher N_2O background for the ^{222}Rn RMB than the MHD NAME method may be due to this minor influence from UK and European N_2O emissions.

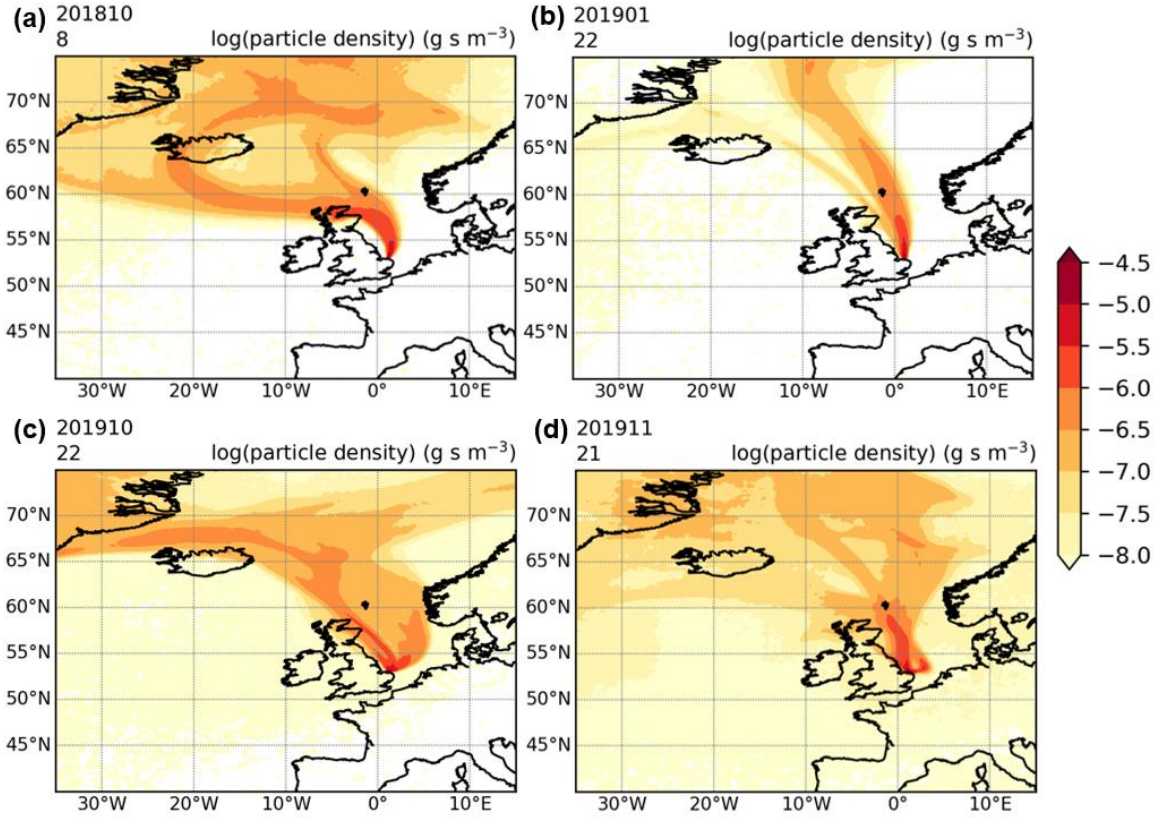

Figure 3.32. NAME 30-day composite footprint for air masses corresponding to data points used in the radon RMB method estimate for (a) October 2018, (b) January 2019, (c) October 2019, and (d) November 2019.

3.4.2.7 Method comparison summary

A summary of the average difference and average of the absolute differences of each method from the radon derived background for each species is shown in Table 3.4.

Generally, with the exception of H_2 and N_2O, the radon derived background is often most similar to the NAME derived background for all species, and most different from the REBS background method results. For H_2 and N_2O, the NAME background is the most different from the radon derived background, as discussed in sections 3.4.2.3 and 3.4.2.6, respectively.

Table 3.5. Average difference ((x-Rn) ± 1σ) and average of the absolute difference (|(x-Rn)| ± 1σ) from the radon derived background estimate for each species

	Background method difference from radon							
	REBS		**NAME**		**STILT**		**MET**	
	x - Rn	**|x-Rn|**	**x - Rn**	**|x-Rn|**	**x - Rn**	**|x-Rn|**	**x - Rn**	**|x-Rn|**
CO_2 (ppm)	-1.29 ±2.57	2.02 ±2.05	0.28 ±0.98	0.77 ±0.66	0.32 ±1.37	1.08 ±0.90	0.09 ±1.47	0.98 ±1.09
O_2 (per meg)	9.73 ±15.77	13.86 ±12.30					1.84 ±8.95	6.48 ±6.44
H_2 (ppb)	-5.75 ±5.17	6.27 ±4.53	11.95 ±4.24	11.95 ±4.24			-2.68 ±4.87	4.21 ±3.63
CH_4 (ppb)	10.51 ±5.01	10.68 ±4.62	0.02 ± 4.14	3.17 ±2.68			5.71 ±4.75	6.21 ±4.06
CO (ppb)	2.60 ±3.94	3.84 ±2.75	-0.42 ±3.87	3.19 2.24			3.05 ±2.29	3.39 ±1.75
N_2O (ppb)	0.31 ±0.12	0.31 ±0.12	0.37 ±0.09	0.37 ± 0.09			0.25 ±0.22	0.27 ±0.20

3.5 Conclusions

The use of radon measurements concurrently with measurements of other atmospheric gas species allows for the calculation of an RMB. Overall, the radon methodology for calculation of RMB shows good agreement with existing methods, with some variability depending on the processes involved in a given species source and sink mechanisms.

The radon method presented here is often based on a very small number of data points each month. Therefore even a small gap in the time series means that there is no estimate for that given month; this is reliant on both radon and the species for which the background is being calculated not having gaps in the time series. This is also the case for the MET method, which explains the large gaps in this method's background estimates. The calculation of these backgrounds using

radon is also dependent on the measurement site experiencing 'background' air masses during each month of the year; but during months in which fewer of these air masses were seen, the thresholds and flagging used in the methodology appropriately filtered air masses and the difference from other methods during these months was no worse than during non-flagged months. The NAME and STILT and MET methods also require the station to have experienced background air masses. Additionally, the use of radon is less computationally intensive than running the NAME or STILT methods, and can also be computed in 'real-time'.

REBS is also a quick and easy method for background calculation that does not require any additional observations, but it is based purely on statistics, so it includes some localised emissions in the background. The input parameters are also very subjective, and as seen in my results, changing the parameters for the different species would bring the REBS estimate closer to the other method estimates; however, if REBS were being used on its own, without comparison, the user would not know that these parameters need tweaking.

The difference from the NAME modelled backgrounds was generally small for all species, which suggests the radon could be used to validate the NAME modelled background results. Additionally, the location of MHD (where the NAME backgrounds were calculated for), means it receives predominantly maritime air masses from the North Atlantic Ocean with very little, if any, terrestrial or pollution sources or sinks; thus, the agreement with the radon background means the radon method is appropriately removing air masses with recent terrestrial influence.

3.5.1 Future work

This chapter demonstrates the use of radon for calculation of an RMB, but there is further research that could be conducted which falls outside the scope of the work I have presented here:

- This analysis should be repeated for non-coastal sites, such as mid-continental and mountain sites, which will present different challenges.
- The use of air quality parameters to screen out any maritime emissions should be investigated as I am currently assuming that there are no emissions over the ocean. Using the lowest percentage of mole fraction

values may account for this, but the use of air quality products could confirm this.

- The methodology used to calculate the radon RMB can be further developed to reduce the subjectivity used in the selection of some of the thresholds used.
- Analysis of the effects of species which have a strong latitudinal gradient on the calculation of an RMB using radon.
- For species with strong latitudinal gradients, investigation into the need for removal of air masses which have been transported from other latitudes before the calculation of the RMB for a site.

References

Adcock, K. E., Pickers, P. A., Manning, A. C., Forster, G. L., Fleming, L. S., Barningham, T., Wilson, P. A., Kozlova, E. A., Hewitt, M. C., Etchells, A. J. and Macdonald, A. (2023) '12-years of continuous atmospheric O_2, CO_2 and APO data from Weybourne Atmospheric Observatory in the United Kingdom', *[In Prep]*.

Apadula, F., Cassardo, C., Ferrarese, S., Heltai, D. and Lanza, A. (2019) 'Thirty Years of Atmospheric CO_2 Observations at the Plateau Rosa Station, Italy', *Atmosphere,* 10(7).

Balzani Lööv, J. M., Henne, S., Legreid, G., Staehelin, J., Reimann, S., Prévôt, A. S. H., Steinbacher, M. and Vollmer, M. K. (2008) 'Estimation of background concentrations of trace gases at the Swiss Alpine site Jungfraujoch (3580 m asl)', *Journal of Geophysical Research: Atmospheres,* 113(D22).

Bartyzel, J., Necki, J. M., Zieba, D., Rozanski, K. and Gasiorek, M. (2013) 'Uptake of atmospheric hydrogen by soils: a case study from southern Poland', 64(5), pp. 597-609.

Brailsford, G. W., Stephens, B. B., Gomez, A. J., Riedel, K., Mikaloff Fletcher, S. E., Nichol, S. E. and Manning, M. R. (2012) 'Long-term continuous atmospheric CO_2 measurements at Baring Head, New Zealand', *Atmos. Meas. Tech.,* 5(12), pp. 3109-3117.

Brantley, H. L., Hagler, G. S. W., Kimbrough, E. S., Williams, R. W., Mukerjee, S. and Neas, L. M. (2014) 'Mobile air monitoring data-processing strategies and effects on spatial air pollution trends', *Atmos. Meas. Tech.,* 7(7), pp. 2169-2183.

Brunke, E. G., Labuschagne, C., Parker, B., Scheel, H. E. and Whittlestone, S. (2004) 'Baseline air mass selection at Cape Point, South Africa: application of ^{222}Rn and other filter criteria to CO_2', *Atmospheric Environment,* 38(33), pp. 5693-5702.

Carslaw, D. C. and Ropkins, K. (2012) 'openair — An R package for air quality data analysis', *Environmental Modelling & Software,* 27-28, pp. 52-61.

Chambers, S., Williams, A., Crawford, J., Griffiths, A., Krummel, P., Steele, L., Law, R., van der Schoot, M., Galbally, I. and Molloy, S. (2017) *A radon-only technique*

for characterising atomspheric 'baseline' constituent concentrations at Cape Grim: Tech. rep.
Chambers, S., Williams, A. G., Zahorowski, W., Griffiths, A. and Crawford, J. (2011) 'Separating remote fetch and local mixing influences on vertical radon measurements in the lower atmosphere', *Tellus B: Chemical and Physical Meteorology,* 63(5), pp. 843-859.
Chambers, S. D., Hong, S. B., Williams, A. G., Crawford, J., Griffiths, A. D. and Park, S. J. (2014) 'Characterising terrestrial influences on Antarctic air masses using Radon-222 measurements at King George Island', *Atmos. Chem. Phys.,* 14(18), pp. 9903-9916.
Chambers, S. D., Williams, A. G., Conen, F., Griffiths, A. D., Reimann, S., Steinbacher, M., Krummel, P. B., Steele, L. P., van der Schoot, M. V., Galbally, I. E., Molloy, S. B. and Barnes, J. E. (2016) 'Towards a Universal "Baseline" Characterisation of Air Masses for High- and Low-Altitude Observing Stations Using Radon-222', *Aerosol and Air Quality Research,* 16(3), pp. 885-899.
Chambers, S. D., Williams, A. G., Crawford, J. and Griffiths, A. D. (2015) 'On the use of radon for quantifying the effects of atmospheric stability on urban emissions', *Atmos. Chem. Phys.,* 15(3), pp. 1175-1190.
Chambers, S. D., Zahorowski, W., Williams, A. G., Crawford, J. and Griffiths, A. D. (2013) 'Identifying tropospheric baseline air masses at Mauna Loa Observatory between 2004 and 2010 using Radon-222 and back trajectories', *Journal of Geophysical Research: Atmospheres,* 118(2), pp. 992-1004.
Crawford, J., Chambers, S. D., Cohen, D. D., Williams, A. G. and Atanacio, A. (2018) 'Baseline characterisation of source contributions to daily-integrated PM2. 5 observations at Cape Grim using Radon-222', *Environmental Pollution,* 243, pp. 37-48.
Cui, J., Pandey Deolal, S., Sprenger, M., Henne, S., Staehelin, J., Steinbacher, M. and Nédélec, P. (2011) 'Free tropospheric ozone changes over Europe as observed at Jungfraujoch (1990–2008): An analysis based on backward trajectories', 116(D10).
Dlugokencky, E. J., Myers, R. C., Lang, P. M., Masarie, K. A., Crotwell, A. M., Thoning, K. W., Hall, B. D., Elkins, J. W. and Steele, L. P. (2005) 'Conversion of NOAA atmospheric dry air CH_4 mole fractions to a gravimetrically prepared standard scale', *Journal of Geophysical Research: Atmospheres,* 110(D18).
Drewnick, F., Böttger, T., von der Weiden-Reinmüller, S. L., Zorn, S. R., Klimach, T., Schneider, J. and Borrmann, S. (2012) 'Design of a mobile aerosol research laboratory and data processing tools for effective stationary and mobile field measurements', *Atmos. Meas. Tech.,* 5(6), pp. 1443-1457.
Ebinghaus, R., Jennings, S. G., Kock, H. H., Derwent, R. G., Manning, A. J. and Spain, T. G. (2011) 'Decreasing trends in total gaseous mercury observations in baseline air at Mace Head, Ireland from 1996 to 2009', *Atmospheric Environment,* 45(20), pp. 3475-3480.
Ehhalt, D. H. and Rohrer, F. (2009) 'The tropospheric cycle of H_2: a critical review', *Tellus B: Chemical and Physical Meteorology,* 61(3), pp. 500-535.
Fang, S. X., Tans, P. P., Steinbacher, M., Zhou, L. X. and Luan, T. (2015) 'Comparison of the regional CO_2 mole fraction filtering approaches at a WMO/GAW regional station in China', *Atmos. Meas. Tech.,* 8(12), pp. 5301-5313.

Fleming, Z. L., Monks, P. S. and Manning, A. J. (2012) 'Review: Untangling the influence of air-mass history in interpreting observed atmospheric composition', *Atmospheric Research,* 104, pp. 1-39.
Forster, G. L., Sturges, W. T., Fleming, Z. L., Bandy, B. J. and Emeis, S. (2012) 'A year of H_2 measurements at Weybourne Atmospheric Observatory, UK', *Tellus Series B-Chemical and Physical Meteorology,* 64, pp. 18.
Gras, J. and Whittlestone, S. (1992) 'Radon and CN: Complementary tracers of polluted air masses at coastal and island sites %J Journal of Radioanalytical and Nuclear Chemistry', 161(1), pp. 293-306.
Griffith, D. W. T., Deutscher, N. M., Caldow, C., Kettlewell, G., Riggenbach, M. and Hammer, S. (2012) 'A Fourier transform infrared trace gas and isotope analyser for atmospheric applications', *Atmos. Meas. Tech.,* 5(10), pp. 2481-2498.
Griffiths, A. D., Chambers, S. D., Williams, A. G. and Werczynski, S. (2016) 'Increasing the accuracy and temporal resolution of two-filter radon–222 measurements by correcting for the instrument response', *Atmos. Meas. Tech.,* 9(6), pp. 2689-2707.
Hagler, G. S. W., Thoma, E. D. and Baldauf, R. W. (2010) 'High-Resolution Mobile Monitoring of Carbon Monoxide and Ultrafine Particle Concentrations in a Near-Road Environment', *Journal of the Air & Waste Management Association,* 60(3), pp. 328-336.
Hall, B. D., Dutton, G. S. and Elkins, J. W. (2007) 'The NOAA nitrous oxide standard scale for atmospheric observations', *Journal of Geophysical Research: Atmospheres,* 112(D9).
IUPAC (1997) *Compendium of Chemical Terminology, 2nd ed. (the "Gold Book").* Compiled by A. D. McNaught and A. Wilkinson. Blackwell Scientific Publications, Oxford (1997). Online version (2019-) created by S. J. Chalk. ISBN 0-9678550-9-8. https://doi.org/10.1351/goldbook.
Janssens-Maenhout, G., Crippa, M., Guizzardi, D., Muntean, M., Schaaf, E., Dentener, F., Bergamaschi, P., Pagliari, V., Olivier, J. G. J., Peters, J. A. H. W., van Aardenne, J. A., Monni, S., Doering, U., Petrescu, A. M. R., Solazzo, E. and Oreggioni, G. D. (2019) 'EDGAR v4.3.2 Global Atlas of the three major greenhouse gas emissions for the period 1970–2012', *Earth Syst. Sci. Data,* 11(3), pp. 959-1002.
Jiang, X., Ku, W. L., Shia, R.-L., Li, Q., Elkins, J. W., Prinn, R. G. and Yung, Y. L. (2007) 'Seasonal cycle of N2O: Analysis of data', *Global Biogeochemical Cycles,* 21(1).
Jones, A., Thomson, D., Hort, M. and Devenish, B. (2007) 'The U.K. Met Office's Next-Generation Atmospheric Dispersion Model, NAME III'. *Air Pollution Modeling and Its Application XVII*. Boston, MA: Springer US, 580-589.
Jordan, A. and Steinberg, B. (2011) 'Calibration of atmospheric hydrogen measurements', *Atmos. Meas. Tech.,* 4(3), pp. 509-521.
Keeling, C. D., Bacastow, R. B., Carter, A. F., Piper, S. C., Whorf, T. P., Heimann, M., Mook, W. G. and Roeloffzen, H. (1989) 'A three-dimensional model of atmospheric CO_2 transport based on observed winds: 1. Analysis of observational data', *Aspects of Climate Variability in the Pacific and the Western Americas Geophysical Monograph Series*, pp. 165-236.
Keeling, R. F., Manning, A. C., Paplawsky, W. J. and Cox, A. C. (2007) 'On the long-term stability of reference gases for atmospheric O_2/N_2 and CO_2 measurements', *Tellus B,* 59(1), pp. 3-14.

Lallo, M., Aalto, T., Laurila, T. and Hatakka, J. (2008) 'Seasonal variations in hydrogen deposition to boreal forest soil in southern Finland', *Geophysical Research Letters,* 35(4).

Lin, J. C., Gerbig, C., Wofsy, S. C., Andrews, A. E., Daube, B. C., Davis, K. J. and Grainger, C. A. (2003) 'A near-field tool for simulating the upstream influence of atmospheric observations: The Stochastic Time-Inverted Lagrangian Transport (STILT) model', *Journal of Geophysical Research: Atmospheres,* 108(D16).

Liu, S. C., McAfee, J. R. and Cicerone, R. J. (1984) 'Radon-222 and tropospheric vertical transport', *Journal of Geophysical Research,* 89(D5), pp. 7291-7297.

Mahadevan, P., Wofsy, S. C., Matross, D. M., Xiao, X., Dunn, A. L., Lin, J. C., Gerbig, C., Munger, J. W., Chow, V. Y. and Gottlieb, E. W. (2008) 'A satellite-based biosphere parameterization for net ecosystem CO2 exchange: Vegetation Photosynthesis and Respiration Model (VPRM)', *Global Biogeochemical Cycles,* 22(2).

Manning, A. J., Redington, A. L., Say, D., O'Doherty, S., Young, D., Simmonds, P. G., Vollmer, M. K., Mühle, J., Arduini, J., Spain, G., Wisher, A., Maione, M., Schuck, T. J., Stanley, K., Reimann, S., Engel, A., Krummel, P. B., Fraser, P. J., Harth, C. M., Salameh, P. K., Weiss, R. F., Gluckman, R., Brown, P. N., Watterson, J. D. and Arnold, T. (2021) 'Evidence of a recent decline in UK emissions of hydrofluorocarbons determined by the InTEM inverse model and atmospheric measurements', *Atmos. Chem. Phys.,* 21(16), pp. 12739-12755.

Molloy, S. and Galbally, I. E. (2014) 'Analysis and Identification of a Suitable Baseline Definition of Tropospheric Ozone at Cape Grim, Tasmania ', *Baseline Atmospheric Program Australia 2009-2010*, pp. 7-16.

Parrish, D. D., Trainer, M., Buhr, M. P., Watkins, B. A. and Fehsenfeld, F. C. (1991) 'Carbon monoxide concentrations and their relation to concentrations of total reactive oxidized nitrogen at two rural U.S. sites', *Journal of Geophysical Research: Atmospheres,* 96(D5), pp. 9309-9320.

Pickers, P. A., Manning, A. C., Quéré, C. L., Forster, G. L., Luijkx, I. T., Gerbig, C., Fleming, L. S. and Sturges, W. T. (2022) 'Novel quantification of regional fossil fuel CO_2 reductions during COVID-19 lockdowns using atmospheric oxygen measurements', 8(16), pp. eabl9250.

Piotrowicz, S. R., Fischer, C. J. and Artz, R. S. (1990) 'Ozone and carbon monoxide over the North Atlantic during a boreal summer', *Global Biogeochemical Cycles,* 4(2), pp. 215-224.

Polian, G., Lambert, G., Ardouin, B., Jegou, A. J. T. B. C. and Meteorology, P. (1986) 'Long-range transport of continental radon in subantarctic and antarctic areas', 38(3-4), pp. 178-189.

Porstendoerfer, J. (1994) 'Properties and behaviour of radon and thoron and their decay products in the air', *Journal of Aerosol Science,* 25(2), pp. 219-263.

Prinn, R. G., Weiss, R. F., Arduini, J., Arnold, T., DeWitt, H. L., Fraser, P. J., Ganesan, A. L., Gasore, J., Harth, C. M., Hermansen, O., Kim, J., Krummel, P. B., Li, S., Loh, Z. M., Lunder, C. R., Maione, M., Manning, A. J., Miller, B. R., Mitrevski, B., Mühle, J., O'Doherty, S., Park, S., Reimann, S., Rigby, M., Saito, T., Salameh, P. K., Schmidt, R., Simmonds, P. G., Steele, L. P., Vollmer, M. K., Wang, R. H., Yao, B., Yokouchi, Y., Young, D. and Zhou, L. (2018) 'History of chemically and radiatively important atmospheric gases from the Advanced Global Atmospheric Gases Experiment (AGAGE)', *Earth Syst. Sci. Data,* 10(2), pp. 985-1018.

Pu, J.-J., Xu, H.-H., He, J., Fang, S.-X. and Zhou, L.-X. (2014) 'Estimation of regional background concentration of CO_2 at Lin'an Station in Yangtze River Delta, China', *Atmospheric Environment,* 94, pp. 402-408.

Rella, C. W., Chen, H., Andrews, A. E., Filges, A., Gerbig, C., Hatakka, J., Karion, A., Miles, N. L., Richardson, S. J., Steinbacher, M., Sweeney, C., Wastine, B. and Zellweger, C. (2013) 'High accuracy measurements of dry mole fractions of carbon dioxide and methane in humid air', *Atmos. Meas. Tech.,* 6(3), pp. 837-860.

Resovsky, A., Ramonet, M., Rivier, L., Tarniewicz, J., Ciais, P., Steinbacher, M., Mammarella, I., Mölder, M., Heliasz, M., Kubistin, D., Lindauer, M., Müller-Williams, J., Conil, S. and Engelen, R. (2021) 'An algorithm to detect non-background signals in greenhouse gas time series from European tall tower and mountain stations', *Atmos. Meas. Tech.,* 14(9), pp. 6119-6135.

Riddick, S. N., Mauzerall, D. L., Celia, M., Harris, N. R. P., Allen, G., Pitt, J., Staunton-Sykes, J., Forster, G. L., Kang, M., Lowry, D., Nisbet, E. G. and Manning, A. J. (2019) 'Methane emissions from oil and gas platforms in the North Sea', *Atmos. Chem. Phys.,* 19(15), pp. 9787-9796.

Ruckstuhl, A. F., Henne, S., Reimann, S., Steinbacher, M., Vollmer, M. K., O'Doherty, S., Buchmann, B. and Hueglin, C. (2012) 'Robust extraction of baseline signal of atmospheric trace species using local regression', *Atmos. Meas. Tech.,* 5(11), pp. 2613-2624.

Ruckstuhl, A. F., Unternaehrer, T. and Locher, R. (2020) 'IDPmisc: Utilities of Institute of Data Analyses and Process Design (www.zhaw.ch/idp)' (Version R package version 1.1.20). Available at: https://cran.r-project.org/web/packages/IDPmisc/index.html (Accessed: 18/08/2022).

Schmithüsen, D., Chambers, S., Fischer, B., Gilge, S., Hatakka, J., Kazan, V., Neubert, R., Paatero, J., Ramonet, M., Schlosser, C., Schmid, S., Vermeulen, A. and Levin, I. (2017) 'A European-wide ^{222}radon and ^{222}radon progeny comparison study', *Atmos. Meas. Tech.,* 10(4), pp. 1299-1312.

Simmonds, P. G., Derwent, R. G., O'Doherty, S., Ryall, D. B., Steele, L. P., Langenfelds, R. L., Salameh, P., Wang, H. J., Dimmer, C. H. and Hudson, L. E. (2000) 'Continuous high-frequency observations of hydrogen at the Mace Head baseline atmospheric monitoring station over the 1994–1998 period', 105(D10), pp. 12105-12121.

Steinbacher, M., Fischer, A., Vollmer, M. K., Buchmann, B., Reimann, S. and Hueglin, C. (2007) 'Perennial observations of molecular hydrogen (H_2) at a suburban site in Switzerland', *Atmospheric Environment,* 41(10), pp. 2111-2124.

Stohl, A. (1998) 'Computation, accuracy and applications of trajectories—A review and bibliography', *Atmospheric Environment,* 32(6), pp. 947-966.

Thoning, K. W., Tans, P. P. and Komhyr, W. D. (1989) 'Atmospheric carbon dioxide at Mauna Loa Observatory: 2. Analysis of the NOAA GMCC data, 1974–1985', *Journal of Geophysical Research: Atmospheres,* 94(D6), pp. 8549-8565.

Trisolino, P., di Sarra, A., Sferlazzo, D., Piacentino, S., Monteleone, F., Di Iorio, T., Apadula, F., Heltai, D., Lanza, A., Vocino, A., Caracciolo di Torchiarolo, L., Bonasoni, P., Calzolari, F., Busetto, M. and Cristofanelli, P. (2021) 'Application of a Common Methodology to Select in Situ CO_2 Observations Representative of the Atmospheric Background to an Italian Collaborative Network', *Atmosphere,* 12(2).

Vardag, S. N., Gerbig, C., Janssens-Maenhout, G. and Levin, I. (2015) 'Estimation of continuous anthropogenic CO_2: model-based evaluation of CO_2, CO,' *Atmospheric Chemistry and Physics,* 15(22), pp. 12705-12729.

Weiss, R. F. and Prinn, R. G. (2011) 'Quantifying greenhouse-gas emissions from atmospheric measurements: a critical reality check for climate legislation', *Philosophical Transactions of the Royal Society A: Mathematical, Physical and Engineering Sciences,* 369(1943), pp. 1925-1942.

Whittlestone, S. and Zahorowski, W. (1998) 'Baseline radon detectors for shipboard use: Development and deployment in the First Aerosol Characterization Experiment (ACE 1)', *Journal of Geophysical Research: Atmospheres,* 103(D13), pp. 16743-16751.

Williams, A. G., Chambers, S. and Griffiths, A. (2013) 'Bulk Mixing and Decoupling of the Nocturnal Stable Boundary Layer Characterized Using a Ubiquitous Natural Tracer', *Boundary-Layer Meteorology,* 149(3), pp. 381-402.

Zahorowski, W., Chambers, S. D. and Henderson-Sellers, A. (2004) 'Ground based radon-222 observations and their application to atmospheric studies', *J Environ Radioact,* 76(1-2), pp. 3-33.

Zanis, P., Ganser, A., Zellweger, C., Henne, S., Steinbacher, M. and Staehelin, J. (2007) 'Seasonal variability of measured ozone production efficiencies in the lower free troposphere of Central Europe', *Atmos. Chem. Phys.,* 7(1), pp. 223-236.

Zellweger, C., Forrer, J., Hofer, P., Nyeki, S., Schwarzenbach, B., Weingartner, E., Ammann, M. and Baltensperger, U. (2003) 'Partitioning of reactive nitrogen (NOy) and dependence on meteorological conditions in the lower free troposphere', *Atmos. Chem. Phys.,* 3(3), pp. 779-796.

Zhao, C. L. and Tans, P. P. (2006) 'Estimating uncertainty of the WMO mole fraction scale for carbon dioxide in air', *Journal of Geophysical Research: Atmospheres,* 111(D8).

Chapter 4 High-precision measurements of atmospheric CO_2 isotopologues at Weybourne Atmospheric Observatory using an 'Aerodyne' TILDAS

4.1 Introduction

Anthropogenic emissions of CO_2 are the most important contributor to global climate change (IPCC, 2021a). Therefore, a quantitative understanding of the carbon cycle, and the source and sink processes which govern it, are crucial for assessing the radiative forcing effects of ongoing anthropogenic emissions. A number of supporting measurements that provide additional information on sources and sinks are used to disentangle carbon cycle processes, so called 'tracer' methods. The stable isotopic composition of atmospheric CO_2 is one such tracer method.

Stable isotopes are non-radioactive forms of an atom which differ only in their number of neutrons, and therefore atomic mass. These mass differences cause fractionation of the molecules during different formation, transport, and removal processes, where the abundance of one isotope becomes enriched relative to another (Affek and Yakir, 2014). Therefore, the measurement of the isotopic composition of CO_2 can be used as a tool to distinguish between anthropogenic and biospheric fluxes (e.g. Pataki et al., 2003a; Zhou et al., 2005; Laskar et al., 2016) and can provide information about the size of carbon fluxes between the atmosphere, terrestrial biosphere, and oceans.

Table 4.1. Natural abundances of the distinct, stable CO_2 isotopologues (Eiler and Schauble, 2004)

Mass	Isotopologue	Abundance fraction of CO_2
44	$^{16}O^{12}C^{16}O$	98.4 %
45	$^{16}O^{13}C^{16}O$	1.1 %
	$^{17}O^{12}C^{16}O$	760 ppm
46	$^{18}O^{12}C^{16}O$	0.41 %
	$^{17}O^{13}C^{16}O$	8.5 ppm
	$^{17}O^{12}C^{17}O$	150 ppb
47	$^{18}O^{13}C^{16}O$	46 ppm
	$^{18}O^{12}C^{17}O$	1.6 ppm
	$^{17}O^{13}C^{17}O$	1.6 ppb
48	$^{18}O^{12}C^{18}O$	4.3 ppm
	$^{17}O^{13}C^{18}O$	18 ppb
49	$^{18}O^{13}C^{18}O$	48 ppb

Carbon has two naturally occurring stable isotopes, ^{12}C and ^{13}C, and oxygen has three, ^{16}O, ^{17}O, and ^{18}O; with the heavier isotopes being rarer (1.1 % for ^{13}C, 0.2

% for ^{18}O, and 0.04 % for ^{17}O; Affek and Yakir (2014)). Considering this, there are eighteen possible isotopologues of CO_2, with only 12 of these being distinct due to symmetry (Table 4.1). Each of these 12 isotopologues has its own distinct thermodynamic and kinetic properties which cause them to fractionate from one another during natural processes (Eiler and Schauble, 2004); these properties mean that measurement of the different isotopologues can be used to investigate these processes.

The $^{13}C/^{12}C$ isotope ratio of atmospheric CO_2 (denoted $\delta^{13}C$) has widely been utilised as a tracer for partitioning the sources and sinks of CO_2 between the ocean, terrestrial biosphere and fossil fuels (e.g. Ciais et al., 1995; Battle et al., 2000; Miller et al., 2003b; Pataki et al., 2003b; Ciais et al., 2005; Keeling et al., 2017; Graven et al., 2020). Photosynthesis and respiration impart distinct isotopic signatures to the atmosphere: during photosynthesis, terrestrial plants preferentially assimilate ^{12}C-CO_2, thereby enriching the $\delta^{13}C$ content of the CO_2 remaining in the atmosphere (Flanagan and Ehleringer, 1998). The reverse is the case for respiration which depletes the $\delta^{13}C$ content of the atmosphere. Fossil fuels originate from plant materials, therefore the preferential uptake of ^{12}C-CO_2 during photosynthesis means that they are depleted in ^{13}C-CO_2 relative to the atmosphere. Fossil fuel emissions therefore dilute the atmospheric $\delta^{13}C$ value (Keeling et al., 2017). Moreover, net uptake of CO_2 from the atmosphere into the ocean leaves the atmospheric $\delta^{13}C$ essentially unchanged. These distinct signatures can thus be used to constrain global carbon sources and sinks. The use of $\delta^{13}C$ does have limitations as a tracer for identifying sources, for example, both petroleum combustion and plant respiration have similar isotopic source signatures. Natural gas also has a varying source signature according to the supply location which can introduce errors into estimates (Lopez et al., 2013), thus additional constraints are required.

In addition to the carbon isotopes of CO_2, the naturally occurring stable isotopes of oxygen can also be used as useful carbon cycle tracers. As with carbon, the relative isotopic composition of oxygen-containing molecules on Earth is affected by processes such as diffusion, evaporation, and condensation. These processes typically depend on the mass of the molecules and therefore result in mass-dependent fractionation of the oxygen isotopes.

The ratio of $^{18}O/^{16}O$ (denoted $\delta^{18}O$) of CO_2 has been widely used to estimate gross carbon fluxes between the atmosphere and the terrestrial biosphere (e.g. Yakir and Wang, 1996; Ciais et al., 1997). As the $\delta^{18}O$ of atmospheric CO_2 is controlled largely by isotopic exchange with water in the leaves of plants, it is an important tool to estimate global primary production (GPP; the gross CO_2 uptake of plants from photosynthesis)(Francey and Tans, 1987). During CO_2 exchange with leaf, soil, and ocean water, the ^{18}O isotopes of CO_2 are exchanged with those of water. Stomatal water in plant leaves is highly enriched in ^{18}O relative to soil water, due to mass-dependent fractionation during evapotranspiration, which imparts contrasting $\delta^{18}O$ signatures in CO_2 released into the atmosphere after CO_2-H_2O exchange (e.g. Cuntz et al., 2003; Barthel et al., 2014). Furthermore, the equilibration and isotope exchange of CO_2 with water in stomata is catalysed by the presence of carbonic anhydrase, which extensively enriches the CO_2 released from plants with ^{18}O from leaf-water. This isotope exchange process can therefore be directly related to gross primary production as first suggested by Farquhar et al. (1993). The difficulty with using ^{18}O-CO_2 to determine GPP is the requirement for a detailed knowledge of $\delta^{18}O$ values for numerous water reservoirs, which can be highly variable due to the number of processes involved in the hydrological cycle. The addition of ^{17}O-CO_2 measurements can remove this requirement (Hoag et al., 2005). Due to mass-dependent fractionation, variations in ^{17}O are strongly correlated to variations in ^{18}O, with any deviation from this correlation (i.e. mass independent fractionation) being expressed as the $\Delta^{17}O$ signature (referred to as the 'triple oxygen isotope', 'CO_2 excess', or 'O_2 anomaly') (see section 4.3.1 for the formal definition).

The processes which affect the isotopic composition of CO_2 usually depend on the mass of the molecules and therefore result in mass-dependent fractionation of the oxygen isotopes. An exception, however, is that compared to tropospheric CO_2, stratospheric CO_2 is anomalously enriched in ^{17}O and ^{18}O (e.g. Thiemens et al., 1991; Lämmerzahl et al., 2002; Yeung et al., 2009). This is linked to mass-independent fractionation of CO_2 during the formation of O_3, which imparts a positive $\Delta^{17}O$ signature (Yung et al., 1991). This enriched stratospheric CO_2 is transported into the upper troposphere (Laskar et al., 2019), where it mixes and comes into contact with water reservoirs in vegetation, soil, and oceans. When CO_2 dissolves in liquid water, there is a mass-dependent exchange of oxygen atoms,

meaning that the $\Delta^{17}O$ signature of the CO_2 released back into the atmosphere is reset to around 0 ‰ (Hoag et al., 2005). As a consequence, variations in the tropospheric $\Delta^{17}O$ signature strongly depend on the magnitude of CO_2 exchange with the leaf water reservoir and can therefore be directly related to biospheric activity (Hoag et al., 2005). However, unlike using $\delta^{18}O$ alone, $\Delta^{17}O$ does not directly depend on the ^{18}O or ^{17}O of soil and leaf water since hydrological cycle processes are largely mass dependent (Hoag et al., 2005). $\Delta^{17}O$ should therefore be a more direct tracer for GPP than variations in $^{18}O/^{16}O$ alone. A schematic summary of the processes affecting the $\Delta^{17}O$ signature of atmospheric CO_2 is displayed in Figure 4.1.

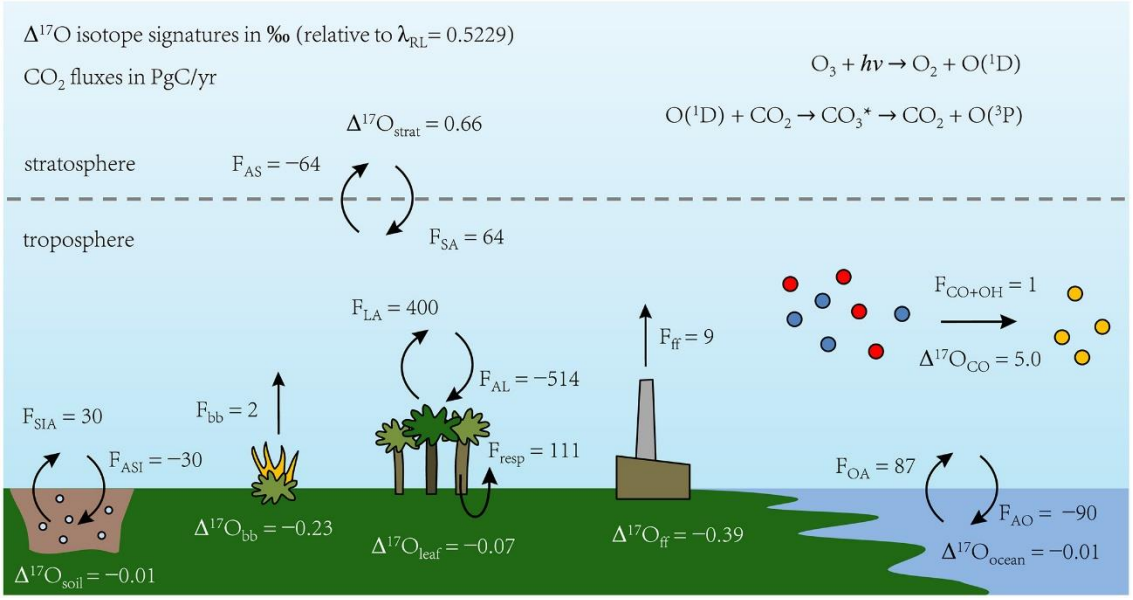

Figure 4.1. Schematic summary of the processes affecting the $\Delta^{17}O$ signature of atmospheric CO_2 as reported by Koren et al. (2019). The CO_2 mass fluxes (F) are global integrated values averaged over 2012-2013 and rounded to integers. CO_2 mass fluxes that increase that tend to increase the tropospheric CO_2 mass are expressed as positive numbers. F_{AS}/F_{SA} is atmosphere (troposphere)-stratosphere exchange; F_{AL}/F_{LA} is atmosphere-leaf exchange; $F_{ASI/SIA}$ is atmosphere-soil exchange; F_{OA} is ocean-atmosphere exchange; and F_{bb} is flux from biomass burning. Figure taken from Koren et al. (2019).

To date, there have been very few published concurrent measurements of $\delta^{13}C$, $\delta^{18}O$, and $\delta^{17}O$, and the subsequent calculation of $\Delta^{17}O$ in the troposphere. Barkan and Luz (2012) presented the first high-precision data on the $\Delta^{17}O$ composition of tropospheric CO_2 from a limited set of flask samples in Spring 2012 in Jerusalem, Israel. Next, Thiemens et al. (2014) presented a decade-long time series of $\Delta^{17}O$ values from flask samples in La Jolla, California. These measurements identified a stratospheric component in tropospheric CO_2, and

discussed the role of El Niño Southern Oscillation indices in tropospheric excursions. They also noted the need for extended global measurements of $\delta^{17}O$ and $\delta^{18}O$ for analysis of $\Delta^{17}O$ in order to further the understanding of these and other processes which influence the carbon cycle. Liang and Mahata (2015) presented the $\Delta^{17}O$ in the troposphere from a total of 81 near-surface samples taken over one year in Taipei, Tiawan, demonstrating that $\Delta^{17}O$ in CO_2 is observable at sea level. More recently, Hofmann et al. (2017) presented high-precision $\Delta^{17}O$ values in tropospheric CO_2 from Göttingen, Germany from air samples taken over the course of two years; demonstrating that observations of $\Delta^{17}O$ captures the seasonal variability in GPP. Koren et al. (2019) presented the first global 3D $\Delta^{17}O$ model, which was used to predict the global signature, seasonal cycle, and vertical and latitudinal gradients. They also suggested that observational time series of $\Delta^{17}O$ could help to further increase understanding of the global $\Delta^{17}O$ budget of tropospheric CO_2.

One of the most challenging aspects of using $\Delta^{17}O$ to better understand GPP is the extremely high measurement precision and accuracy that is needed for both ^{17}O and ^{18}O to be able to define spatial gradients and seasonal cycles of $\Delta^{17}O$. For example, Hofmann et al. (2017) states that a measurement precision of ± 0.01 ‰ (10 per meg) or better would be required to capture seasonal variations and for $\Delta^{17}O$ to be useful as a tracer for GPP. Studies of $\Delta^{17}O$ in CO_2 have in the past been limited by the precision of the measurements and limitations in technology. Historically, high-precision measurements of stable isotopes have been done using isotope ratio mass spectrometry (IRMS), which requires the extraction of CO_2 from an air sample before analysis. This extraction process is not only time-consuming but is also a major contributor of scale differences between labs. Further, due to $^{16}O^{13}C^{16}O$ and $^{17}O^{12}C^{16}O$ having the same atomic mass, IRMS techniques are sensitive to isobaric interference therefore, determination of $\delta^{17}O$ in a sample is extremely complex and limited to only a few laboratories (see Adnew et al., 2019). In recent years there have been a number of developments in optical spectroscopy measurement techniques for $\Delta^{17}O$, increasing the precision of measurements (e.g. Barkan and Luz, 2012; Mahata et al., 2016; Adnew et al., 2019). Furthermore, high-precision measurements of $\Delta^{17}O$ in whole air samples have been made possible with the development of new analysers which use optical spectroscopy, with precision close to, or exceeding, IRMS measurements (McManus et al., 2015;

Stoltmann et al., 2017); this also means that air can be measured continuously, rather than from discrete samples. As well as removing the need for extraction of CO_2 from an air sample, optical spectroscopy is also free of isobaric interferences as the individual isotopologues are directly measured; it is therefore possible to directly measure $\delta^{17}O$ in addition to $\delta^{13}C$ and $\delta^{18}O$.

In this chapter, I present concurrent measurements of $\delta^{13}C$, $\delta^{17}O$ and $\Delta^{17}O$ using new state-of-the-art technology from Aerodyne Research Inc., a tunable infrared laser direct adsorption spectroscopy (TILDAS) CO_2 isotopologue analyser, collecting in-situ continuous data from the Weybourne Atmospheric Observatory (WAO; see Chapter 1.4 for a WAO site description). These data are calibrated using two different methodologies, and the resulting values are compared. The repeatability and compatibility are then investigated. These analyses are then contextualised with respect to the observed seasonality in the observations.

4.2 Aerodyne TILDAS dual-laser trace gas analyser

Measurements of $\delta^{13}C$, $\delta^{17}O$, and $\delta^{18}O$, at the Weybourne Atmospheric Observatory (WAO) are performed using a tunable infrared laser direct adsorption spectroscopy (TILDAS) dual-laser CO_2 analyser, designed and manufactured by Aerodyne Research, Inc. (ARL, Billerica, MA, USA) (McManus et al., 2015). The TILDAS analyser has been running at WAO since September 2021.

The TILDAS analyser measures the individual absorption lines of $^{12}C^{16}O^{16}O$, $^{13}C^{16}O^{16}O$, $^{12}C^{16}O^{18}O$ and $^{12}C^{16}O^{17}O$, which are referred to as 626, 636, 628, and 627, respectively, following the HITRAN database notation (Gordon et al., 2017). Two mid-infrared interband-cascade lasers (Nanoplus Nanosystems and Technologies, GmbH) are used, which operate at wavelengths of 2310 cm^{-1} targeted at 626, 628 and 636, and 2349 cm^{-1} targeted at 627 (and 626) (Hare et al., 2022). The total path length of the lasers in the optical cell is 36 m, which is depicted in Figure 4.2. To avoid absorption by CO_2 other than from gas in the optical cell, the optical cell and detectors are contained within a casing that is continually flushed with nitrogen (N_2) at a flow rate of several litres per minute. The lasers and data acquisition of the absorption spectra are controlled by 'TDLWintel' software, (McManus et al., 2015), which produces isotopologue mole

fractions at a frequency of 1 Hz. An extended description of the operating principles can be found in McManus et al. (2015).

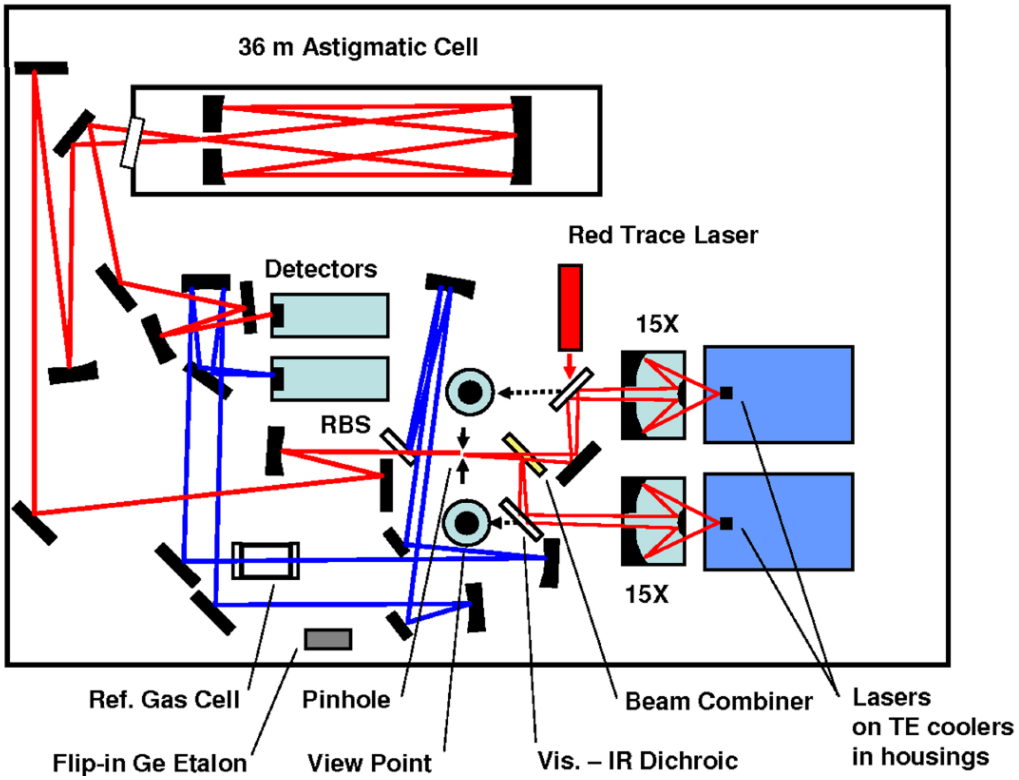

Figure 4.2. Diagram of the optical layout of the Aerodyne Research, Inc. TILDAS instrument. The main sample beam path is coloured in red, which passes through a 36 m absorption cell. The reference beam path, which splits into two, is shown in blue. One reference beam path contains a short reference gas cell and the other contains an etalon that may be flipped into the beam for measurement of laser tuning rates. Figure is from McManus et al. (2015) and Steur et al. (2021).

4.2.1 Gas handling setup at WAO

The gas handling setup of the TILDAS analyser at WAO is shown in Figure 4.3, and is set up to measure continuous sample air flow. Calibration is performed with four calibration standards (see section 4.2.4), and a target tank (TT) is run regularly to quality check the performance of the analyser. A reference tank (RT) is also run, before and after every sample measurement, which reduces variations due to analyser baseline drift.

The sample air is drawn in from a mast 10 m above ground level (20 m a.s.l.) at a flow rate of 150 ml/min (controlled by a mass flow controller; 'MFC' in Figure 2) and first passes through a switchable chiller at ~-30°C to dry the air, before entering a 50 ml intermediate volume (V2; Figure 4.3). The intermediate volume (V2) is filled with sample air until it reaches a pressure of 270 torr. At that

point the inlet volume is isolated via the automated actuated valves before being injected into the sample cell (by opening V18 and V21; Figure 4.3). Prior to injection, the sample cell is fully evacuated to 0 torr; the sample is then expanded into the optical cell to a pressure of 40 torr. V21 and V22 are closed while the sample is analysed. While sample air is being analysed in the sample cell, the inlet volume is simultaneously filled with gas from the RT (by opening V16 and V10). After measuring the sample air for 2 minutes the TILDAS cell is evacuated to 0 torr again, and the RT gas is then injected into the TILDAS cell for measurement while the inlet volume is again filled with sample air. Measurements continually alternate between RT and sample every 2 minutes; this switching sequence is analogous to that used in dual-inlet IRMS measurements. Similarly, when measuring the calibration standards, these are also alternated every 2 minutes with measurement of the RT. The 2-minute switching time was chosen as the result of an Allan variance test on the raw 1 second data. As the calibration standards and RT share tubing into the inlet volume, this is evacuated (by opening V14) before switching between gas measurements to avoid contamination from any gas remaining in this dead volume (Figure 4.3). The temperature of the TILDAS optics box is regulated using an Oasis chiller, which circulates fluid at a constant temperature of 296 K around the lasers.

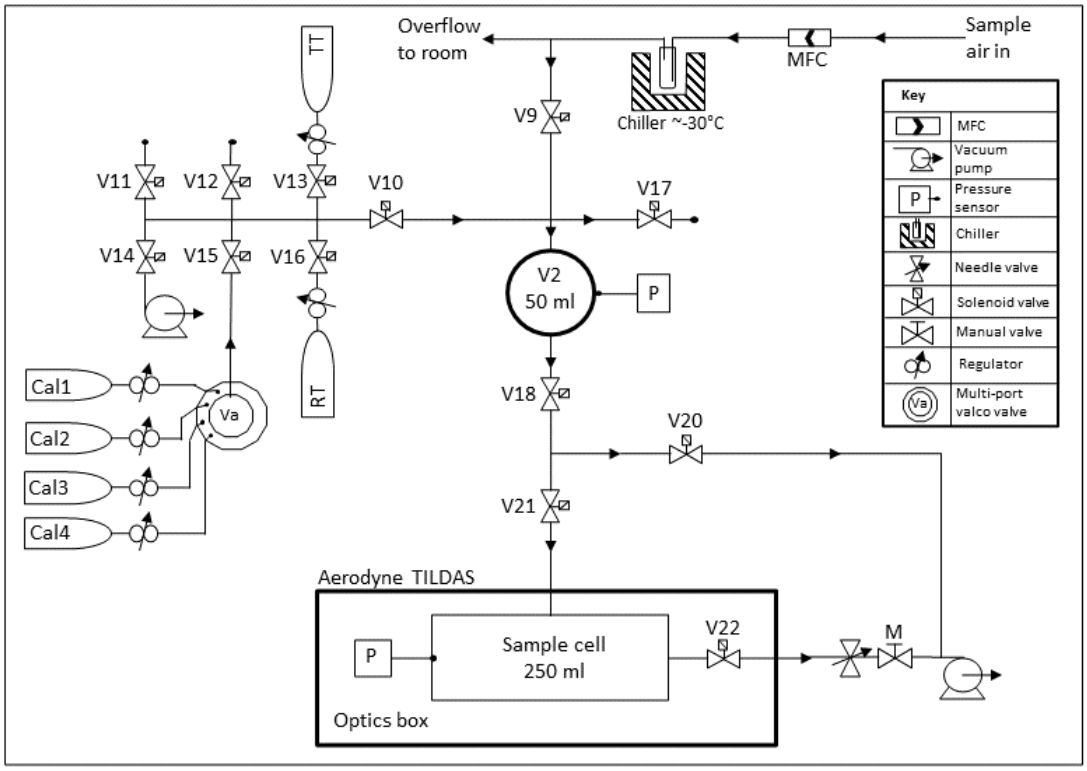

Figure 4.3. Gas handling diagram for the Aerodyne TILDAS at Weybourne Atmospheric Observatory. Custom scripts have been written for the TDLWintel software to achieve the routine and repeated analyses of sample air, reference tank (RT), calibration standards (Cal1 - Cal4) and a quality control target tank (TT) as described in the text.

4.3 Isotope notation

Of the 12 distinct isotopologues of CO_2 and assuming the substitution of each isotope at each position in the molecule follows its bulk statistical abundance (i.e. no clumping, where the CO_2 molecule contains two minor isotopes), only 4 independent quantities are required to define the total amount and full isotopic composition of CO_2 (Griffith, 2018). These quantities are the total amount of CO_2 and the $^{13}C/^{12}C$, $^{17}O/^{16}O$, and $^{18}O/^{16}O$ isotopic ratios.

Since routine measurements of absolute isotopic concentrations are very difficult, results are obtained from relative measurements and expressed as the ratio, *r*, of the rare to the abundant isotope (Eqs. (4.1), (4.2), and (4.3)) (Griffith, 2018).

$$^{13}r = \frac{n(^{13}C)}{n(^{12}C)} \qquad (4.1)$$

$$^{17}r = \frac{n(^{17}O)}{n(^{16}O)} \qquad (4.2)$$

$$^{18}r = \frac{n(^{18}O)}{n(^{16}O)} \qquad (4.3)$$

where n() is the number of moles of each isotope in a sample. In addition, isotope ratios are typically referred to using delta notation which expresses the variation of an isotope ratio of an element, relative to a standard on the Vienna Pee Dee Belemnite scale (VPDB-CO_2) that is assumed to have a constant and known isotope ratio. This delta notation reduces variations due to analyser baseline drift. For the three isotopologues discussed in this chapter, the delta notation is defined as follows and expressed in 'per mil' (‰) units (Griffith, 2018):

$$\delta^{13}C = \frac{(^{13}r)_{sample} - (^{13}r)_{ref}}{(^{13}r)_{ref}} \cdot 1000\ ‰ \qquad (4.4)$$

$$\delta^{17}O = \frac{(^{17}r)_{sample} - (^{17}r)_{ref}}{(^{17}r)_{ref}} \cdot 1000\ ‰ \qquad (4.5)$$

$$\delta^{18}O = \frac{(^{18}r)_{sample} - (^{18}r)_{ref}}{(^{18}r)_{ref}} \cdot 1000\ ‰ \qquad (4.6)$$

4.3.1 $\Delta^{17}O$ notation

The isotopic composition of CO_2 is altered by many processes which depend upon the mass of the molecules and therefore result in mass-dependent fractionation (Brenninkmeijer et al., 2003). $\delta^{17}O$ and $\delta^{18}O$ in CO_2 thus typically follow the mass dependent relationship as defined by Eq. (4.7) from a three oxygen $\delta^{17}O$/ $\delta^{18}O$ isotope plot.

$$\delta^{17}O = \lambda_{RL} \times \delta^{18}O \quad (4.7)$$

which is referred to as the 'reference line', and where λ_{RL} is the slope of the reference line. If we are interested in pure mass-dependent fractionation, we choose, λ_{RL} is 0.5, representing the fact that the mass difference between isotopes ^{17}O and ^{16}O is half of the mass difference between the isotopes ^{18}O and ^{16}O. $\Delta^{17}O$ is defined as any deviation from this mass dependent fractionation reference line, as defined by Eq. (4.8), using the logarithmic definition and shown schematically in Figure 4.4 (Miller, 2002; Young et al., 2002).

$$\Delta^{17}O = \ln(\delta^{17}O + 1) - \lambda_{RL} \times \ln(\delta^{18}O + 1) \qquad (4.8)$$

$\Delta^{17}O$ data are normally expressed in per mil (‰), or per meg (0.001 ‰) units, depending on the size of the $\Delta^{17}O$ signature, and λ_{RL} is the slope of the reference line (Eq (4.7)). As well as this 'logarithmic definition' of $\Delta^{17}O$, there is also an 'exponential definition' (e.g., Assonov and Brenninkmeijer, 2005) and a

'linear definition' (e.g. Hoag et al., 2005), which you can convert between (Koren et al., 2019). Each form of this definition is suited to a specific research problem; in most older studies the linear definition was commonly used, whereas more recent studies of $\Delta^{17}O$ in CO_2 use the logarithmic definition (e.g. Hofmann et al., 2017; Koren et al., 2019).

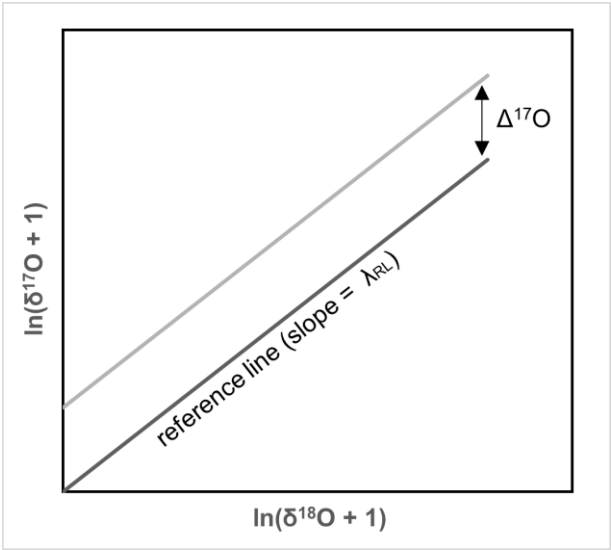

Figure 4.4. Schematic representation of an oxygen three isotope plot.

In addition to the different forms of Eq. (4.8) used to define $\Delta^{17}O$, there are also a number of different values used for λ_{RL} in the published literature, which are representative of different fractionation processes and therefore chosen based on the aim of the research. In essence, mass-independent fractionation of CO_2 occurs from photochemical reactions in the stratosphere involving O_3 and $O(^1D)$. In the troposphere, this mass-independent fractionation of oxygen atoms in CO_2 is mostly, but not entirely, cancelled out by mass-dependent exchange of oxygen between CO_2 and H_2O in leaves. In some applications, $\lambda_{RL} = 0.528$ has been used, which is equal to the both the isotopic composition of precipitation water (Landais et al., 2006) and the VSMOW-SLAP reference line which is linked to two international water standards (Barkan and Luz, 2012); $\lambda_{RL} = 0.525$ has also been used, based on the isotopic composition of rocks and minerals (e.g. Hofmann and Pack, 2010; Hofmann et al., 2012); $\lambda_{RL} = 0.5305$ is defined from the equilibrium end member for isotopic fractionation at high temperatures (e.g. Pack and Herwartz, 2014; Gehler et al., 2016); and $\lambda_{RL} = 0.516$ is representative of the isotopic composition of tropospheric CO_2 entering the stratosphere (e.g. Boering et al., 2004; Liang and Mahata, 2015). In this chapter, $\lambda_{RL} = 0.5229$ is used, based on the

CO_2-water equilibrium fractionation factor (e.g. Barkan and Luz, 2012; Hofmann et al., 2017; Koren et al., 2019), and has been widely used in the published literature (e.g. Hofmann et al., 2017; Koren et al., 2019). It should be noted that although there is no agreed value for the reference line, the choice is somewhat arbitrary since $\Delta^{17}O$ is calculated from $\delta^{17}O$ and $\delta^{18}O$ measurements and is not itself a measured quantity (Pack and Herwartz, 2014).

4.4 Calibration

4.4.1 Calibration methods

There are two methods which can be used for calibration of an isotopologue analyser, in brief these are: (1) calculate the delta values and then calibrate (isotopologue ratio method (RM); see section 4.2.4.1) or (2) calibrate the individual isotopologue mole fractions and then calculate the isotopologue ratios (isotopologue abundance method (AM); see section 4.2.4.2).

The RM is similar to the methods developed for the calibration of traditional IRMS based analysers. This method uses calibration standards which cover a range of delta values and directly determines calibration equations in terms of these delta values (Griffith, 2018). However, this method of calibration introduces a CO_2 mole fraction dependence (CMFD) in the calibration equations which needs to be accounted for (Griffith, 2018). The AM is more fundamental for optical analysers (such as the TILDAS) as they are measuring the amounts of the individual isotopes; therefore, the AM is a natural choice of calibration method for such analysers (Griffith, 2018). Additionally, as each isotopologue is calibrated separately the introduced CMFD does not need to be accounted for (Griffith, 2018; Steur et al., 2021). In this chapter, the data collected at WAO has been calibrated using both methods, which will then be compared.

For both calibration methods, 4 calibration standards were run on the TILDAS. The CO_2 mole fraction is defined on the WMO-X2019 scale, the $\delta^{13}C$ and $\delta^{18}O$ values of these standards are defined on the VPDB-CO_2 scale (Table 4.2). They were assigned at the ICOS Flask and Calibration Laboratory, hosted by the Max Planck Institute for Biogeochemistry in Jena. The $\delta^{17}O$ value of the calibration

standards is unknown but is calculated using the mass dependent fractionation relationship with $\delta^{18}O$, where $\delta^{17}O = 0.528*\delta^{18}O$ (Brand et al., 2010; Griffith, 2018).

Table 4.2. CO_2, $\delta^{13}C$ and $\delta^{18}O$ assigned values of the four calibration standards used for calibration of the TILDAS at WAO.CO_2 is reported on the WMO-X2019 and the isotopologues areon the VPDB-CO_2 scale. Note that the $\delta^{17}O$ value of these cylinders is calculated from $\delta^{17}O=0.528*\delta^{17}O$.

Cylinder ID	CO_2 (ppm)	$\delta^{13}C$ (‰)	$\delta^{18}O$ (‰)	$\delta^{17}O$ (‰)
D251500	372.097	-8.3	-13.59	-7.18
D251502	400.195	-9.05	-3.04	-1.61
D251503	418.961	-9.58	-2.18	-1.15
D477509	499.907	-10.9	-3.04	-1.61

A calibration of the analyser was performed on 21Jun2022 and applied to all data presented in this chapter (14Sep2021 to 12Oct2022). The measurement of the calibration standards for both the RM and AM follows the same procedure outlined in section 3.2.1 for sample measurement. Measurement of the calibration standard and RT is alternated every 2 minutes allowing for drift correction of the measurement value as in Eqs. (4.4)-(4.6).

4.4.1.1 Isotopologue ratio method calibration

In the isotopologue ratio method calibration (RM), isotopologue ratios are used to calculate the delta values, defined on the VPDB-CO_2 scale by the 4 calibration standards. This method was originally developed for the calibration of measurements made using IRMS analysers. The method outlined here follows that of Griffith (2018) and Steur et al. (2021).

First, the uncalibrated measured delta values (δ^*_m) are calculated from the 2-minute calibration standard (r_{*m}) and linearly interpolated 2-minute raw RT (r_{*RT}) isotopologue ratios, which corrects for short-term analyser drift:

$$\delta^*_m = \left(\frac{{}^*r_m}{{}^*r_{RT}} - 1\right) \qquad (4.9)$$

where * denotes the isotopologue being calibrated (i.e., 636, 627, or 628). Next, these 2-minute uncalibrated δ^*_m values are averaged for each calibration standard and linearly regressed against the assigned delta values of each standard (δ^*_a) (Table 4.2) and a linear fit is added. As delta values of each isotopologue in the RT (δ^*_{RT}) on the VPDB-CO_2 scale are unknown, these are then determined from the y-axis intercept. This can be assumed as if the RT were to be measured against

itself then δ^*_m would be zero (from Eq. (4.9)), thus δ^*_a would equal the y-axis intercept. The $\delta^{13}C$, $\delta^{18}O$, and $\delta^{17}O$ sample measurements (δ^*_{sam}) are then calibrated (δ^*_{cal}) based on these δ^*_{RT} values:

$$\delta^*_{cal} = (1 + \delta^*_{RT}) \cdot \delta^*_{sam} + \delta^*_{RT} \qquad (4.10)$$

where δ^*_{sam} is calculated for each isotope using Eqs. (4.4), (4.5), and (4.6). The CO_2 mole fraction is then calibrated with a linear calibration curve calculated by fitting the assigned CO_2 mole fraction of the calibration standards against the measured mole fractions and applying this to the raw measured air sample measurements.

As this RM of calibration has historically been used to calibrate mass spectrometers, an important consideration for calibration of spectroscopic analysers, such as the TILDAS, when using the RM is the concentration dependence of the measured isotope ratios (and therefore delta values) on the mole fraction of CO_2. This CO_2 mole fraction dependency (CMFD) must be corrected for as part of the calibration procedure (Griffith, 2018). CMFD from ratio calibration methods have been published in a number of papers (e.g. Griffith et al., 2012; Wen et al., 2013; Rella et al., 2015; Pang et al., 2016; Steur et al., 2021). A non-zero y-axis intercept in the relationship between the measured and assigned values of the calibration standards is indicative of CMFD(Griffith, 2018). A non-zero intercept results in an approximate inverse relationship between the measured $\delta^{13}C$ and the CO_2 mole fraction (Griffith et al., 2012). Even if the concentration dependence is small, this can be amplified in Keeling plot-type analyses (Wen et al., 2013).

In order to correct for this, first Eq. (4.10) is applied to the δ^*_S values calculated from Eq. (4.9) to produce calibrated values for each calibration standard measurement for each isotopologue. The residual of each calibration standard from the assigned delta value on the VPDB scale (calibrated δ^*_S – assigned δ^*_S), including a residual of 0 for the RT, are then plotted against the CO_2 mole fractions assigned for each standard, and a quadratic fit is produced. This equation is then subtracted from the calibrated sample from Eq. (4.10) to correct for any CMFD as follows:

$$\delta^*_{VPDB} = \delta^*_{cal} - ((d \cdot [CO_2]^2) + (e \cdot [CO_2]) + f) \qquad (4.11)$$

where δ^*_{VPDB} is the final air sample isotope delta value on the VPDB-CO_2 scale, $[CO_2]$ is the calibrated CO_2 mole fraction of the air sample, and δ^* is the

calibrated isotopologue values obtained from Eq. (4.10). Finally, $\Delta^{17}O$ is calculated from $\delta^{17}O$ and $\delta^{18}O$ using Eq. (4.8).

4.4.1.2 Isotopologue abundance method calibration

In short, the isotopologue abundance method (AM) calibrates each CO_2 isotopologue abundance (y) individually as if they were separate species, and then uses these values to calculate the isotope ratios and delta values. The method outlined here follows that of Griffith (2018) and Steur et al. (2021).

First, the isotope ratios of each calibration standard, ${}^{13}r$, ${}^{18}r$ and ${}^{17}r$ (${}^{*}r$), are calculated from the assigned delta values, through inverting Eqs. (4.4), (4.5), and (4.6), i.e.:

$$ {}^{*}r = (1 + \delta^{*}) \cdot {}^{*}r_{VPDB} \qquad (4.12) $$

where δ^* is the assigned delta value of the calibration gas (Table 4.2) and r_{VPDB} is the standard isotope ratio on the VPDB-CO_2 reference scale (Table 4.3).

Table 4.3. Standard isotope ratios for the VPDB-CO_2 reference scale (Brand et al., 2010).

Element	Ratio	VPDB-CO_2
C	${}^{13}r = {}^{13}C/{}^{12}C$	0.0111802
O	${}^{18}r = {}^{18}O/{}^{16}O$	0.00208835
O	${}^{17}r = {}^{17}O/{}^{16}O$	0.0003931

Next, the 'assigned' isotopologue abundances, y, in each of the calibration standard and the RT are calculated.

$$ y_{626} = \frac{y_{CO2}}{R_{sum}} \qquad (4.13) $$

$$ y_{636} = y_{626} \cdot {}^{13}r \qquad (4.14) $$

$$ y_{627} = 2 \cdot y_{626} \cdot {}^{17}r \qquad (4.15) $$

$$ y_{628} = 2 \cdot y_{626} \cdot {}^{18}r \qquad (4.16) $$

where y_{CO_2} is the assigned CO_2 mole fraction of the calibration standard (Table 4.2), r is the 'assigned' isotope ratio calculated from Eq. (4.12), and $R_{sum} = (1 + {}^{13}r)\cdot(1 + {}^{17}r + {}^{18}r)^2$ (Griffith, 2018). The assigned values of y_{CO2} in the calibration standards are chosen to span the CO_2 mole fractions observed in sample air, as the method is only valid for samples within this span. As per Table

4.2, the calibration standards CO_2 mole fraction has a range of 372.097 - 499.907 ppm.

The uncalibrated isotopologue abundances measured for each calibration standard, y_{*S}, are then calculated relative to the RT, to correct for drift:

$$y_* = \frac{y_{*S}}{y_{*RT}} \qquad (4.17)$$

where y_{*S} and y_{*RT} are the measured isotopologue abundances in each calibration standard and the RT.

Quadratic calibration curves are then calculated by fitting the assigned isotopologue abundances, from Eqs. (4.13) to (4.16) as a function of the measured isotopologue abundances for each calibration standard. The calibration equations for each isotopologue are then applied to the uncalibrated sample air measurements (y_{*sam}), to produce calibrated isotopologue abundances (y_{*cal}):

$$y_{*cal} = (\alpha \cdot {y_{*sam}}^2) + (\beta \cdot y_{*sam}) + \gamma \qquad (4.18)$$

The CO_2 mole fraction is then just the sum of these calibrated isotopologue abundances. The final step for calculating $\delta^{13}C$, $\delta^{17}O$ and $\delta^{18}O$, is to convert these calibrated isotopologue abundances to delta values on the VPDB-CO_2 scale. This is done by first inverting Eqs. (4.14) to (4.16) to calculate the calibrated isotope ratios ^{13}r, ^{17}r and ^{18}r, and then inverting Eq. (4.12) to calculate the delta values:

$$\delta^*_{VPDB} = \left(\frac{{}^*r_{cal}}{{}^*r_{VDPB}} - 1\right) \cdot 1000\ ‰ \qquad (4.19)$$

where $^*r_{cal}$ is the calibrated isotope ratio of each isotopologue in the sample measurement, $^*r_{VPDB}$ is the standard isotope ratio on the VPDB-CO_2 reference scale (Table 4.3), and δ^*_{VPDB} is the final air sample isotope delta value on the VPDB-CO_2 scale. The introduced CMFD will not occur using this calibration method, thus a correction for this is not necessary. $\Delta^{17}O$ is calculated using Eq. (4.8) and the $\delta^{17}O_{VPDB}$ and $\delta^{18}O_{VPDB}$ values calculated from Eq. (4.19).

4.4.2 Sources of uncertainty in the calibrations

4.4.2.1 Assigned values of calibration standards

Two of the calibration standards (D251502 and D477509; Table 4.2) have the same assigned $\delta^{18}O$ value of -3.04 ‰ on the VPDB-CO_2 scale; however, when run on the TILDAS the analyser response for these two cylinders is consistently

different. From Eq. (4.9) (section 4.4.1.1) in the RM, the uncalibrated drift-corrected measured values of $\delta^{18}O$ in these two standards differ by 0.11 ‰; this discrepancy will then propagate through the calibration procedure leading to error in the final calibrated air measurements. Crucially, in the RM the residuals of the 'calibrated' measured $\delta^{18}O$ values from the assigned values in the calibration standards are used for the CMFD correction (Eq. (4.11); section 4.4.1.2). This difference in the measured values of the calibration standards could be due to an assignment issue, which $\delta^{18}O$ is known to be susceptible to. D447509 was purchased, and assigned, at a different time to the other three standards therefore it is likely that this is the misassigned standard. To confirm this, the calibration standards need to be sent for reanalysis.

Although the measured $\delta^{18}O$ values are not directly used in the AM calibration, if this is an assignment issue then the AM will also be sensitive to this, as the assigned $\delta^{18}O$ values are required in Eq. (4.12) to calculate the isotope ratios of each calibration standard. Again, this error would then propagate through the AM calibration procedure leading to uncertainty in the final calibrated sample air measurements. For both calibration methods, the $\delta^{17}O$ value is unknown in the calibration standards and is instead calculated from the assigned $\delta^{18}O$ values. Therefore, the uncertainty in the $\delta^{18}O$ assignment is also present in the $\delta^{17}O$ values.

The calculation of $\delta^{17}O$ from $\delta^{18}O$ is also reliant on the assumption of mass dependent fractionation. Most fractionation processes in nature are thermodynamic or kinetic – both of which are mass-dependent, but mass independent fractionation from processes such as photolysis can cause small deviations from this mass dependent relationship. However, these deviations are typically < 1 ‰ (e.g. Miller, 2002), and thus negligible in this context (Griffith, 2018).

4.4.2.2 Unassigned reference tank

The delta values of the isotopologues in the RT used in the calibrations has not been assigned, i.e., they are unknown. For the purposes of drift-correction in Eq. (4.9) of the RM and Eq. (4.17) of the AM, this is irrelevant. The AM calibration is independent of the RT, however, a key step in the RM of calibration is dependent

on the RT delta values of each isotopologue. As these values are not assigned, they have been assumed from the y-axis intercept of a linear fit of the assigned values of the four calibration standards against their measured values. As these linear regressions do not result in a perfect fit (Table 4.4), there is uncertainty in the δ^*_{RT} values used in the calibration, and therefore in the final calibrated air sample values, particularly due to the potential misassignment of one of the calibration standards previously discussed. Even a small change in this y-axis intercept can lead to much larger difference later in the calibration when converting to ‰ or per meg.

Table 4.4. R^2 values obtained from the linear regression of the assigned values of the calibration standards against the measured values.

Isotopologue	R^2
636	0.9987
628	0.9998
627	0.9989

In Steur et al. (2021), their RT had been assigned on the VPDB-CO_2 scale and they obtained a perfect fit from the linear regression; however they only performed a 2-point calibration. We have performed a 4 point calibration which, in theory, should provide a more robust calibration, but due to the RT not being assigned, the y-axis intercept is not anchored which leads to additional uncertainty.

4.4.2.3 CO_2 mole fraction dependence

Although the CMFD introduced through the RM of calibration is corrected for, CMFD can also result from non-linearities in the relationship between the CO_2 mole fraction and the measured isotopologue abundances (Wen et al., 2013; Steur et al., 2021). This source of CMFD should be characterised through the measurement of a gas with known CO_2, $\delta^{13}C$, $\delta^{17}O$ and $\delta^{18}O$ values which is then diluted back to different CO_2 mole fractions. The CMFD can then be determined from the analysis of the linear fits of the measured isotopologue (y_{636}, y_{628}, y_{627}) abundance as a function of the measured 626 abundance (Steur et al., 2021). Such experiments have not been completed for the TILDAS at WAO, and as such this CMFD has not yet been characterised. In their experiments on the TILDAS, Steur et

al. (2021) found that non-linearities occurred for y_{636} and y_{627} but are only significant if the range of the measured CO_2 mole fraction is greater than 100 ppm. For y_{628}, however, even when the CO_2 mole fraction range was much greater than 100 ppm significant non-linearities were not observed and they concluded that the nonlinearities were below the range of detection in their experiments. At WAO, the observed CO_2 mole fraction typically ranges between 410 and 490 ppm, therefore the CMFD resulting from non-linearities may not be significant; however, this is uncertain and experiments to characterise this CMFD should be undertaken in the future.

4.4.2.4 Pressure anomaly

As described in section 2.4.1, before injection into the TILDAS optical cell, the gas to be measured is held in an intermediate volume until it reaches a pressure of 270 torr, at which point it is then injected into the optical cell. The pressure in the intermediate volume is read by a pressure gauge and fed back to the computer, which makes a prediction to determine when to open the valve to allow the gas to inject into the cell. However, the TILDAS computer has been inconsistently lagging, meaning that the valve to allow injection was not always opening at the correct time. This then caused pressure spikes in the measurements, which thus affected the precision of the measurements. The key diagnostic for this is the 'pressure anomaly' which is the difference between the cell pressure of the sample gas and the RT gas, calculated as ((sample pressure/RT pressure)-1)*1000. For any data point, if the pressure anomaly fell outside the range of -2 to 1, this data were flagged. This pressure anomaly affects both the calibration gas measurements, and the sample air measurements. To solve this issue in the future, the TILDAS computer is being replaced.

4.5 Comparison of calibration methods

4.5.1 Calibrated ambient air measurements method comparison

The calibrated $\delta^{13}C$, $\delta^{17}O$, $\delta^{18}O$ and $\Delta^{17}O$ values and CO_2 mole fractions from the air measurements from September 2021 to October 2022 are displayed in Figure

4.5a-e for the AM calibration methods. The RM results are not displayed here as they are relatively close to those of the AM and would not be visible on the plots; Figure 4.5f-j show the differences between the calibrated delta values and CO_2 values between the RM and AM methods. In this section I focus only on the calibration methods themselves and the difference between the results.

The average difference in the CO_2 mole fraction between the AM and RM (AM-RM) over the entire time series is -0.066 ± 0.019 ppm, this is within the WMO compatibility goal of 0.1 ppm. The difference in the CO_2 mole fraction between the two methods is not consistent, i.e., one method is not always higher than the other. Instead the AM produces a larger range of values than the RM with the values at the lower end of the observed range being lower and those at the higher end being higher than the RM results. At WAO, CO_2 has been measured continuously, in situ, since 2008 using an Ultramat 6E NDIR analyser (Siemens Corp.) and is reported on the WMO-X2019 scale. The average difference over the entire time series between the AM and the Siemens CO_2 data is -0.157 ppm. The RM shows a better agreement with the Siemens CO_2 data with an average difference of -0.092 ppm.

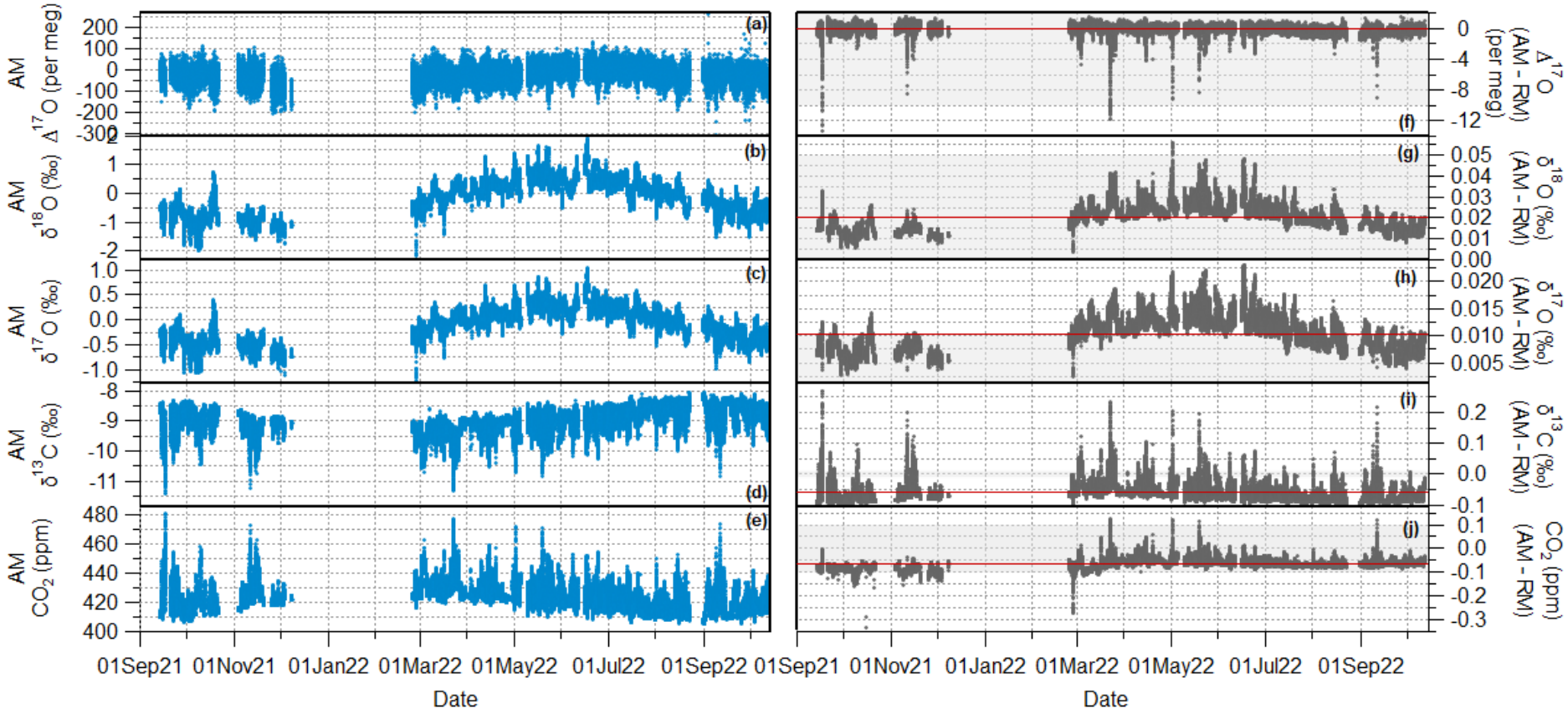

Figure 4.5. (a) – (e) Time series data from the Aerodyne TILDAS at Weybourne from 14Sep2021 to 12Oct2022 with a data point every 4 min, using the AM for analyser calibration; the RM was not plotted here as the values are so close to those from the AM. All data are reported on the VPDB-CO_2 scale. The large gap in the data from Dec2021 to Feb2022 was due to temperature control issues with the oasis chiller. (f) – (j) The difference in the isotope's delta values and CO_2 mole fraction calculated from the two different calibration methods (AM - RM), where the red line indicates the average difference over the entire time series and the shaded area represents the WMO compatibility goals

The average difference in the $\delta^{13}C$ value between the two calibration methods (AM-RM) over the entire time series is -0.062 ± 0.029 ‰. For $\delta^{13}C$ the WMO compatibility goal is ± 0.01 ‰, the difference between the two methods is well outside of this, but is within the extended goal of ± 0.1 ‰. In general, the RM results have a larger range than the AM results, with the values at the lower end of the observed range being slightly lower and those at the higher end being higher. This is visible in Figure 4.5(i), where the difference between the two methods does not centre around zero, but instead is anti-correlated with the $\delta^{13}C$ values in Figure 4.5(d). The difference between the $\delta^{13}C$ values from the two methods also displays a distinct diurnal and seasonal cycle (Figure 4.6), with a larger difference in the afternoon and during the summer. This diurnal and seasonal pattern is anti-correlated with that of $\delta^{13}C$, which is lower overnight and during the autumn.

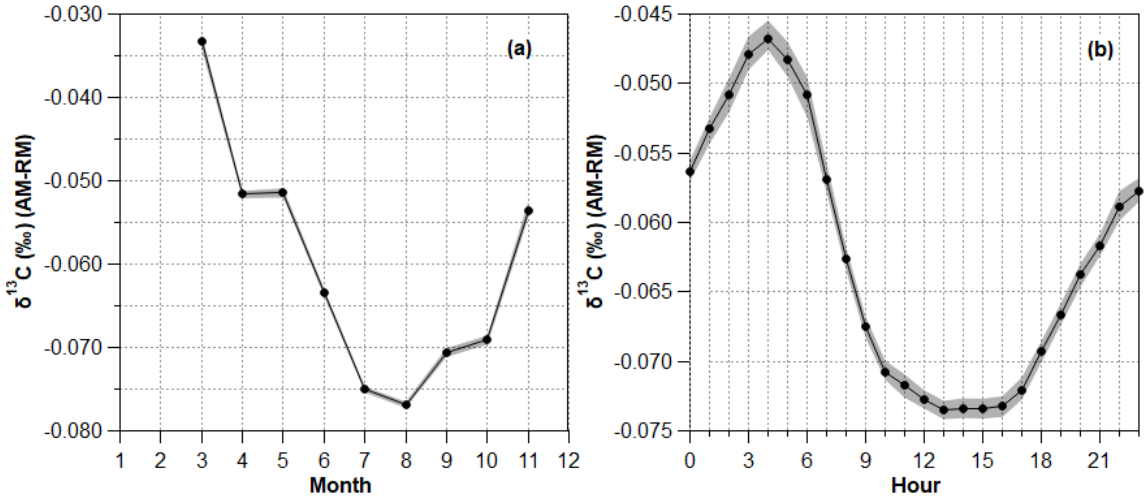

Figure 4.6. (a) Monthly and (b) hourly means of the difference in the $\delta^{13}C$ values from the AM and RM calibrations (AM-RM). Shading indicates 95% confidence intervals on the means. Note, the monthly means for December-February have been excluded due to the gap in the time-series.

The difference between the two calibrated time series for $\delta^{13}C$ is not only anti-correlated with the $\delta^{13}C$ time series, but is also correlated with the CO_2 mole fraction time series (Figure 4.7). The differences between the two calibration method values for $\delta^{13}C$ are smaller between ~435 – 445 ppm, and then diverge again outside this range i.e., for values below 440 ppm the RM results are lower than those from the AM with the converse being true above a CO_2 mole fraction of ~440 ppm. This relationship between the difference between the calibration methods and the CO_2 mole fraction implies that the CMFD has not been fully corrected for in the RM, and would explain the seasonal and diurnal pattern in the difference – as CO_2 mole

fractions are higher over the autumn/winter months and overnight. Due to the sources of uncertainty in the calibrations discussed in section 4.4.2, particularly the unassigned RT and CMFD of the RM, it is therefore more likely that the AM values are reliable than the RM values

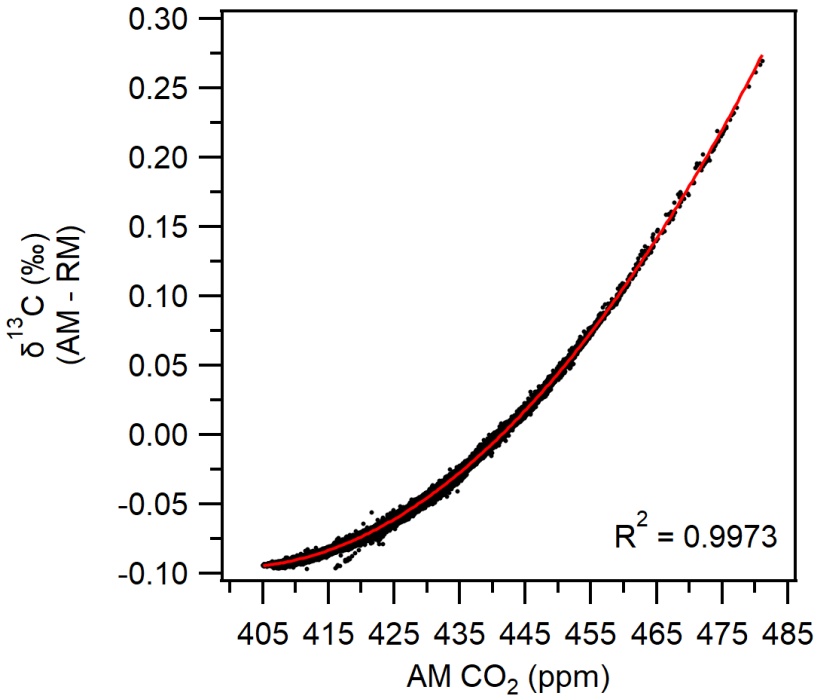

Figure 4.7. Difference between the AM and RM calibrated $\delta^{13}C$ values, illustrating a quadratic dependence with CO_2 mole fraction (with AM calibration).

The average difference in the $\delta^{17}O$ values between the two calibration methods (AM-RM) over the entire time series is 0.010 ± 0.003 ‰, this is the same as our compatibility goal; however, due to the seasonality in the difference, a large period of the time series during the spring and summer is not within this goal Figure 4.5(h). For $\delta^{18}O$ the average difference is 0.020 ± 0.006 ‰, which is well within the WMO compatibility goal of 0.05 ‰. Unlike the difference between the $\delta^{13}C$ values for each calibration method, the AM results are consistently higher than the RM results for both $\delta^{17}O$ and $\delta^{18}O$. Again, for $\delta^{17}O$ and $\delta^{18}O$, there is a correlation between the difference in the values between the two calibration methods and the CO_2 mole fraction; however, for both of these species the differences are more closely correlated with the measured values of the species themselves (Figure 4.8) with a larger difference in the values produced between the two calibration methods when the observed value is higher. This relationship is also demonstrated in Figure 4.5,

where the seasonal peak in values for both $\delta^{17}O$ and $\delta^{18}O$ is during May/June, whereas for CO_2 this is during March.

The average difference in the $\Delta^{17}O$ value between the two calibration methods (AM-RM) over the entire time series is -0.17 ± 0.59 per meg, and is generally centred around zero (with the exception of some excursions, to be discussed). The magnitude of the difference between the two methods, in the context of the accuracy required for scientifically useful observations will be discussed in section 4.6. As with $\delta^{13}C$, the difference between the two methods exhibits a quadratic dependence on the CO_2 mole fraction (Figure 4.9a), with the difference initially decreasing as the CO_2 mole fraction increases until ~440 ppm and then decreasing.

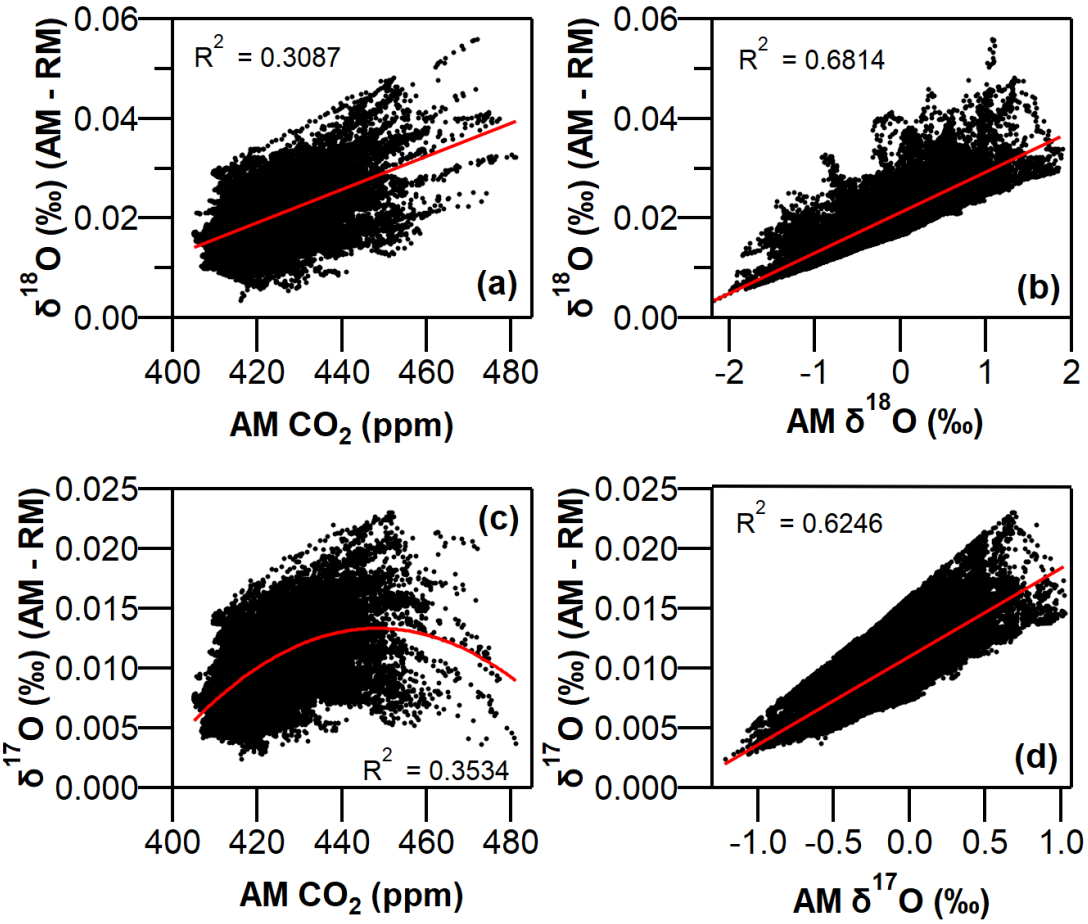

Figure 4.8. (a) $\delta^{18}O$ calibration method differences and AM calibrated CO_2 mole fraction, with a linear relationship shown in red. (b) $\delta^{18}O$ calibration method differences and AM calibrated $\delta^{18}O$ values, with a linear relationship shown in red. (c) $\delta^{17}O$ calibration method differences and AM calibrated CO_2 mole fraction, with a quadratic relationship shown in red. (d) $\delta^{17}O$ calibration method differences and AM calibrated $\delta^{17}O$ values, with a linear relationship shown in red.

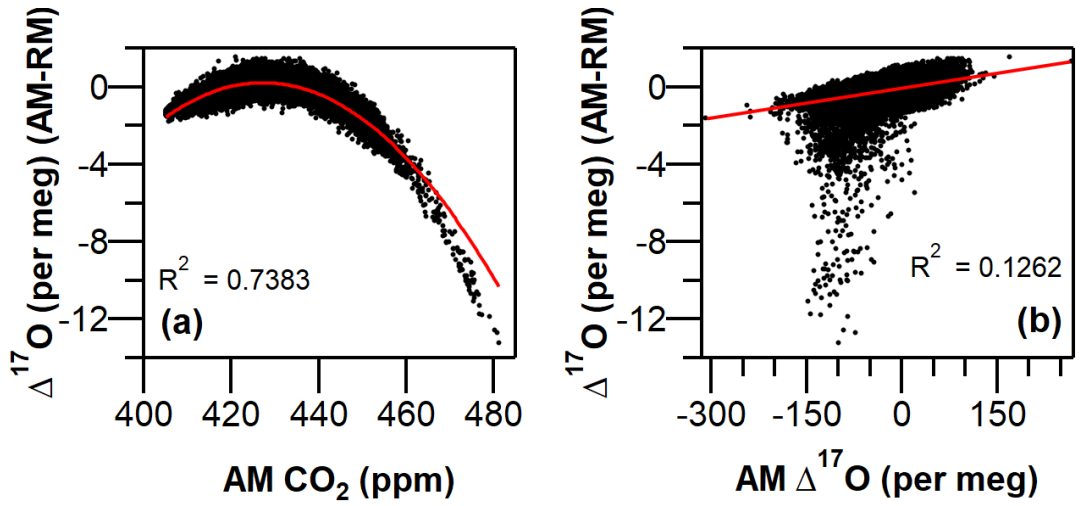

Figure 4.9. (a) $\Delta^{17}O$ calibration method differences and AM calibrated CO_2 mole fraction, with a quadratic relationship shown in red. (b) $\Delta^{17}O$ calibration method differences and AM calibrated $\Delta^{17}O$ values, with a linear relationship shown in red.

The large excursions from the zero line seen in Figure 4.5f all occur during periods of high CO_2 (e.g. Figure 4.10), again this is indicating a problem with the CMFD correction applied to the RM, likely due to the unassigned RT as discussed in section 4.4.2.

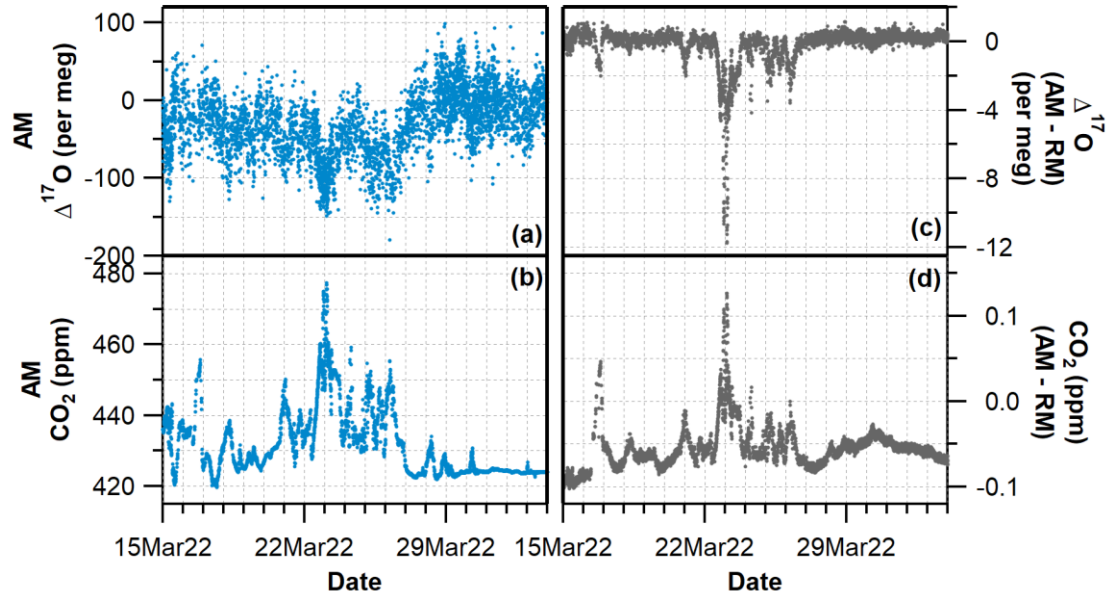

Figure 4.10. (a) $\Delta^{17}O$ and (b) CO_2 mole fraction time-series calibrated using the AM and (c) $\Delta^{17}O$ and (d) CO_2 mole fraction difference between the calibration methods (AM – RM) from 15Mar2022 – 03Apr2022.

Overall, there are differences between the two calibration methods which, with the exception of $\delta^{13}C$, fall within the compatibility goals for each species; however, there are distinct seasonal cycles and dependence on CO_2 mole fraction of

these differences. Due to the unassigned reference tank causing large uncertainties in the RM calibration for CMFD correction it is likely that this is the cause of these differences between the methods. For this reason, I will only present the AM calibrated data in section 4.6.

4.5.2 Target tank

As the signals in the isotopic composition of CO_2 are very small, it is crucial to assess the TILDAS's precision over time. It is particularly important to assess the precision and accuracy of both the $\delta^{18}O$ and $\delta^{17}O$ measurements over time, as $\Delta^{17}O$ is calculated from these values. The World Meteorological Organization (WMO) Global Atmospheric Watch (GAW) strongly recommend the regular analyses of a 'target tank' (TT) to estimate measurement system performance, even if this measurement does not cover all sources of uncertainty (Crotwell et al., 2020). The TT cylinder was run 12 times in the period between 03Aug2022 and 11Oct2022, all calibrated using the 21Jun2022 calibration. For the first 7 runs the TT was measured on the TILDAS for 1 hour. For the final 4 runs measurement time was increased to 5 hours, to see if this improved the TT results. The TT was measured in the same way as the calibration gases, where flow through the TILDAS was alternated with the RT every 2 minutes, resulting in one drift-correct TT measurement every 4 minutes. For the 1 hour runs, the first 4 minutes were removed to account for the cell sweepout time. For the 5 hour runs, between 44 and 68 minutes were removed at the start of each run due to drifting values in the first half of the run. Additionally, some of the 4 minute data points within each run were filtered out due to spiking in the pressure anomaly, as discussed in section 4.4.2.3. Therefore, for the 1 hour and 5 hour runs, the actual length of data used in the calculation of the TT measured value was variable. The number of 4 minute points used in the calculation of the average of each TT run are given in Table 4.5.

Table 4.5. The number of 4 minute data points used in the calculation of the average of each TT run.

Date of TT run	No. of points used
03Aug2022	12
04Aug2022	11
08Aug2022	14
10Aug2022	14
11Aug2022	15
15Aug2022	14
17Aug2022	13
22Aug2022	13
05Sep2022	13
19Sep2022	71
16Sep2022	68
04Oct2022	48
11Oct2022	72

In order to assess the precision of the delta value measurements a TT with unknown delta values was measured repeatedly on the TILDAS to assess the 'repeatability' of the measurements over time, as well as the difference between the two calibration methodologies. Repeatability is defined as the closeness of agreement between results of successive measurements of the same measure carried out under the same conditions, and is considered as a proxy for the precision of a measurement system (Crotwell et al., 2020). Therefore, I calculated the repeatability as the mean ± 1σ standard deviations of the average of two consecutive data points within the same run of the TT. I deliberately only used two data points to calculate each standard deviation to more closely mimic in-situ continuous measurements where one can only measure an outside air sample once at any given time (whereas when measuring air from a cylinder, in principle we could measure it multiple times and expect to get a smaller standard deviation). The results are then compared to the WMO/GAW repeatability goals, which are assumed to be half of the WMO/GAW 'compatibility goals', where compatibility refers to the acceptable level of agreement between two laboratories when measuring the same air sample (Crotwell et al., 2020).

Compatibility is often used as a measurement of the accuracy of a measurement system (Crotwell et al., 2020). As the delta values of the TT have not been assigned on the VPDB-CO_2 scale, I cannot calculate how far the measured values are from the assigned values; however, the compatibility goals can be used to assess the drift in the measured TT delta values over time. The $\delta^{13}C$ network compatibility

goal is 0.01 per mil, with an extended goal of ± 0.1 ‰; the $\delta^{18}O$ goal is ± 0.05 ‰, with an extended goal of ± 0.1 ‰. There are no established goals for $\delta^{17}O$ or $\Delta^{17}O$, but my research group has set out goals of ± 0.01 ‰ for $\delta^{17}O$ and ± 10 per meg for $\Delta^{17}O$, aimed at obtaining scientifically useful data based on anticipated natural spatial and temporal variability (Koren et al., 2019).

The $\delta^{13}C$, $\delta^{17}O$, $\delta^{18}O$ and $\Delta^{17}O$ values obtained for the TT for each calibration method are displayed in Figure 4.11. When considering the results in the following sections, it is important to note that many background station measurements continue to show persistent offsets that are much larger than those stipulated by the WMO/GAW network goals (Crotwell et al., 2020), demonstrating that these goals are very challenging and the measurement community struggles to routinely meet them.

Table 4.6 presents the repeatability results for the 1 and 5 hour TT runs for each delta value. For each delta value, the repeatability of the measurements is worse for the 5 hour runs than the 1 hour runs. This is predominantly due to an outlying run within the 5 hour runs; Figure 4.12, as an example, shows the average repeatability of each TT run which were used to calculate the RM $\delta^{13}C$ values in Table 4.6, the TT on 04Oct2022 has a much larger average and SD than each of the other runs. The 04Oct2022 TT was run for 5 hours, but only 48 out of the 75 4 minute points were retained for the final calculation after removing the cell sweepout time and filtering for pressure anomaly spikes. The large number of filtered points during this run indicates that the pressure anomaly spikes were particularly frequent thus affecting the general precision of the instrument. However, in general, running the TT for a longer period of time did not improve the repeatability. The repeatability is slightly worse for the AM than the RM for all of the isotope's delta values, for $\Delta^{17}O$ the repeatability of the RM is slightly better than the AM when running the TT for 5 hours (a 0.012 per meg difference). For each method the only delta value within the WMO/GAW repeatability goal is $\delta^{18}O$; $\delta^{13}C$ is within the extended goal. If we were to apply the WMO/GAW extended goal to $\delta^{17}O$, both methods would be within this goal. The repeatability obtained for $\Delta^{17}O$ on the TILDAS analyser is far outside of the goal, but closer to the 'extended goal' for measurement precision of ± 10 per meg that Hofmann et al. (2017) reported would be required to capture seasonal variations and for $\Delta^{17}O$ to be useful as a tracer for GPP. It is again worth noting that these goals are very challenging, and that it is expected that after the TILDAS computer is replaced

and the other sources of uncertainty in the calibrations (section 4.4.2) are resolved, that the repeatability of these measurements will improve.

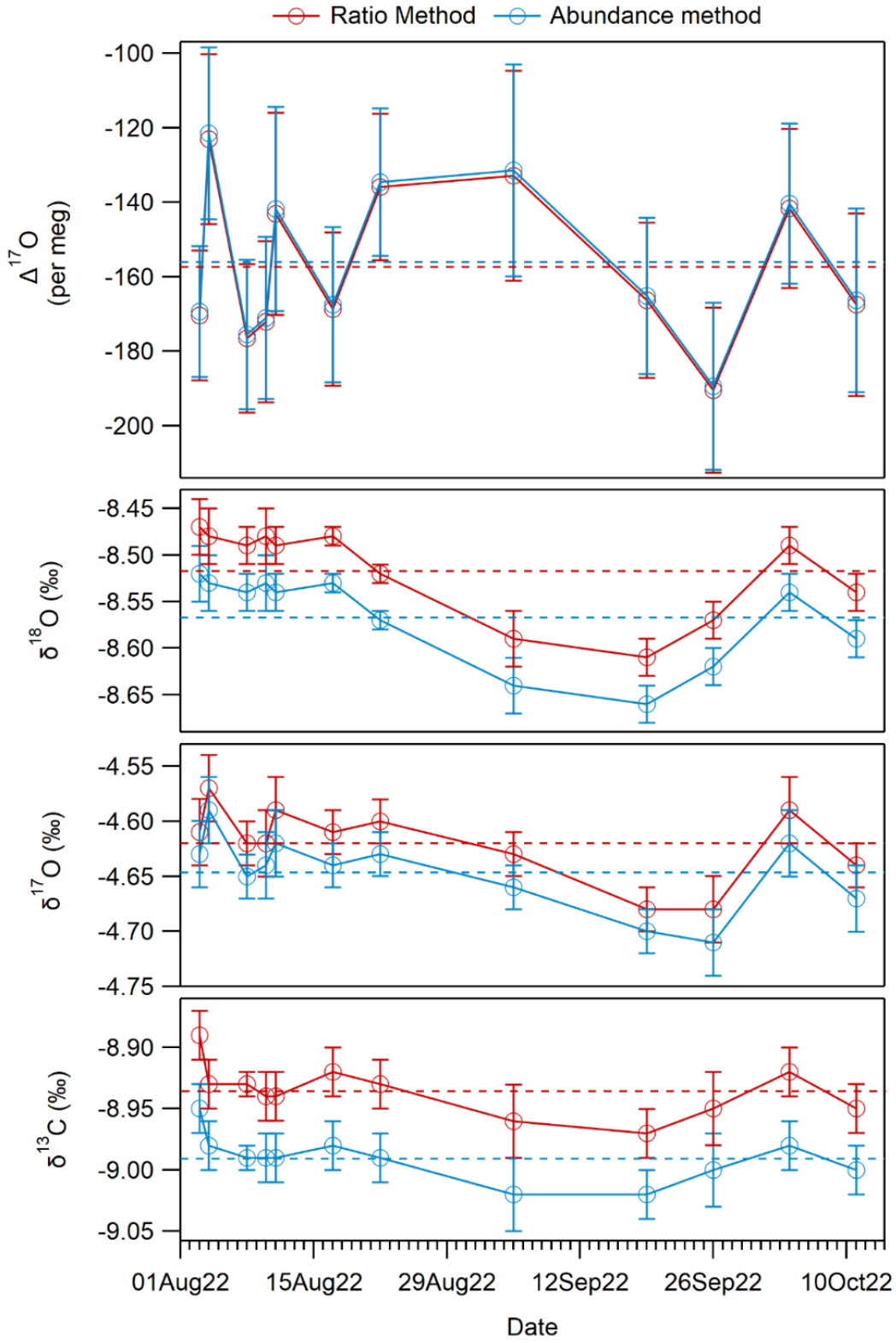

Figure 4.11. $\delta^{13}C$, $\delta^{17}O$, $\delta^{18}O$, and $\Delta^{17}O$ values from repeated measurement of the TT, calibrated using the RM (red) and AM (blue). Error bars indicate ± 1 σ SD. Dashed lines indicate average values for the RM (red) and AM (blue). Before 19Sep22 TT runs were 1 hour, after this they were 5 hours. Note the different units for $\Delta^{17}O$, where 1 ‰ equals 1000 per meg.

Table 4.6. Repeatability of each isotope's delta value for the TILDAS, for '1 hour' and '5 hour' runs

	$\delta^{13}C$ (‰)		$\delta^{17}O$ (‰)[d]		$\delta^{18}O$ (‰)		$\Delta^{17}O$ (per meg)[d]	
	1 hr	**5 hr**	**1 hr**	**5 hr**	**1 hr**	**5 hr**	**1 hr**	**5 hr**
RM repeatability[a]	±0.016 ±0.008	±0.025 ±0.015	±0.017 ±0.001	±0.023 ±0.007	±0.016 ±0.009	±0.022 ±0.007	±13.98 ±5.54	±17.52 ±0.43
AM repeatability[a]	±0.017 ±0.008	±0.027 ±0.019	±0.018 ±0.007	±0.023 ±0.007	±0.017 ±0.009	±0.023 ±0.010	±14.09 ±5.58	±17.64 ±0.043
WMO/GAW goal[b]	±0.005		±0.005		±0.025		±5	
'Extended goal'[c]	±0.05		±0.05		±0.05		±10	

[a] Values are calculated using the method in Kozlova and Manning (2009) and Pickers et al. (2017). Mean ± 1σ standard deviations of the average of two consecutive data point measurements within each run of the TT. Uncertainties are given on these mean standard deviations, illustrating that the analytical repeatability is variable over time.
[b] The repeatability of a measurement should be at most half of the value of the WMO/GAW compatibility goal. WMO/GAW's compatibility goals are the scientifically desirable level of for measurements of well-mixed background air.
[c] 'Extended goals' are also provided by WMO/GAW as guidelines for studies in which the more stringent goals are not required (Crotwell et al., 2020).
[d] WMO/GAW do not provide goals for $\delta^{17}O$ or $\Delta^{17}O$. The values listed are the goals my research group has set themselves based on obtaining scientifically useful data based on anticipated natural spatial and temporal variability.

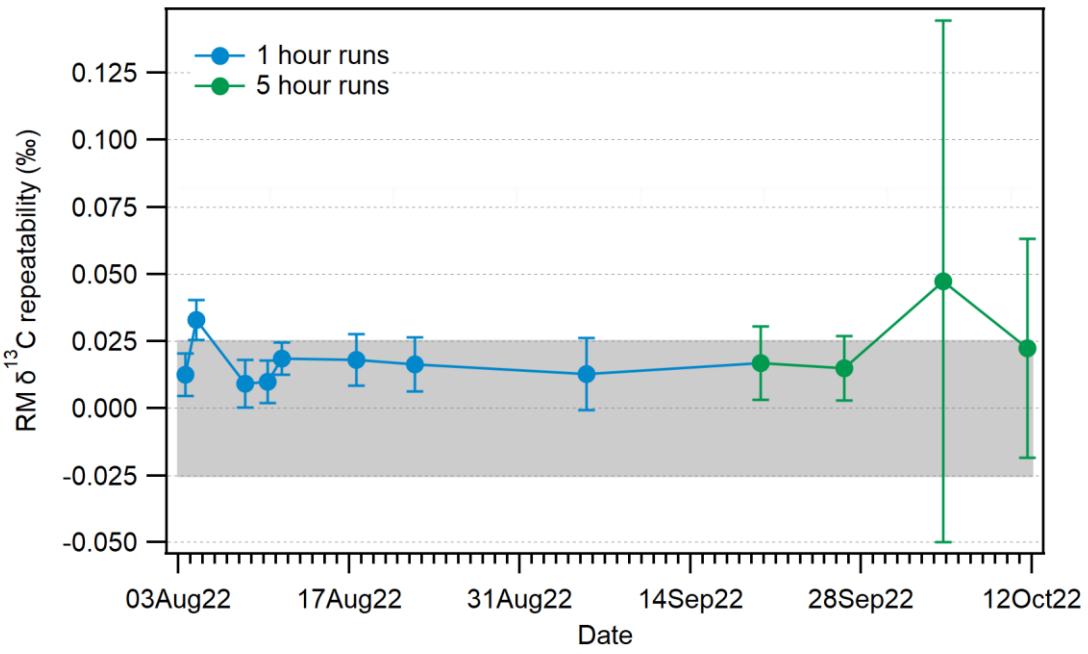

Figure 4.12. RM $\delta^{13}C$ repeatability values obtained for each TT run (± 1 σ SD). Blue points are 1 hour runs and green pints are 5 hour runs. The grey shading indicates the WMO/GAW extended compatibility goals.

Table 4.7 presents the average values for each species over all the TT runs, as well as the average difference between the two calibration methods. The average difference between the two methods has a very low standard deviation, again this is due to the same calibration being used over the entire time period.

Although the compatibility cannot be directly calculated, as the isotope delta values of the TT are unknown, the range of the TT results (Table 4.7) are far outside of the WMO compatibility goals of ± 0.01 ‰ for $\delta^{13}C$ and ± 0.05 ‰ for $\delta^{18}O$. However, in the last WMO round robin large discrepancies were observed among laboratories of up to 0.09 ‰ and 0.4 ‰ for $\delta^{13}C$ and $\delta^{18}O$, respectively (Crotwell et al., 2020), demonstrating the challenge of routinely meeting these goals. The ranges of $\delta^{17}O$ and $\Delta^{17}O$ are also outside the goals set out by my research group of ± 0.01 ‰ and 10 per meg, respectively, although $\delta^{17}O$ is within the extended goal. As the range of values obtained for $\Delta^{17}O$ are far outside the goals, the variability in the results implies that the compatibility goals would not be met. As a caveat to this, it is likely that the analyser performance is being impaired by the pressure anomaly spikes, even after filtering, and the performance should improve once the computer is swapped out, with further improvement if the sources of uncertainty in the calibrations are resolved.

Table 4.7. Average (± 1σ SD) and range of values for each isotope's delta value measured by the TILDAS for the unknown cylinder.

	$\delta^{13}C$ (‰)	**$\delta^{17}O$ (‰)**	**$\delta^{18}O$ (‰)**	**$\Delta^{17}O$ (per meg)**
Compatibility goal	±0.01	±0.01	±0.05	±10
RM avg.	-8.937 ±0.021	-4.620 ±0.035	-8.519 ±0.049	-157.40 ±20.97
RM range	0.08	0.11	0.14	67.35
AM avg.	-8.990 ±0.020	-4.645 ±0.035	-8.568 ±0.049	-156.15 ±21.13
AM range	0.07	0.12	0.14	67.86
Average difference (RM – AM)	0.054 ±0.001	0.024 ±0.000	0.049 ±0.004	-1.25 ±0.16

4.6 Seasonal amplitudes

In order to put the differences between calibration methods and precisions of the TILDAS discussed in the previous sections into context, the seasonal cycles of each isotope's delta values were calculated. The data were averaged to hourly values, and can be seen in black in Figure 4.13. For analysis of the seasonal amplitudes, the atmospheric background of each isotope's delta values was calculated. Due to measurement gaps in both the TILDAS and radon analysers, using the radon method I present in Chapter 3 a background could only be produced for 4 months; therefore, backgrounds for each isotope's delta values were calculated using rfbaseline. A full description of the rfbaseline method for calculation of backgrounds can be found in section 3.4.1.1. In brief, rfbaseline was developed by Ruckstuhl et al. (2012) and can be implemented using the 'rfbaseline' function from the 'IDPmisc' package in R (Ruckstuhl et al., 2020). This function uses a statistical approach, based on local regression of the time series, over a moving time window. As smoothing window (or span) equivalent to approximately 4 weeks was used for each species, with a B value of 0.4 for $\delta^{13}C$ and 4 for the other three isotope's delta values. For $\Delta^{17}O$ an additional background with a smoothing window of approximately 8 weeks, to increase the stiffness of the background so that the fit is more representative of the seasonal variability, was also produced. These backgrounds are also displayed in Figure 4.13. Using these background values, the monthly average signal for each isotope's delta values was then calculated (Figure 4.14).

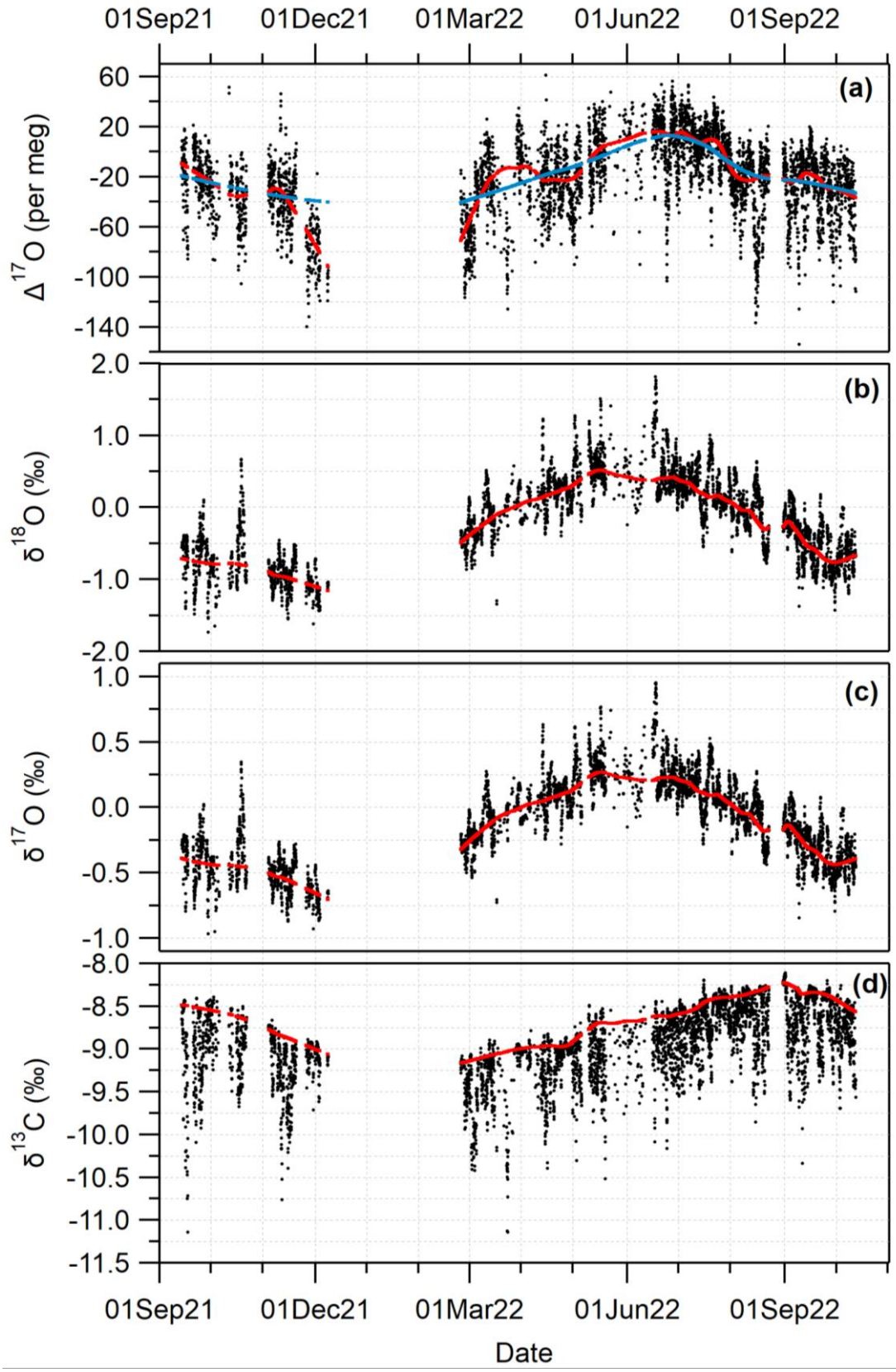

Figure 4.13. Hourly averaged data calibrated using the AM for (a) $\Delta^{17}O$, (b) $\delta^{18}O$, (c) $\delta^{17}O$, and (d) $\delta^{13}C$. The red lines indicate the background as calculated using rfbaseline. The blue line in (a) indicates an alternate background for $\Delta^{17}O$ using a stiffer rfbaseline fit. Note the different units for $\Delta^{17}O$, where 1 ‰ equals 1000 per meg.

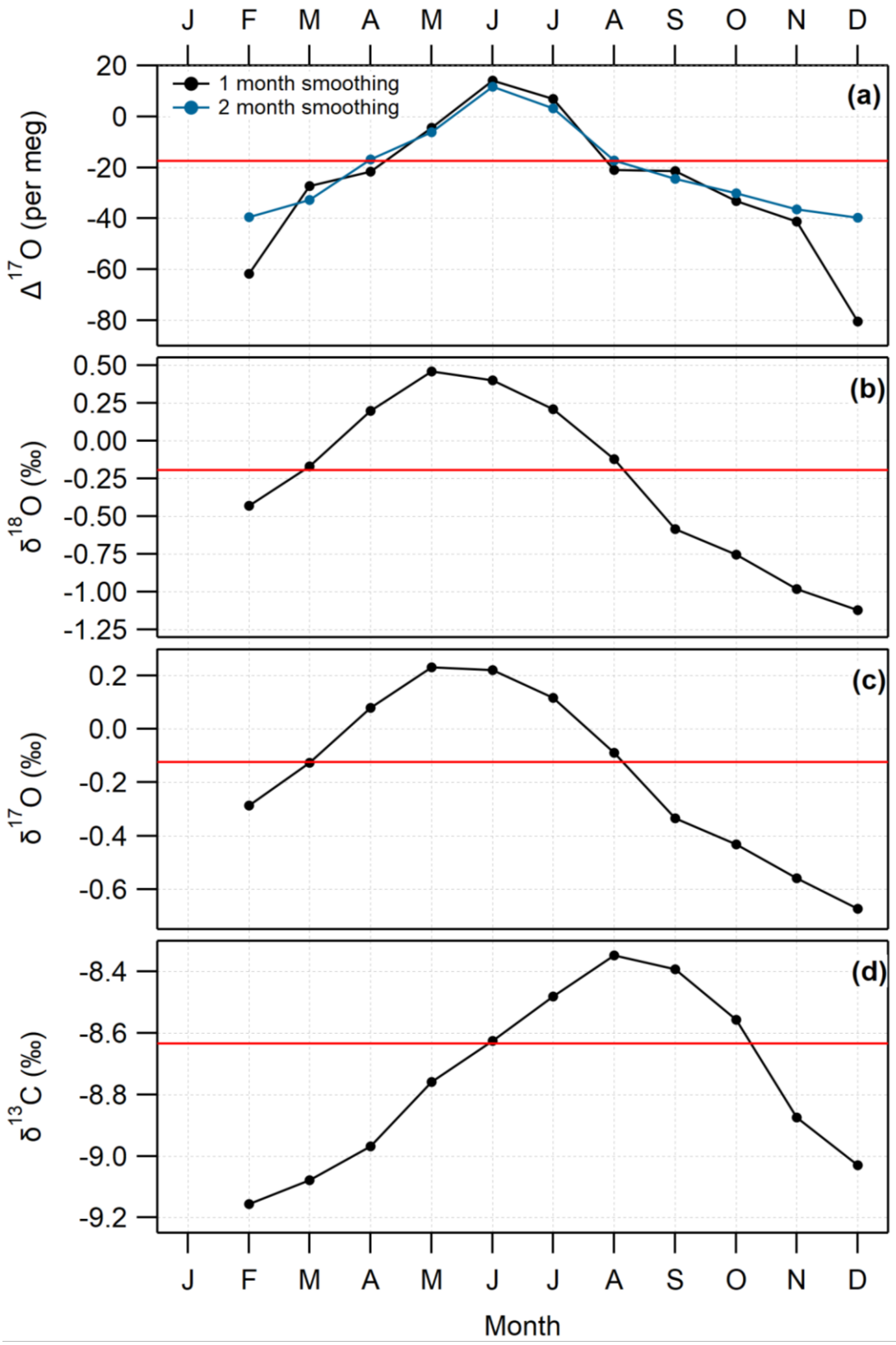

Figure 4.14. Average monthly background values of (a) $\Delta^{17}O$, (b) $\delta^{18}O$, (c) $\delta^{17}O$, and (d) $\delta^{13}C$. The red lines display the background average across all months. Note the different units for $\Delta^{17}O$, where 1 ‰ equals 1000 per meg. The background average for the 2 months smoothing of $\Delta^{17}O$ has not been plotted as it sits on top of the 1 month smoothing average on this scale.

The monthly average $\delta^{13}C$ value is highest in August and lowest in February, with a peak-to-peak amplitude of 0.81 ‰ and an average signal of -8.61 ± 0.26 ‰ (Figure 4.14d). In section 4.5.2 when comparing the two calibration methods, the average difference was -0.062 ± 0.029 ‰, or 7 % of the seasonal amplitude. The repeatability calculated for the AM (1 hour runs) was ± 0.017 ± 0.008 ‰ , or 2.10 % of the seasonal amplitude; thus, the signal-to-noise ratio here is large. The seasonal cycle of $\delta^{13}C$ is driven by the net uptake of carbon during the growing season increasing $\delta^{13}C$ and net release of $\delta^{13}C$ during the winter, and the timings of the peaks in $\delta^{13}C$ in Figure 4.14d align with this process.

The monthly average $\delta^{17}O$ is highest in May and lowest in December, with a peak-to peak seasonal amplitude of 0.90 ‰ and with an average signal of -0.12 ± 0.27 ‰. In section 4.5.2 when comparing the two calibration methods, the average difference between the two calibration methods was 0.010 ± 0.003 ‰, or 1.11 % of the seasonal amplitude; therefore, even though the calibration methods differ, this difference is small in the context of the signals being investigated. The repeatability calculated for the AM (1 hour runs) was ± 0.017 ± 0.009 ‰, or 1.89 % of the seasonal amplitude; again, the seasonal cycle is clearly visible with a high signal-to-noise ratio.

The monthly average $\delta^{18}O$ is highest in May and lowest in December, with a peak-to-peak seasonal amplitude of 1.58 ‰. In section 4.5.2 when comparing the two calibration methods, the average difference between them was 0.020 ± 0.006 ‰, or 1.3 % of the seasonal amplitude; as with $\delta^{17}O$, the difference between the methods is small compared to the magnitude of the seasonal cycle. In terms of repeatability from the TT measurements, $\delta^{18}O$ was within the goal with a value of ± 0.017 ± 0.009 ‰, which is equivalent to 1.08 % of the seasonal cycle. In the northern hemisphere, exchange with the terrestrial biosphere dominates the signal $\delta^{18}O$, with isotopic exchange with leaf-water during photosynthesis enriching the $\delta^{17}O$ and $\delta^{18}O$ content of CO_2 released from plants (Cuntz et al., 2003). Thus, the peak in these isotope's delta values observed in May is consistent with this.

When using a smoothing window of 1 month to calculate the background, $\Delta^{17}O$ is highest in June and lowest in December, with a peak-to-peak seasonal amplitude of 94.71 per meg. In section 4.5.2 when comparing the two calibration methods, there was an average difference of -0.17 ± 0.59 per meg, or 0.17 % of the seasonal amplitude; thus, indicating that even though the calibration methods differ, this difference is far smaller than the signals being investigated. The repeatability of the

$\Delta^{17}O$ measurements for the AM calibration method is ±14.09 ± 5.58 ‰ (1 hour runs), or 14.88 % of the calculated seasonal amplitude; this smaller signal-to-noise ratio may hinder the use of these observations for useful scientific interpretation, nevertheless, the signal of the seasonal cycle is clearly distinguishable above the noise of the data. Additionally, there is a lot of variation within the TT results for $\Delta^{17}O$, with large changes between neighbouring runs (Figure 4.11). Although the TT was not run for the entire period for which I have presented observations, the variability in the measured values of the TT mean that the TILDAS observations may also be subject to this short-term variability caused by the analyser itself; thus, some of the short-term variability of the signal observed in the $\Delta^{17}O$ time series may not be 'real'. For this reason, I ran the rfbaseline function on $\Delta^{17}O$ with a 2 month smoothing window, to create a 'stiffer' background which is less influenced by short-term variations. With the longer smoothing window, $\Delta^{17}O$ is still highest in June, and lowest in December, but the peak-to-peak seasonal amplitude reduced to 51.38 per meg. Again, the repeatability of the $\Delta^{17}O$ measurements for the AM calibration method is ± 14.09 ± 5.58 ‰ (1 hour runs), which in this case is 27.42 % of the seasonal amplitude.

In terms of comparison to values from the published literature, the available observational data on the $\Delta^{17}O$ composition of tropospheric CO_2 is limited. The first published high precision data was from Barkan and Luz (2012) from a limited set of flask samples in Spring 2012 in Jerusalem, Israel; from these samples they found an average $\Delta^{17}O$ signal of +37 ± 9 per meg (VSMOW scale, λ_{RL} = 0.5229). Thiemens et al. (2014) report a decadal record of $\Delta^{17}O$ from flask samples in La Jolla, California, USA, they observed a mean $\Delta^{17}O$ signal of +30 ± 40 per meg (SMOW scale, λ_{RL} = 0.5229). Further, Liang and Mahata (2015) observed an average $\Delta^{17}O$ signature of +60 ± 40 per meg (VSMOW scale, λ_{RL} = 0.5229), from flask samples in Taiwan. Finally, Hofmann et al. (2017) reported an observed average $\Delta^{17}O$ value of -20 ± 50 per meg (VSMOW scale, λ_{RL} = 0.5229), from a year's worth of two-weekly samples from Göttingen, Germany, which is at a similar latitude to WAO (location displayed in Figure 4.15). Between these values from the literature there is variability between different sampling locations and a large SD on the reported values. From the $\Delta^{17}O$ values calculated for WAO (Figure 4.14), I calculated an average background value (with 2 months smoothing) of -6.9 ± 15.7 per meg (VPDB-CO_2 scale, λ_{RL} = 0.5229) and an average for all of the data of -21.5 ± 31.6 per meg. Although these values can't be

directly compared to the values quoted above due to the differing reporting scales, there is good agreement in the general magnitude and SD of the average signal.

The seasonal cycle of $\Delta^{17}O$ in atmospheric CO_2 has been modelled by Koren et al. (2019) using a global 3D simulation. In this study they calculated a northern hemispheric seasonal cycle peak-to-peak amplitude of 15.7 per meg. The seasonal amplitude calculated from the TILDAS data is a factor of three larger than this when using the smaller result from the 2 month smoothing window. However, the $\Delta^{17}O$ signature and cycle was found to be variable with the hemisphere; Koren et al. (2019) also modelled $\Delta^{17}O$ the global peak-to-peak seasonal amplitude (Figure 4.15). From this global simulation the peak-to-peak amplitude at WAO is around 20 per meg, compared to our observed amplitude of 51.4 per meg. Hofmann et al. (2017) presented a comparison of their observed $\Delta^{17}O$ values compared to 3D simulated atmospheric $\Delta^{17}O$ values, for Göttingen, Germany, which is at a similar latitude to WAO, and also reported the modelled amplitude to be around a factor of three smaller than observed, which indicates that the amplitude observed at WAO is reasonable, even with the disagreement from the simulated values.

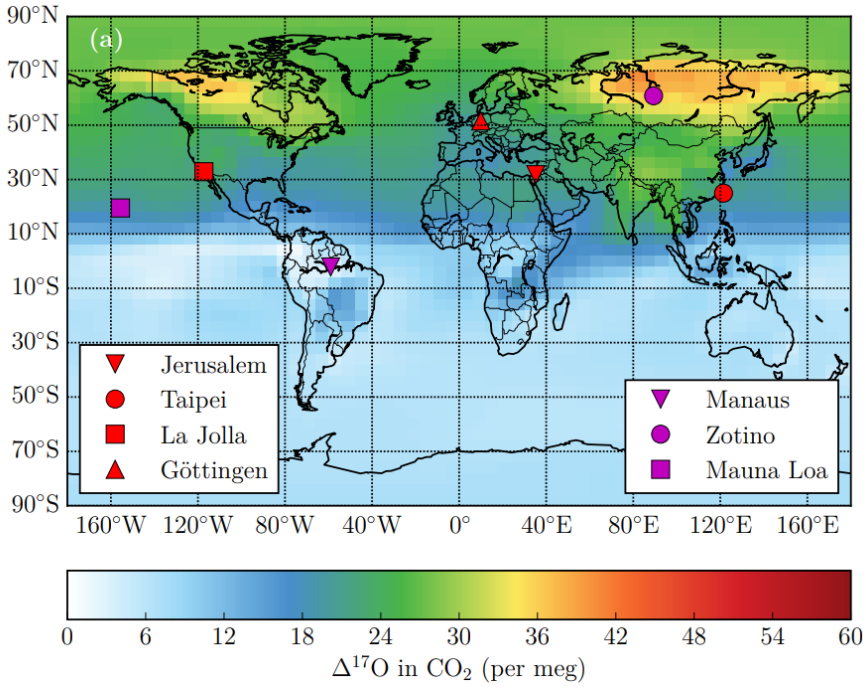

Figure 4.15. Simulated $\Delta^{17}O$ peak-to-peak seasonal amplitude for the lowest 500 m of the atmosphere from TM5 model predictions. Locations for which published measurements of $\Delta^{17}O$ in CO_2 exist are indicated with red symbols. Figure taken from Koren et al. (2019).

4.7 Conclusions

A year long time-series of $\delta^{13}C$, $\delta^{18}O$ and $\delta^{17}O$ in tropospheric CO_2 from WAO using an Aerodyne TILDAS analyser has been presented, and $\Delta^{17}O$ calculated from these measurements. The differences between two calibration methods used in isotopologue research were assessed and the potential sources of uncertainty in these calibrations were discussed. The performance of the TILDAS analyser was then evaluated in the context of the WMO/GAW goals and in the context of the signals observed in the time-series.

When comparing the AM and RM methods of calibration, I found small differences between the results, with an average difference over the entire time-series of -0.07 ± 0.02 ppm for CO_2, -0.06 ± 0.03 ‰ for $\delta^{13}C$, 0.02 ± 0.01 ‰ for $\delta^{18}O$, 0.01 ± 0.00 ‰ for $\delta^{17}O$, and -0.17 ± 0.59 per meg for $\Delta^{17}O$. This difference is likely caused by the CMFD not being fully corrected for when calibrating using the RM method due to the unassigned RT values. Additional sources of uncertainty between the methods of calibration included unassigned $\delta^{17}O$ values for all of the calibration standards, uncertainty in the assigned $\delta^{18}O$ value of one of the calibration standards, and anomalous pressure spiking when switching between the RT and sample gas.

From repeated measurements of a TT, I found the repeatability of the $\delta^{13}C$ and $\delta^{18}O$ measurements to be well within the WMO/GAW extended goal of ± 0.05 ‰, with very similar values obtained for both calibration methods. Additionally, $\delta^{17}O$ is well within the goal set out by my research group. The repeatability of the $\Delta^{17}O$ measurements for both calibration methods is outside of the goal but within the wider goal needed to assess seasonal variations and for $\Delta^{17}O$ to be useful as a tracer for GPP. Additionally, these results would be expected to improve with the resolution of the main calibration method uncertainties.

In the context of the seasonal amplitude of the signal in the delta values and $\Delta^{17}O$, neither the difference between the calibration methods nor the repeatability of the measurements mask this. Additionally, the $\Delta^{17}O$ seasonal signal observed at WAO is comparable to the one seen in Göttingen by Koren et al. (2019).

With an extended time-series and resolution of uncertainties, the measurements of $\delta^{13}C$, $\delta^{18}O$, and $\delta^{17}O$ can be used to further increase understanding of the global $\Delta^{17}O$ budget of tropospheric CO_2.

4.7.1 Future work

The measurements presented in this chapter from the TILDAS have been shown to be precise enough to resolve seasonal changes in $\delta^{13}C$, $\delta^{18}O$, $\delta^{17}O$ and $\Delta^{17}O$; however, there are a number of uncertainties that need to be resolved to further improve these measurements:

- Replacement of the instrument's computer to stop the anomalous pressure spikes when switching between the RT and sample air.
- Assignment of the RT CO_2, $\delta^{13}C$, $\delta^{17}O$ and $\delta^{18}O$ values, which will improve the CMFD correction for the RM.
- Assignment of $\delta^{17}O$ values for all of the calibration cylinders.
- Re-assignment of the $\delta^{18}O$ value of one of the calibration standards.
- Experiments to characterise the CMFD should be undertaken.
- Continued in situ measurements to examine analyser performance.

Additionally, continued measurements of these isotopologues at WAO over multiple years will allow for the assessment of long-term trends in the time series to increase understanding of the $\Delta^{17}O$ budget of tropospheric CO_2 and to constrain GPP.

References

Adnew, G. A., Hofmann, M. E. G., Paul, D., Laskar, A., Surma, J., Albrecht, N., Pack, A., Schwieters, J., Koren, G., Peters, W. and Röckmann, T. (2019) 'Determination of the triple oxygen and carbon isotopic composition of CO_2 from atomic ion fragments formed in the ion source of the 253 Ultra high-resolution isotope ratio mass spectrometer', *Rapid Communications in Mass Spectrometry,* 33(17), pp. 1363-1380.

Affek, H. P. and Yakir, D. (2014) '5.7 - The Stable Isotopic Composition of Atmospheric CO_2', in Holland, H.D. & Turekian, K.K. (eds.) *Treatise on Geochemistry (Second Edition)*. Oxford: Elsevier, pp. 179-212.

Assonov, S. S. and Brenninkmeijer, C. A. M. (2005) 'Reporting small $\Delta^{17}O$ values: existing definitions and concepts', *Rapid Communications in Mass Spectrometry,* 19(5), pp. 627-636.

Barkan, E. and Luz, B. (2012) 'High-precision measurements of $^{17}O/^{16}O$ and $^{18}O/^{16}O$ ratios in CO_2', *Rapid Communications in Mass Spectrometry,* 26(23), pp. 2733-2738.

Barthel, M., Sturm, P., Hammerle, A., Buchmann, N., Gentsch, L., Siegwolf, R. and Knohl, A. (2014) 'Soil $H_2{}^{18}O$ labelling reveals the effect of drought on $C^{18}OO$ fluxes to the atmosphere', *Journal of Experimental Botany,* 65(20), pp. 5783-5793.

Battle, M., Bender, M. L., Tans, P. P., White, J. W. C., Ellis, J. T., Conway, T. and Francey, R. J. (2000) 'Global carbon sinks and their variability inferred from atmospheric O_2 and $\delta^{13}C$', *Science,* 287(5462), pp. 2467-2470.

Boering, K., Jackson, T., Hoag, K., Cole, A., Perri, M., Thiemens, M. and Atlas, E. J. G. R. L. (2004) 'Observations of the anomalous oxygen isotopic composition of carbon dioxide in the lower stratosphere and the flux of the anomaly to the troposphere', 31(3).

Brand, W. A., Assonov, S. S. and Coplen, T. B. (2010) 'Correction for the ^{17}O interference in $\delta(^{13}C)$ measurements when analyzing CO_2 with stable isotope mass spectrometry', *Pure and Applied Chemistry,* 82(8), pp. 1719-1733.

Brenninkmeijer, C. A. M., Janssen, C., Kaiser, J., Röckmann, T., Rhee, T. S. and Assonov, S. S. (2003) 'Isotope Effects in the Chemistry of Atmospheric Trace Compounds', *Chemical Reviews,* 103(12), pp. 5125-5162.

Ciais, P., Cuntz, M., Scholze, M., Mouillot, F., Peylin, P. and Gitz, V. (2005) '14 - Remarks on the use of ^{13}C and ^{18}O isotopes in Atmospheric CO_2 to Quantify biospheric carbon fluxes', in Flanagan, L.B., Ehleringer, J.R. & Pataki, D.E. (eds.) *Stable Isotopes and Biosphere Atmosphere Interactions*. San Diego: Academic Press, pp. 235-267.

Ciais, P., Denning, A. S., Tans, P. P., Berry, J. A., Randall, D. A., Collatz, G. J., Sellers, P. J., White, J. W. C., Trolier, M., Meijer, H. A. J., Francey, R. J., Monfray, P. and Heimann, M. (1997) 'A three-dimensional synthesis study of $\delta^{18}O$ in atmospheric CO_2: 1. Surface fluxes', *Journal of Geophysical Research: Atmospheres,* 102(D5), pp. 5857-5872.

Ciais, P., Tans, P. P., White, J. W. C., Trolier, M., Francey, R. J., Berry, J. A., Randall, D. R., Sellers, P. J., Collatz, J. G. and Schimel, D. S. (1995) 'Partitioning of ocean and land uptake of CO_2 as inferred by $\delta^{13}C$ measurements from the NOAA Climate Monitoring and Diagnostics Laboratory Global Air Sampling Network', *Journal of Geophysical Research: Atmospheres,* 100(D3), pp. 5051-5070.

Crotwell, A., Lee, H. and Steinbacher, M. (2020) *Report of the 20th WMO/IAEA Meeting on Carbon Dioxide, Other Greenhouse Gases and Related Measurement Techniques (GGMT-2019)*, Jeju Island, South Korea: World Meteorological Organization Global Atmospheric Watch (Report Series #255. Available at: https://library.wmo.int/

Cuntz, M., Ciais, P., Hoffmann, G., Allison, C. E., Francey, R. J., Knorr, W., Tans, P. P., White, J. W. C. and Levin, I. (2003) 'A comprehensive global three-dimensional model of $\delta^{18}O$ in atmospheric CO_2: 2. Mapping the atmospheric signal', *Journal of Geophysical Research: Atmospheres,* 108(D17).

Eiler, J. M. and Schauble, E. (2004) '$^{18}O^{13}C^{16}O$ in Earth's atmosphere', *Geochimica et Cosmochimica Acta,* 68(23), pp. 4767-4777.

Farquhar, G. D., Lloyd, J., Taylor, J. A., Flanagan, L. B., Syvertsen, J. P., Hubick, K. T., Wong, S. C. and Ehleringer, J. R. (1993) 'Vegetation effects on the isotope composition of oxygen in atmospheric CO_2', *Nature,* 363(6428), pp. 439-443.

Flanagan, L. B. and Ehleringer, J. R. (1998) 'Ecosystem-atmosphere CO_2 exchange: interpreting signals of change using stable isotope ratios', *Trends in Ecology & Evolution,* 13(1), pp. 10-14.

Francey, R. J. and Tans, P. P. (1987) 'Latitudinal variation in oxygen-18 of atmospheric CO_2', *Nature,* 327(6122), pp. 495-497.

Gehler, A., Gingerich, P. D. and Pack, A. J. P. o. t. N. A. o. S. (2016) 'Temperature and atmospheric CO2 concentration estimates through the PETM using triple oxygen isotope analysis of mammalian bioapatite', 113(28), pp. 7739-7744.

Gordon, I. E., Rothman, L. S., Hill, C., Kochanov, R. V., Tan, Y., Bernath, P. F., Birk, M., Boudon, V., Campargue, A., Chance, K. V., Drouin, B. J., Flaud, J. M., Gamache, R. R., Hodges, J. T., Jacquemart, D., Perevalov, V. I., Perrin, A., Shine, K. P., Smith, M.

A. H., Tennyson, J., Toon, G. C., Tran, H., Tyuterev, V. G., Barbe, A., Császár, A. G., Devi, V. M., Furtenbacher, T., Harrison, J. J., Hartmann, J. M., Jolly, A., Johnson, T. J., Karman, T., Kleiner, I., Kyuberis, A. A., Loos, J., Lyulin, O. M., Massie, S. T., Mikhailenko, S. N., Moazzen-Ahmadi, N., Müller, H. S. P., Naumenko, O. V., Nikitin, A. V., Polyansky, O. L., Rey, M., Rotger, M., Sharpe, S. W., Sung, K., Starikova, E., Tashkun, S. A., Auwera, J. V., Wagner, G., Wilzewski, J., Wcisło, P., Yu, S. and Zak, E. J. (2017) 'The HITRAN2016 molecular spectroscopic database', *Journal of Quantitative Spectroscopy and Radiative Transfer,* 203, pp. 3-69.

Graven, H., Keeling, R. F. and Rogelj, J. (2020) 'Changes to Carbon Isotopes in Atmospheric CO_2 Over the Industrial Era and Into the Future', *Global Biogeochemical Cycles,* 34(11), pp. e2019GB006170.

Griffith, D. W. T. (2018) 'Calibration of isotopologue-specific optical trace gas analysers: a practical guide', *Atmos. Meas. Tech.,* 11(11), pp. 6189-6201.

Griffith, D. W. T., Deutscher, N. M., Caldow, C., Kettlewell, G., Riggenbach, M. and Hammer, S. (2012) 'A Fourier transform infrared trace gas and isotope analyser for atmospheric applications', *Atmos. Meas. Tech.,* 5(10), pp. 2481-2498.

Hare, V. J., Dyroff, C., Nelson, D. D. and Yarian, D. A. (2022) 'High-Precision Triple Oxygen Isotope Analysis of Carbon Dioxide by Tunable Infrared Laser Absorption Spectroscopy', *Analytical Chemistry,* 94(46), pp. 16023-16032.

Hoag, K. J., Still, C. J., Fung, I. Y. and Boering, K. A. (2005) 'Triple oxygen isotope composition of tropospheric carbon dioxide as a tracer of terrestrial gross carbon fluxes', *Geophysical Research Letters,* 32(2).

Hofmann, M. E. G., Horváth, B. and Pack, A. (2012) 'Triple oxygen isotope equilibrium fractionation between carbon dioxide and water', *Earth and Planetary Science Letters,* 319-320, pp. 159-164.

Hofmann, M. E. G., Horváth, B., Schneider, L., Peters, W., Schützenmeister, K. and Pack, A. (2017) 'Atmospheric measurements of $\Delta^{17}O$ in CO_2 in Göttingen, Germany reveal a seasonal cycle driven by biospheric uptake', *Geochimica et Cosmochimica Acta,* 199, pp. 143-163.

Hofmann, M. E. G. and Pack, A. (2010) 'Technique for High-Precision Analysis of Triple Oxygen Isotope Ratios in Carbon Dioxide', *Analytical Chemistry,* 82(11), pp. 4357-4361.

IPCC (2021a) *Climate Change 2021: The Physical Science Basis. Contribution of Working Group I to the Sixth Assessment Report of the Intergovernmental Panel on Climate Change.* Cambridge, United Kingdom and New York, NY, USA: Cambridge University Press.

Keeling, R. F., Graven, H. D., Welp, L. R., Resplandy, L., Bi, J., Piper, S. C., Sun, Y., Bollenbacher, A. and Meijer, H. A. J. (2017) 'Atmospheric evidence for a global secular increase in carbon isotopic discrimination of land photosynthesis', *Proceedings of the National Academy of Sciences,* 114(39), pp. 10361-10366.

Koren, G., Schneider, L., van der Velde, I. R., van Schaik, E., Gromov, S. S., Adnew, G. A., Mrozek Martino, D. J., Hofmann, M. E. G., Liang, M.-C., Mahata, S., Bergamaschi, P., van der Laan-Luijkx, I. T., Krol, M. C., Röckmann, T. and Peters, W. (2019) 'Global 3-D Simulations of the Triple Oxygen Isotope Signature $\Delta^{17}O$ in Atmospheric CO_2', *Journal of Geophysical Research: Atmospheres,* 124(15), pp. 8808-8836.

Kozlova, E. A. and Manning, A. C. (2009) 'Methodology and calibration for continuous measurements of biogeochemical trace gas and O_2 concentrations from a 300-m tall tower in central Siberia', *Atmos. Meas. Tech.,* 2(1), pp. 205-220.
Lämmerzahl, P., Röckmann, T., Brenninkmeijer, C. A. M., Krankowsky, D. and Mauersberger, K. (2002) 'Oxygen isotope composition of stratospheric carbon dioxide', *Geophysical Research Letters,* 29(12), pp. 23-1-23-4.
Landais, A., Barkan, E., Yakir, D. and Luz, B. (2006) 'The triple isotopic composition of oxygen in leaf water', *Geochimica et Cosmochimica Acta,* 70(16), pp. 4105-4115.
Laskar, A. H., Mahata, S., Bhattacharya, S. K. and Liang, M.-C. (2019) 'Triple Oxygen and Clumped Isotope Compositions of CO_2 in the Middle Troposphere', *Earth and Space Science,* 6(7), pp. 1205-1219.
Laskar, A. H., Mahata, S. and Liang, M.-C. (2016) 'Identification of Anthropogenic CO_2 Using Triple Oxygen and Clumped Isotopes', *Environmental Science & Technology,* 50(21), pp. 11806-11814.
Liang, M. C. and Mahata, S. (2015) 'Oxygen anomaly in near surface carbon dioxide reveals deep stratospheric intrusion', *Scientific Reports,* 5.
Lopez, M., Schmidt, M., Delmotte, M., Colomb, A., Gros, V., Janssen, C., Lehman, S. J., Mondelain, D., Perrussel, O., Ramonet, M., Xueref-Remy, I. and Bousquet, P. (2013) 'CO, NOx and $^{13}CO_2$ as tracers for fossil fuel CO_2: results from a pilot study in Paris during winter 2010', *Atmospheric Chemistry and Physics,* 13(15), pp. 7343-7358.
Mahata, S., Bhattacharya, S. K. and Liang, M.-C. (2016) 'An improved method of high-precision determination of $\Delta^{17}O$ of CO_2 by catalyzed exchange with O_2 using hot platinum', *Rapid Communications in Mass Spectrometry,* 30(1), pp. 119-131.
McManus, J. B., Nelson, D. D. and Zahniser, M. S. (2015) 'Design and performance of a dual-laser instrument for multiple isotopologues of carbon dioxide and water', *Optics Express,* 23(5), pp. 6569-6586.
Miller, J. B., Tans, P. P., White, J. W. C., Conway, T. J. and Vaughn, B. W. (2003b) 'The atmospheric signal of terrestrial carbon isotopic discrimination and its implication for partitioning carbon fluxes', *Tellus B: Chemical and Physical Meteorology,* 55(2), pp. 197-206.
Pack, A. and Herwartz, D. (2014) 'The triple oxygen isotope composition of the Earth mantle and understanding ΔO^{17} variations in terrestrial rocks and minerals', *Earth and Planetary Science Letters,* 390, pp. 138-145.
Miller, M. F. (2002) 'Isotopic fractionation and the quantification of ^{17}O anomalies in the oxygen three-isotope system: an appraisal and geochemical significance', *Geochimica et Cosmochimica Acta,* 66(11), pp. 1881-1889.
Pang, J., Wen, X., Sun, X. and Huang, K. (2016) 'Intercomparison of two cavity ring-down spectroscopy analyzers for atmospheric $^{13}CO_2$ /$^{12}CO_2$ measurement', *Atmos. Meas. Tech.,* 9(8), pp. 3879-3891.
Pataki, D. E., Bowling, D. R. and Ehleringer, J. R. (2003a) 'Seasonal cycle of carbon dioxide and its isotopic composition in an urban atmosphere: Anthropogenic and biogenic effects', *Journal of Geophysical Research-Atmospheres,* 108(D23), pp. 8.
Pataki, D. E., Ehleringer, J. R., Flanagan, L. B., Yakir, D., Bowling, D. R., Still, C. J., Buchmann, N., Kaplan, J. O. and Berry, J. A. (2003b) 'The application and interpretation of Keeling plots in terrestrial carbon cycle research', *Global Biogeochemical Cycles,* 17(1), pp. 15.

Pickers, P. A., Manning, A. C., Sturges, W. T., Le Quéré, C., Mikaloff Fletcher, S. E., Wilson, P. A. and Etchells, A. J. (2017) 'In situ measurements of atmospheric O_2 and CO_2 reveal an unexpected O_2 signal over the tropical Atlantic Ocean', *Global Biogeochemical Cycles*.

Rella, C. W., Hoffnagle, J., He, Y. and Tajima, S. (2015) 'Local- and regional-scale measurements of CH_4, $\delta^{13}CH_4$, and C_2H_6 in the Uintah Basin using a mobile stable isotope analyzer', *Atmos. Meas. Tech.,* 8(10), pp. 4539-4559.

Ruckstuhl, A. F., Henne, S., Reimann, S., Steinbacher, M., Vollmer, M. K., O'Doherty, S., Buchmann, B. and Hueglin, C. (2012) 'Robust extraction of baseline signal of atmospheric trace species using local regression', *Atmos. Meas. Tech.,* 5(11), pp. 2613-2624.

Steur, P. M., Scheeren, H. A., Nelson, D. D., McManus, J. B. and Meijer, H. A. J. (2021) 'Simultaneous measurement of $\delta^{13}C$, $\delta^{18}O$ and $\delta^{17}O$ of atmospheric CO_2 – performance assessment of a dual-laser absorption spectrometer', *Atmos. Meas. Tech.,* 14(6), pp. 4279-4304.

Stoltmann, T., Casado, M., Daëron, M., Landais, A. and Kassi, S. (2017) 'Direct, Precise Measurements of Isotopologue Abundance Ratios in CO_2 Using Molecular Absorption Spectroscopy: Application to $\Delta^{17}O$', *Analytical Chemistry,* 89(19), pp. 10129-10132.

Thiemens, M. H., Chakraborty, S. and Jackson, T. L. (2014) 'Decadal $\Delta^{17}O$ record of tropospheric CO_2: Verification of a stratospheric component in the troposphere', *Journal of Geophysical Research: Atmospheres,* 119(10), pp. 6221-6229.

Thiemens, M. H., Jackson, T., Mauersberger, K., Schueler, B. and Morton, J. (1991) 'Oxygen isotope fractionation in stratospheric CO_2', *Geophysical Research Letters,* 18(4), pp. 669-672.

Wen, X. F., Meng, Y., Zhang, X. Y., Sun, X. M. and Lee, X. (2013) 'Evaluating calibration strategies for isotope ratio infrared spectroscopy for atmospheric $^{13}CO_2$ /$^{12}CO_2$ measurement', *Atmos. Meas. Tech.,* 6(6), pp. 1491-1501.

Yakir, D. and Wang, X.-F. (1996) 'Fluxes of CO_2 and water between terrestrial vegetation and the atmosphere estimated from isotope measurements', *Nature,* 380(6574), pp. 515-517.

Yeung, L. Y., Affek, H. P., Hoag, K. J., Guo, W., Wiegel, A. A., Atlas, E. L., Schauffler, S. M., Okumura, M., Boering, K. A. and Eiler, J. M. (2009) 'Large and unexpected enrichment in stratospheric $^{16}O^{13}C^{18}O$ and its meridional variation', *Proceedings of the national academy of sciences,* 106(28), pp. 11496-11501.

Young, E. D., Galy, A. and Nagahara, H. (2002) 'Kinetic and equilibrium mass-dependent isotope fractionation laws in nature and their geochemical and cosmochemical significance', *Geochimica et Cosmochimica Acta,* 66(6), pp. 1095-1104.

Yung, Y. L., DeMore, W. B. and Pinto, J. P. (1991) 'Isotopic exchange between carbon dioxide and ozone via $O(^1D)$ in the stratosphere', *Geophysical Research Letters,* 18(1), pp. 13-16.

Zhou, L., Conway, T. J., White, J. W. C., Mukai, H., Zhang, X., Wen, Y., Li, J. and MacClune, K. (2005) 'Long-term record of atmospheric CO_2 and stable isotopic ratios at Waliguan Observatory: Background features and possible drivers, 1991–2002', *Global Biogeochemical Cycles,* 19(3).

Chapter 5 Conclusions

5.1 High-precision atmospheric O_2 measurements using a Picarro G2207-*i*

High-precision measurement of atmospheric O_2, together with concurrent CO_2 measurement, provides valuable insight into many carbon cycle processes, mechanisms, and fluxes. Despite their value, however, only a very small community of researchers carry out atmospheric O_2 measurements. The main reason why this research community is so small is because high-precision O_2 measurements are technically very challenging. With this in mind, I have examined the potential of the Picarro G2207-*i* O_2 analyser for high precision measurement. Picarro analysers typically have two key advantages over many other analysers: (1) long-term baseline stability, which significantly reduces consumption of calibration and reference gases (a key logistical and financial challenge in all atmospheric greenhouse gas (GHG) measurement applications); and (2) built-in correction of water vapour influences on both the spectroscopic measurement and the mole fraction dilution of the gas species of interest. The latter property means that air samples do not need to be dried prior to analysis (or sometimes partial drying is sufficient), a key advantage in GHG measurement, where water vapour can cause numerous problems and can result in significant downtime for in-situ measurement systems. In addition to these two key advantages, Picarro analysers also incorporate built-in, very stable temperature and pressure regulation, assisting high-precision measurement.

When measuring a suite of cylinders of air with known $\delta(O_2/N_2)$ values within the typical range of ambient air, the average difference between the G2207-*i* and the declared values was 3.4 ± 2.5 per meg, which is slightly greater than the United Nations World Meteorological Organization Global Atmosphere Watch (UN WMO/GAW) programme's compatibility goal of ± 2 per meg but does fall within the extended goal of ± 10 per meg, and is similar to what can be achieved by the Sable Systems 'Oxzilla II' O_2 analyser currently employed at the Weybourne Atmospheric Observatory (WAO), Norfolk, UK.

Disappointingly, however, the built-in water-correction of the G2207-*i* does not perform as intended. During in situ tests of the G2207-*i* analyser at WAO, with both no drying and partial drying (fridge only) of the sample air there were very large differences between the values measured by the Picarro and that of the

existing Oxzilla system. An average difference of 850 ± 31 per meg for no drying and -613 ± 32 per meg for partial drying was found. The $\delta(O_2/N_2)$ values reported by the G2207-*i* were highly correlated with the reported water vapour, suggesting that a revised water correction procedure might significantly improve these results.

With full drying of sample air (< 1 ppm H_2O content), the in situ performance of the G2207-*i* was much improved. But when measuring completely dried air, the G2207-*i* overestimates the required water correction. The average difference between the Oxzilla and the water-corrected values was 22.6 ± 7.4 per meg compared to 13.6 ± 7.5 per meg for the uncorrected values. Thus, the non-water corrected values should be used in this case.

The use of a 'reference tank' (RT) to reduce the impact of drift in the analyser baseline is necessary. We found that the long-term (several days) analyser baseline was very stable, however on shorter timeframes (tens of minutes to a few hours), the baseline was more variable, compromising the precision of measurements. The average difference between the Oxzilla system and the G2207-*i* when measuring completely dried ambient air at WAO and employing an RT (every 5 hours) was 13.6 ± 7.5 per meg. From measurement of a quality control cylinder referred to as a 'target tank' (TT; every ~11 hours during the in situ WAO measurement period), the repeatability of the G2207-*i* was calculated to be ± 5.7 ± 5.6 per meg, just outside of the WMO/GAW extended repeatability goal of ± 5 per meg, and compared to ± 2.2 ± 2.0 per meg for the Oxzilla. The compatibility of the G2207-*i*, also from TT measurements, was calculated to be ± 10.0 ± 6.7 per meg, within the extended WMO/GAW compatibility goal of ± 10 per meg, compared to ± 3.0 ± 2.6 per meg for the Oxzilla.

I also investigated the use of the G2207-*i* in a recently developed application at UEA of quantifying fossil fuel CO_2 (ffCO2) using atmospheric O_2 measurements. The G2207-*i* found higher $ffCO_2$ values than the Oxzilla, with a greater uncertainty of ± 13.0 ppm, which was roughly double that from the Oxzilla (± 5.8 ppm). The larger uncertainty of the G2207-*i* results is predominantly due to measurement uncertainty. Unless it is developed further, the G2207-*i* may only be suitable for $ffCO_2$ applications with large CO_2 signals, due to the high noise-to-signal ratio.

5.1.1 Future work

Although the G2207-*i* was found to not be sufficiently precise and accurate for highly demanding atmospheric O_2 applications, there is definitely potential for future development and improvement, such as:

- Improvement to the short-term baseline drift of the G2207-*i*, either by improving the stability of the analyser itself, or via more frequent use of an RT. In this thesis, I only explored an RT frequency of once every 5 hours, but this could conceivably be much faster. Other high-precision O_2 analysers introduce RT analyses much more frequently to correct for baseline drift, for example, every 2 seconds, in the case of the vacuum ultraviolet analyser, which is the most precise atmospheric O_2 analyser presently available.
- Improvement of the built-in water correction procedure of the G2207-*i* to allow for fewer drying requirements of sample air. The high correlation between the reported O_2 and water vapour measurements implies that there is significant potential for improvement to this correction procedure.

5.2 Radon-222 as a tracer for maritime background air masses

'Background' air masses are well-mixed air masses that contain constituent gas species at mole fractions that can be considered representative of regional or hemispheric background value due to having little influence from localised sources of the constituent species. To accurately assess long-term natural and anthropogenic emissions influences and short-term pollution events on the atmosphere, it is first necessary to identify these background atmospheric conditions. Defining of a background is therefore critical for many GHG applications, yet this is challenging and within the atmospheric research community there is no universally established methodology. I have developed a novel method for calculating a 'regional maritime background' (RMB) using measurements of radon-222 at WAO, and tested it on six atmospheric gas species that are of interest in atmospheric research: CO_2, O_2, hydrogen (H_2), methane (CH_4), carbon monoxide (CO), and nitrous oxide (N_2O). The radon method involves

selecting radon activity concentration 'thresholds' that would filter out air masses with recent terrestrial influence. Any months where there were not many air masses arriving at WAO with radon activity concentrations below the set threshold were flagged for 'potential terrestrial influence' and further investigated.

The resulting backgrounds were then compared to those from a number of existing methods. Two modelled backgrounds were used for comparison: one calculated from the Met office's Numerical Atmospheric Modelling Environment (NAME), a dispersion model, and one using the Stochastic Time-Inverted Lagrangian Transport (STILT) back trajectory model. The radon results were also compared to a background derived from meteorological and statistical filtering (MET), and a purely statistical method called Robust Extraction of Baseline Signal (REBS).

I found that the use of lower radon thresholds reduces the terrestrial influence on an air mass but also reduces the number of observations available for the background calculation. Therefore, a balance needs to be found between obtaining enough data to represent the RMB and avoiding the adverse effects of terrestrial influences. At WAO, of the thresholds investigated, 200 mBq m^{-3} provided the least terrestrial influence while still providing a suitable number of observations to define the background. During the measurement period analysed, over the winter the predominant wind direction at WAO is SE, with few observations from the direction of the North Sea; therefore, WAO does not experience as many air masses representative of a RMB. The implication of this is that the radon-based RMB calculation method may be less successful during the winter; however, in comparison to other methodologies, I did not find the RMB method to be any worse over winter. RMB calculated from radon during months which were flagged for potential terrestrial influence were not more dissimilar from the other methodologies than the non-flagged months. For example, for CO_2 the difference between the NAME and radon methods during non-flagged months was 1.0 ± 0.9 ppm, and 1.0 ± 0.9 ppm for flagged months; this was similar for comparison with the other methodologies. This indicates that even during the months where WAO is experiencing fewer air masses from the maritime sector, the thresholds used in the radon method are appropriately filtering the time series. I also found that it is crucial to manually check the underlying data used in the

calculation of radon RMB's, as gaps in the datasets mean that an estimate may be produced from only one value which can significantly bias the monthly estimate.

In comparison to pre-existing background calculation methodologies the differences from the radon background were generally small with some variability depending on the processes involved in a given species' source and sink mechanisms. Other findings include:

- For CO_2 and O_2, and H_2, with large seasonal differences in sources and sinks, the differences between RMB and REBS were predominantly due to the statistical nature of the REBS method assigning these localised fluxes to the background component.
- For all gas species examined, the offset in the difference between the REBS and radon methodologies could be corrected for by 'tweaking' the input parameters used in REBS. However, if one were to only use REBS, these offsets would not be known about.
- Generally, the agreement between the NAME and radon methods was good, particularly as the NAME background was calculated using data from Mace Head (MHD), Ireland which is located on the west coast of Ireland, receiving predominantly maritime air masses from the North Atlantic Ocean with very little, if any, terrestrial or pollution sources or sinks, and thus is a good site for determining background signals.
- For H_2 there were larger disagreements between the NAME and radon methods, with an average difference of is 12.0 ± 4.2 ppb, likely due to the strong latitudinal meaning that a background measured at MHD would not be suitable for WAO. Interestingly, however, this was not the case for CO, which also displays strong latitudinal gradients, with an average difference of -0.4 ± 3.9 ppb.
- The agreement between the NAME and radon backgrounds indicates that radon could be used to validate NAME modelled backgrounds.

5.2.1 Future work

The use of radon was demonstrated as a suitable method for calculation of a monthly RMB at WAO, but there is research that can be conducted to further improve this methodology, including:

- My analysis should be repeated for non-coastal sites, such as mid-continental and mountain sites, which will present different challenges.
- The use of air quality parameters to screen out maritime emissions should be investigated as I have assumed that there are no emissions, of the gas species being investigated, over the ocean. Using the lowest percentage of mole fraction values may account for this, but the use of air quality parameters could confirm this.
- The methodology used to calculate the radon RMB can be further developed to reduce the subjectivity used in the selection of some of the thresholds used.
- Analyses should be carried out on the effects of species which have a strong latitudinal gradient on the calculation of an RMB using radon.
- For species with strong latitudinal gradients, investigation into the need for removal of data derived from air masses that have been transported from other latitudes before the calculation of the RMB for a site.

5.3 High-precision atmospheric CO_2 isotopologue measurements using an Aerodyne TILDAS analyser

High-precision measurements of the isotopologues $\delta^{13}C$, $\delta^{17}O$ and $\delta^{18}O$ of atmospheric CO_2, and the calculation of $\Delta^{17}O$ from these measurements, can provide additional information on the fluxes of CO_2 involved in the carbon cycle. To date, there have been very few published concurrent measurements of $\delta^{13}C$, $\delta^{18}O$, and $\delta^{17}O$, and the subsequent calculation of $\Delta^{17}O$ in the troposphere. This is due to the challenging requirements of the extremely high measurement precision and accuracy that is needed for both $\delta^{17}O$ and $\delta^{18}O$ to be able to define spatial gradients and seasonal cycles of $\Delta^{17}O$, with past studies being limited by the available technology. Aerodyne Research Inc. have developed a state-of-the-art tunable infrared laser adsorption spectroscopy (TILDAS) CO_2 isotopologue analyser. Unlike previous isotopologue measurement techniques it allows for the measurement of $\delta^{17}O$, in addition to $\delta^{13}C$ and $\delta^{18}O$, without the extraction of CO_2 from an air sample before analysis (which is time-consuming and complex); this capability also means that air can be measured continuously, rather than from discrete samples.

I have compared the two methods which can be used for calibration of an isotopologue analyser: the ratio method (RM), which calculates the delta values and then calibrates, and the abundance method (AM), which calibrates on individual isotopologue mole fractions and then calculate the isotopologue ratios. I found that calibration of the analyser using the RM and AM produced differences in the isotopologue and $\Delta^{17}O$ values. When measuring ambient air, the average difference in $\Delta^{17}O$ between the two methods was 0.2 ± 0.6 per meg. These differences are correlated with differences in the CO_2 mole fraction for each method, indicating that the CO_2 mole fraction dependency (CMFD) has not been fully corrected for, most likely in the RM. These differences may also be caused by a number of sources of uncertainty in the calibration methods, including:

- The TILDAS analyser's computer was not fast enough, causing pressure differences when switching between the sample and reference tank (RT).
- The RT used in the calibrations did not have assigned values of the isotopologues; the AM calibration is independent of the RT, however, a key step in the RM calibration is dependent on the RT delta values of each isotopologue.
- The $\delta^{17}O$ values were unassigned (unknown) in the calibration standards, so these were calculated based on the mass-dependent fractionation relationship with $\delta^{18}O$.
- One of the calibration standards appeared to have a misassigned $\delta^{18}O$ value. Crucially, in the RM, the residuals of the 'calibrated' measured $\delta^{18}O$ values from the assigned values in the calibration standards are used for the CMFD correction. Additionally, this value was used to calculate the $\delta^{17}O$ and $\Delta^{17}O$ in that calibration standard.

From analysis of TT measurements, the repeatability of the measurements was calculated. For $\delta^{13}C$, $\delta^{17}O$ and $\delta^{18}O$ the RM calibration method was slightly better than that of the AM calibration; both were within the extended repeatability goals of ± 0.05 ‰ for each:

- For $\delta^{13}C$ the repeatability was ± 0.016 ± 0.008 ‰ for the RM and ± 0.017 ± 0.008 ‰ for the AM.
- For $\delta^{17}O$ the repeatability was ± 0.017 ± 0.001 ‰ for the RM, and ± 0.018 ± 0.007 ‰ for the AM.

- For $\delta^{18}O$ repeatability for was ± 0.016 ± 0.009 ‰ for the RM, and ± 0.017 ± 0.009 ‰ for the AM.

The repeatability of $\Delta^{17}O$ did not meet the extended goals of ± 10 per meg, with a repeatability ± 14.0 ± 5.5 per meg for the RM and ± 14.1 ± 5.6 per meg for the AM. In the context of the observed seasonal cycles in all of the time series, the repeatability results and the differences between the calibration methods represent a small fraction of the signal.

5.3.1 Future work

The TILDAS analyser was shown to produce precise measurements of $\delta^{13}C$, $\delta^{17}O$, and $\delta^{18}O$, which can be used to further increase understanding of the global $\Delta^{17}O$ budget of tropospheric CO_2. However, there were a number of uncertainties which need to be resolved in future work:

- Replacement of the instrument's computer to stop the anomalous pressure spikes when switching between the RT and sample air.
- Assignment of the RT CO_2, $\delta^{13}C$, $\delta^{17}O$ and $\delta^{18}O$ values, which will improve the CMFD correction for the RM.
- Assignment of $\delta^{17}O$ values for all of the calibration cylinders.
- Re-assignment of the $\delta^{18}O$ value of one of the calibration standards.
- Experiments to characterise the CMFD should be undertaken.
- Continued in situ measurements to examine analyser performance.

Additionally, continued measurements of these isotopologues at WAO over multiple years will allow for the assessment of long-term trends in the time series to increase understanding of the $\Delta^{17}O$ budget of tropospheric CO_2 and to constrain GPP.

List of abbreviations

^{222}Rn – Radon-222

AM – Abundance method

APO – Atmospheric Potential Oxygen

CH_4 – Methane

CMFD – CO_2 mole fraction dependency

CO – carbon monoxide

CO_2 – Carbon dioxide

CRAM – Carbon related atmospheric measurements laboratory at UEA

CRDS – Cavity ring-down spectroscopy

ffCO_2 – fossil fuel CO_2

GAW – Global atmospheric Watch

GPP – Gross Primary Production

HYSPLIT – Hybrid Single-Particle Lagrangian Integrated Trajectory

ICOS - Integrated Carbon Observation System

IRMS - Isotope ratio mass spectrometry

MET – meteorological and statistical filtering

MHD – Mace Head observatory

N_2 – Nitrogen

N_2O – Nitrous oxide

NAME – Numerical Atmospheric Modelling Environment from the UK Met. Office

NCAS – National Centre for Atmospheric Science

O_2 – Oxygen

$O_{2,NC}$ – $\delta(O_2/N_2)$ without the Picarro water correction procedure

$O_{2,WC}$ – $\delta(O_2/N_2)$ with the Picarro water correction procedure

O_3 – Ozone

per meg – A dimensionless unit equivalent to 0.001 ‰

ppb – parts per billion

ppm – parts per million

REBS – Robust extraction of baseline signal

RM – Ratio method

RMB – Regional maritime background

RT – Reference tank

TILDAS - Tunable infrared laser direct adsorption spectroscopy

TT – Target tank

VPDB – Vienna Pee Dee Belemnite

WAO – Weybourne Atmospheric Observatory

WMO - World Meteorological Organization

WSS – Working secondary standard

$\delta(O_2/N_2)$ – atmospheric O_2/N_2 ratio

$\Delta^{17}O$ – Deviation from the mass-dependent fractionation of ^{17}O and ^{18}O

$\delta^{17}O$ – $^{17}O/^{16}O$ ratio in atmospheric CO_2

$\delta^{18}O$ – $^{18}O/^{16}O$ ratio in atmospheric CO_2